MARE

Microcalorimeter Arrays for a Rhenium Experiment

F. Gatti, G. Gallinaro, D. Pergolesi, P. Repetto, M. Ribeiro-Gomez
University of Genova, Department of Physics, and INFN-Genova, Italy

R. Kelley, C.A. Kilbourne, F. S. Porter
Goddard Space Flight Center, NASA, Maryland, USA

C. Enss, A. Fleischmann, L. Gastaldo
University of Heidelberg, Kirkhhof-Institute of Physics, Germany

L. Foggetta, A. Giuliani, M. Pedretti, M. Prest, S. Sangiorgio
University of Insubria (Como), Department of Physics and Mathematics, and INFN-Milano, Italy

C. Arnaboldi, C. Brofferio, S. Capelli, F. Capozzi, O. Cremonesi, E. Fiorini, P. Gorla, C. Nones, A. Nucciotti, M. Pavan, G. Pessina, E. Previtali, D. Schaeffer, M. Sisti
University of Milano-Bicocca, Department of Physics, and INFN-Milano, Italy

K. D. Irwin
National Institute of Standards and Technology, Boulder, Colorado, USA, USA

B. Margesin, A. Monfardini
ITC-irst, Trento, and INFN-Padova, Italy

J. Beyer
Physikalisch-Technische Bundesanstalt, Fachbereich 7.51, Berlin, Germany

P. de Bernardis, M. Calvo, S. Masi
University of Roma "La Sapienza", Department of Physics, and INFN-Roma, Italy

S. Petcov
SISSA - Scuola Internazionale Superiore Studi Avanzati, Trieste, Italy

D. McCammon
University of Wisconsin, Madison, Wisconsin, USA

19th May 2006

Contents

Chapter 1

Introduction and summary

1.1 Neutrinos and elementary particle physics

Assuming the conventional distinction between "matter", composed by fermions, and "forces", described by bosons, one immediately notices that neutrinos are the most common form of matter. Their number exceeds by far the total count of atoms in the universe. Neutrinos, being elusive, are at the same time common and mysterious. The difficulty in detecting and studying them explains why much of what we know on neutrino properties was learned in just the last six years.

We know now that neutrino flavors oscillate. From oscillations, we can evaluate the neutrino mixing matrix. The crucial feature is that unlike quark mixings, neutrino mixings are large. The meaning of this difference is not presently understood. Furthermore, oscillations inform us on mass square differences, not on the masses themselves. We know that they are much smaller than charged lepton masses, but the mass pattern is unknown.

Anyway, the discovery that neutrinos have mass is a breakthrough by itself. It is the first serious crack in the Standard Model building, after 30 years of almost boring successes. The smallness of the neutrino masses turns out to play a major role in improving our understanding of GUTs. Some GUTs allow to explain naturally small neutrino masses – if they are their own antiparticles, a fundamental issue addressed by the study of neutrinoless double β decay ($0\nu2\beta$) – and the matter-antimatter asymmetry of the universe via leptogenesis. GUTs have also the potential to provide relations among the quark mixing matrix, the lepton mixing matrix, the quark masses, and the lepton masses. The peculiar properties of neutrinos, and in particular their mass scale, are a crucial challenge for GUTs and for any unified theoretical framework.

1.2 Neutrino masses: experiments and observations

Laboratory experiments aiming at fixing the absolute neutrino mass scale are based on the study of proper nuclear processes. Single β decay is the traditional and most direct clue to investigate the electron neutrino mass. $0\nu2\beta$ can be induced by an exchange of a virtual neutrino between two nucleons bound in a single nuclide, and allows us to probe basic neutrino properties. However, only kinematical direct measurements permit to estimate neutrino masses in a model-independent approach. Nuclear β decay is by far the most sensitive process, due to the very low energy available to the particles in the final state. Unfortunately, even taking advantage of the lowest Q–value β processes in nature ($Q = 2.5$ keV for ^{187}Re and $Q = 18.6$ keV

for ^{3}H), it is very hard to get sensitivities much lower than ~ 1 eV.

From these considerations, it is clear that β decay experiments are in the game only if the neutrinos masses are quasi-degenerate. However, they are at the same time *the only safe method* to investigate this aspect, and remain therefore key experiments in neutrino physics. The other two approaches allowing to fix the absolute neutrino mass scale are not so clean and free from side assumptions as the direct kinematical analysis: $0\nu2\beta$ needs to assume Majorana nature of neutrino; cosmological bounds, also based on kinematical effects, depend however on the delicate interplay between CMB and galaxy power spectra, and are therefore much less robust in comparison with laboratory measurements. In addition, the interest for single β decay experiments is renewed by the recent re-analysis of the ^{76}Ge Heidelberg-Moscow data, claiming a most probable value for the Majorana neutrino mass of 0.4 eV and higher than 0.05 eV with 95% confidence level. If confirmed, this observation would increase the discovery potential of next generation single β decay experiments.

The best and most direct upper limits to date for the electron antineutrino mass come from electrostatic β spectrometers measuring Tritium decay end-points, with limits around 2.5 eV (Mainz and Troitzk). A much larger successor experiment (KATRIN) could reduce this limit by another factor of 10 if it is built successfully. However, these experiments suffer from difficult systematic problems with final state corrections and energy loss in the source and scattering losses throughout the spectrometer. It is inherent in this type of measurement that confidence in the results can be obtained only through confirmation by independent experiments that have different systematics.

A quite different approach to β decay end-point measurements, introduced in chapter 2.4.3, is to embed the source in the detector and make a calorimetric measurement of the decay energy. Only the neutrino escapes from the detector, so this gives a direct measurement of the desired quantity, which is the total decay energy minus that carried away by the neutrino. The advent of very sensitive cryogenic thermal calorimeters (see chapter 3) has made this a practical method. These devices currently have energy resolutions of a few eV. This technique couples naturally to the study of the ^{187}Re β spectrum, whose end-point energy is by far the smallest in nature. In addition, natural Rhenium has a specific β activity of the order of 1 Hz/mg, almost ideally suited to the typical size and time response of the thermal calorimeters. With some additional development it should be possible to implement a next generation experiment that reaches mass limits of the order of 0.2 eV. We propose here the realization of such a Rhenium experiment, named MARE (Microcalorimeter Arrays for a Rhenium Experiment), proceeding through an intermediate step (MARE-1) accompanied by a parallel R&D activity towards the final sub-eV set-up (MARE-2).

1.3 Executive summary of MARE

MARE-1 will be realized thanks mainly to the convergence of three experiences.

1. The MANU group (Genova) has realized a single device in metallic Rhenium able to set an upper limit of 26 eV for the neutrino mass at the 95% of the confidence level, and has gathered much experience in microcalorimeters of various types. They are now setting up a multi-element experiment based on transition edge sensors which will be discussed more in detail later (see chapter 4.2).

2. The MIBETA group (Milano) has achieved a remarkable result with a calorimetric mea-

surement of the decay of ^{187}Re. This was a small experiment with ten hand-assembled detectors, and reached a 2-sigma upper limit of 22 eV for the neutrino mass. A further accumulation of statistics has recently allowed to bring this limit down to 15 eV. The β source, which coincides with the sensitive part of the detector, consisted of dielectric crystals of $AgReO_4$. The MIBETA group has also shown in the past to be able to realize relatively massive microcalorimeters with record energy resolution ($\sim$5 eV FWHM) at the ^{55}Mn X-ray energies (5.9 keV and 6.4 keV). MIBETA set-up and results are described in chapter 4.3.

3. In a NASA-supported effort, the Wisconsin X-ray group and their collaborators at the Goddard Space Flight Center are making arrays of 36 microcalorimeter detectors on $\sim$20 mm square silicon chips for application to X-ray astronomy. A new array currently being developed for the Wisconsin sounding rocket instrument seems almost perfectly matched to the requirements of the Rhenium neutrino experiment.

MARE-1, which is carefully described in chapter 5, will be implemented thanks to the concurrence of the specific know-how developed by the Genoa group on transition edge sensors and by the Milano-Wisconsin-NASA collaboration on semiconductor thermistor technology. In addition to the technical experience on the sensors, these groups have also accumulated a lot of information on the β decay features and its analysis (spectral shape, calibration, background, solid state effects like BEFS, off-line analysis).

Arrays used in MARE-1 will consist of $\sim$ 300 elements, based on transition edge sensors and semiconductor thermistors, with typically 0.25 decays/s/element. Assuming an energy resolution of 10 eV FWHM and a time resolution of 100 μs for each element (reasonable parameter values based on the results presently achieved by MANU and MIBETA), the statistics gathered in three years will allow to set a limit of the order of $\sim$2 eV on neutrino mass. This will allow to scrutinize the Mainz/Troitzk results with a completely independent approach. This result can be achieved *before* KATRIN full data taking. The deployment of the whole 300 element arrays will be achieved through a gradual approach. The intermediate steps will allow the fine tuning of the final array. Other detector technologies (Neutron Transmutation Doped Ge thermistors, Magnetic Calorimeters and Kinetic Inductance Detectors) will be pursued in parallel.

The calorimetric approach to the measurement of neutrino mass would be less interesting if MARE-1 were just a dead end. It would help confirm the current Mainz/Troitzk limits, but, if no major difficulty shows up, KATRIN will eventually push this limit down another factor of 10, and the important thing would be to find a way to obtain a parallel corroboration of that result, with a technique allowing a further increase of the sensitivity. Current efforts should be aimed in a direction that offers a plausible path to this goal. A significant brute-force expansion of the MARE-1 calorimetry experiment would require $\sim$ 10000 times as many detectors: a daunting prospect. However, new microcalorimeter technologies are being developed that can reduce by a significant factor the number of individual channels required to set a sub-eV limit.

Three new approaches, discussed in chapter 6, will be pursued to reach these goals. One consists of metallic magnetic temperature sensors coupled to rhenium absorbers, described in § 6.4. Detectors based on this approach have proven to be suitable tools for high resolution x-ray spectroscopy thanks to the pioneering work of the group now operating in the University of Heidelberg. Metallic magnetic calorimeters (MMCs) function on the basis of the temperature dependence of the magnetization of a paramagnetic material, such as Au doped with Er in a small magnetic field. The temperature of an energy absorber, in thermal contact with the paramagnetic material, can be monitored with high sensitivity by using a SQUID. Higher energy

resolutions and much faster response time can be achieved with respect to the semiconductor thermistor technology.

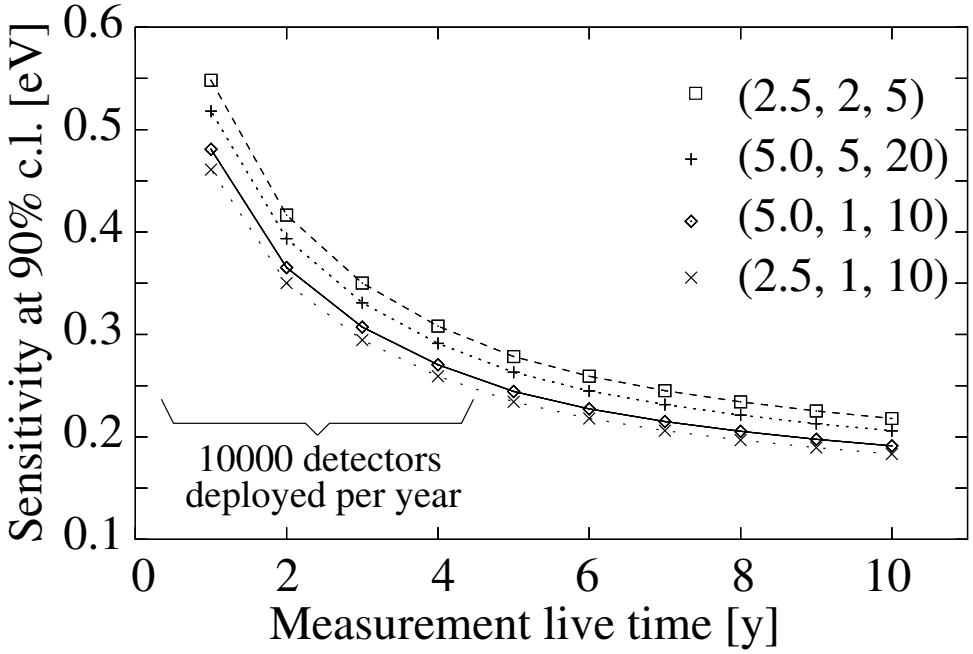

Figure 1.1 - Temporal evolution of the sensitivity to neutrino mass in MARE-2 experiment. Four different experimental configurations are considered. The triplet of numbers that label each curve indicate respectively FWHM energy resolution [eV], pulse-pair resolving time [μs] and activity of the single channel [s^{-1}].

As a second approach, Multiplexed Kinetic Inductance Detectors (MKIDs) will be explored, since these devices can provide in principle high energy resolution, fast response and the possibility to multiplex up to 10^3 – 10^4 channels on a single coaxial cable and with a single cold stage amplifier. MKIDs, described in § 6.5, are based on the fact that the inductance of a superconductive strip varies as a consequence of the absorption of quasiparticles generated in an external Re absorber, properly coupled to the strip. The strip is made part of a resonator circuit and the resonator frequency is modified by the power absorbed in form of quasiparticles. The incident power is measured through a "phase pulse" at a given frequency, which corresponds to the circuit proper one.

A third technology (presently the baseline approach for MARE-2) that can improve dramatically the sensitivity of a Re experiment consists of the already mentioned superconducting transition edge temperature sensors, or TES (see § 6.3). These are simply small strips of superconducting metal operated in the middle of the steep superconducting-to-normal transition at the critical temperature. So the TES can be thought of as simply temperature-sensitive resistors, and can be analyzed the same way as doped semiconductor thermistors. The two major differences are that the logarithmic temperature sensitivity is 60 times larger than for a practical doped semiconductor thermistor, and since the TES is metallic, the electron phonon coupling time (which limits the speed of semiconductor thermistors) is up to 100 times shorter at 50 mK for commonly-used materials. The combination of faster risetime and better signal-to-noise ratio should enable the required improvement in the pulse-pair resolving time and in the energy resolution. In addition, the DC SQUID readouts used with TES thermometers can

be integrated into the detector arrays, and their very good noise performance margin allows the construction of multiplexers that read out a number of sensors on a single channel. The Genova group is developing TES specifically for high resolution fast β spectroscopy, with an original read-out based on low temperature transformers. Intensive efforts, with remarkable intermediate successes, are on the way in many laboratories (including that one of the Wisconsin X-ray groups), with the aim to develop TES-based arrays for astronomical applications. This R&D activity is funded in preparation of the instruments for the next generation X-ray satellite observatories (XEUS, Constellation-X, NeXT). The accumulation of experience and results in this field can be profitably applied to the neutrino mass calorimetric experiment under discussion.

We propose therefore an experimental development designated as MARE-2 (see chapter 6), consisting of a R&D activity phase on faster and more sensitive phonon sensors (in parallel with MARE-1) and of a subsequent direct measurement of the neutrino mass with a global beta-event statistics several orders of magnitude higher than in MARE-1. From the point of view of systematics, MARE-2 will take advantage of the extensive information gathered in MARE-1. The aim of MARE-2 is to reach a sensitivity of the order of 0.2 eV on the neutrino mass, similar to or slightly better than that planned for the KATRIN experiment. This sensitivity will be achieved by means of a constant progression of the number of sensitive elements, in space and time. This will allow a more-than-linear growth with time of the totally collected statistics. The basic array planned for MARE-2 will be a matrix of typically $\sim$ 5000 elements with 5 eV FWHM energy resolution and 1 μs time resolution. Initially, a single array of this type will be realized and operated. This would not be a trivial experiment, but it could be physically similar in size to CUORICINO, the cryogenic pilot for the CUORE $0\nu2\beta$ experiment that is currently operating in the Gran Sasso laboratory. In terms of number of independent channels, it would be analogous to CUORE, which is generally considered as the most viable of the next generation $0\nu2\beta$ experiments.

This first array will be a pilot step, able anyway to attain a sub-eV sensitivity to the neutrino mass. In parallel, new identical or improved basic arrays will be realized and installed in other dilution refrigerators. (There are presently about five fridges in the collaboration laboratories that can technically host such arrays. Furthermore, each fridge can host 2 or 3 basic arrays simultaneously.) We foresee therefore an increase of the number of elements by 10000 single detectors per year, in different laboratories, just exploiting the existing cryogenic facilities. The final set-up will consist of a spatially-distributed array of 50000 elements, 5 years after the data-taking start-up. The sensitivity to neutrino mass achievable by this experiment is below 0.2 eV, as reported in fig. 1.1. This prediction was obtained by generating the ^{187}Re beta spectrum by a Monte Carlo method, taking into account the energy and the time resolution of the single channel. We would like to remark that, unlike KATRIN, which is technologically the ultimate ^{3}H experiment mainly because of the physical size of the spectrometer, a successful basic array in MARE-2 would make the subsequent expansion of the experiment just a solvable technical problem, consisting of the repeated replication of the first matrix. This is a clear advantage of the intrinsic modularity of the proposed approach. The smallness of the individual devices does not pose particular problems for the physical size of the cryogenic set-ups, which do not need to be realized *ad hoc* for this experiment.

Chapter 2

Science motivations

2.1 The role of neutrino mass in particle physics and cosmology

The Standard Model of electroweak interactions describes neutrinos as left-handed massless partners of the charged leptons. The experimental identification of the third generation of quarks and leptons completed the model, incorporating also a description of CP violation. The invisible width of the Z boson, caused by its decay into unobservable channels and measured at the e^+-e^- annihilation experiments, show quite confidently that there are just three active neutrinos with masses of less than $M_Z/2$.

Efforts to unify the strong and electroweak interactions led to the development of Grand Unified Theories (GUTs), which provide a natural framework for neutrino masses. In the context of GUTs it is possible to develop predictive models for the fermion masses in general and for the neutrino masses in particular. The smallness of neutrino masses is explained by means of the seesaw mechanism, which is often incorporated in GUTs in various forms. In this context, neutrino is naturally a Majorana particle. Therefore, the experimental determinations of the neutrino mass scale, pattern and nature are crucial bench tests for predictive GUTs and for the improvement of our understanding of the basic theory of fundamental interactions.

In parallel, the understanding of Big-Bang Nucleosynthesis and the features of the Cosmic Microwave Background (CMB) illustrate the important role of neutrinos in the history of the early universe. Neutrino flavor oscillations and other bounds tell us that the heaviest neutrino mass is in the range 0.04 - 0.6 eV. Therefore, neutrinos are a component of dark matter, but their total mass, although it outweighs the stars, gives only a minor contribution to invisible matter density. Neutrinos are so light to have streamed freely away from developing aggregations of matter until quite recently (in cosmological terms), when they eventually cooled and their speed has decreased to significantly less than the speed of light. What is then the neutrino role in shaping the universe? Do neutrinos allow to understand the matter-antimatter asymmetry of the universe, via leptogenesis? The answer to these questions requires the precise knowledge of the neutrino mass values.

It is clear therefore that the neutrino mass scale is crucial over two fronts: progress in the comprehension of elementary particles and solution of hot astroparticle problems. The studies of neutrinoless double beta (0ν-$\beta\beta$) decay and end-point anomalies in beta decay, in particular, are essential and unique in their potential to fix the neutrino masses and to answer key-questions beyond neutrino physics itself. Beta-decay endpoint measurements, frequently

Table 2.1 - Cosmological determination of the neutrino mass according to different authors and on the basis of different data set and assumptions. The systematic spread in the limits/values is apparent.

author	WMAP	CMB_{hi-l}	SDSS	2dF	other data	$\sum m_\nu$ [eV]
Bar'03	x	x	x	x	h(HST)	< 0.75
Teg'03	x	x	x		SNIa	< 1.7
ASB'03	x	x		x	XLF	$= 0.36 - 1.03$
WMAP	x	x		x	Lyα, h(HST)	< 0.7
Bla'03	x			x	$\Omega_m = 1$	$= 2.4$
Han'03	x	x		x	h(HST) , SNIa	< 1.01
Han'03	x	x		x		< 1.2
Han'03	x			x		< 2.12

referred to as "direct searches" for neutrino mass, are essentially free of theoretical assumptions about neutrino properties, and are not just complementary to the search of 0ν-$\beta\beta$ decay. In fact, both types of measurements will be required to fully untangle the nature of the neutrino mass.

In particular, high precision end-point study of beta decay is a physics program to be pursued with high priority and, if possible, with diverse techniques for several good reasons, discussed below.

- The constrain and the possible estimation of the neutrino mass is based *only* on kinematical assumptions and is therefore totally model independent (this is a unique case in the experimental methods to investigate neutrino mass).

- The achievable sensitivity (down to 0.2 eV) matches the present sensitivities of other, model dependent, searches, such as cosmological determination through the study of CMB fluctuations and 0ν-$\beta\beta$ decay. The former method, even if very sensitive, depends critically on astrophysical assumptions and requires therefore independent checks. The situation is summarized in table 2.1, where one notes that *finite* values of the neutrino mass in the single beta decay sensitivity range are claimed by some authors, and the spread of the limits show the intrinsic uncertainties of this approach. The latter method relies on the Majorana nature of neutrino. Even in this case, crucial information can come from single beta decay. In fact, the claim of Klapdor-Kleingrothaus *et al.* (best value for Majorana neutrino mass around 0.4 eV) can be confirmed independently by a pure kinematical approach.

- The investigated range corresponds to the degenerate case of neutrino mass pattern. Due to the somewhat surprising properties of neutrinos with respect to charge fermions, there is no real serious reason to have prejudice against this behavior of neutrino masses.

- The beta decay end-point represents a quite unusual physical situation in fundamental interaction experiments, involving very low energy neutrinos, almost at rest in the limit of electrons with energy ($Q - m_\nu c^2$). This is a favorable case for new, unexpected phenomena to show up.

- The proposed beta decay experiments are quite difficult and dominated by a complicated systematics. This imposes the use of at least two complementary techniques. The

technique proposed in this document, although less sensitive at the moment, has the advantage of having no "a priori" limitation for future expansions, either of fundamental or technological reasons.

2.2 The neutrino mass pattern and mixing matrix

Neutrino oscillations can take place since the neutrinos of definite flavor (ν_e, ν_μ, ν_τ) are not necessarily states of a definite mass (ν_1, ν_2, ν_3). On the contrary, they are generally coherent superpositions of such states:

$$|\nu_l\rangle = \sum_i U_{li}|\nu_i\rangle \tag{2.1}$$

When the standard model is extended to include neutrino mass, the mixing matrix U is unitary. As a consequence the neutrino flavor is no longer a conserved quantity and for neutrinos propagating in vacuum the amplitude of the process $\nu_l \to \nu_{l'}$ is not vanishing.

The probability of the flavor change is the square of this amplitude. Due to the unitarity of U there is no flavor change if all masses vanish or are exactly degenerate. The idea of oscillations was discussed early on by Pontecorvo, and by Maki, Nakagawa and Sakata. Hence, the mixing matrix U is often associated with these names and the notation U_{MNS} or U_{PMNS} is used. In general, the mixing matrix of 3 neutrinos is parametrized by three angles, conventionally denoted as Θ_{12}, Θ_{13} and Θ_{23}, one CP violating phase δ and two Majorana phases α_1, α_2. Using c for the cosine and s for the sine, the mixing matrix U is then expressed as

$$\begin{pmatrix} \nu_e \\ \nu_\mu \\ \nu_\tau \end{pmatrix} = \begin{pmatrix} c_{12}c_{13} & s_{12}c_{13} & s_{13} \\ -s_{12}c_{23} - c_{12}s_{23}s_{13}e^{i\delta} & c_{12}c_{23} - s_{12}s_{23}s_{13}e^{i\delta} & s_{23}c_{13} \\ s_{12}s_{23} - c_{12}c_{23}s_{13}e^{i\delta} & -c_{12}s_{23} - s_{12}c_{23}s_{13}e^{i\delta} & c_{23}c_{13} \end{pmatrix} \begin{pmatrix} e^{i\alpha_1/2}\nu_1 \\ e^{i\alpha_2/2}\nu_2 \\ \nu_3 \end{pmatrix}$$

The three neutrino masses m_i have to be added to the parameter set that describes this matrix, giving therefore nine unknown parameters altogether. The evidence for oscillations of solar (ν_e and atmospheric (ν_μ and $\overline{\nu_\mu}$ neutrinos is compelling and generally accepted.

Two of the three angles and the two mass square differences have been determined reasonably well. The unknown quantities, subjects of future oscillation experiments, are the angle Θ_{13} and the sign of Δm^2_{13}. If that sign is positive, the neutrino mass pattern is called a normal mass ordering ($m_1 < m_2 < m_3$) and when it is negative it is called inverted mass ordering ($m_3 < m_1 < m_2$). The extreme mass orderings, $m_1 < m_2 \ll m_3$ and $m3 \ll m_1 < m_2$, are called the normal and, respectively, inverted hierarchies. When $m_1 \sim m_2 \sim m_3$, one speaks of degenerate pattern. In addition, the phase δ governing CP violation in the flavor oscillation experiments remains unknown, and a topic of considerable interest. The remaining unknown quantities, i.e. the absolute neutrino mass scale and the two Majorana phases α_1 , α_2, are not accessible in oscillation experiments. Their determination is the ultimate goal of 0ν-$\beta\beta$ and beta decay experiments.

2.3 Single and double beta decay and neutrino mass scale

Direct neutrino mass measurements are performed by analyzing the kinematics of charged leptons and/or pions emitted together with flavor state neutrinos in suitable weak decays. The most sensitive neutrino mass measurement to date, involving electron type neutrinos, is based

on studying the shape of the beta spectrum, subject of the present document, following an idea belonging to Enrico Fermi and tracing back to the primordial era of weak interactions. In such measurements the quantity

$$m_{\nu_e} = \sqrt{\sum_{i=1}^{3} |U_{ei}|^2 m_i^2}. \tag{2.2}$$

is determined or constrained, where the sum is over all mass eigenvalues m_i, too close each other to be resolved experimentally. A limit on m_{ν_e} implies trivially an upper limit on the minimum value m_{min} of all m_i , independent of the mixing parameters U_{ei}: $m_{min} \leq m_{\nu_e}$, i.e., the lightest neutrino cannot be heavier than m_{ν_e} .

However, if experiments on neutrino oscillations provide us with the values of all neutrino mass-squared differences Δm_{ij}^2 (including their signs) and the mixing parameters $|U_{ei}|^2$, and the value of $m_{\nu_e}^2$ has been determined in a future search, then the individual neutrino mass squares can be determined:

$$m_j^2 = m_{\nu_e}^2 - \sum_{i=1}^{3} |U_{ei}|^2 \Delta m_{ij}^2 \qquad (\Delta m_{ij}^2 = m_i^2 - m_j^2) \tag{2.3}$$

On the other hand, if only the absolute values $|\Delta m_{ij}^2|$ are known (but all of them), a limit on $m_{\nu_e}^2$ from beta decay may be used to define an upper limit on the maximum value m_{max} of m_i:

$$m_{max}^2 \leq m_{\nu_e}^2 + \sum_{i<j} |\Delta m_{ij}^2| \tag{2.4}$$

In other words, knowing $|\Delta m_{ij}^2|$ one can use a limit on m_{ν_e} to constrain the heaviest active neutrino.

The neutrinoless double beta decay is a rare nuclear process, energetically possible for a few tens of candidate nuclides and experimentally interesting for less than ten nuclides. It consists in the transformation

$$(Z, A) \rightarrow (Z + 2, A) + e_1^- + e_2^- \tag{2.5}$$

which violates by two unities lepton number conservation. Experimentally, it can be identified versus the SM allowed two neutrino process by its electron sum energy spectrum, which exhibits a peak at the Q-value of the decay.

The 0ν-$\beta\beta$ decay requires a mechanism changing two neutrons into two protons with the emission of two electrons and nothing else. One can visualize it by assuming that the process involves the exchange of proper virtual particles between two single-beta-decay-like vertices, e.g. light or heavy Majorana neutrinos, right-handed weak interaction mediated by the W_R boson, SUSY particles, and other more exotic options. Of primary interest is the process mediated by the exchange of light Majorana neutrinos interacting through the left-handed V-A weak currents. The decay rate is then,

$$(T_{0\nu}^{1/2})^{-1} = G_{0\nu}(Q, Z) \cdot M_{0\nu} \cdot m_{ee}^2 \tag{2.6}$$

where $G_{0\nu}$ is the accurately calculable phase space integral, M_{ee} is the effective neutrino mass, and $M_{0\nu}$ the nuclear matrix elements. If the 0ν-$\beta\beta$ decay is observed, and the nuclear matrix elements are known, one can deduce the corresponding m_{ee} value, which in turn is related to the oscillation parameters by

$$m_{ee} = \left| \sum_{i=1}^{3} |U_{ei}|^2 m_i e^{i\alpha_i} \right| \tag{2.7}$$

Due to the presence of the unknown Majorana phases α_i, cancellation of terms is possible, and m_{ee} could be smaller than any of the m_i. Thanks to the information we have from oscillations, it is useful to express m_{ee} in terms of three unknown quantities: the mass scale, represented by the mass of the lightest neutrino m_{min}, and the two Majorana phases. It is then useful to distinguish the already discussed three mass patterns: normal hierarchy (NH), inverted hierarchy (IH), and the quasi-degenerate spectrum (QD) where $m_{min} \gg \sqrt{|\Delta m^2_{31}|}$ as well as $m_{min} \gg \sqrt{|\Delta m^2_{21}}$.

In the case of normal hierarchy, and assuming that $m_1 = m_{min}$ can be neglected, $\Theta_{13} = 0$ and inserting the parameters as presently known from the analysis of the oscillation experiments, one obtains $m_{ee} = 2.6 \pm 0.3$ meV. On the other hand, there are possible combinations of Θ_{13}, Θ_{12}, Δm^2_{31} and Δm^2_{21} which provide a partial or complete cancellation, leading to a vanishing m_{ee}. Not only, if $m_{min} > 0$ then m_{ee} may vanish even for $\Theta_{13} = 0$.

In the case of the inverted hierarchy, and again assuming that $m_3 = m_{min}$ can be neglected, $\Theta_{13} = 0$ and inserting the oscillation-derived parameters, one obtains $m_{ee} \simeq 14 - 51$ meV, depending on the Majorana phases.

Finally, for the quasi-degenerate spectrum, m_0 being the common mass value and making the same assumption as above, $m_{ee} \simeq (0.71 \pm 0.29) \cdot m_0$. Detailed discussion of the relation between m_{ee} and the absolute neutrino mass scale can be found in numerous papers.

If one can experimentally establish that $m_{ee} \geq 50$ meV, one can conclude that the QD pattern is the correct one, and one can extract an allowed range of m_{min} values from the figure. On the other hand, if m_{ee} lies in the range 20-50 meV, only an upper limit for m_{min} can be established, and the pattern is likely IH, even though exceptions exist. Eventually, if one could determine that $m_{ee} < 10$ meV but non-vanishing (which is unlikely in a foreseeable future), one could conclude that the NH pattern is the correct one.

Altogether, observation of the 0ν-$\beta\beta$ decay, and accurate determination of the m_{ee} value, would not only establish that neutrinos are massive Majorana particles, but would contribute considerably to the determination of the absolute neutrino mass scale. Moreover, if the neutrino mass scale would be known from independent measurements, one could possibly obtain from the measured m_{ee} also some information about the CP violating Majorana phases.

As shown above, 0ν-$\beta\beta$ and β decays both depend on different combinations of the neutrino mass values and oscillation parameters. The 0ν-$\beta\beta$ decay rate is proportional to the square of a coherent sum of the Majorana neutrino masses because the process originates from exchange of a *virtual* neutrino. On the other hand, in beta decay one can determine an incoherent sum because a *real* neutrino is emitted. That shows clearly that a complete neutrino physics program cannot renounce either of these two experimental approaches. The various methods that constrain the neutrino absolute mass scale are not redundant but rather complementary. If, ideally, a positive measurement is reached in all of them (0ν-$\beta\beta$ decay, β decay, cosmology) one can test the results for consistency and with a bit of luck determine the Majorana phases.

2.4 The direct neutrino mass measurement via single beta decay

As already pointed out, the most useful process to constrain kinematically the neutrino mass is the study of the "visible" energy in single beta decay. The most stringent present limits are obtained by studying the distribution of the electron energy in proximity of the end-point of

Table 2.2 - Classification and terminology for beta decays.

$L = 0, 1$	$\pi_f \pi_i = +1$	Allowed transitions
$L = 0, 1$	$\pi_f \pi_i = -1$	Non unique first forbidden transitions
$L > 1$	$\pi_f \pi_i = (-1)^L$	Non unique L-th forbidden transitions
	$\pi_f \pi_i = (-1)^{L-1}$	Unique (L-1)-th forbidden transitions

the decay. These limits are 2.5 eV for electrostatic spectrometer and 16 eV for calorimeters, the two most powerful methods that will be discussed extensively in the following. The particle emitted in the experiments performed up to now is, for the precision, the electron antineutrino $\overline{\nu}_e$. Since the CPT theorem assures that particle and antiparticle have the same rest mass, from now on we will speak simply of "neutrino mass" both for ν_e and $\overline{\nu}_e$.

The beta decay is a nuclear transition involving two nuclides $(A, Z-1)$ and (A, Z):

$$(A, Z-1) \rightarrow (A, Z) + e^- + \overline{\nu}_e \tag{2.8}$$

The energy E_0 available in the final state is given by:

$$E_0 = M(A, Z-1)c^2 - M(A, Z)c^2 \tag{2.9}$$

where M indicates the mass of the *atoms* in the initial and final state.

Single beta decays can be classified according to the selection rules reported in table 2.2. In the reported table, $L = \Delta J = |J_i - J_f|$; J_i, J_f, π_i and π_f are respectively the spins and the parities of the initial and final nuclides.

If one neglects the nucleus recoil energy, the energy spectrum of the emitted electrons is described in the most general form by

$$N_\beta(Z, E_\beta, m_{\nu_e}) = p_\beta E_\beta (E_0 - E_\beta)\sqrt{(E_0 - E_\beta)^2 - m_{\nu_e}^2 c^4}\, F(Z, E_\beta) S(E_\beta)[1 + \delta_R(Z, E_\beta)] \tag{2.10}$$

where, by indicating with p_β e E_β the momentum and the energy of the emitted electron respectively, the following terms appear:

- $p_\beta E_\beta (E_0 - E_\beta)\sqrt{(E_0 - E_\beta)^2 - m_{\nu_e}^2 c^4}$ is the phase space term in a three-body decay, for which the nuclear recoil is neglected.
- $F(Z, E_\beta)$ is the term called *Coulombian correction* (or Fermi function) which accounts for the effect of the nuclear charge on the wave function of the emitted electron. In a model dealing with the relativistic effects and the finite size of the nucleus, this term appears as

$$F(Z, E_\beta) = 4\left(\frac{2p_e R}{\hbar}\right)^{2\gamma-2} \exp(\pi\eta) \frac{|\Gamma(\gamma + i\eta)|^2}{|\Gamma(2\gamma+1)|^2} \approx \frac{2\pi\eta}{1 - \exp(-2\pi\eta)} \tag{2.11}$$

  where $\eta = \alpha Z E_\beta / p_e$, $\gamma = (1 - (\alpha Z)^2)^{1/2}$, R is the nuclear radius, approximated by $R = 1.2A^{1/3}$ fm, and α is the fine structure constant. The formula (2.11) can be derived by the solution of the Dirac equation with point-like nucleus, computed at a distance R from the nucleus. One can find also computations for extended nuclear charge distributions in the literature. In (2.11), the shielding effect of the $Z-1$ electrons of the initial atom was

neglected. This effect is accounted for by replacing the energy E_β of the emitted electron with the term $E'_\beta = E_\beta - \langle V_s \rangle$, where $\langle V_s \rangle$ is the average potential experimented by the electron at the nuclear surface due to the atomic electrons. That allows to modify (2.11) to the form

$$F'(Z, E_\beta) = F(Z, E_\beta - \langle V_s \rangle) \frac{E_\beta - \langle V_s \rangle}{E_\beta} \tag{2.12}$$

In the Thomas-Fermi atomic model, one obtains that $\langle V_s \rangle = 1.45\, m_e \alpha^2 Z^{4/3}$.

- $S(E_\beta)$ is the *form factor* of the beta spectrum, which contains the nuclear matrix element of the electroweak interaction $\mathcal{M}(\mathcal{E}_\beta)$ and can be written as

$$S(E_\beta) = G_F^2 \left(\frac{m_e^5 c^4}{2\pi^3 \hbar^7} \right) cos^2\theta_c |\mathcal{M}(\mathcal{E}_\beta)|^\in \tag{2.13}$$

  where G_F is the Fermi constant and θ_c the Cabibbo angle. The matrix element can be calculated by describing the interaction with a Hamiltonian including a vector and an axial term (V-A theory).

- $\delta_R(Z, E_\beta)$ is the radiative electromagnetic correction, usually neglected due to its exiguity.

The experimental beta spectra are normally analyzed by means a transformation which produces a quantity generally linear with the energy E_β of the emitted electron:

$$K(E_\beta) \equiv \sqrt{\frac{N_\beta(Z, E_\beta, m_{\nu_e})}{p_\beta E_\beta F(Z, E_\beta) S(E_\beta)[1 + \delta_R(Z, E_\beta)]}} = (E_0 - E_\beta) \left(1 - \frac{m_{\nu_e}^2 c^4}{(E_0 - E_\beta)^2} \right)^{1/4} \tag{2.14}$$

The graph of this quantity as a function of E_β is named Kurie plot.

Assuming massless neutrinos and infinite energy resolution, the Kurie plot is a straight line intersecting the X-axis at the transition energy E_0. In case of massive neutrino, the Kurie plot is distorted close to the end-point and intersects the X-axis at the energy $E_0 - m_\nu$. The two situations are depicted in figure 2.1. Most of the information on neutrino mass are therefore contained in the final part of the Kurie plot. Unluckily enough, this is the region where the counting rate is lower. In particular, the relevant energy interval is $\delta E \approx 3 m_{\nu_e}$ and the fraction of events occurring there is

$$F(\delta E) = \int_{E_0 - \delta E}^{E_0} N_\beta(Z, E, m_{\nu_e} = 0) dE \approx 2 \left(\frac{\delta E}{E_0} \right)^3 \tag{2.15}$$

In order to give the feeling of the difficulty, we apply this formula to the case of tritium ($E_0 = 18.6$ keV) assuming a "huge" neutrino mass equal to 5 eV: the useful event fraction is only 1.5×10^{-9}.

Other factors complicate the extraction of the neutrino mass from the final part of the Kurie plot. First of all, no instrument has an infinite energy resolution. This distorts the Kurie plot in an opposite way with respect to the neutrino mass effect. It is therefore mandatory to evaluate and/or measure the detector response function, which includes the energy resolution but is not entirely determined by it. Secondly, the atom or the molecule containing the decaying nucleus can be left in an excited state, leading even in this case to dangerous distortions of the Kurie

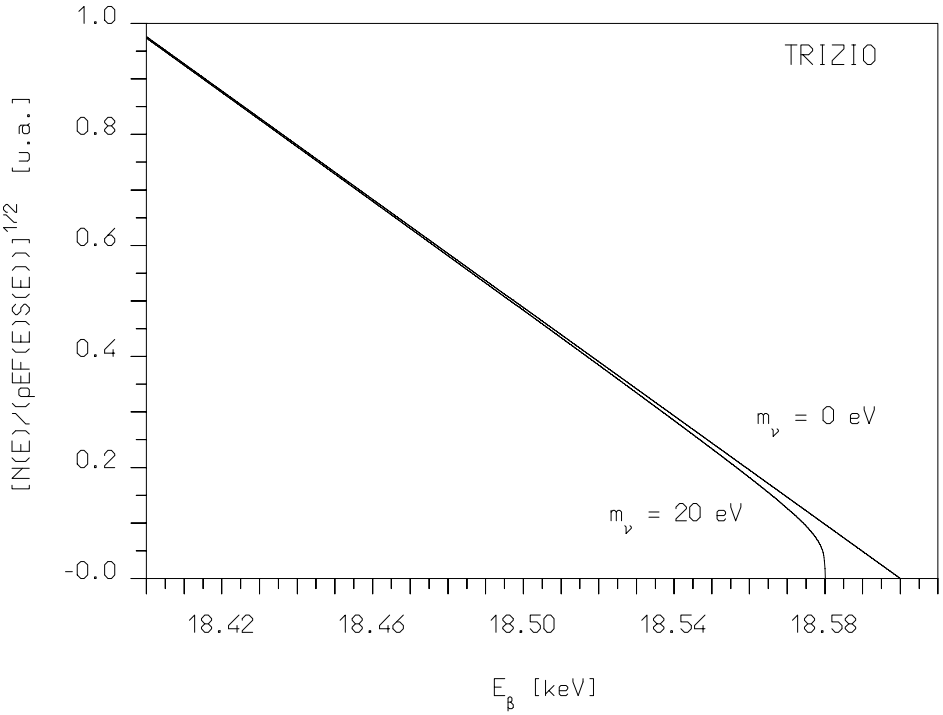

Figure 2.1 - ^{3}H Kurie plot close to the end-point, computed for neutrino masses equal to 0 and 20 eV.

plot. This topic will be treated extensively later, due to the different role that it plays in the two most powerful techniques adopted today. Finally, the analysis of the final part of the Kurie plot is complicated by the background due to cosmic rays and environmental radioactivity. Because of the low beta counting rate in the interesting region, spurious background counts may affect the neutrino mass determination. It is possible to show that an uncertainty δB in the radioactive background evaluation modifies the spectrum according to

$$N_\beta(Z, E_\beta, 0) \approx p_\beta E_\beta (E_\beta - E_0)^2 \left(1 + \frac{\delta B}{p_\beta E_\beta (E_\beta - E_0) F(Z, E_\beta) S(E_\beta)}\right) F(Z, E_\beta) S(E_\beta) \quad (2.16)$$

simulating therefore a negative $m^2_{\nu_e}$ equal to $-2\delta B/(p_\beta E_\beta F S)$ (the background rate B, and equivalently the uncertainty δB is expressed as counts per time and energy unity).

2.4.1 The cases of ^{3}H and ^{187}Re

Two beta decays will be discussed here, the tritium (^3H or T) beta decay, extensively used in the last thirty years with magnetic and electrostatic spectrometers, and the rhenium (^{187}Re) beta decay, ideal candidate for calorimetric experiments based on bolometers, main subject of the present document.

Tritium beta decay

$$^3H \rightarrow ^3He + e^- + \overline{\nu}_e \quad (2.17)$$

is an allowed transition with $E_0 = 18.6$ keV, one of the lowest in nature. The type of transition poses no problem for the analytical determination of the electron energy spectrum, at least as far as nuclear effects are concerned (see table 2.2). In addition, its lifetime of only 12.3 y allows to realize sources with high specific activity.

The ^{187}Re beta decay

$$^{187}Re(5/2^+) \rightarrow ^{187}Os(1/2^-) + e^- + \overline{\nu}_e \tag{2.18}$$

is a unique first forbidden transition, as can be deduced from table 2.2. Unlike non-unique transitions, the nuclear matrix element is computable, even if the calculation is not straight forward as in the case of T. In literature, it is possible to find detailed calculations both of the matrix element and of the Fermi function for this process. The transition energy is 2.47 keV (the lowest known) and the half lifetime is 43.2 Gy. These values were determined with bolometric experiments, as extensively exposed later on in this document. The large isotopic abundance (62.8 %) of ^{187}Re in natural rhenium allows to get useful source without any isotopic separation process. The beta decay rate in natural rhenium is of the order of ∼1 Bq/mg, almost ideally suited to bolometric detection. Thanks to the much lower transition energy, the useful fraction of events close to the end-point is ∼350 times higher in rhenium than in tritium. We note also that a precise direct determination of the lifetime of the ^{187}Re beta decay is of great interest in geochronology for the determination of the age of minerals and meteorites from their Re-Os relative abundance.

2.4.2 The electrostatic spectrometers: pros and cons

Since the Sixties of the last century, many experiments were performed for the determination of the neutrino mass using tritium beta decays and magnetic or electrostatic spectrometers. Magnetic spectrometers select electrons with given energy by means of the bending effect of a proper magnetic field. They allowed to obtain the most sensitive results until the Nineties. Since then, the leading technique has become that using electrostatic spectrometers with adiabatic magnetic collimation. In these devices, the electrons are collimated by means of a magnetic field with a characteristic space profile and selected by an electrostatic potential barrier. Higher energy resolutions and luminosities can be achieved with respect to magnetic spectrometers. The history of the results obtained with these techniques, up to the present most stringent limits, is reported in table 2.3. The electrostatic spectrometers have two main advantages, which make them the most sensitive devices in this field at the moment.

- Only the useful fraction of electrons whose energies are close to the transition energy can be selected. This allows to concentrate the analysis on the relevant part of the Kurie plot, without disturbances coming from the lower energy electrons. Therefore, a very high statistics can be accumulated in the interesting interval.

- A very high energy resolution can be achieved (of the order of 1 eV for next generation experiment), better than that provided by energy dispersive counters based on nuclear techniques.

There is however a main disadvantage that produces a chain of inconvenient effects: the radioactive source is *external* at the detector. Therefore, it is necessary to deconvolve the so-called response function of the instrument from the data, in order to trace back to the pure shape of

Table 2.3 - Summary of the most sensitive experiments using spectrometers. In the second column, M indicates magnetic and E electrostatic spectrometers.

Group	**Type**	**Source**	ΔE_{FWHM} [eV]	m_ν^2 [eV^2]	m_ν [eV]
ITEP [1]	M	Valine	25	1215 ± 130	35
INS [2]	M	$C_{20}H_{40}O_2$ (2 layers)	30	$-65 \pm 85 \pm 65$	< 13
Zürich [4]	M	OTS (1 layer)	17	$-24 \pm 48 \pm 61$	< 11
LANL [3]	M	T_2 (gas)	23	$-147 \pm 68 \pm 41$	< 9.3
LLNL [5]	M	T_2 (gas)	18	$-130 \pm 20 \pm 15$	< 7
Troitzk [6]	E	T_2 (gas)	3.2	$-1.9 \pm 3.4 \pm 2.2$	< 2.5
Mainz [7]	E	T_2 (solid)		$-1.2 \pm 2.2 \pm 2.1$	< 2.2

the electron energy distribution. The experimentally observed beta decay $N_\beta^{exp}(E)$ is given by

$$N_\beta^{exp}(E) \propto (1 + \alpha(E - E_0))S(E)(R \otimes E_L \otimes N_\beta(E)) \tag{2.19}$$

where $N_\beta(E)$ is the spectrum described by (2.10). A discussion follows of the other terms.

- R accounts for the energy resolution of the spectrometer, that can be determined either experimentally (using monochromatic electron sources) or numerically. This introduces a systematics.
- E_L describes the self-absorption in the source, which modifies the energy of the emitted electrons.
- $(1 + \alpha(E - E_0))$, present when the source is deposited on a solid substrate, represents the mechanism according to which an electron emitted towards the support is reflected backwards and enters the spectrometer. α is a free parameter of the analysis.
- $S(E)$ contains the energy dependence of the spectrometer acceptance and can be computed analytically.

The experience with the Mainz and Troitzk experiments shows that other factors can appear *after* the data taking and analysis, not predicted *a priori*. In the Mainz experiment, convincing results were obtained only after the inclusion of an unexpected effect due to the roughness of the solid tritium source. In the Troitzk experiment, a step function of unknown origin in the electron integral spectrum must be added in order to get meaningful results on the neutrino mass. This demonstrated that a precise evaluation of the response function is extremely difficult and subjected to systematical uncertainties.

Another important effect is connected to the already mentioned role of the excited states in the source. Since this is one of the main points that distinguish the spectrometers from the calorimeters, it will be treated in detail in sub§ 2.4.4.

2.4.3 The calorimetric method: pros and cons

In an ideal calorimetric experiment, the source is embedded in the detector and therefore only the neutrino energy escapes to detection. The part of the energy spent for the excitation of

atomic or molecular levels is measured through the de-excitation of these states, provided that their lifetime be negligible with respect to the detector time response. In other terms, the kinematical parameter which is effectively measured is the neutrino energy, in the form of a missing energy, common situation in experimental particle physics. As shown in chapter 3, we propose here to realize a true calorimeter by implementing bolometers based on rhenium or a compound of its.

The advantages of a calorimetric measurement are summarized in the following.

- Measurement of the energy stored in excited states.
- No self-absorption problem.
- No backscattering from the detector.
- No reflection on the source substrate.

However, there is an important inconvenience which represents a serious limitation for this approach. It is not exaggerate to say that most of the technical and fundamental difficulties in calorimetric experiments are connected to this inconvenience. In a calorimeter, the whole beta spectrum is acquired. This forces to keep a low counting rate in order not to generate distortions of the spectral shape due to pulse pile-up. Therefore, serious limitations to the statistics that can be accumulated take place.

Decays which occur within a definite time interval cannot be resolved by a calorimetric detector, giving rise to the phenomenon of pile-up. This implies that a certain fraction of the detected events is the sum of two or more single events. In particular, two low energy events can sum up and contribute with a count in the region close to the transition energy, contaminating the spectral shape in the most critical interval. This is even more serious in a bolometer, which is intrinsically slow, in particular if the temperature sensor is a semiconductor thermistor.

Assuming that the pulse-pair resolving time of the detector be τ_R, the fraction of events which suffer with not-identified pile-up (for Poissonian time distribution) is

$$P(\Delta t < \tau_R) = 1 - e^{-A\tau_R} \tag{2.20}$$

where A is the source activity and Δt is the time separation between two events. The beta spectrum observed in presence of pile-up is the convolution product

$$N'_\beta(Z,E) = N_\beta(Z,E) + (1 - e^{-A\tau_R}) \int_0^{E_0} N_\beta(Z,E') N_\beta(Z,E-E') dE'. \tag{2.21}$$

The spurious counting rate due to pile-up in the interval ΔE below the transition energy is given by

$$A_{pile-up}(m_{\nu_e}, \Delta E) = A(1 - e^{-A\tau_R}) \int_{E_0-\Delta E}^{E_0} dE \int_0^{E_0} dE' N_\beta(Z,E') N_\beta(Z,E-E'). \tag{2.22}$$

It can be computed that the ratio between spurious events and genuine single beta events in the interval ΔE is approximately provided by

$$\frac{A_{pile-up}(0,\Delta E)}{A(0,\Delta E)} \approx 0.25 \, \frac{\tau_R A E_0^2}{\Delta E^2} \tag{2.23}$$

Imposing that this ratio be less 10% in a calorimetric rhenium experiment for a 10 eV energy resolution and for $\tau_R \sim$100 μs, the source decay rate must be less than 0.2 Bq.

Another critical phenomenon which characterizes calorimetric detection is a solid state effect known as Beta Environmental Fine Structure (BEFS). A beta spectrum can be deformed by an effect similar to the Extended X-ray Absorption Fine Structure (EXAFS). The EXAFS is the oscillatory pattern observed in X-ray absorption spectra just above the absorption edges. EXAFS is caused by the reflection of the ejected photoelectron by neighbouring atoms producing a standing wave in the region immediately surrounding the absorbing atom; these oscillations depend on the interatomic distance, while their amplitude is tied to the electron-atom scattering cross section. An analogous effect is expected when the electron emitted by a nucleus is reflected by the neighbouring atoms of a molecule or of a crystal, where the emitting nucleus is embedded. This effect, named BEFS as pointed out, could be of considerable interest for the study of materials. It could be detected in the low energy region of a spectrum, which is generally more populated when the transition energy is low. BEFS has been detected in metallic rhenium and in a compound (silver perrhenate $AgReO_4$). As far as the effect on the neutrino mass determination is concerned, a careful study of the phenomenon is mandatory, in order to include it in the theoretical spectral shape used to perform the analysis. It is worthwhile to say however that BEFS is detectable at low energies, while its effect at the end-point is likely negligible in the first phase of the experimental plan here exposed.

2.4.4 Calorimeters and spectrometers: critical comparison

A general consideration that derives from the analysis performed above is that the spectrometer and the calorimeter methods have both complicated but totally different systematic effects. Therefore, once that one demonstrates that the achievable sensitivities are of the same order of magnitude in the two cases, it is very sound scientifically to develop complementary experiments exploiting these two techniques. Given that a next generation experiment based on spectrometers (KATRIN) is approved and in course of development, we propose here that a next generation bolometric experiment, following the experience of MANU and MIBETA, be developed and realized in the next years.

We do not repeat here the clear and complementary advantages and disadvantages of the two approaches, but we would like to stress a strong point in favor of the calorimetric mode, which concerns the excited state problem.

Due to the excited final states, the measured beta spectrum is a combination of different spectra characterized by different transition energies ($E_0 - V_i$, where V_i is the energy of the i-th excited state):

$$N_\beta(Z, E_\beta, m_{\nu_e}) \approx \sum_i w_i p_\beta E_\beta (E_0 - E_\beta - V_i)^2 \left(1 - \frac{m_{\nu_e}^2 c^4}{(E_0 - E_\beta - V_i)^2}\right)^{1/2} F(Z, E_\beta) S(E_\beta) \tag{2.24}$$

where w_i is the transition probability to the final i-th excited state. The spectral shape induced by the excited states is misleading when one tries to extract the value of the neutrino mass. Assuming that the neutrino mass is null and summing up over all the final states, from the equation (2.24) one obtains:

$$N_\beta(Z, E_\beta, 0) \approx p_\beta E_\beta (E_0 - E_\beta - \langle V_i \rangle)^2 \left(1 + \frac{\langle V_i^2 \rangle - \langle V_i \rangle^2}{(E_0 - E_\beta - \langle V_i \rangle)^2}\right) F(Z, E_\beta) S(E_\beta) \tag{2.25}$$

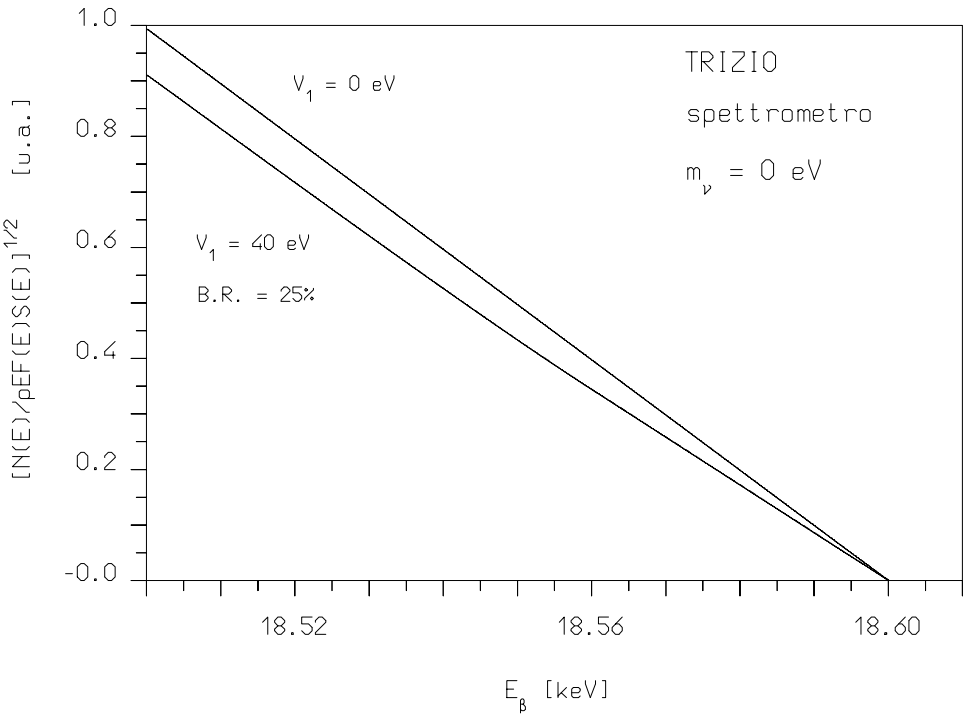

Figure 2.2 - Tritium Kurie plot assuming a null neutrino mass. The lower Kurie plot is calculated assuming an excited final state of tritium with energy V_i equal to 40 eV and transition probability w_i equal to 25%. This final state is fictitious and serves only to illustrate the final state effect.

which approximates the single beta spectrum (2.10) with a negative squared-mass neutrino equal to $-2\sigma^2 < 0$, where σ is the variance of the final state spectrum given by ($\sigma^2 = \langle V_i^2 \rangle - \langle V_i \rangle^2$) (figura 2.2). In case of tritium atom, the Shrödinger equation can be solved analytically and one gets σ^2 =740.5 eV^2. In all the other cases, the final state distributions are estimated numerically.

The situation changes completely in the calorimetric approach. Even in this case the observed spectrum is a combination of different spectra. It can be obtained by operating the following replacements:

$$\begin{aligned} E_\beta &\rightarrow E'_\beta = E_\beta - V_i \\ p_\beta = (E_\beta^2 - m_e^2 c^4)^{1/2} &\rightarrow p'_\beta = \left((E_\beta - V_i)^2 - m_e^2 c^4\right)^{1/2} \end{aligned} \tag{2.26}$$

motivated by the distinguishing feature of the calorimeters to measure simultaneously the beta electron energy *and* the de-excitation energy V_i of the final state.

By combining (2.24) and (2.26) one gets:

$$N_\beta(Z, E_\beta, m_{\nu_e}) \approx (E_0 - E_\beta)^2 \left(1 - \frac{m_{\nu_e}^2 c^4}{(E_0 - E_\beta)^2}\right)^{1/2}$$

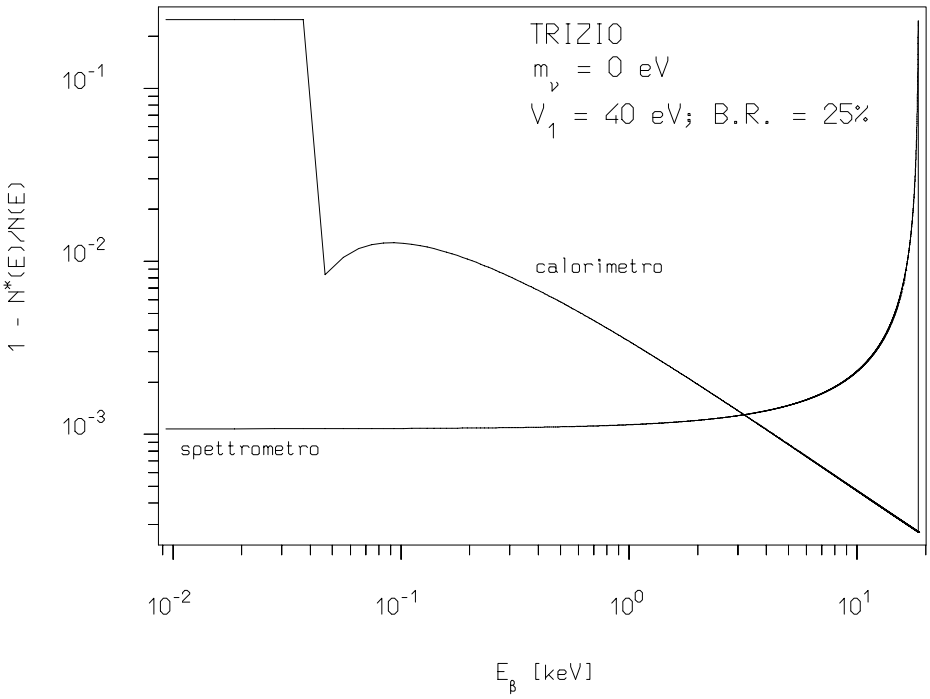

Figure 2.3 - Effect of a final excited state (under the same assumptions made in figure 2.2) on the beta spectrum measured with a calorimeter and with a spectrometer. The Y-axis reports the quantity $1 - N^*(E_\beta)/N(E_\beta)$, where $N^*(E_\beta)$ and $N(E_\beta)$ are respectively the observed beta spectra with and without excited final state.

$$\sum_i w_i (E_\beta - V_i) \left((E_\beta - V_i)^2 - m_e^2 c^4 \right)^{1/2} \; F(Z, E_\beta - V_i) S(E_\beta - V_i)$$

Observing that $F(Z, E_\beta - V_i)S(E_\beta - V_i) \approx F(Z, E_\beta)S(E_\beta)$ and developing in powers of V_i/E_β, one obtains:

$$\begin{aligned} N_\beta(Z, E_\beta, m_{\nu_e}) \;\approx\; & p_\beta E_\beta (E_0 - E_\beta)^2 \left(1 - \frac{m_{\nu_e}^2 c^4}{(E_0 - E_\beta)^2} \right)^{1/2} F(Z, E_\beta) S(E_\beta) \\ & \sum_i w_i \left(1 - \frac{V_i}{E_\beta} - \frac{V_i E_\beta}{E_\beta^2 - m_e^2 c^4} + \frac{V_i^2}{2(E_\beta^2 - m_e^2 c^4)} \right) \end{aligned} \tag{2.27}$$

A part from the sum term, for a null neutrino mass the equation (2.27) describes a beta spectrum with a linear Kurie plot in the final region ($E_\beta \gg V_i$); figure 2.3 shows as the influence of the excited final state on the beta spectrum is confined at low energy. For a large range below the end point therefore a calorimeter provides a faithful reconstruction of the beta spectral shape. This is not true for spectrometers. The possibility to observe a substantial undistorted fraction of the spectrum is very useful to check systematic effects and to prove the general reliability of the experiment.

2.4.5 Sensitivity of calorimeters: analytical evaluation

It is interesting to derive an approximate analytic expression for the statistical sensitivity of a calorimetric neutrino mass experiment. The primary effect of a finite mass m_ν on the beta spectrum is to cause the spectrum to turn more sharply down to zero a distance m_ν below the endpoint E_0(higher panel of figure 2.4). To rule out such a mass, we must be sensitive to the number of counts expected in this interval. The fraction of the total spectrum within ΔE of the endpoint E_0 given by

$$F_{\Delta E}(m_\nu) = \int_{E_0-\Delta E}^{E_0} N_\beta(E, m_\nu) dE \tag{2.28}$$

For 0 mass we have approximately

$$F_{\Delta E}(0) \approx 2A_\beta \left(\frac{\Delta E}{E_0}\right)^3 \tag{2.29}$$

where A_β is the total beta activity of the source. For a finite mass we have

$$F_{\Delta E}(m_\nu) \approx F_{\Delta E}(0)\left(1 - \frac{3m_\nu^2}{2\Delta E^2}\right) \tag{2.30}$$

In addition to the counting statistics, the effect must be detected in the presence of an external background, and the background due to undetected pile-up of two events. In a first approximation we can neglect the external background. We can then crudely approximate the pile-up spectrum by assuming a constant pulse-pair resolving time, τ_R, such that events with greater separation are always detected as being doubles, while those at smaller separations are always interpreted as singles with an apparent energy equal to the sum of the two events. In fact, the resolving time will depend on the amplitude of both events, and the sum amplitude will depend on the separation time and the filter used, so a proper calculation would have to be done as a Monte Carlo with the actual filters and pulse-pair detection algorithm being used. However, this approximation is good enough to get the correct scaling and an approximate answer. In practice τ_R is of the order of the detector rise time.

With these assumptions, the coincidence rate is $\tau_R A_\beta^2$ and as shown in the lower part of figure 2.4, a fraction $F_{\Delta E}^{pp}$ these events will fall in the region within ΔE of the endpoint E_0 and can be approximated by

$$F_{\Delta E}^{pp} \approx \tau_R A_\beta^2 \int_{E_0-\Delta E}^{E_0} N_\beta(E,0) \otimes N_\beta(E,0) dE \approx \frac{9}{5}\tau_R A_\beta^2 \frac{\Delta E}{E_0} \tag{2.31}$$

If we count for a length of time t_M we can write the signal-to-background ratio in the region within ΔE of the endpoint E_0 as

$$\frac{signal}{background} = \frac{|F_{\Delta E}(m_\nu) - F_{\Delta E}(0)| t_M}{\sqrt{F_{\Delta E}(0) t_M + F_{\Delta E}^{pp} t_M}} \tag{2.32}$$

This ratio must be about 1.7 for a 90% confidence limit. For evaluating (2.24), we can consider the two limiting situations where square root is dominated by one of the two terms.

The pile-up is going to be negligible when the following condition is met

$$\tau_R A_\beta \ll \frac{10}{9}\frac{\Delta E^2}{E_0^2} \tag{2.33}$$

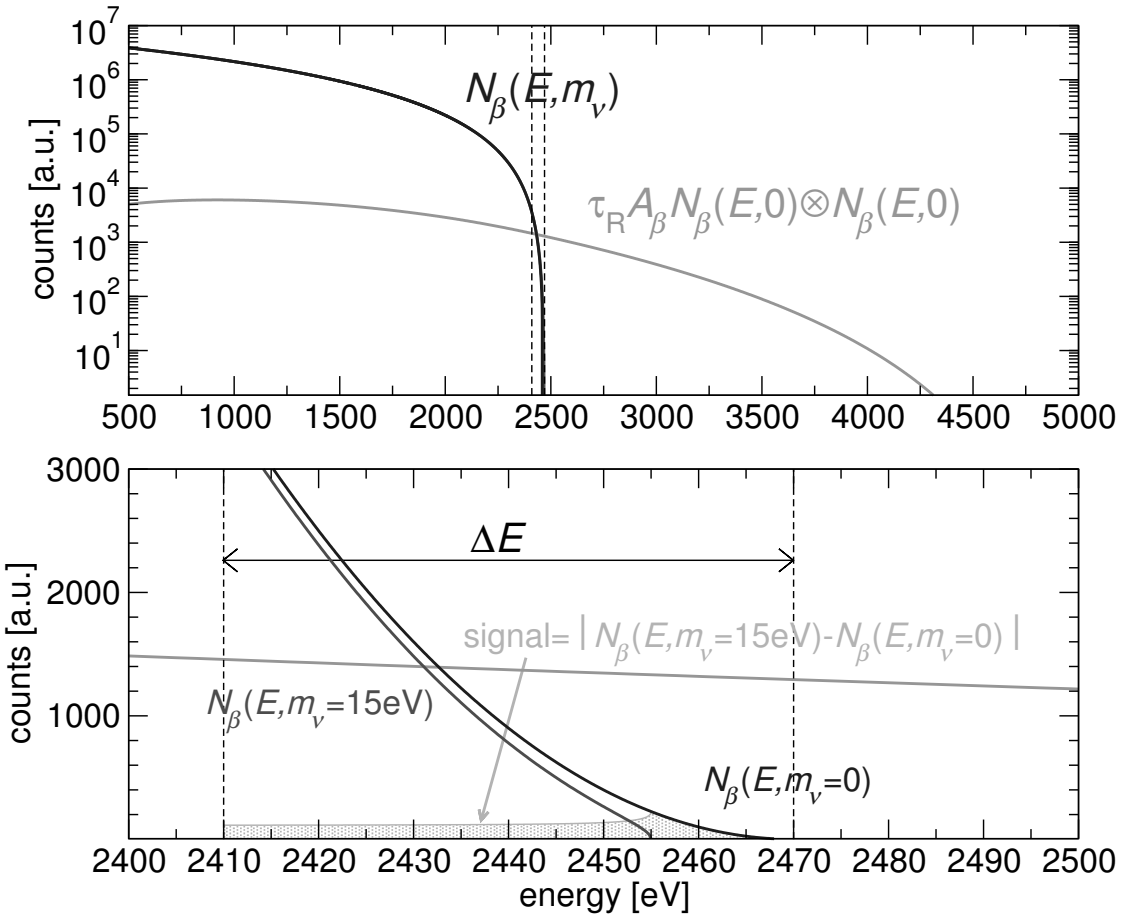

Figure 2.4 - Effects of pile-up on experimental beta spectrum. Higher panel: beta spectrum compared with pile-up spectrum. Lower panel: zoom around the end point, with a comparison between 0 and finite-neutrino-mass beta spectra

In this conditions from (2.24) one can then write the 90% confidence limit sensitivity as

$$\Sigma_{90}(m_\nu) \approx 0.89 \sqrt[4]{\frac{E_0^3 \Delta E}{A_\beta t_M}} \tag{2.34}$$

The energy interval ΔE in (2.34) cannot be taken smaller than about 2 times the detector energy resolution ΔE_{FWHM}. It is then apparent that to increase sensitivity one has to improve the energy resolution, but, above all, the statistics $A_\beta t_M$ is the most important factor. Increasing A_β and decreasing ΔE_{FWHM}, condition (2.33) maybe not satisfied anymore and one could come to the other limit where the pile-up dominates. Then the 90% confidence limit sensitivity can be written as

$$\Sigma_{90}(m_\nu) \approx 0.87 \sqrt[4]{\frac{E_0^5 \tau_R}{t_M \Delta E}} \tag{2.35}$$

In this limit the role of the source activity A_β is substituted by $1/\tau_R$. The sensitivity can be improved by acting on the pulse-pair resolving time τ_R and the energy interval ΔE. For

thermal detectors this becomes quickly impractical because the source activity required for keeping the pile-up dominating becomes too large.

Chapter 3

Low temperature microcalorimeters for ^{187}Re β spectroscopy

3.1 Basic principles of thermal detectors of particles

Nowadays, phonon-mediated detectors (PMD) operated at low temperatures (sometimes defined bolometers) provide better energy resolution, lower energy thresholds and wider material choice than conventional detectors in many applications. Furthermore, they exhibit the unique feature to be sensitive to low or non-ionizing events. A complete overview is offered by the proceedings of the specific low temperature detector conferences.

PMDs were proposed initially as perfect calorimeters, i.e. as devices able to thermalize thoroughly the energy released by the impinging particle (the term *microcalorimeters* is used when the detector total mass does not exceed 1 mg and the linear dimensions are a few hundreds of μm maximum). In this approach, the energy deposited by a single quantum into an energy absorber (weakly connected to a heat sink) determines an increase of its temperature T. This temperature variation corresponds simply to the ratio between the energy E released by the impinging particle and the heat capacity C of the absorber, i.e. is given by $\Delta T = E/C$. The only requirements are therefore to operate the device at low temperatures (usually < 0.1 K and sometimes < 0.015 K) in order to make the heat capacity of the device low enough, and to have a sensitive enough thermometer coupled to the energy absorber.

The thermometer is usually a resistive element with a heavy dependence of the resistance on the temperature. It can be either a semiconductor thermistor or a superconducting film kept at the transition edge, named usually transition edge sensor (TES). In a more general approach, when the thermalization of the deposited energy is not guaranteed, the thermometer should be more correctly defined as a *phonon-sensor*, as the phonon energy distribution is not necessarily in thermal equilibrium during detection.

There are also other less conventional approaches, which are particularly relevant in our case. A very sensitive, low noise, multiplexable thermometer can be realized by registering a temperature change through a magnetization change (*magnetic calorimeters*), as discussed in § 6.4. On the other hand, since the initial excitations in a superconductive absorber are quasiparticles resulting from a pair-breaking process, it is possible to realize a Re-based detector out of the PMD domain and aiming at the direct detection of quasiparticles. The very small energy required to produce a couple of quasiparticles from a Cooper pair (a few meV) allows to achieve an energy resolution of the order of what needed for MARE-2. Very promising devices for quasiparticle-mediated detectors consists in the so-called Kinetic Inductance Detectors,

treated in § 6.5. The following part of this chapter will serve as an introduction to the two baseline approaches to MARE: semiconductor thermistors (MARE-1) and TESs (MARE-1 and II), while the innovative solutions will be treated in chapter 6.

3.1.1 Energy absorber and thermalization process

The energy absorbing part of the detector is usually a diamagnetic dielectric material in order to avoid dangerous contributions to the specific heat in addition to the Debye term, proportional to $(T/\Theta_D)^3$ at low temperatures, where Θ_D is the Debye temperature. In such devices, the energy resolution can be fantastically high and close to the so-called *thermodynamical limit*

$$\Delta E_{rms} \sim \sqrt{k_B T^2 C} \tag{3.1}$$

corresponding to the statistical fluctuation of the internal energy of the calorimeter in the hypothesis of weak thermal link to the heat bath. A crucial parameter of the energy absorber is therefore Θ_D, which should be as high as possible in order to reduce the specific heat. For this reason, small mass number, light materials, are better energy absorbers in terms of heat capacity. Even superconductors are in principle suitable, since the electronic contribution to the specific heat vanishes exponentially below the critical temperature. In this document, we will treat and discuss two approaches, the former considering metallic rhenium, which is a superconductor, and the latter dealing with dielectric rhenium compounds.

In fact, the real situation is far more complicated as far as operation principles of calorimeters are concerned. The interaction of an elementary particle with a solid detecting medium produces excitations of its elastic field. In other terms, the energy spectrum of the target phonon system is modified. Only when the time elapsed after the interaction is long enough to allow the phonon system to relax on a new equilibrium distribution, the detector works really as a calorimeter. On the contrary, if the sensor response is very fast, excess non-equilibrium phonons are detected long before they thermalize. In many experimental situations, it is difficult to distinguish between these two extreme cases, and the nature of the detection mechanism is still poorly known. Nevertheless, even when PMDs are not pure calorimeters, their intrinsic energy resolution is better than for conventional detectors, since the typical energy of the excitations produced (high frequency phonons) is the order of the Debye energy ($\sim$ 10 meV), instead of 1 eV or more as in ordinary devices. (In conventional Ge detectors for instance the energy required to produce an electron-hole pair is around 3 eV). Since the energy resolution is limited intrinsically by the fluctuations of the number of the excitations, its value scales as the square root of the energy required on the average to produce a single excitation. Detection of non-equilibrium phonons is very attractive because it can in principle provide information about the interaction position (space resolution was already proved with this method), discrimination about different types of interacting radiation, and direction of the primary recoil in the target material. The last two points remain to be proved. On the contrary, an important non-equilibrium phonon component is annoying when the main goal is high energy resolution. In fact, the weigh of this component can be connected to the impact point. This determines an excess systematic broadening of the peaks in energy spectra due to the inhomogeneity of the spatial response.

Another possible cause for a deterioration of the energy resolution is the activation of mechanisms which store part of the deposited energy, preventing from a full conversion to heat. This problem shows up typically in dielectrics, where impurities and defects can act as traps which lie energetically inside the forbidden band-gap. In case of ionizing events, like those

interesting for this research, electrons and holes can get trapped before their recombination to phonons. The fluctuation of the trapped energy carrier number can also lead to excess broadening of the energy peaks (*thermalization noise*). This problem can be cured by using metallic, quasi-metallic or small band-gap energy absorbers.

3.1.2 Phonon sensors

Semiconductor thermistors consist usually of Ge or Si small crystals with a dopant concentration slightly below the metal-to-insulator transition. This implies a steep dependence of the sensor resistivity on the temperature at low temperatures, where the variable range hopping (VRH) conduction mechanism dominates. These high impedance sensors (typically 1-100 $M\Omega$) are usually parameterized by the sensitivity A, defined as $-dlogR/dlogT$, which typically ranges from 1 to 10. Semiconductor thermistors can be realized also in amorphous film form, like NbSi. The mathematical form of the resistivity dependence on the temperature is expressed by the so-called generalized Mott equation

$$\rho(T) = \rho_0 \exp\left(\frac{T_\circ}{T}\right)^p \tag{3.2}$$

where the exponent p depends on the temperature range and the compensation degree. For compensated doping at temperature below 1 K p is normally equal to 1/2.

A thermal decoupling between phonons and electrons appearing at low temperatures limits semiconductor thermistor performance. This phenomenon, whose theoretical bases are not very clear, can be well represented by a finite thermal conductance G_{ep} between phonons and electrons. Of course, this decoupling tends to spoil detector performances: it causes long signal rise times and incomplete transmission of energy to the electrons of the thermistor.

Experimental observations of several groups lead to the introduction of this thermal decoupling and to the development of the so-called *hot electron model*, which postulates that the conduction electrons constitute a thermal system with temperature T_e, thermally coupled to the phonon bath through G_{ep}. As a consequence, the VRH theory is modified so that the thermistor resistivity depends no longer on the lattice temperature T_{ph}, but on the electron temperature T_e:

$$\rho(T_e) = \rho_0 \exp[(T_\circ/T_e)^{1/2}] \tag{3.3}$$

The hot electron model assumes that the power P_e dissipated in the thermistor for its polarization or for spurious effects flows from the electron system to the phonon system through G_{ep}, which is supposed to be described by

$$G_{ep}(T_e) \equiv \frac{d\,P_e}{d\,T_e} = \alpha g_{ep} T_e^{\alpha-1} \tag{3.4}$$

and proportional to the thermistor volume. Once the lattice temperature T_{ph} is fixed, the electron temperature T_e is given then by

$$T_e = \left(T_{ph}^\alpha + \frac{P_e}{g_{ep}}\right)^{\frac{1}{\alpha}} \tag{3.5}$$

In spite of the excellent agreement with the experimental data, it is not clear how this model can reconcile with the VRH theory, which is based on the assumptions that the electrons are

strongly localized and does not form a thermodynamical ensemble for which the temperature is a meaningful concept.

Since G_{ep} is proportional to the thermistor volume, it is convenient to realize large thermistors, without exceeding of course the heat capacity of the energy absorber. A very useful technique to dope uniformly large volumes is the neutron transmutation doping (NTD). In this approach, which is commonly used for Ge, the semiconductor sample is bombarded by neutrons, which induce nuclear reactions on the various target isotopes leading to the formation of n and p dopants. A thermal treatment is necessary to activate the dopants. On the contrary, small low-heat-capacity thermistors can be obtained by ion implantation in Si, following the standard planar Si technology. These sensors are however useful only in microcalorimeters, where the heat capacity of the absorber is very small and must not be dominated by the sensor's one. Silicon microcalorimeters are crucial devices for the application described in this document, since they represent one of the two baseline solutions for MARE-1 arrays. However, some R&D work will be performed also on NTD sensors, since they can successfully compete in principle with implanted silicon sensors.

TESs are much more sensitive devices ($A \sim 1000$), since their resistivity changes rapidly from a finite value to zero in a very narrow temperature interval. Normally, the superconductive film is deposited on the absorber crystal, with a typical thickness of few hundreds of nanometers, and the shape is defined after deposition by photolitography and wet etching. With a rectangular shape the normal resistance near the critical temperature is typically between several $m\Omega$ and several ohms, and SQUID technology is an ideal solution for the readout. Films are usually made of a single superconductor. (The lowest critical temperature has been obtained with tungsten.) In another approach, the film consists of two layers: a normal metal in contact with a superconductor. The normal metal is driven superconductive by Cooper pair diffusion (proximity effect) and the resulting critical temperature T_C can be much lower than that of the pure superconductor. It is possible to tune T_C by means of the layer thickness.

A very powerful way to use a TES consists in the so-called extreme electrothermal feedback operation mode. In this approach the film is biased at a constant voltage V, so that the Joule power dissipated by the bias current keeps the film electrons around the critical temperature, substantially higher than the temperature of the substrate upon which the film is deposited. The operation point of the film is therefore self-regulated. A temperature fluctuation (for example a temperature increase) increases the film resistance and therefore reduces the Joule power, compensating for the original variation. When some energy reaches its electrons, the film reacts with a current pulse $i(t)$ which relaxes very fast (much faster than the thermal relaxation constant) and is self-calibrated: the integral over time of $V \cdot i(t)$ is equal to the deposited energy. If used as a phonon sensor, the particle impinges on an energy absorber which acts as a substrate for the film, and the high energy phonons produced by the particle interaction couple directly to the electrons in the film. Thermal transmission of energy is inhibited in this case, due to the large thermal decoupling between the film electrons and the phonon thermal bath of the substrate.

TESs are a solution that will be pursued preliminarily in MARE-1 (in parallel with a development using semiconductor devices) and that represents the most viable option for MARE-2.

3.2 The absorber-embedded ^{187}Re source

As previously stated, one of the positive features of PMDs in general and of microcalorimeters in particular is that the requirements for the energy absorber material are quite loose. It is therefore conceivable to develop a device whose absorber is based on natural rhenium, containing automatically the ^{187}Re source. Nature was very kind from this point of view: natural abundance of ^{187}Re, its lifetime, and the typical microcalorimeter optimum size, combine so that 1 mg-scale rhenium-based devices have typical activities of the order of 1 Bq. Both the mass and the counting rate match quite well the requests of microcalorimeter technology. Two possible approaches will be described below: the use of metallic rhenium, which is a feature of the MANU experiment, and dielectric rhenium compounds, employed up to now in the MIBETA experiment. In the common development proposed here, both technologies will be pursued in parallel. Either has in fact the potential to reach 2-3 eV sensitivity to m_ν in MARE-1, and a cross check will be very useful in order to understand the systematics of the experiment (BEFS, spectrum shape, beta decay parameters such as E_0 and lifetime).

3.2.1 Metallic rhenium

Natural metallic rhenium contains almost 63% of the isotope 187, the expected activity from 1 mg is roughly 1 Bq. The main properties of metallic rhenium are summarized in Table 3.1, the heat capacity of the normal state is given by:

$$C = 40.6\,T^{-2} + 0.034\,T^{-3} + 2290\,T + 27\,T^3 \quad \mu\ \mathrm{J/(mol\ K)} \tag{3.6}$$

where the first two terms are a representation of the nuclear heat capacity in an applied field, the third one is the contribution of normal conduction electron and the last term represents the lattice contribution. The heat capacity of the superconducting state for temperatures below half the critical temperature, can be written as: $C_\mathrm{s} = a\,\gamma\,T_\mathrm{c} e^{-bT_\mathrm{c}/T}$ with $a = 8.5$, $\gamma = 2.3 \times 10^{-3}$ J/(mol K) and $b = 1.46$. The possibility of working with a superconducting rhenium absorber at temperatures well below the transition temperature, would provide us low heat capacity and higher emitted electrons count-rate. However, the use of superconducting metallic rhenium as energy absorber might not be an optimum choice since microscopic calculations from the BCS theory predict that a large part of the released energy inside the absorber itself can be trapped in quasi particles states which live for many seconds at temperatures below 100 mK. The energy release inside a superconductor leads to a state far from equilibrium in which many Cooper pairs are broken and quasiparticles created. A model describing this situation was proposed by Kaplan [8] and he found that the time the quasi particles needed to recombine would be somewhere between 1 and 10 seconds. Analogous results were obtained by the analysis of Kozorezov [9]. Despite of these theoretical considerations it is an experimental fact that some superconducting materials perform well as absorbers in cryogenic detectors. So far no general accepted explanation has been given for this apparent discrepancy between experimental results and theory.

It is therefore of crucial importance that the thermalization process in superconducting Rhenium is studied in the first phase of the proposed experiment. Previous experiments by the Genova group that studied the heat capacity, the detection efficiency and thermalization of superconducting rhenium in magnetic fields gave encouraging results, but need to be repeated for the parameters necessary in our experiment [10]. In addition, the thermalization needs to be studied for the case that the surface of the rhenium is covered with a normal metal.

Table 3.1 - Properties of rhenium relevant to the proposed experiment

Z	75
isotopes	^{185}Re (37.4%) ^{187}Re (62.6%)
A	186 g/mol
molar volume	11.3 cm^3
electronic. configuration	[Xe] $4f_{14}5d_5 6s_2$
crystal structure	hcp
density	21.02 g/cm^3
Debye temperature	417 K
transition temperature	1.69 K
electrical resistivity (300 K)	$18.4 \times 10^{-6}\,\Omega$cm
critical field	20 mT

3.2.2 Dielectric rhenium compounds

In order to overcome possible problems with incomplete energy conversion to phonons in superconducting, metallic rhenium at low temperatures, a possibility is to select proper dielectric rhenium compounds which do not exhibit excessive thermalization noise. One of the first MIBETA experiment achievements was indeed to test several dielectric rhenium compounds in order to single out at least one of them with good physical/thermal/practical properties to be adopted as a microcalorimeter absorber.

From the beginning, the most suitable compounds looked like those based on the ReO_4^- (perrenhate) anion. A non exhaustive list of tested compounds includes: $Re_2(CO)_{10}$, K_2ReCl_6, $(NH_4)ReO_4$, $KReO_4$, $AgReO_4$. The tests with $Re_2(CO)_{10}$ are quite difficult, since this compound sublimates in vacuum at room temperature. In the second-to-fourth case, despite the good theoretical expectations and the excellent S/N electronic noise (baseline noise), the actual energy resolution resulted quite poor, exceeding 100 eV at 6 keV. Possible traps populating the band-gap and preventing complete thermalization could explain the results.

Silver perrhenate ($AgReO_4$), on the other hand, immediately exhibited good properties not showing a considerable excess thermalization noise. The calibration peaks were sufficiently symmetric, and energies resolutions as good as 18 eV FWHM at 6 keV have been achieved. $AgReO_4$ crystals are transparent, crumbly and slightly hygroscopic. Taking into account the known properties ($PM = 358.066, PA_{Re} = 186.2, ^{187}Re \approx 62.8\%$) and the density, the β-decay rate is about $5.4 \cdot 10^{-4} Hz/\mu g$. A possible target for the single crystal mass, resulting from a trade-off between rate, pile-up and energy resolution is around $250\mu g$, corresponding to a single detector rate of the order of 0.1Hz.

In the literature, a certain amount of papers are dedicated to the study of perrhenates crystal structure. As a general result, it is accepted that $MReO_4$-type perrhenates ($M = Na, K, NH_4, Rb, Ag$) assume an $I4_1/a$ tetragonal cell form, while in $TlReO_4$ and $CsReO_4$ the structure is deformed into orthorhombic, with phase transitions below room temperature. Interesting electronic properties have been observed concerning silver perrhenate, where the standard gap 3.7 eV wide is strongly dependent on the pressure. For sufficiently high pressures a possible metallic behaviour is still matter of debate. The good thermalization properties, if

compared to the bad behaviour of similar compounds, are quite interesting and could reflect a fundamental difference in the electronic structure at low temperatures.

The precise silver perrhenate crystal structure is *scheelite*, with four molecules per unit cell and tetragonal symmetry. Within the cell, rhenium and silver atoms are found in the following positions:

- Ag: 0,0,1/2; 1/2,0,1/4; 1/2,1/2,1; 1,1/2,3/4
- Re: 0,0,0; 0,1/2,1/4; 1/2,1/2,1/2; 1/2,1,3/4

At room temperature the cell is characterized by $a_0 = b_0 = 5.378\mathring{A}; c_0 = 11.805\mathring{A}$.

The decaying rhenium atom is surrounded, with almost tetrahedral symmetry, by four oxygens

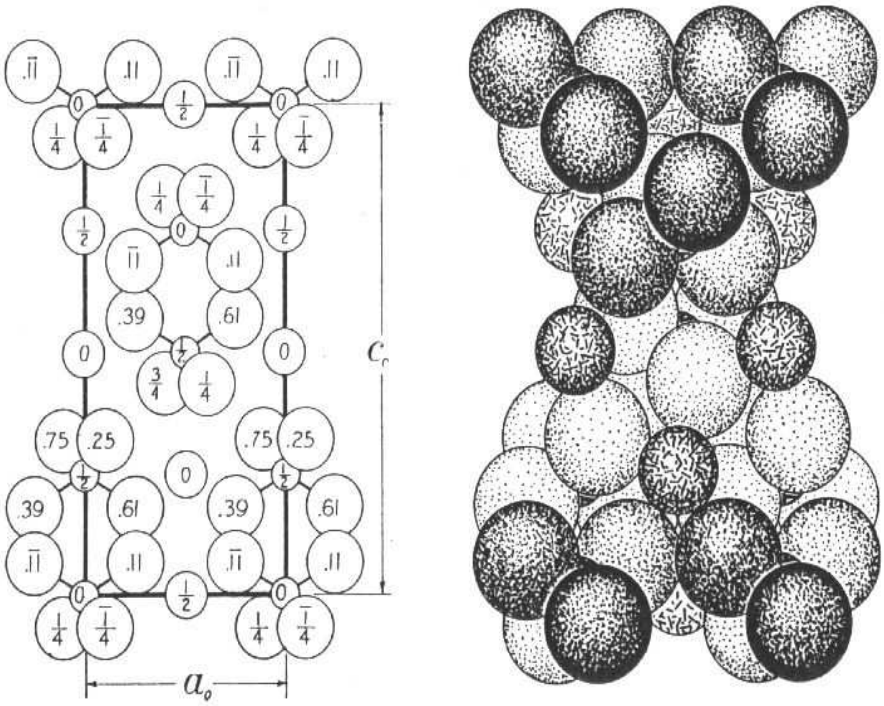

Figure 3.1 - *$AgReO_4$ structure. On the right panel, Oxygen atoms are the biggest, while silver are the smallest ones.*

located at an approximate distance of $1.7\mathring{A}$. Four equivalent covalent bonds are responsible for the anion structure. The Ag^+ ion is $3.8\mathring{A}$ away at room temperature.

It is important to remark the difference between the extremely compact metallic rhenium structure reflected by the high density ($\rho = 20.8$ g/cm^3) and the relatively low-density $AgReO_4$ ($\rho = 7.05$g/cm^3). In metallic rhenium absorbers, no unused atoms (additional heat capacity) are added. On the other hand, however, by keeping the decaying nucleus as far as possible from matter waves reflectors (external heavy atoms) the net result is a substantially cleaner Kurie plot. We point out that in this case the O atoms are basically transparent at energies $E > 200$ eV. The BEFS effect (see §5.1.2) is almost one order of magnitude reduced for $AgReO_4$ with respect to the metallic rhenium case (assuming the same detector energy resolution). Even taking into account the increased complexity in the physical modeling, in case of the proposed

high statistics experiment a substantial *apriori* reduction of one of the possible systematics source is extremely important.

Chapter 4

State of the art of ^{187}Re calorimetric experiments

4.1 Historical introduction

After the claims of the observation of a finite neutrino mass from the experiment of Lubimov et al. [1], the application of cryogenic detectors to the precision beta spectroscopy for neutrino mass measurements have been considered promptly and independently by Dan McCammon [11] and Sandro Vitale [12] in 1984. The aims of the proposals were motivated by the need to verify the controversial result of Liubimov et al. with an independent methodology , and to clarify the problem of the apparently negative squared mass of the antineutrino, that a series of experiments on the tritium beta decay were suggesting. In particular, in 1985, Sandro Vitale, [13] proposed to investigate the feasibility of an experiment with a cryogenic detector containing ^{187}Re, in order to study the end point region with a true calorimetric method. He recognized that this beta isotope, thanks to the lowest Q-value known in nature, allows to afford a calorimetric experiments within a realistic time scale. A calorimetric measurement with similar sensitivity, which makes use of tritium, requires a higher statistics of about 400 times. On the other hand, he addressed also several problems related to the use of rhenium; among them: (1)the validity of the approximations on the nuclear physics approximation for the calculation of the spectral shape and (2) the performance of absorbers containing ^{187}Re

The direct detection of the nuclear decay of ^{187}Re is quite recent. After several attempts made with Geiger counters and scintillating detectors on metallic sample of rhenium, the ^{187}Re beta decay has been unambiguously observed in the sixties by R.L. Brodzinsky and D.C. Conway [14] and E. Huster and H. Verbeek [15]. The two groups synthesized a Re gaseous compound that allowed to perform the beta spectroscopy by means of a gas proportional counter. Because of poor quality of the gas, i.e., low chemical stability and high electron affinity, the threshold was higher than 1 keV and the energy resolution was only 1 keV FWHM at 3 keV. However, the two groups established the end point energy at 2.65 keV about and the half life at 45 Gy.

The group of Genova started to work on calorimetric detectors for Rhenium in the 1986, within the project MANU. The first calorimetric detection of ^{187}Re beta decay was obtained in the fall of 1991, with a metallic superconducting sample of rhenium cooled at about 100 mK [16, 17]. The group of Milan detected for the first time the ^{187}Re beta decay in 1998 using a dielectric compound of rhenium as an energy absorber, within the project MIBETA. Since the beginnings of these investigations, the Genova and Milano groups are the only two who have pursued with success the aim of developing high sensitivity rhenium microcalorimeters.

4.2 The Genova experiment (MANU)

MANU (MAss of NU) was proposed as a project for establishing a new method for precise calorimetric beta spectroscopy. In the first years, the activities of MANU were devoted to the development of superconducting rhenium detectors. Indeed, among the several issues addressed by calorimetric technique, the understanding of the physics of superconducting metal as radiation absorbers has been the fundamental subject of investigation. This phase of MANU was completed in 1995, from which promising results in energy resolution were achieved: 30 eV FWHM with superconducting Re absorber, while 35 eV FWHM has been obtained with superconducting Sn absorber. The second phase of MANU has been devoted to the preparation and acquisition of the ^{187}Re beta spectrum measurement.

4.2.1 Results of the investigation on metallic superconducting absorbers

The most straightforward way to build a thermal detector for ^{187}Re beta decay can be done by simply using a sample of pure Re metal, which contains about 63% of the beta decaying isotope ^{187}Re. The metallic rhenium is superconducting at temperatures below 1.69 K. At early times of the MANU project, it was not clear if superconducting absorber were suitable for particle detection (see § 3.2.1) . In metals, the large electronic term $C_e=\gamma T$ in the low temperature specific heat for the normal state is reduced, with the onset of superconductivity, to $C_s = \gamma\ T_c\ \exp\Delta/T$, where Δ is the superconducting energy gap and T_c is the critical temperature, which is negligible for $T \ll T_c$. The heat capacity of a micro-calorimeter built with a superconducting absorber may then be low enough to provide a good energy resolution. It is difficult, however, to figure out the features of the thermalization process. Indeed, for ideal superconductors in thermal equilibrium, a very long lifetime τ_{qp} is expected for quasiparticles resulting from Cooper pairs breaking. However, since the process conditions are far from equilibrium, at least a fraction of the particle energy should be quickly converted into phonons, so that the recombination might be speeded up. Indeed, deviations from the ideal T dependence of quasiparticle lifetime τ_{qp} were reported for lead at values of $T/T_c < 0.25$, and the trend of experimental data suggests a constant value of τ_{qp} for $T/T_c < 0.1$. The first detection of α-particles in composite bolometers with superconducting Re acting as absorbers has been successfully demonstrated in 1990. Others groups reported positive results in radiation detection with superconducting absorber.

In order to better understand the properties of such a superconducting microcalorimeter and in absence of theoretical models capable of predicting its characteristics, it has been decided to experimentally investigate the efficiency in heat transfer of the absorber. Referring as η the thermalization efficiency, i.e., the ratio between the energy measured by the calorimeter as heat and the energy of the incident particle, it is obvious to try to classify the quality of an absorber with its η value. An ideal microcalorimeter should have $\eta = 1$ at very short time, provided that the incoming energy E is fully thermalized. To better define the role of η the following assumptions can be taken as guidelines.

If we assume as a general model of an absorber a coupled system of phonons and electrons, which can exhibit a band-gap energy Δ, then the primary energy of the particle is shared among the two systems: a fraction η goes into phonons and $1 - \eta$ into electron excitations (above the energy gap). These fractions changes with time until the thermal equilibrium is reached. At very low temperatures, however, a complete thermal equilibrium is not reached in a short time. With dielectric absorbers, or wide band-gap semiconductors, that have very low

specific heat, electrons and holes may recombine in long times and a fluctuating fraction of the incoming energy is trapped in metastable states. If w is the average energy needed to produce a long living electron excitation (ex., e-h pair) and F the Fano factor, the energy resolution can written as sum of two contribution,

$$\Delta E^2 = \chi^2(kT^2C) + (1-\eta)^2 EFw = \chi^2(kT^2C) + \Delta^2 EF/w \tag{4.1}$$

in which $\eta = 1 - \Delta/w$ is assumed. Consequently, the relevance of a small gap approach is evident, in a dielectric micro-calorimeter absorber, the phonon noise limits the energy resolution. Indeed the use of a small band-gap TeCdHg semiconductor as an absorber for X-ray detection allowed the Goddard-Wisconsin group to achieve an energy resolution close to the intrinsic limit. It is then suggestive to extend the above ideas to the case of superconducting metals, where the energy gap to break the Cooper pairs is very small. Being w = 1.7Δ for many superconductors, and Δ around 1 meV, suggests that even in a non-fully thermalization, the effect on energy resolution should be negligible. The present models for the down conversion of the primary energy doesn't allow to verify directly this extrapolation to the superconductors, with the well established empirical law for the solid state semiconducting detectors. For example, it is expected that in the case of spatially correlated quasiparticle density and energy-gap suppression phenomena, higher fluctuations of the thermalized energy should increase. Therefore the thermalization efficiency η should be taken as a merit parameter: at low η values, other possible contributions to the above energy resolution expression could be observed.

The value of η for rhenium and other superconductors have been measured in different conditions, with the method described in the Figure 4.1 , in which is schematically shown the small calorimeter used in the experiment and its equivalent thermal model.

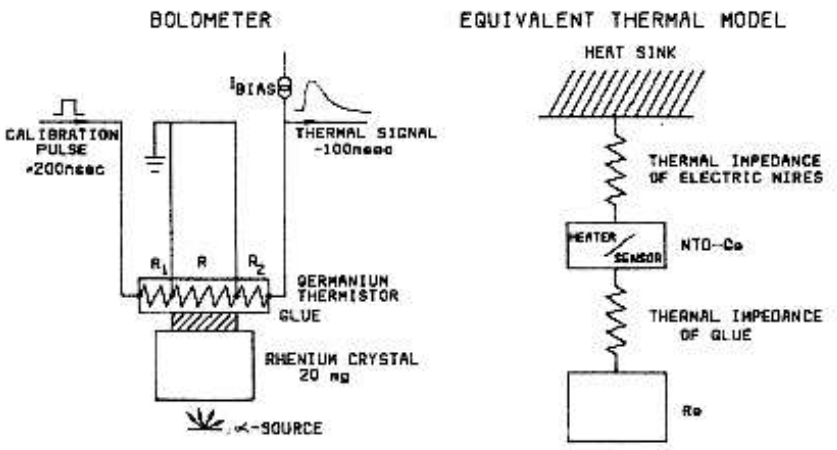

Figure 4.1 - Sketch of the measurement method for the thermalization efficiency of superconducting absorbers.

The bolometer was built with a piece of rhenium in form of single and poly-crystal and a germanium thermistor operating from 50 mK to 200 mK. The thermistor has been arranged with four wire connections in order two have two independent resistors R_1 as pulsed heater and R_2 biased at constant current, as sensor. The detector response to a delta-like heat release is a pulse whose decay time, lO ms, is dominated by the device thermal capacity and the thermal impedance to the heat sink. The risetime is limited to about 200 μs by the conductance between

the rhenium crystal and the thermistor. This slow risetime prevented us to study the details of fast thermalization processes at lower time scale. A linear calibration curve is obtained by delivering fixed energy pulses to R_1 and recording the area of the thermal pulse detected by R_2. We evaluate the efficiency η as the ratio of the averaged area of thermal pulses due to particles to that produced by electrical pulses of corresponding energy. A typical result is shown in Figure 4.2 When the detector is cooled down in zero magnetic field, from above the critical

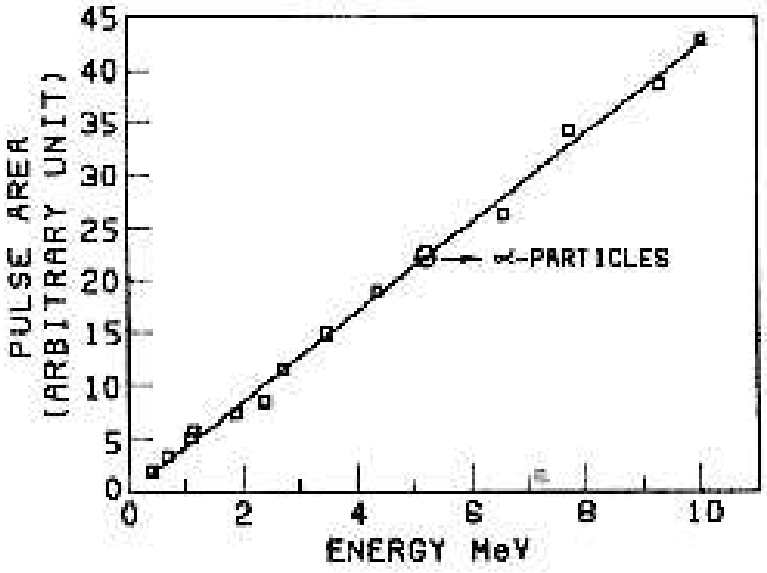

Figure 4.2 - The thermalization efficiency for alpha particles is 1, within 3%, when compared with electrically excited thermal pulses (fitted data).

temperature of rhenium to the operating temperature of the bolometer T it results, at T = 117 mK, $\eta = 1.00 \pm 0.03$ and, at T =138 mK, $\eta = 0.99 \pm 0.03$ indicating that, at these temperatures the particle energy is completely thermalized in a time much shorter than the thermal time constant of the microcalorimeter. No change is observed when a magnetic field up to 20 G is applied to the system without rising the temperature above T_c. When the bolometer is cooled below T_c in the magnetic field, the thermal pulse height is reduced because of an increase of the device thermal capacity, as expected from the increase of normal conducting volume in the vortices. Moreover, η decreased unexpectedly. The same methods has been applied to others superconductors in form of small single crystals ($1mm^3$) of Al, Pb, In, Ti, Nb, Va, Zn and Re. The results shown in Figure 4.3 indicated that the thermalization time follows a quasi universal dependence on the ratio of the operating temperature T to the Debye temperature T_D with a sharp threshold effect around $T = 2 \times 10^{-4} T_D$. Below this value, a fast drop of the fraction of energy quickly thermalized is observed.

4.2.2 Experimental apparatus

In the MANU experiment, we used a microcalorimeter composed of a Neutron Transmutation Doped (NTD) germanium thermistor (100x100x230 μm^3) coupled to the superconducting rhe-

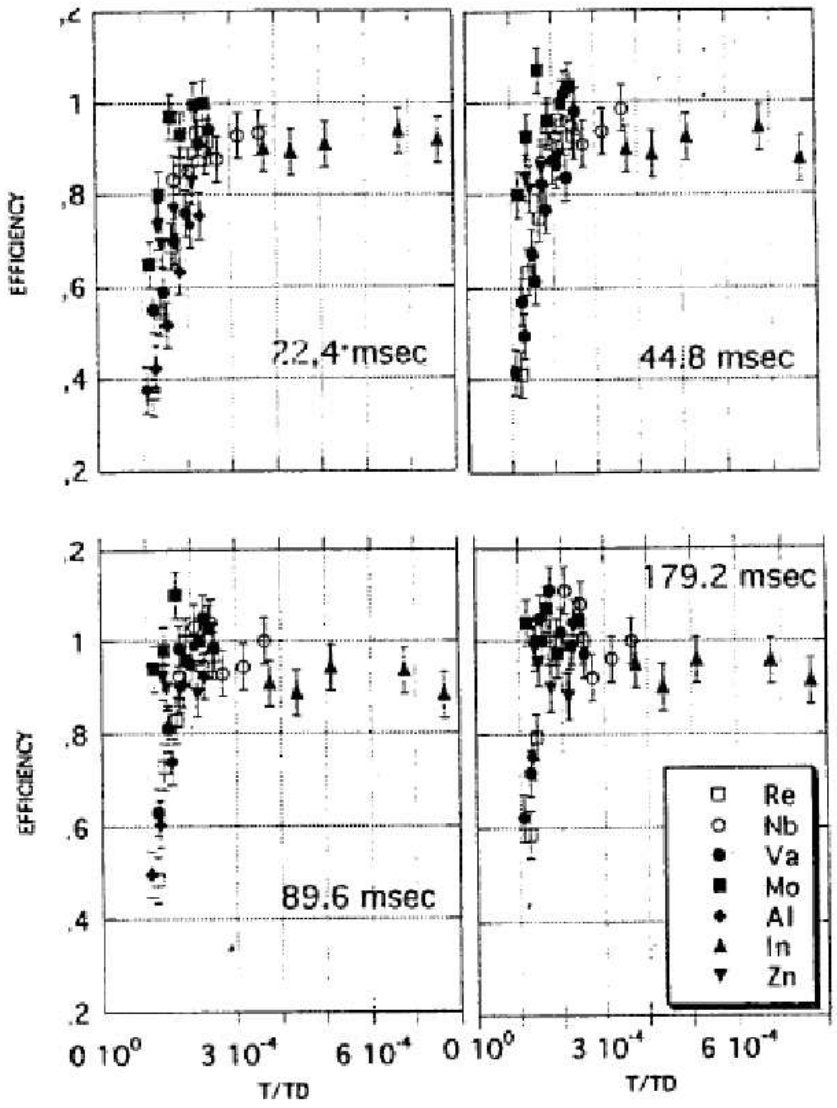

Figure 4.3 - The thermalization efficiency for Al, Pb, In, Ti, Nb, Va, Zn and Re vs T/T_{Debye}, for four different integration times.

nium absorber using epoxy. The thermistor is constant-current biased and the temperature rise is measured as voltage variation in the thermistor. An ^{55}Fe X-ray source (5898 and 6490 eV) and an X-ray fluorescence source (Cl, Ca, Va) have been alternatively used for the energy monitoring and calibration. The detector was installed in a TLE200 dilution refrigerator from Oxford Instr. Ltd. The thermal connection to the refrigerator mixing chamber and the electrical connections were provided by two ultrasonic bonded 15 μm-diameter aluminum wires. The signal was readout using a low noise preamplifier (white noise 0.8 nV/$\sqrt{Hz}$, 1/f noise corner frequency 20 Hz) working at a temperature of about 100 K and installed inside the cryostat, and a room temperature amplifier used also as anti-aliasing filter before the A/D conversion. A 12-bit CAMAC waveform recorder (LeCroy Model 6820) has been used to digitize the signal

for the successive off-line analysis. The instruments were set to record a file of 1024 12-bit data words, at every trigger, with the trigger event at the sample 256. The pre-trigger samples were used to establish a base line by assuming a constant function for the base line dependence. The process was controlled by a Digital VAX station 4000/60. An on-line system displayed selected pulses and a preliminary spectrum to check the acquisition chain; the final analysis was made off-line. The figure 4.4 shows the detector in the holder, which was mounted on the mixing chamber of the Oxford TLE dilution refrigerator, with the rotatable calibration source, and the holder dismounted.

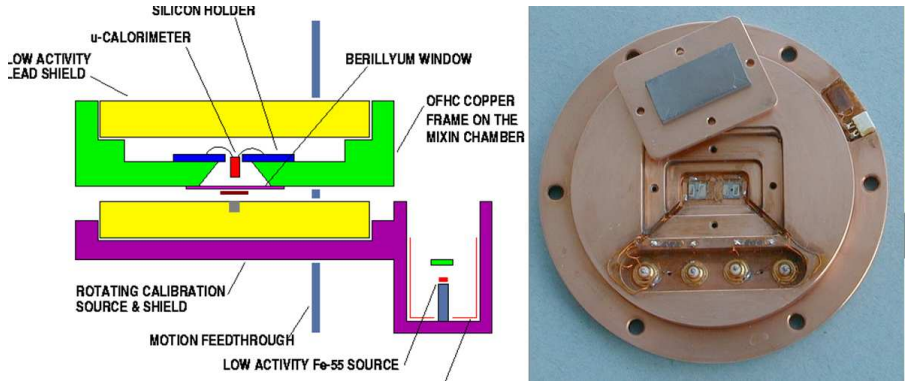

Figure 4.4 - Sketch of the microcalorimeter holder with the rotatable calibration source and picture of the dismounted holder.

4.2.3 Analysis tools

In experiments where high-energy resolution and low-energy threshold are required, the effectiveness of cryogenic detectors has already been demonstrated. Due to the low counting rate and the slow pulses of this kind of detectors it is relatively easy to use a digital signal processor to analyze the pulses. In particular, the use of an on-line digital processing (filtering) allows to get nearly the optimum energy resolution of the detector. The on-line data analysis chain is composed of two parts: energy evaluation and neutrino mass determination from the spectrum shape analysis. The chain has been tested both with experimental data and with a full system Monte Carlo simulation.

At the end of an acquisition run, all the thermal pulses of the micro-calorimeter are recorded on disk. At this point, it is possible to start with the second step of the chain which consists in the analysis of the pulses. The main goals of the analysis are: (1) to measure the energy of each pulse with the best estimator; (2) to avoid distortions of the spectral shape due to pile-up, external noise and microphonics.

Pulse amplitude estimation

The amplitude of the pulses can be determined in three ways:

- by integration of the pulses
- using optimum filter

- using adaptive filters

The relative efficiency of the three methods depends on the characteristics of the thermal pulses and the noise. The optimum filter is realized with the convolution of each pulse with a reference pulse, built averaging good pulses (generally at least 30), visually selected without pile-up and noise spikes; the maximum of the convolution is taken as best amplitude estimation. The adaptive filter is a traditional digital adaptive filter using the reference pulse as the reference channel. It has been experimentally shown that, even in the case of white or pink noise, the goodness of the optimum filter and of the adaptive one is the same. There is a key difference which is that the optimum filter is much faster; in the case of microphonic noise, the adaptive filter shows a better performance.

Pulse shape analysis

Generally, the pulses have a very defined shape: fast rise time (less then 100 μs) followed by a slow slope (a few tens of ms). This allows to use pulse shape analysis: for every recorded pulse, chi-square function between the pulse and the normalized reference pulse is evaluated in order to reject spurious pulses, pulses with noise spikes superimposed and pile-up not previously detected. For each pulse rise time, decay time, pre-trigger slope and noise are also computed for a successive shape analysis using PAW.

Pile-up rejection

To reject pile-up without being fooled by noise fluctuations, generally a derivative method is used. With this method the signal is first filtered with a low-pass digital filter, then it is differentiated and the crossing of a threshold by the resultant signal is searched for. The integrity of this method has already been reported. In order to improve the pile-up detection and to approach the intrinsic limit of the detector, we tested a convolutive method which uses the available reference pulse and compares it with the derivative one.

In order to extract real pulses with respect to the noise spikes, we convolve the recorded waveform with the leading edge of the reference pulse, then we use a differential detector that identifies steps in the convolution greater than the noise fluctuations previously quantified. This method eliminates time information shorter than the rise time, but it is insignificant since the rise time is, in any case, the intrinsic limit of the detector. This method is very efficient in singling out real temperature rises instead of noise spikes because it is a matched filter between the signal and the averaged temperature rise.

The shape of the pulses generally depends from the microcalorimeter characteristics. The parameters of the convolutive method, due to the matched filtering, are always automatically self-optimized for the single run, while in the case of a traditional lowpass digital filter the parameters (shape, cut-off frequency, etc) should be generally studied and optimized for every microcalorimeter. In order to evaluate the relative efficiency of the derivative and the convolutive methods, a series of tests have been made with real and simulated pulses. In particular, a series of simple pile-up waveforms are generated as follows: from a sample of low rate monochromatic X-ray recorded waveforms a pulse with the noise of about the 5% of the pulse height was extracted; then by software a second pulse ranging from 10% to 100% of the first one was added to the waveform; the relative delay between the two pulses has been varied from -50 to 50 samples. The rise time of the pulses was equal to 20 samples. This test has shown a greater rejection efficiency of the convolutive method at low time differences between the

pulses, where the derivative one fails. Both convolutive and derivative methods have been used for analyzing the generated waveforms. The importance of the introduction of the convolutive methods in the rhenium experiment is shown in figure 4.5. This figure shows the analysis of a real measurement made with a bolometer composed of a high activity ^{187}Re absorber crystal, that has been analyzed with both methods, and compared with a measurement made with a low activity bolometer (negligible pile-up).

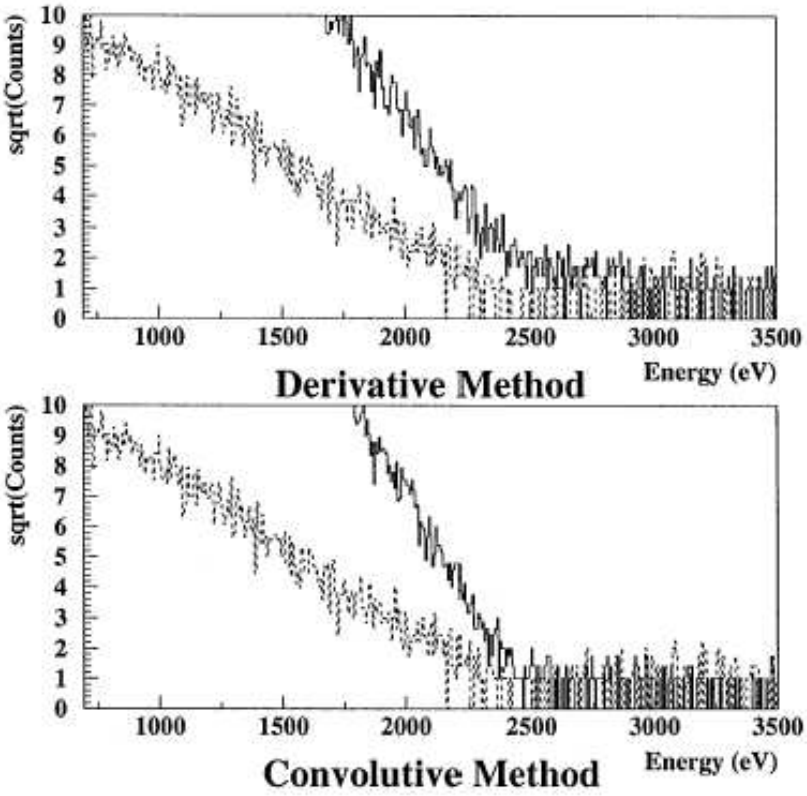

Figure 4.5 - Comparison between the derivative and the convolutive methods for pile-up rejection.

With the derivative methods non-negligible undetected pile-up causes a distortion of the spectrum shape which influences the measurement, while using the convolutive methods the spectra of the low activity source and of the high activity one are in good agreement. Operatively, when we have identified how many pulses are present in a registered waveform and where they are located, we analyze the waveform. If only one or zero pulses are detected we simply analyze the waveform; we discard the multiple pile-up (generally very rare cases) and we try to separate the two original pulses in case of simple pile-up. We estimate the amplitude of the first pulse convolving the acquired waveform with the reference pulse windowed by a rectangular window smaller than the distance between the two pulses, then we subtract the reference pulse normalized to this amplitude and we obtain the original second pulse. Interactively when we have the second pulse, we use the same procedure in order to subtract this pulse from the original waveform and we have the original first pulse. At this point, we can analyze both pulses separately. The information regarding the pile-up is stored in order to check the

coherence of the results.

4.2.4 β Spectrum Parameter Estimation in MANU

In the environment of the experiment for the electron anti-neutrino mass determination with microcalorimeters, we developed a full system to analyze data and extract sensible results. In order to evaluate the parameters of the β distribution we fit the obtained experimental spectrum to the theoretical function plus a flat background, convoluted with a Gaussian of fixed width to take into account the experimental resolution. Free parameters are: a global multiplicative factor, maximum energy of rhenium decay, neutrino mass and background level. To obtain sensible results, energy resolution is a priori evaluated using the ^{55}Fe calibration source; it has already been experimentally demonstrated that in our detector the energy resolution does not depend on the energy. Following the indications of the Particle Data Group (PDG), for the estimation of the parameters we utilize the Maximum-Likelihood method. To search for the best fit we use the well-known CERN program Minuit and for the confidence intervals evaluation we utilize the ordering principle proposed by Feldman and Cousins and accepted by the PDG, which allows the separation between the confidence interval, C.L., and the goodness of C.L. fit; for the goodness of fit calculation we implemented χ^2 test. In order to be independent from eventual human mistakes, two fit procedures have been independently implemented. As a check of the fit procedure, a method which utilize the KolmogorovSmirnov test has been developed too.

4.2.5 Montecarlo Simulation for MANU

To check our acquisition and analysis system we used a Monte Carlo simulation. In the simulation, all the known physical processes which can influence the results are reproduced according to the theoretical predictions. The data furnished by Monte Carlo are in a format ready to be processed by the analysis chain so that it can be tested. To simulate the waveform digitizer we have to reproduce the sampling process taking into account all emitters contained in the sample and their activity, to do that for each emitter in turn a random number is extracted and, depending on the result, 0, 1, 2 or 3 decays are produced; the probability of having more than 3 decays in the same sampling time is completely negligible. The released energy is then generated according to the expected distribution: monochromatic for calibration signal, flat for background and beta distribution according to the calculations shown earlier for rhenium. In this last case, since the distribution is rather complicated, the process is completed in 2 steps, during the first one the Coulomb shape factor is roughly introduced and the energy spectrum is generated without taking into account screening factors; during the second step we reject events to shape the distribution to the theoretical one. When one decay is produced, a pulse is generated with a time evolution mimicking pulses seen on the real bolometer. Last but not least, white or pink noise is added and the amplitude is properly truncated to reproduce the quantization noise of the digitizer. When the signal crosses the software threshold the data are acquired and written on disk in two versions: as raw data ready to be processed and as nominal values to be compared against analysis results. To check all the analysis system we generated 4 million Monte Carlo rhenium decays with a maximum energy E_0=2490 eV and a neutrino mass m_ν=20 eV, the random noise was adjusted to obtain an experimental resolution of 15 eV RMS, the simulated activity was of 1 Bq (relevant to check for pileup effects). The Monte Carlo also generated 43 000 calibration events coming from a virtual ^{5}5Fe source and a

flat background corresponding to 0.35 events/h. We assumed that pulse shape does not depend on the released energy: this is in agreement with our analysis of real pulses made with χ^2 test. The results are stable and predict that with such a detector it is possible to put an upper limit to the electron anti-neutrino mass of 20 eV at 95% C.L. in 3 months of data taking.

4.2.6 High statistics measurements in MANU

In order to have good confidence in the physical results, all the known experimental behaviors that could affect the interpretation of the data have been analyzed in detail, and are described as follows.

Detector response in MANU

In general the resolution function of a microcalorimeter is Gaussian, but the presence of a small tail either toward low energies or toward high energies could affect the experimental results. Figure 4.6 reports, in logarithmic scale, a close view of the ^{55}Fe K$_\alpha$ line fitted with a Gaussian distribution. The energy response of the detector is good agreement with a Gaussian distribution.

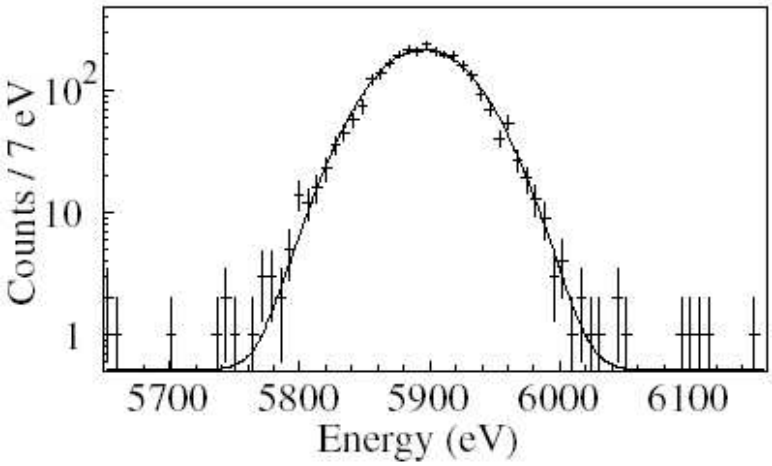

Figure 4.6 - ^{55}Fe K_α line monitored over the whole duration of the experiment.

Any low energy or high-energy tail, if present, contributes to less than 0.1% to the total counts. The effect of such a possible tail on the ^{187}Re spectrum has been evaluated by Monte Carlo simulation and it is negligible with respect to the statistical uncertainties.

Detector energy resolution in MANU

In conventional detectors the energy resolution depends on the energy, while in microcalorimeters in general it does not, but such an effect must be investigated for a good interpretation of the data. In figure 4.7 the energy resolution σ of the microcalorimeter does not show any significant energy dependence, with a slope a final energy resolution of energy calibration.

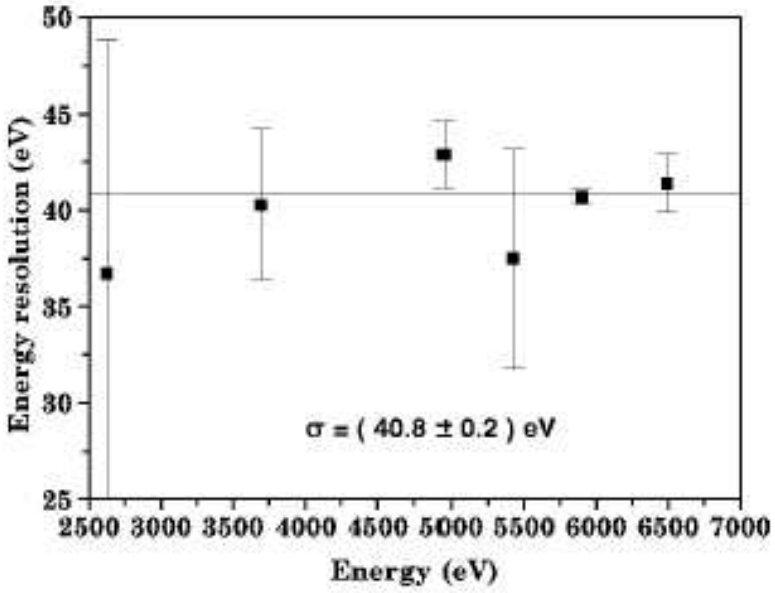

Figure 4.7 - Energy resolution versus energy of calibration lines

Energy Calibration in MANU

The measurement made with the fluorescence source shows a detector nonlinearity. This is well described by a parabolic distribution of the energy versus the pulse amplitude. The effect of the nonlinearity is about 0.5% for the ^{55}Fe K_α line and about 0.16% in the region of the end point. The high statistics measurement was performed without the fluorescence source, so that a long term change in the detector nonlinearity would not have been detected directly. Two considerations give good confidence that this is not a concern: the detector nonlinearity depends on the working conditions, which, with and without the fluorescence source, were exactly the same; and the energy nonlinearity in the high statistics measurement, evaluated using the two ^{55}Fe peaks and assuming that the calibration line passes through the origin, is in perfect agreement with the detector nonlinearity evaluated with the fluorescence source. The detector nonlinearity introduces a systematic error in the end-point energy evaluation which has been evaluated from the parabolic fit and has been included in the experimental results.

Effects of unidentified pileup in MANU

To properly evaluate the undetected pileup that could affect the measurement, three different methods have been used. A Monte Carlo simulation to generate pulses in a format compatible with the analysis procedure has been made. The simulation also keeps track of the original pulses generated. Therefore for a set of simulated data it is possible to check how correctly the analysis program reconstructs the original information. It is then possible to build a spectrum of pileup, composed of pulses classified as good pulses by the analysis program, while actually composed of more than one event. In particular, a set of 10 000 000 simulated events has been generated with the same characteristics as the microcalorimeter events. The spectrum of pileup is smoothed and added to the theoretical spectral shape in the fit procedure.

An extra parameter which represents the ratio between the beta spectrum and the pileup is then introduced in the fit. The pileup spectrum has also been theoretically calculated. The theoretical calculation assumes an energy dependence of the pileup compatible with the experiment. The result of the theoretical calculation is in good agreement with the spectrum of pileup obtained using the Monte Carlo simulation. The experimental results have also been compared with the results obtained using a second microcalorimeter, with smaller activity and different energy resolution, and therefore smaller influence of the pileup (the unidentified pileup in the second microcalorimeter is evaluated to be about 1/3 of that in the first one). The results from the two microcalorimeters are in good agreement, indicating that the evaluation of unidentified pileup does not introduce any systematic effect on the physical results of the experiment.

Energy distortion due to electron escape

The absorber is a rhenium crystal, then the radiation source is uniformly distributed in it. This means that if a b decay happens in a nucleus close enough to the surface of the crystal the emitted electron could escape from the surface, or could produce an X-ray that escapes from the surface. This effect has been investigated and the conclusion has been that it affects a very thin layer near the surface of the crystal, equal to less than 0.01% of the total volume. The distortion introduced by the escape is therefore completely negligible with respect to the statistical uncertainties.

The data reduction in MANU

An important point that is the base for every analysis is how well the spectrum produced can be trusted. In particular, if some of the parameters of the pulse shape analysis are energy dependent, the cuts of the analysis could introduce an artificial distortion to the spectrum. The analysis has therefore been done avoiding most of the cuts that are generally included. This worsens a little the energy resolution of the detector, but strongly improves the confidence on the results. Only a light cut on the $\chi 2$ parameter has been used in order to remove possible noise spikes or other experimental artifacts that could affect the measurement. Two spectra have been reduced using two different cuts, and the analysis has been performed on both. No systematic difference in the results has been found. Moreover the complete data reduction procedure has been repeated independently by two members of the team and the results do not show any evidence of a systematic difference between the two sets of data. Confidence on the fit procedure. The program to perform the fit on the experimental data is relatively complicated. A small error in the software could pass undetected even to an accurate inspection. For this reason the fit procedure has been checked using Monte Carlo simulated data. In addition two completely independent fit routines have been realized by two members of the team and the results obtained are in good agreement.

4.2.7 The ^{187}Re end-point energy measured with MANU

In an experiment measuring the end-point energy and half-life of a β decay, the effect of the neutrino mass is negligible. In the approximation of an electron antineutrino with mass zero, the theoretical spectral shape of ^{187}Re can be represented as

$$N(E,Z) \propto F(Z,E)S(E)Ep_e(Q-E)^2 \tag{4.2}$$

where E is the calorimetric energy of the decay (i.e., the energy of the emitted electron, plus the energy of the final excited states), Z is the number of protons in the original nucleus, F(Z,E) and S(E) are, respectively, the Fermi function and the shape factor of the decay, pe is the momentum of the emitted electron, and Q is the end-point energy. The term $F(Z,E)S(E)Epe$ has been theoretically calculated by Buring. This is almost constant and changes less than 5% in the whole energy interval. The theoretical calculation has been compared with the experimental spectrum from 420 eV to the end-point energy and the result shows good agreement between the two. The residuals of the fit are reported in Figure 4.7.

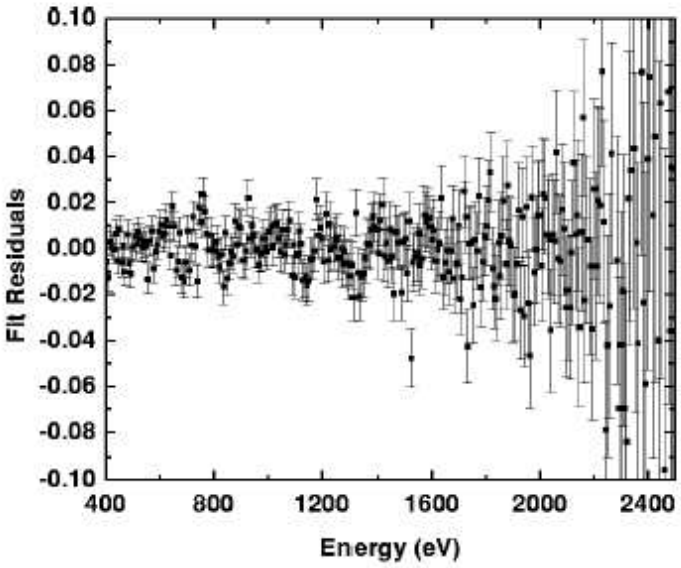

Figure 4.8 - Residuals of the best fit of the $^{1}87$Re spectrum data.

Having good confidence in the reduced data it is possible to analyze them for the determination of the end-point energy. In order to evaluate the parameters of the b distribution, the experimental spectrum is fitted with the expected distribution which includes the theoretical b spectrum, a flat background, and the unidentified pileup distribution. This distribution is convoluted with the detector response which is a Gaussian with width 40.8 eV independent of the energy. Following the recommendations of the PDG, for the estimate of the parameters we utilized the Maximum Likelihood method, which has already been treated in detail by many authors. For the goodness-of-fit calculation a χ^2 test is also implemented. The parameters that are free in the fit are the end-point energy Q, the amplitude of a flat the background B, and the relative amplitude of the unidentified pileup P. The total amplitude of the distribution has been calculated normalizing the integrals of the theoretical and experimental distributions. The effect of distortions in the background with respect to a flat distribution is negligible, since in the energy range of interest the background is always a negligible term, dominated by the spectrum and by the pileup. For the evaluation of the end-point energy the effect of the BEFS has not been included in the fit, since we verified that its average in the full energy range is zero, and therefore it affects neither the calculation of the end-point energy, nor that of the half-life. The upper limit of the fitting interval has been varied between 2650 eV and 2800 eV,

without any change in the value of the end-point energy. The lower limit of the fitting interval has been varied between 420 eV and 1750 eV. The statistical error is about 1 eV and the results are stable in the full energy range. The error due to the choice of the energy interval is smaller than 1 eV. The convergence of the fit routine is good in the full interval and the reduced χ^2 function is about 1 in the full range (χ^2=257 with 257 degrees of freedom for the energy range 10002800 eV, with similar results in the other ranges), indicating a very good agreement between experimental data and theoretical distribution. It is a remarkable result that the shape of the spectrum is stable and in agreement with the theoretical prediction over such a wide energy range, considering that in the experiments with tritium only a small fraction of the spectrum is not distorted. The dependence of the end-point energy on the assumed energy resolution has also been investigated. In the energy interval 4202800 eV the experimental spectrum has been fitted varying the energy resolution between 30 and 50 eV. As expected from trivial considerations, the end-point energy decreases when the energy resolution is increased, but the dependence is very slow: the end-point energy varies about 1 eV when the energy resolution σ is varied by 5 eV. The effect of the unidentified pileup has been investigated too. The total unidentified pileup resulting from the fit is P=0.0628±0.0017. Changing the shape of the unidentified pileup does not affect appreciably the calculation of the endpoint energy. Even using the drastic assumption of a flat pileup spectrum the end-point energy changes of only 2 eV. From the previous considerations it is possible to set the end-point energy of the ^{187}Re β-decay equal to

$$Q = [2470 \pm 1(stat) \pm 4(syst)]eV \tag{4.3}$$

where the systematic error is due to the influence of the energy nonlinearity, as mentioned before, plus the choice of the energy interval.

4.2.8 The ^{187}Re Half-Life measured with MANU

The determination of the ^{187}Re half-life was possible thanks to the very pure rhenium sample. Since the characteristics of the sample are known, the total number of radioactive nuclei is a known quantity. Thus measuring the total activity of the sample extrapolating the b spectrum to zero it is possible to calculate the half-life of the isotope. In the case of ^{187}Re the relation that links the activity of the sample to the half-life is

$$\tau_{1/2} = \frac{NmfFln2}{AR} \tag{4.4}$$

where N is the Avogadro number, m is the mass of the crystal, f is the relative amount of radioactive nuclei in the sample, F is the factor that takes into account the extension to zero of the spectrum, A is the atomic mass, and R is the measured count rate of the sample above threshold. The value of F depends on the energy threshold of the detector, on the end-point energy, and on the theoretical spectral shape at very low energy; the other parameters are known or measured quantities. The measurement of the ^{187}Re half-life has been done in two days of data taking with a special setup for the evaluation of the dead time. The trigger channel has been connected to a counter unit in order to count the total number of triggers coming from the trigger circuit plus the number of triggers coming from the trigger system happening during the dead time of the A/D converter. Since the dead time of the trigger circuit is negligible, this allows us to quantify with good accuracy the dead time of the A/D converter, equal to (8.571±0.073)%. Data have been acquired in this configuration for a total real time t=(164124±20) s. The data have been analyzed without cuts in the pulse shape routine. Other

factors that have been included in the calculation of the half-life are the following. The dead time of the analysis. When the trigger algorithm finds more than two pulses in a waveform, it discards the waveform. The analysis program keep track of the number of pulses identified and of the number of pulses discarded so that it is possible to correct the count rate. This software dead time is equal to (3.09±0.26)%.

Double pulses in MANU

Whenever the program finds two pulses in the same waveform it is able to separate the two and analyze them independently, so that the pulses are not lost. The contribution of such events corresponds to (29.99±0.24)% of the total counts.

Pileup events in MANU

The unidentified pileup events are in principle counted as single event instead of double. To correct for that we used the result of the fit routine used for the end-point energy determination. One of the fit parameters is in fact the ratio P between the unidentified pileup and the total number of counts, equal to 0.0628±0.0017. Two different energy thresholds 350 eV and 500 eV have been used to calculate the detector count rate. This allows one to avoid any possible effect of low energy spurious noise. The total count rate measured above 350 eV, when the previously described effects are taken into account, is 1.112±0.006 Hz. The count rate above 500 eV is 0.912±0.005 Hz. The two count rates are in perfect agreement with the expected distribution.

The theoretical expression has been experimentally tested from 60 eV to the end point; but its reliability below 60 eV is unknown. An absolute systematic error has been therefore estimated considering two extreme possibilities: the upper limit in the number of counts below 60 eV comes from an extension to zero energy which follows the almost quadratic distribution of higher energies, while the lower limit comes from a distribution that goes rapidly to zero below the energy of 60 eV. The half-life which is obtained in this way is

$$\tau_{1/2} = [4.12 \pm 0.02(stat) \pm 0.11(syst)^{10}]yr. \tag{4.5}$$

This result is in agreement with the previous measurements made with geochemical and mass spectrometer experiments and it , the best estimate of the ^{187}Re half-life of MANU.

4.2.9 Limits on neutrino mass set in MANU

The limit on electron neutrino mass results from the fitting procedure with the function $N_\beta = N(E, m_e)$. Taking into account all the previous considerations on the analysis, the squared neutrino mass is m^2=-462$^{+579}_{-679}$ eV^2/c^4, that gives rise to an upper limit m$_e \leq$ 26 eV/c^2 at 95% C.L., or 19 eV/c^2 at 90% C.L.

In heavy neutrino investigations it is useful to assume that the electron neutrino ν_e is a linear combination of two mass eigenstates n$_1$ and n$_2$, of masses m$_1$ and m$_2$:

$$\nu_e = \nu_1 cos\theta + \nu_2 sin\theta \tag{4.6}$$

then the beta spectral shape can be written

$$N_\beta(W, Z, m_1, m_2, \theta) = N_\beta(W, Z, m_1)cos^2\theta + N_\beta(W, Z, m_2)sin^2\theta. \tag{4.7}$$

In order to investigate the existence of a heavy neutrino mixed with a light one we assume a zero-mass light neutrino and we investigate the rhenium spectrum using the previous equation with m_2 and $\sin^2\theta$ as free parameters. The theoretical distribution used in our investigation also includes a flat background and a contribution due to unidentified pileup obtained with Monte Carlo simulation. The ratio between the unidentified pileup and the total number of counts resulting from the fit is P=0.0628±0.0017, while the flat background is compatible with zero. This is due to the fact that the background, in the whole energy interval of the fit, is dominated either by the spectrum or by the unidentified pileup. We analyzed the data using the unified approach proposed by Feldman and Cousins. No evidence of a heavy mass neutrino in the range 50÷1000 eV has been found, and the upper limits at 95% C.L. of the mixing angle $\sin^2\theta$ as a function of the neutrino mass in the range 0÷1000 eV are reported in Figure 4.9.

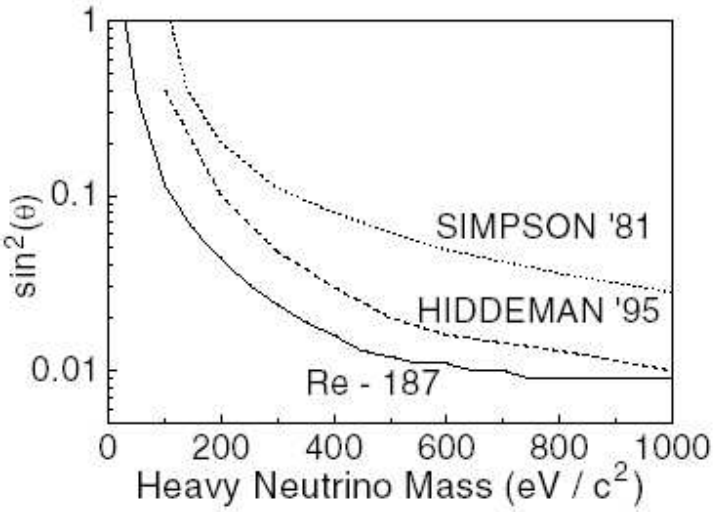

Figure 4.9 - Exclusion plot for mixing of massive neutrino in comparison with similar analysis from tritium experiments (see PDG)

4.3 The Milano experiment (MIBETA)

In Milano we have developed thermal microcalorimeters to measure the β spectrum of ^{187}Re with high statistics and high energy resolution. We use $AgReO_4$ absorbers coupled to silicon implanted thermistors acting as thermometers (Fig. 4.10). The mass of every microcalorimeter is limited to about 300 μg to avoid event pile-up and we performed an experiment with 10 such microcalorimeters at a time to be able to collect enough statistics. The MIBETA activity started early in the '90s in collaboration with the ITC-irst MEMS group to develop the silicon thermistor. The first high statistics measurement with a 10 detector array dates back to year 2000. The R&D and the experiments have been carried out until 2003 with an Oxford Instruments TL200 dilution refrigerator installed in the Laboratori Acceleratori e Superconduttività Applicata (LASA) of University of Milano/INFN-Mi.

For the MIBETA experiment special care have been devoted to the energy calibration, to the gain monitoring, to the background reduction and to settling of a reliable data analysis

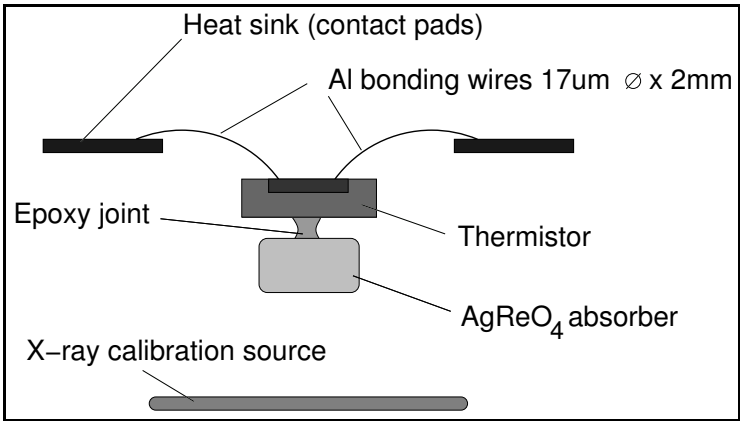

Figure 4.10 - Structure of a $AgReO_4$ microcalorimeter (left).

procedure. Some efforts are still devoted to the full understanding of all systematic uncertainty sources.

The stability of neutrino mass searches, like for other long lasting experiments, is in fact a crucial issue to avoid deformations of the measured β spectrum. Since the resulting Kurie plot does not have any peak-like feature, one or more reference energy lines are required both to monitor the gain stability and to calibrate the non-linear energy scale. Moreover, it is very important to carefully estimate the detector response, in order to properly include it in the Kurie plot fit function.

The fraction of events giving statistically significant information about the electron antineutrino mass m_ν are contained in a bin of width m_ν below the nominal end-point E_0 and are proportional to $(m_\nu/E_0)^3$. In the case of ^{187}Re this fraction equals about 10^{-7}, assuming $m_\nu = 10\,\mathrm{eV}$. Moreover in a calorimeter the β source is contained in the detector, so it is not possible to have an independent measurement of the background spectrum below E_0. It is then clear that the signal-to-background ratio is a crucial issue to get a significant sensitivity on m_ν.

In a direct neutrino mass experiment it is crucial to achieve both high energy and time resolutions together with a high statistics, in order to get a significant sensitivity on m_ν. It is also very important to distinguish between real β decay events and various kind of spurious signals, to avoid fake distortions of the resulting Kurie plot. Therefore it is also very important to have a fast and stable acquisition program and powerful analysis techniques.

4.3.1 The MIBETA detectors: choice of the energy absorber

In the MIBETA experiments, several metallic Re absorbers were initially tested, both with Ge NTD and Si:P sensors. Different forms were studied (single crystals and metallic foils), coming from various companies. Several types of glues (Stycast, Araldit, Silver Epoxy) were also tested. All these experiments gave no satisfactory results. It was never possible to get energy resolutions better than 70 eV FWHM at 6 keV. In addition, the response function was not gaussian at all, presenting a tail on the low energy side, and correlations between the pulse shape indices (in particular the decay time) and the amplitude showed up. As already reported in § 3.2, rhenium is a superconducting transition metal with $T_c = 1.698K$. Due to the long recombination time of Cooper pair in such materials, the thermalization mechanism can be slowed down and the detector response to a single energy deposition can consist of two

separate components: a fast spike, due to the non-thermal phonons generated by the small fraction of promptly recombined Cooper pairs, and a long tail connected with the subsequent delayed recombination. The observed pulse shapes corroborate this hypothesis. The energy resolution is therefore spoiled because of the fluctuating fraction of energy contained in the fast component. It is interesting to note that this problem should get less and less important by increasing the temperature, since this should speed up the recombination time. Indeed, tests conducted at 200 mK produced a nice pulse shape without initial fast component and a gaussian response. Unfortunately, at those temperatures the heat capacity was too high to give reasonable energy resolutions.

This mechanism can be modified by particular conditions external to the absorber characteristics, e.g. the presence of a magnetic field and more in general the magnetic history of the detector during cooling down, or even the type of phonon sensor and the method of sensor-absorber coupling. This can explain why the Genova experiments provided better performance with metallic rhenium.

The Milano group decided to move to dielectric absorbers, and in particular the choice fell on silver perrhenate $AgReO_4$, as discussed in § 3.2.

4.3.2 The MIBETA detectors: optimization of the Si sensors

The thermometric element is a crucial component of the detector. As thermometers for MIBETA, we have developed Si thermistors doped by ion implantation which have proved to be extremely sensitive [20] and which can be fabricated with high reproducibility by means of the Si microelectronics technology. The operation principle of these thermometers is based on the pronounced increase of the resistivity exhibited by properly doped silicon at low temperatures, as reported in general in § 3.1.2. Unfortunately, other effects appear, like electron-phonon decoupling and low frequency excess noise, which affect thermistor performances and need therefore to be carefully investigated. We have already discussed the dependence of the resistance on the temperature in this class of devices (see equation (3.2)). This formula holds only for low current flowing in the thermistor. When the current increases, non-ohmic effects appear. The theoretical models foresee indeed a *field effect* which should modify eq. (3.2): at a given temperature, a lower resistivity is expected when a finite electric field is applied; the temperature sensitivity is consequently reduced. However, not all the experimental non-linear behaviours can be explained in the *field effect* frame. In many cases a phenomenological model, the already introduced *Hot Electron Model, HEM* holds [21], which leads to higher electron temperatures T_e than phonon temperatures T_{ph}, as described by equation (3.4). The parameter g_{ep} is proportional to the thermistor volume (*power density effect*), while the exponent α has a value between 5 and 6 in our samples when data are described according to the *HEM*. The resistivity behaviour of the Si:P,B samples used in MIBETA as a function of the temperature and of the power can be satisfactorily described in the *HEM* frame.

Detector optimization considerations

The maximization of the signal to noise ratio S/N is a complicated task in a microbolometer. We do not treat here the problem from the general point of view, for which we refer to the specific literature [18, 19, 22], but we shall focus the attention on some topics strictly connected to the static properties of the thermistors. After starting with a simple modellization (a), we will briefly discuss the effects of the *HEM* (b) and of low frequency thermistor intrinsic noise,

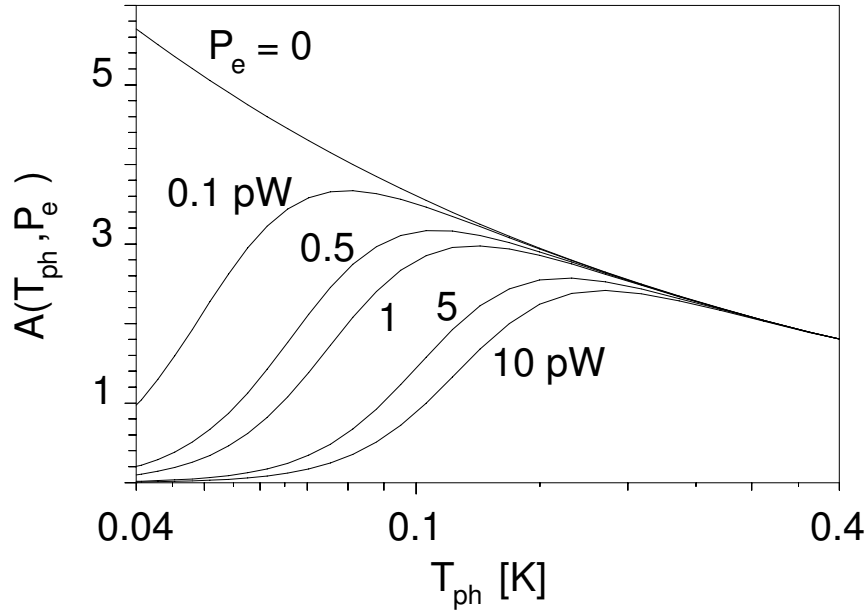

Figure 4.11 - Sensitivity vs. Phonon Temperature for increasing power on a typical thermistor.

often named "1/f" noise for its frequency dependence (c).

a) In a naive bolometer modellization, neglecting the *HEM* effects, the signal amplitude ΔV is given by the formula

$$\Delta V = V_{bias} \cdot A \cdot \frac{\Delta T}{T} \tag{4.8}$$

where $A \equiv -d\log(R)/d\log(T)$ is the sensitivity, $\Delta T = E/C$ the temperature signal, inversely proportional to the detector heat capacity C, and V_{bias} the voltage applied across the thermistor. In this approach, the bolometer contains only one thermal stage at the temperature T.

b) In the *HEM* frame however one should consider separately the electron temperature T_e and the phonon temperature T_{ph}, which refers both to thermistor lattice and to the particle absorber connected to it. Therefore, the sensitivity A must be re-defined:

$$A(T_{ph}, P) \equiv -\frac{d\log R(T_e(T_{ph}))}{d\log T_{ph}} = \gamma \left(\frac{T_\circ}{T_{ph}}\right)^{\gamma} \left(1 + \frac{P}{g_{ep} T_{ph}^{\alpha}}\right)^{-\frac{\alpha+\gamma}{\alpha}} \tag{4.9}$$

where resistance variations are related to *phonon* temperature variations, since particle interactions increase the *lattice* temperature. In (4.9), T_{ph} is connected to T_e according to (3.5). Note that $A(T_{ph}, P)$ is equal to the usual $A = -d\log(R)/d\log(T_e)$ only in the limit of $P \to 0$. When the detector is operated, a current I must be flowed in the thermistor and a bias $V_{bias} = IR$ allows to convert resistance variations into a voltage pulse given by (4.8); therefore, an electrical power P_e is inevitably developed and the sensitivity $A(T_{ph}, P)$ reduces according to eq. (4.9). Furthermore, the presence of any

background power P_b can reduce even more $A(T_{ph}, P)$. The effects of the bias power and of the background power are reported in fig. 4.11, where the typically measured HEM parameters are chosen to evaluate eq. (4.9). Unfortunately, $G_{ep}(T)$ increases with volume and decreases with $T_\circ$ (i. e. with the steepness of the $R(T)$ curve): as a consequence, there exist optimum values both for the thermistor volume and for $T_\circ$, which can be determined only after an accurate thermistor characterization and acting in the proper way on the fabrication process.

c) One more important parameter to be taken into account is the intrinsic thermistor noise. A detailed analysis of the noise in bolometers operated as particle detectors is contained in the now classical paper of J. Mather et al. [22]. However, in that analysis an additional intrinsic noise source is neglected, consisting of a low frequency excess noise which characterizes mostly Si-implanted *VRH* thermistors. (We were not able to observe an analogous noise source in NTD Ge thermistors). Following the discussion reported in [23], this noise can be attributed to resistance fluctuations expressed by the semi-phenomenological equation

$$\frac{\Delta R^2}{R^2} = \frac{\alpha_H}{N_d V f} \tag{4.10}$$

where R is the resistance, ΔR^2 the spectral density of the resistance fluctuations, f the frequency, N_d the dopant concentration, V the thermistor volume and α_H the Hooge coefficient, a dimensionless scale parameter. Experimentally, the level of this low frequency noise increases as $T_\circ$ increases, and scales as the inverse of the volume [23].

In practice, a Si-implanted thermistor consists of a sensitive volume doped just below the *MIT* (i.e. on the insulator side), whose resistance depends on the temperature; two smaller volumes doped well above the *MIT* (i.e. degenerate), which provide a low resistance electrical contact to the sensitive element; and two superconducting metal pads, which allow to bond the wires connecting to the outside world. The cross section is shown in fig. 4.12. To exploit the

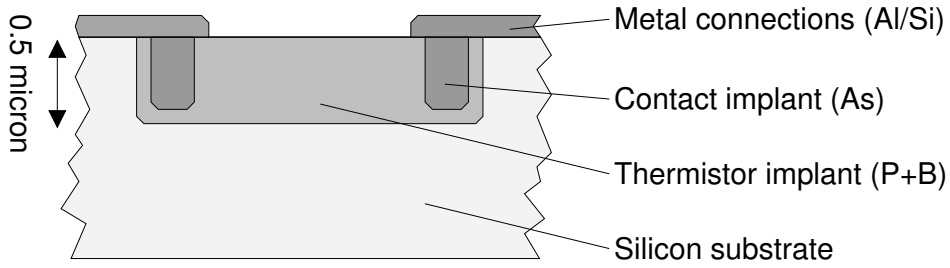

Figure 4.12 - Sketch of the cross section of a silicon implanted thermistor.

steep temperature dependence of the resistance typical of the *VRH Coulomb-gap regime*, the doped volume must be highly uniform and as deep as possible: this is accomplished by means of a series of successive ion-implants with different doses and energies, followed by an appropriate annealing step. The two $n+$ degenerate contact volumes are instead obtained through a single implant. These two implants, which are necessary to achieve a good electrical contact to the metal pads, must be minimized in volume because of their high (metal-like) specific heat which can be otherwise detrimental to the bolometer energy resolution performances.On the contrary the superconducting metal pads have negligible heat capacity below their critical temperature.

4.3.3 The MIBETA detectors

The detectors are made using the Si implanted thermistors described above and more precisely in [24]. The thermal and electrical coupling is provided by 4 ultrasonically bonded Al wires 2 mm long and 17 μm in diameter. The Si implanted thermistors have a $T_\circ$ of about 3.3 K, an implant area of $600\times600\,\mu m^2$ or $800\times800\,\mu m^2$ and an implant length-to-width ratio of 2:1. The value of $T_\circ$ and the thermistor volume, determined by the implanted area, were carefully selected among large ranges for these parameters ($T_\circ$ from 1.4 K to 19 K and volumes from 1250 to 45000 μm^3), according to the criteria discussed in § 4.3.2. The silicon substrates are thinned from 525 μm to about 80 μm by manual polishing.

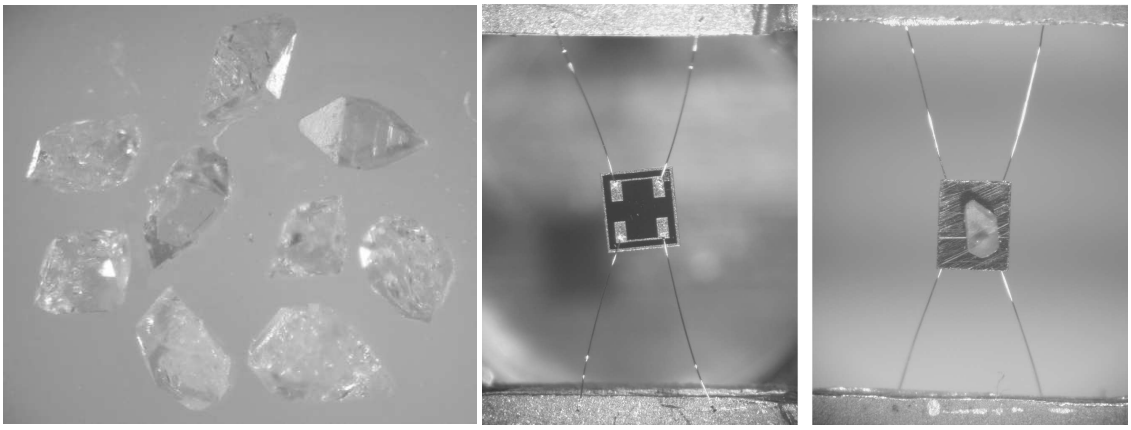

Figure 4.13 - .

The $AgReO_4$ absorbers are single crystals with masses ranging from 250 to 350 μg to avoid event pile-up. The natural fraction of ^{187}Re in $AgReO_4$ gives a decay rate of about 5.4×10^{-4} Hz/μg. Starting from a 98+ purity commercial $AgReO_4$ powder, the $AgReO_4$ are grown by Mateck Gmbh (Germany) in variable sizes around 1 mg. $AgReO_4$ crystals selected by optical inspection for their quality are then manually cut with a scalpel and cleaned in an U/S bath for few seconds with ethanol.

The crystals are glued to the back of the thermistors with a tiny drop (about 50 μm diameter) of epoxy resin ST2850FT with Catalyst 9. All assembly is done manually under a microscope.

4.3.4 The MIBETA cryogenic set-up

The 10 microcalorimeters are mounted inside 2 copper holders thermally connected to the dilution refrigerator mixing chamber. The holder temperature is kept at ~25 mK by means of a PID controller. Just about 5 cm below the detector holders is placed the JFET box kept at about 2 K by means of a copper thermal link to the refrigerator 1 K pot. The JFET box is mechanically connected to the cold plate above the mixing chamber by means of 3 Vespel SP-22 thermally isolating rods.

On the bottom cover of each holder, 5 holes allow the energy calibration of the detectors: to prevent thermal radiation from warming the detectors, the holes are covered with 6 μm Al foil.

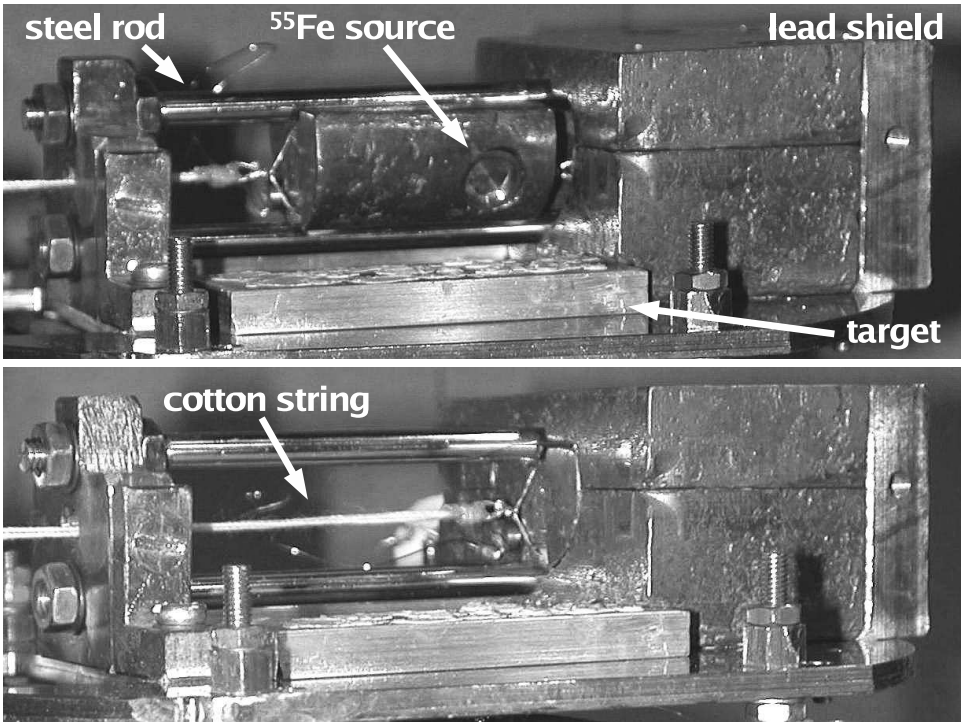

Figure 4.14 - Open (upper) and closed (lower) cryogenic source.

The calibration source sits just below the detector holders on the JFETs box at a temperature of about 2 K. It is made of two primary 5 mCi ^{55}Fe sources irradiating two composite targets, containing Al, CaF_2, Ti, and NaCl. Therefore the detectors are exposed to the Rayleigh scattered 5.9 keV K_α X-rays of Mn and to the fluorescence K_α X-rays at 1.5, 2.6, 3.7, and 4.5 keV excited in Al, Cl, Ca, and Ti respectively. To shield the Internal Bremsstrahlung radiation accompanying ^{55}Fe E.C. decay – which was producing an intense background [28] in our first high statistics measurement of the ^{187}Re β spectrum – the ^{55}Fe sources are mounted on a half-cylinder, made out of Roman lead [26] and are not directly facing the detectors (Fig. 4.14). When acquiring pure β decay signals, the half-cylinder fits inside a massive shield, also made out of Roman lead, laterally displaced with respect to the holder calibration holes. The movement of the cylinder is guided by two stainless steel rods and slides on 4 Teflon bearings: this design has been carefully tested to minimize frictions at cryogenic temperatures. When a calibration period is needed, usually every two hours [25], the cylinder is pulled out of the massive shield by means of a string made of 6 twisted and slightly epoxied cotton threads. This string, after passing through 4 pulleys, reaches room temperature across one of the refrigerator feedthroughs. The pulleys required an extensive testing at low temperature to assure the lowest friction while turning: the final design uses Vespel SP-22 bearings. Inside a high vacuum box, the room temperature end of the string is anchored to a nut moving vertically on a threaded shaft, which is connected to an external electrical DC motor through a ferro-fluid sealed rotating feedthrough. The motor is remotely controlled by the acquisition program to move up and down the end of the string between two adjustable optoelectronic sensors. While pulling the cylinder out of the lead shield, a metal spring, also connected to the cylinder by means of another cotton string, is stretched. When the 25 min of calibration are over, the motor

releases the cotton string so the spring can relax dragging the cylinder back into the container. The entire design has been optimized to guarantee a long working life: during almost one year of measurement and uninterrupted work at about 2K, the source has been moved more than 6000 times without causing problems. At the same time the combination of shielding and displacement permit to achieve a low background condition.

4.3.5 The MIBETA electronics

Since both NTD Ge and Si thermistors have a high impedance, the parasitic capacitance between their two terminals must be minimized in order to avoid excessive signal integration. The variation of this capacitance is furthermore responsible for microphonic noise generated by wire vibrations.

The front-end electronics is therefore operated a few centimeters away from the detector, at cryogenic temperatures.

The cold stage front-end consists of a common drain silicon JFETs. Ten of these devices are mounted on an aluminum plate, suspended by means of low conductance, tensioned Kevlar fibers inside a copper box. The box is mechanically connected to the 50 mK plate of the dilution refrigerator.

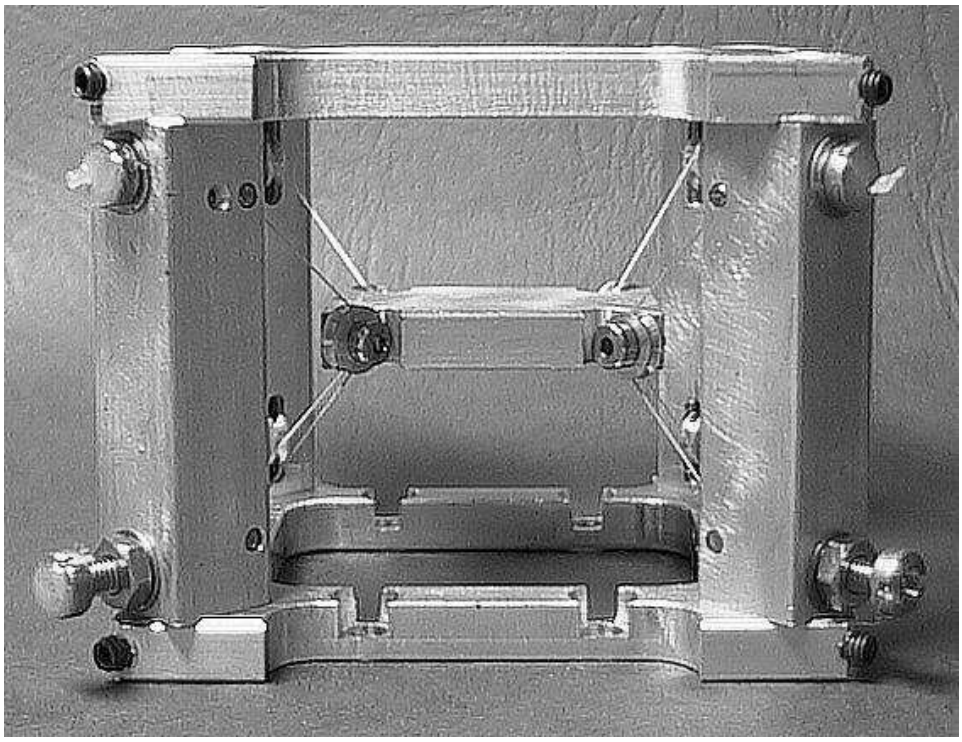

Figure 4.15 - .

A thermal connection is established by means of copper rods between the JFET box and the 1.2 K stage of the refrigerator. During JFET operation, the total power dissipated on the JFET plate is around 20 mW. All the thermal connections were calibrated in such a way that this power increases the plate temperature to about 120 K, the optimum JFET operating

temperature. The copper JFET box temperature was around 2 K, and all the 20 mW power flowed to the 1.2 K stage.

Great care was taken to shield the black body radiation emitted by the 120 K plate, which could heat up the detectors.

The signal wires which connect the detectors terminal to the JFET gates (the other terminals are grounded) were CuBe spring tensioned by 33 μm diameter, 5 cm long manganine wires, which provide electrical connection and negligible thermal conductance. To further minimize the input electrical capacitance and microphonic noise the gate leads from the JFET at 120 K up to the CuBe springs at 2 K at were bootstrapped.

For the JFET source wires which go from the cold stage to the room temperature electronics, long wires can be afforded without substantial signal integration and degradation because of the low output impedance.

The schematic diagram of each front-end set-up is shown in figure 4.16. The detector is buffered by the cold stage Q_1. A chain composed of PA, PGA and PGF amplify and filter the signal. A low noise linear optical buffer amplifier, LOC, [36, 39] allows to obtain galvanic isolation between the amplifying chain and the acquisition system. To be able to exploit fully the dynamic range of the acquisition system the parameters governing the amplification, the filtering and the detector bias are all programmable. Details regarding the description of PA and the operation of the all front-end can be found in refs. [38, 43].

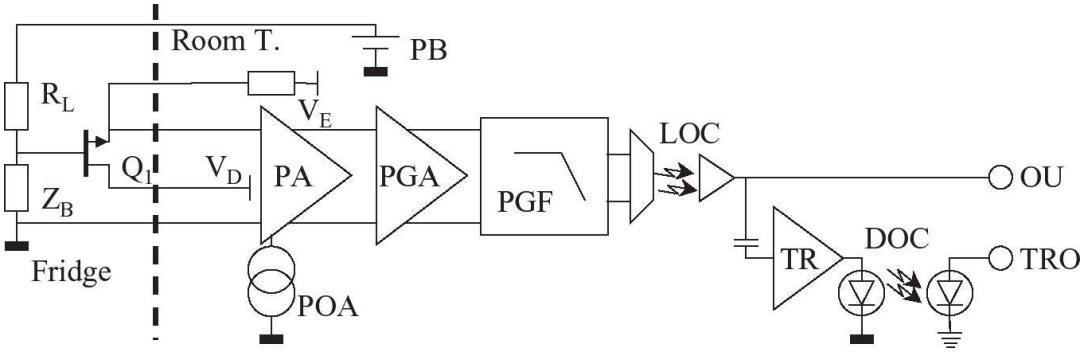

Figure 4.16 - Schematic diagram of the front-end set-up of MIBETA.

The noise feature of the front-end was dominated by the cold stage. It shows a white voltage noise of about 4 nV/Hz$^{1/2}$. At 1 Hz it rises to 15 nV/Hz$^{1/2}$ due to the low frequency contribution. Parallel noise is totally negligible, since the vanishing value of the gate current at 120 K. The cold JFETs were biased in a region of small power dissipation: $V_{DS} = 1$ V (Drain-to-Source voltage), $I_{DS} \approx 0.3$ mA (Drain current). The cold front-end used in MIBETA gives a negligible contribution to the energy resolution if the array are operated at about 60 mK, where the signal to noise ratio has a maximum. At the chosen operating condition of about 75 mK, a trade-off between high speed and adequate energy resolution, the detector intrinsic noise lowered and the front-end RMS noise rises its intrinsic contribution to a factor smaller than $\approx \sqrt{2}$. A better factor of merit would be obtained at larger Drain currents. Since the final detector high energy resolution was affected also by other systematic contribution we decided to let the front-end biasing not optimised in the final operating point, limiting the liquid He consumption. The detector load impedance, R_L, in figure 4.16 has a value of 750 MΩ and is put at about 20 mK. This choice allowed to make totally negligible its parallel noise.

The trigger signal is generated at the end of the read-out link, just close to the data acquisition system. The trigger threshold is tunable and the trigger signal is optically coupled to the DAQ.

4.3.6 The MIBETA data acquisition system

Signals coming from the 10 microcalorimeters are processed and amplified by the electronic chain [34] and then fed to the data acquisition system (DAQ). This is a VXI system composed of a Tektronix 16-channel 16-bit digitizer capable of 100 ks/s per channel (ADC), of a Tektronix 16-channel trigger module and of an embedded PC controller. The interesting feature of the DAQ is the use of one circular memory buffer for each active input channel, extending 4 times the pulse record length: the free-running digitizers keep on sampling the input signals and storing the samples in the buffers. When one channel triggers, the record containing the corresponding pulse is taken from the circular buffer and saved to disk, together with the information about the event arrival time. This minimizes dead times, thanks to the fast access of the hardware devices to the controller memory. This configuration allows also to acquire asynchronously the different channels and to save independently the pulses even if they are less than a record length apart. During data taking the analog discriminator was set to have a 40 ms *non-paralyzing* dead time to avoid DAQ breakdown in case of sudden noise bursts. To avoid trigger drifts caused by the different time resolution of the modules, the trigger module clock is continuously synchronized to the controller master clock (which serves also the ADC). Tests have shown that the uncertainty on the pulse starting point is $\sigma_t \approx 33\,\mu$s. The acquisition program is based on the Labwindows/CVI software package. To efficiently use the computer resources while keeping a fast collection time, the program is divided into several independently executing *threads* with different priorities and the communication with the instruments is made through hardware interrupts. The acquisition proved to stand up to about 15 Hz of total continuous counting rate with 10 active channels.

For the experiment described in [25], the chosen record length is 2048 channels - the first 256 used as pre-trigger - with a time base of 26 μs; each pulse is then 53 ms long. The acquisition sequence starts with 25 min of X-ray source calibration followed by 2 h of pure β decay measurement and then goes on cycling. In order to monitor the evolution of the noise of each detector during the entire measurement, random triggers are collected every 10 s during source-open periods and every 60 s during source-closed periods. Measurements are on a one-day basis (for dilution refrigerator daily service) and have always to finish with a source-open period, to be able to eventually apply off-line gain drift corrections [25]. Typically blocks of about one month measurements are then analysed altogether.

4.3.7 Background in MIBETA

The first array of 10 $AgReO_4$ microcalorimeters of the Milano neutrino mass experiment was run at the end of year 2000. The experimental set-up was identical to the one described in [25] and [30], except for the ^{55}Fe source holder. In this run (hereafter Run 9), in fact, the two primary sources were mounted on a Cu holder placed just below the detectors. During β acquisition periods, they were shielded by 0.2 mm of Cu and 1 mm of Roman lead [26], enough to stop the 6 keV X-rays of ^{55}Mn. Another small difference was the presence of 3 mm of Roman lead on the top cover of the 10 detector Cu holders, to shield the microcalorimeters from above coming low energy radiation.

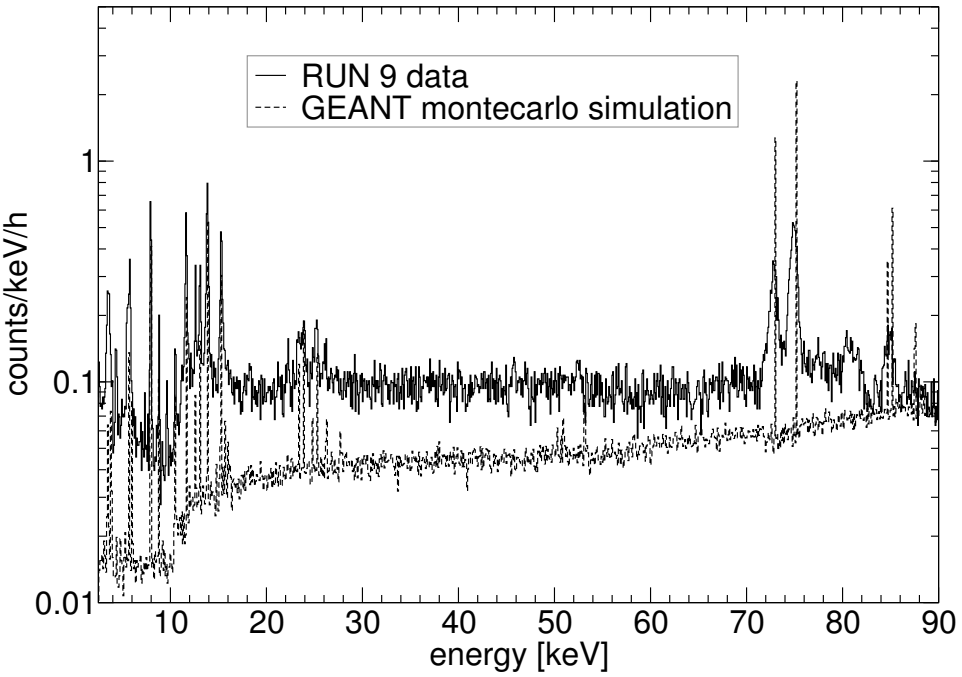

Figure 4.17 - Experimental background in the high energy region compared with a Monte Carlo simulation.

Run 9 lasted a total of 3.5 months. The acquisition sequence was identical to the one described in [25]. Due to a defect of the 16-bit 16-channel transient digitizer firmware, which could not be fixed by the manufacturer, we were able to acquire no more than 8 channels at once. Therefore the data presented here were obtained with an array of 8 detectors, for a total mass of 2.34 mg. After the same analysis procedure of [29], the final beta and calibration spectra resulting from the sum of all detectors add up to 2354 hours×mg and 517 hours×mg, respectively. A poor sensitivity on the antineutrino mass is determined by the background of spurious counts, shown by the upper curve of Fig. 4.17. The estimated background level in the energy region around the β end-point is 0.06 c/keV/h, while the ratio between the β decay signal and the background fluctuations in the 35 eV below the end-point is 3.2. Above 3.3 keV the background spectrum presents also many peaks, mostly due to Pb X-rays (K and L lines) and to Pb-Re and Pb-Ag K-K escape peaks, as will be discussed later.

To understand the origin of such a high background level, we performed a measurement (Run 10) with the same experimental set-up but without the ^{55}Fe primary sources. In this run we also set different shielding conditions for the calorimeters: one of the detector Cu holder had 3 mm of Roman lead on the top cover and 2 mm of the same lead on the bottom; from the other holder, instead, we completely removed the lead. The acquired statistics in these experimental conditions amounts to 1538 hours×mg. Because of the absence of any calibration source, the energy scale was linearly extrapolated from the position of the β end-point. In the resulting summed spectrum the background is extremely reduced with respect to Run 9 and almost constant at a level of $\sim$0.009 c/keV/h. There are also interesting differences between the spectra of detectors placed in different holders. In particular, the detectors screened both from above and below by an additional lead shield show peaks roughly at the position of Pb L X-rays and of Pb-Re K-K escape lines (the energy scale, as already noted, is not very accurate). These

features are completely absent for detectors of the other holder. Summing up only the spectra measured in the bare Cu holder we obtain a constant background level of ~ 0.007 c/keV/h.

These results together with a Monte Carlo simulation (shown by the lower curve of Fig. 4.17) allowed us to precisely identify in the Internal Bremsstrahlung (IB) accompanying ^{55}Fe E.C. decay (with a branching ratio $\sim 3.2\times10^{-3}\%$) the origin of the background which spoiled Run 9. This radiation extends up to 232 keV with an estimated activity, in our case, of 12 kBq and was responsible for most of the continuum observed in Run 9 spectrum. Its energy was also enough to produce the fluorescence K and L lines of Pb, due to the presence of lead shields both inside the detector holders and in front of the ^{55}Fe sources, together with many escape peaks resulting from the photoelectric interaction of the Pb X-rays mainly with Re and Ag atoms in the $AgReO_4$ absorbers.

The interesting feature of these escape peaks is that they are much larger than X-ray lines. For example, the escape peak at 5.7 keV, originating from the energy difference between the incoming Pb Kα_1 and the escaping Re Kβ_1 X-rays, has a FWHM resolution of 130 eV, to be compared with the 39.4 eV FWHM width of the fluorescence Ti Kα peak at 4.5 keV (produced by the targets of the fluorescence source [30]). This enlargement is caused by the intrinsic Pb and Re X-ray line widths, respectively of ≈ 60.2 and ≈ 42.1 eV, which broaden the peak to already 102 eV.

Experimental set-up improvements

With the experience accumulated in the previous runs for the new and final high statistics measurement (Run 14) several improvements were introduced in the set-up.

First of all, in order to suppress the ^{55}Fe IB, we prepared a source moving mechanism described in §4.3.4: the improvement is apparent in figure 4.18. The background level achieved in this run is practically constant at 0.007 c/keV/h up to 20 keV, thus demonstrating the efficiency of the new source shield. Measuring with Run 14 source configuration is equivalent to measuring without ^{55}Fe source. In the 30 eV ($\sim$ one resolution width) below the ^{187}Re end-point, the ratio between the β decay signal and the background fluctuations is 12.4. The lower curve of Fig. 4.18 shows Run 14 background just above the β end-point. From this figure it is possible to see the contribution of ^{187}Re event pile-up, which extends up to ~ 5 keV (twice the energy of the β end-point) and the residual background mainly caused by cosmic rays and environmental radioactivity. Further background reduction could be achieved by careful selection of all materials surrounding the detector holders and by shielding the experimental region from the dilution refrigerator components. Since our experiment is performed at sea level, the use of an active veto shield just above the detectors (for example a Si photodiode) could also help.

Other improvements aimed at the reduction of the microphonic noise. First of all, we replaced one of the refrigerator 1 K-pot needle valves by a fixed impedance. Then we constructed a more compact circuit for the electrical connection between the load resistors of the detector biasing network and the microcalorimeters, to diminish wire vibrations. As a consequence, the detectors showed a much reduced sensitivity to microphonic noise and a faster time response.

4.3.8 Analysis of MIBETA

The off-line data analysis extensively applies the optimal filter (OF) technique,which maximizes the signal-to-noise ratio to get the best estimate of the pulse amplitude. To evaluate the OF

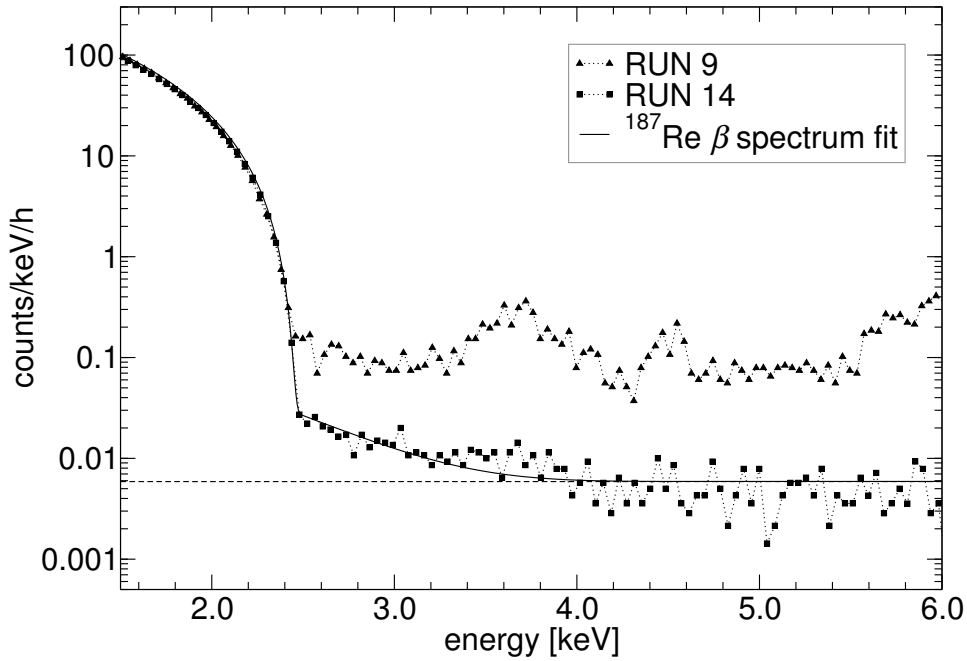

Figure 4.18 - Background in the various measurements.

transfer function $H_{\mathrm{OF}}(\omega)$ it is necessary to know the signal in a zero noise condition, and the noise. Therefore the first step of the analysis is the creation, for each detector, of an average β pulse $S(t)$ and of a noise power spectrum $N(\omega)$ from all the source-open and the source-closed periods. This procedure is repeated for each one-day measurement of a block to obtain an overall average. The OF transfer function is then given by $H_{\mathrm{OF}}(\omega) \propto S(\omega)^*/N(\omega)$.

The next step is the calculation of *n-tuples* (one for every measurement) from each digitized pulse. They contain all useful pulse parameters, like the channel number, the absolute time, the OF amplitude, the signal rise and decay times, some shape factors (see later), the amplitude and delay of any post-trigger secondary pulses (pile-up events), etc. The identification of secondary pulses with the smallest possible time separation is crucial in a neutrino mass experiment to avoid deformation of the measured β spectrum: the best results are obtained searching for secondary pulse exceeding a threshold of few times the RMS noise after applying the optimal Wiener Filter (WF), whose transfer function $H_{\mathrm{WF}}(\omega)$ is given by $H_{\mathrm{WF}}(\omega) \propto S(\omega)^*/(|S(\omega)|^2 + |N(\omega)|^2)$. Afterwords the *n-tuples* are divided into single channel ones requiring a detector multiplicity < 4 for each event in order to reject electrical disturbances triggering more detectors at once (within a time window of about 10 ms).
The next step is the gain drift correction by means of X-ray peak position stabilization [25]. The higher energy X-rays (Al and Cl lines are never employed in this procedure) are then used to correct any system instabilities by fitting the time behaviour of the peaks and stabilizing them to straight lines [29]. Fig. 4.19 shows the result of this gain drift correction for a typical detector during a one-day measurement.

Finally source-open and source-closed *n-tuples* (as tagged by the acquisition) are generated for each channel. The source-open *n-tuples* serve to create X-ray spectra, whose energy scale is then obtained by fitting the Al, Cl, Ca, Ti and Mn Kα peak positions with a second order

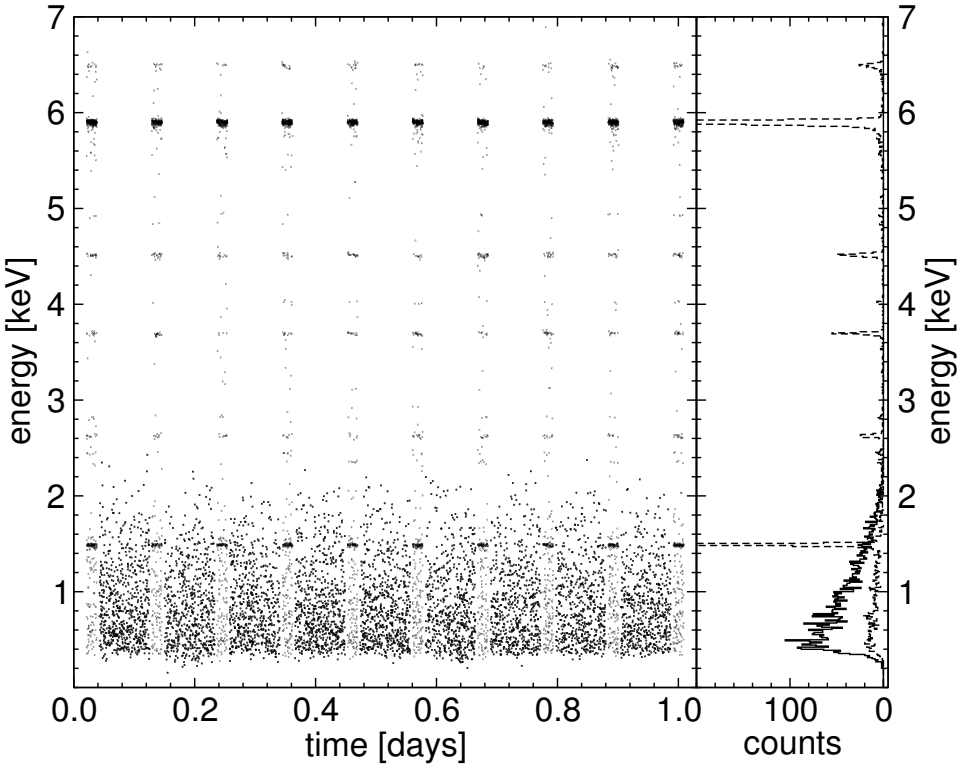

Figure 4.19 - A sample one day measurement, after gain stability correction, showing the periodical exposure to the calibration source.

polynomial.
Residual instabilities will be included in the broadening of the X-ray peaks; they are expected to contribute less than 0.2% to the detector response function. After stabilization, the X-ray peak positions are used to calibrate the energy scale of the spectra. It turned out that all $AgReO_4$ detectors show slightly asymmetric X-ray peaks; their shape can be satisfactorily reproduced by means of two symmetric gaussians of equal width. A dedicated measurement to possibly infer a physical explanation for such a behaviour has been performed after RUN14 and the data analysis is presently in progress (see §5.1.2).

The source-closed *n-tuples* are used to create the β spectra. This is the most delicate point, because it is very important to carefully select only true β decay pulses and not to apply cuts which could differently weight the various energy bins of the Kurie plot. For this purpose several pulse shape parameters are calculated by comparison with the average pulse $S(t)$: the most sensitive parameters are the root mean square deviation of the optimally filtered pulses and the output of an Artificial Neuronal Network (ANN). The ANN is a 3-layered network whose 60 input nodes are fed with 600 pulse samples averaged to 60 and taken in a window which extends from 1.5 ms before to 14 ms after the pulse starting point. One single ANN is used and is trained with good β pulses and a collection a various identified spurious pulses from all channels. The combined use of the ANN and the above mentioned pile-up identification algorithm proved to be very effective: in most cases they are enough to reject all spurious pulses (silicon thermistor hits, electrical disturbances, etc.) and to remove pile-up events with a time separation as small as about 3 rise times, with an efficiency better than 99%.

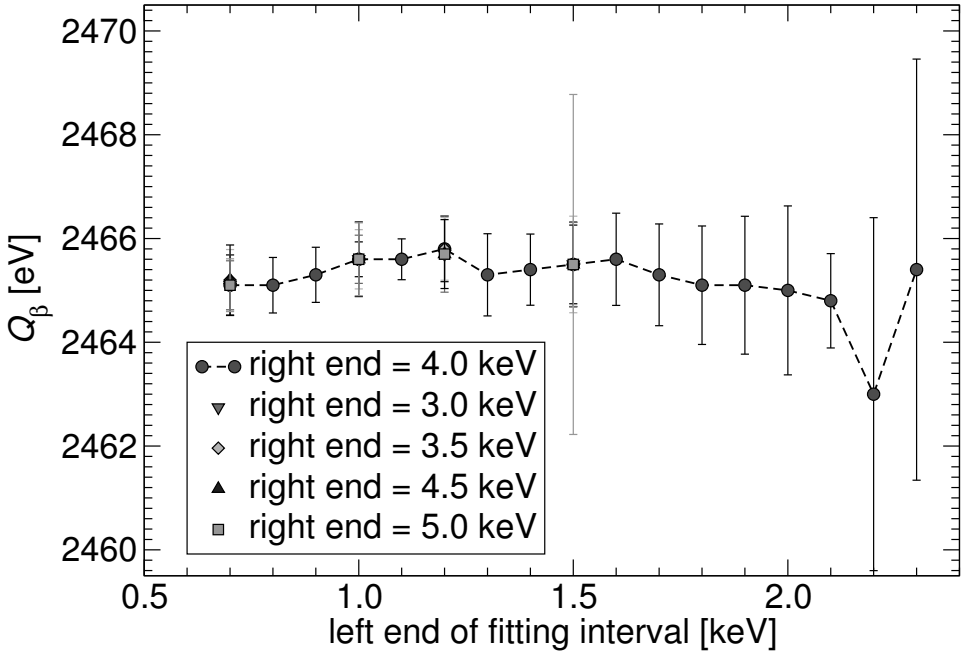

Figure 4.20 - Dependence of the end-point energy on the fitting interval limits.

Once the pure ^{187}Re decays are selected, calibrated β spectra are generated for each detector using the energy scale previously calculated from the source-open periods. The spectra from the various microcalorimeters are then added to create the sum β spectrum.

β SPECTRUM FIT

The β spectrum is fit with the function $F = (f_{th} + f_{pup} + f_{bck}) \otimes f_{det}$, where f_{th} is the theoretical spectrum calculated by W. Bühring [32] for first forbidden unique β transitions, $f_{pup} \propto f_{th} \otimes f_{th}$ is the pile-up spectrum, f_{bck} is the unknown background, and f_{det} is the detector energy response function.

The β end-point, the β and pile-up spectrum normalizations, the background level, and the squared electron antineutrino mass $m^2_{\overline{\nu}_e}$ are all free parameters of the fit. The fit procedure uses the estimator $\Xi^2 = 2\sum_i [f_i - s_i - s_i \ln(f_i/s_i)]$. For the evaluation of the neutrino mass upper limit the Bayesian approach is used for non-physical regions (i.e. $m^2_{\overline{\nu}_e} < 0$). The best fit parameters of [25] were obtained in the energy interval $0.8 \div 4$ keV. By varying both the upper - between 3 and 5 keV - and the lower - between 0.7 and 2.1 keV - limits of the fitting interval, all fit parameters (Fig. 4.20 shows the results for the β end-point) remained stable within the errors, thus confirming the good description of the data given by the function F.

Systematic sources of uncertainties in the evaluation of $m^2_{\overline{\nu}_e}$, as well as of the end-point, are determined varying some of the fit hypotheses: (*i*) the detector energy resolution (which has an energy dependence described by $\Delta E^2_{FWHM} = a + bE + cE^2$); (*ii*) the detector response function [30]; (*iii*) the background shape below the β spectrum (as described above); and (*iv*) the parametrization of the theoretical β spectrum.

Table 4.1 - Detector characteristics and their performance at the chosen optimal operating point.

Det. #	$AgReO_4$ mass [μg]	R_{op} [MΩ]	T_{op} [mK]	$\Delta E_{\rm FWHM}$ baseline [eV]	$\Delta E_{\rm FWHM}$ @ 1.5 keV [eV]	$\Delta E_{\rm FWHM}$ @ 2.6 keV [eV]	τ_{rise} [μs]
1	272.0±3.0	3.02	78.6	20.1	23.7	26.3	440
2	259.0±6.0	4.38	70.2	19.4	23.2	26.6	340
3	280.3±6.5	3.03	78.5	25.8	28.7	30.5	670
4	249.7±2.0	2.78	80.6	21.0	25.4	28.9	590
5	284.0±3.0	5.04	67.4	22.5	25.7	29.2	500
6	282.0±3.4	9.09	57.3	24.6	29.3	33.4	510
7	268.7±5.9	3.68	74.0	18.4	21.3	24.9	430
8	278.3±1.5	3.28	76.6	23.9	29.2	34.5	445

4.3.9 Results of MIBETA

The last high statistics measurement (Run 14) started on June 2002 with a partially renewed array of 10 $AgReO_4$ microcalorimeters, and was stopped on April 2003 due to a problem in the fluorescence source moving mechanism. The data from 2 detectors, with poorer resolution, are not included in our statistics, so the effective total mass of the array is 2.174 mg, for a ^{187}Re activity of 1.17 Hz. The total live time adds up to 210 days, 42 of which have been devoted to the periodic calibrations while 168 days correspond to pure β acquisition. The total efficiency of this run is therefore of 67%, which includes daily servicing to our refrigerator (∼2 hours a day), calibration test measurements and a few lab power failures; the pure β acquisition efficiency is of 54%. The final beta and calibration spectra obtained, as described in [29], from the sum of all 8 detectors correspond to 8751 hours×mg and 2168 hours×mg, respectively.

The performance of the detectors were quite stable during the run. The FWHM resolution at 1.5 keV in the single detector final spectra ranges from 21.3 to 29.3 eV, with an average of 25.5 eV. The FWHM resolution of the entire array extrapolated at the energy of the β end-point (2.46 keV) is 28.5 eV. At this energy, the two symmetric gaussians used to interpolate the X-ray peak shape are separated by 37 eV, the area ratio between the left and the right one being 3.4%. With this detector response function, the displacement of the Cl line from its nominal position in the summed spectrum is 0.5 eV [28]. The 10 to 90 % risetime of the 8 detectors is in the range 340 - 680 μs, with an average value of 492 μs.

Fig. 4.21 shows the X-ray calibration spectrum obtained from the sum of the 8 working detectors of the Milano neutrino mass experiment array [25]. It corresponds to 2168 h×mg. Besides the K_α lines, and corresponding K_β, produced by the fluorescence source, there are several other peaks due to fluorescence of the materials surrounding the detectors. One can recognize the M lines of Pb (at 2.35 and 2.44 keV) and the Cr K_α peak (at 5.41 keV); with smaller statistics, there are probably the fluorescence lines of K, Au, Sn. These peaks are not present when the source is inside the lead shield [28].

All X-ray peaks show tails on the low energy side and cannot be fit by a symmetric gaussian. A possible way to satisfactorily reproduce the peak shape is to fit with two symmetric gaussians of equal width. The distance between the left and the right gaussian is typically around 40 eV with an area ratio of less than 5 %. Other fit solutions, for example a symmetric gaussian with exponential tails, are presently under study.

A physical motivation for such a behaviour is not yet known. The attenuation length of

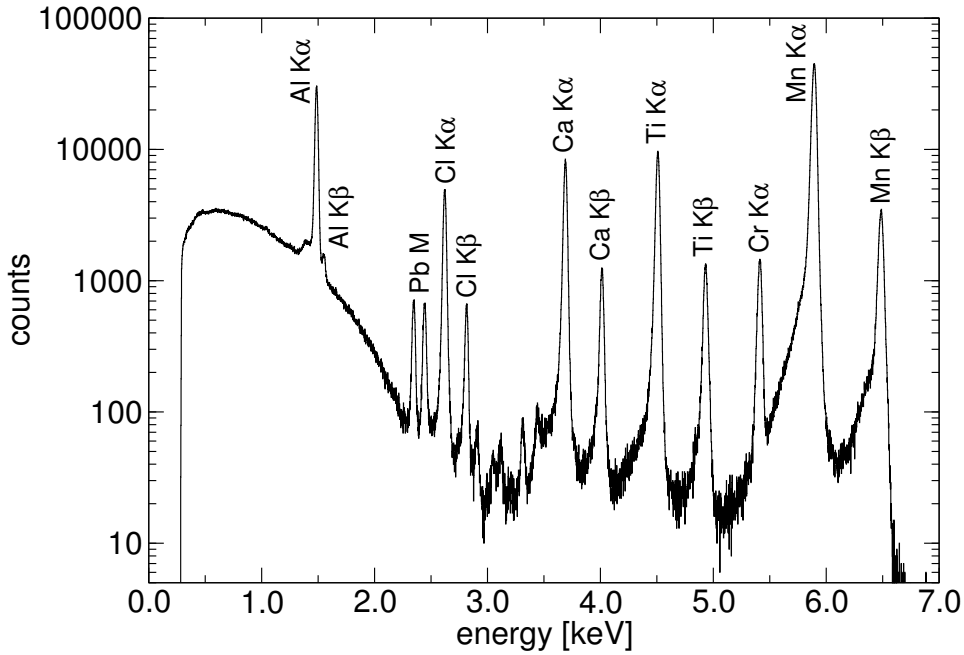

Figure 4.21 - Total X-ray calibration spectrum.

a 6 keV photon in $AgReO_4$ is $\approx 3\,\mu$m, so all calibration X-rays do not penetrate much in the absorbers – the $AgReO_4$ absorbers have linear dimensions of about 300 μm. Since $AgReO_4$ single crystals present quite rough surfaces and they are slightly hygroscopic – when exposed too long to air, a yellowish patina forms which can be removed by ethanol – the peak shape could reflect a surface effect and not a detector characteristics. Therefore electrons from ^{187}Re β decay, which are emitted all over the volume, could in principle still give a pure gaussian response. The fit of the Kurie plot is then made under both assumptions [29]: a single symmetric gaussian and two symmetric gaussians with distance and area ratio as explained before. The differences in the fit results are included in the quoted systematic errors [25]. Moreover the peak FWHMs have an energy dependency which can be described by $\Delta E^2_{\rm FWHM}(E) = a + bE + cE^2$. We attribute the linear term to statistical fluctuation in the thermalization in $AgReO_4$ and the quadratic term to uncorrected gain instabilities (Fig. 4.22). The latter in particular contribute to about 2% of the peak broadening. For sake of simplicity, the Kurie plot is fit assuming an energy constant peak width [29] as obtained by extrapolation of $\Delta E^2_{\rm FWHM}(E)$ at the β end-point: the effect of this simplification has been tested by Montecarlo simulations and the estimated uncertainty is included in the systematic errors.

The final Kurie plot resulting from the sum of the 8 detectors is shown in Fig. 4.23. It corresponds to $\sim 6.2 \times 10^6$ ^{187}Re decays above the common energy threshold of 700 eV. It was fit with the theoretical spectrum calculated by W. Bühring [32] in the energy interval $0.9 \div 4$ keV; details of the fitting procedure are given in [29]. The χ^2/DOF of the fit is 0.905. The inset of Fig. 4.23 shows a blow-up of the fit result in the region around the β end-point. The measured value for the end-point is $2465.3 \pm 0.5(stat.) \pm 1.6(syst.)$ eV. The systematic error is determined by the uncertainties in the energy resolution, in the detector response function, in the shape of the background below the beta spectrum and in the theoretical spectral shape for the ^{187}Re beta decay. By fitting the distribution of the time intervals between two

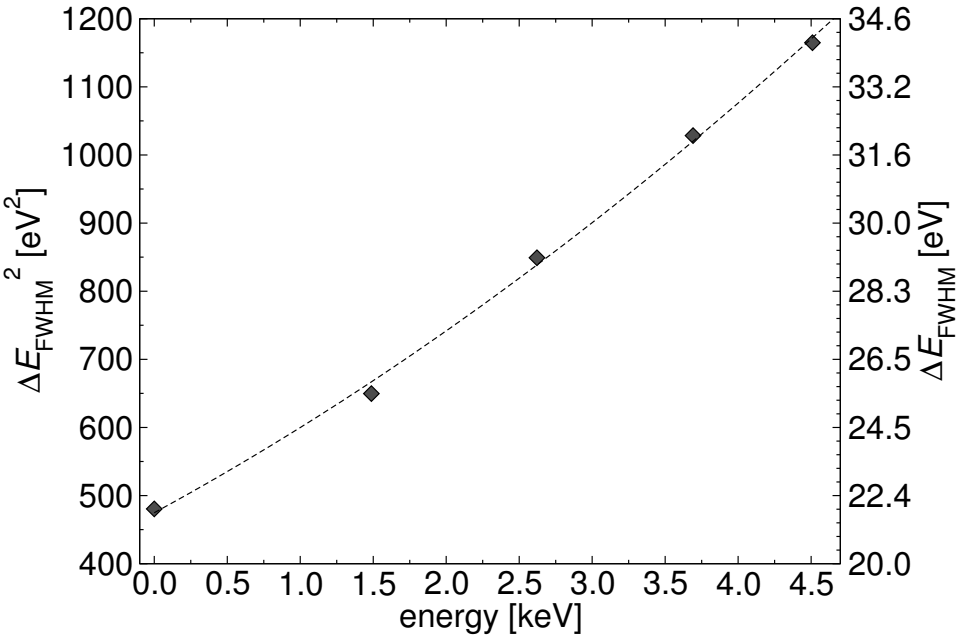

Figure 4.22 - Energy dependence of the peak FWHM in the total calibration X-ray spectrum.

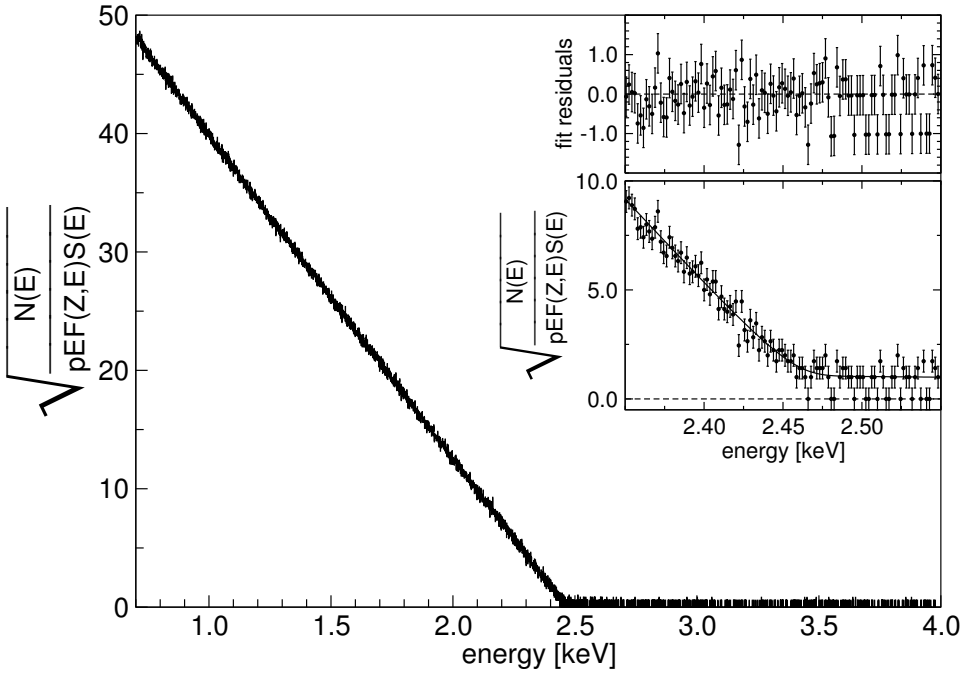

Figure 4.23 - Kurie plot obtained from the sum of all 8 detectors, where p is the electron momentum, E is the electron kinetic energy, $F(Z,E)$ is the Coulomb factor and $S(E)$ is the shape factor. In the inset, fit residuals and fit function superimposed to the data in the energy region around the β end point.

successive β decays, we could precisely determine the effective decay rate of ^{187}Re, which was

found to be $[43.2 \pm 0.2(stat.) \pm 0.1(syst.)] \times 10^9$ years. Here the statistical error is due to the uncertainties in the measurement of the mass of the absorbers and the systematic error is due to the uncertainties in the pile-up discrimination. The values for the end-point energy and for the half lifetime are the most precise existing in the literature. The latter has considerable impact in geochronology.

The squared electron antineutrino mass $m^2_{\overline{\nu}_e}$ is $-112 \pm 207(stat.) \pm 90(syst.)\,\mathrm{eV}^2$, where the systematic error has the same origin as for the end-point energy quoted above. The 90 % C.L. upper limit to the electron antineutrino mass is 15 eV. This result is in agreement with the expected sensitivity deduced from a Monte Carlo simulation of an experiment with the same statistical significance as our data set.

The fit residuals in the energy interval between 470 eV (the common energy threshold for 7 of the 8 detectors) and 1.3 keV show a clear evidence of an oscillatory modulation of the data due to the Beta Environmental Fine Structure (BEFS) in $AgReO_4$ /figure 4.24). This important effect was first observed for metallic rhenium [64]. A quantitative analysis in terms of $AgReO_4$ lattice structure is presently on the way.

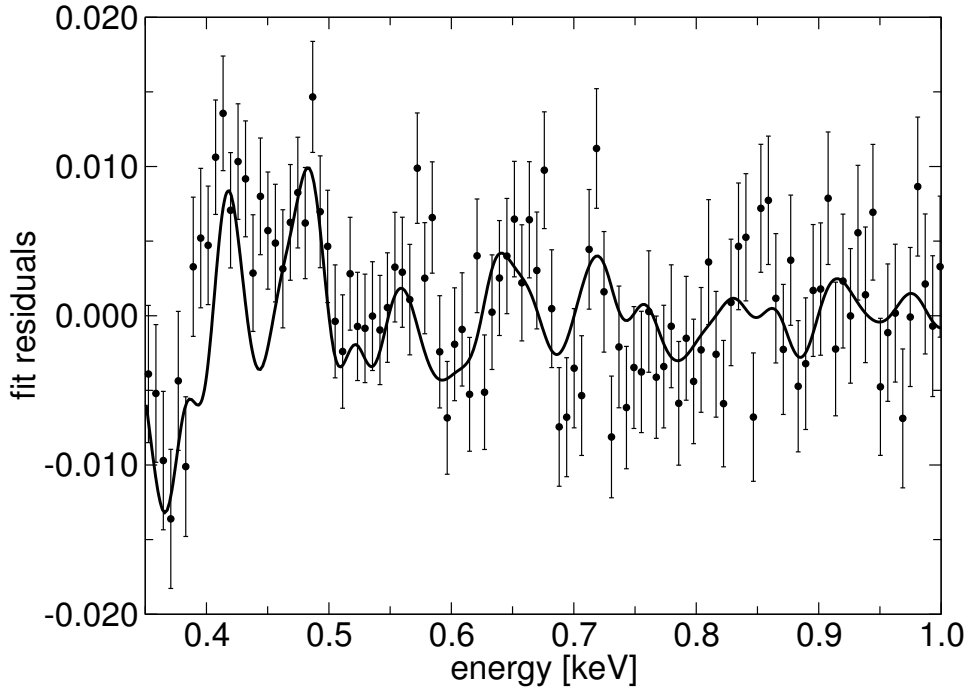

Figure 4.24 - .

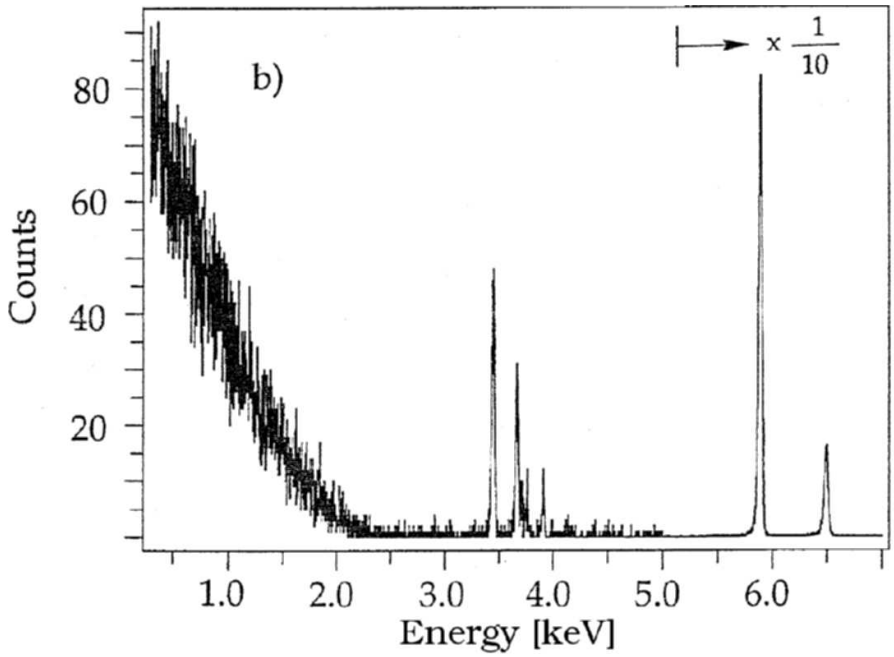

Figure 4.25 - .

4.3.10 Alternative sensors and absorbers in MIBETA activity

Beside the detectors developed and used for the high statistics measurement, in the frame of the MIBETA experiment R&D many other different kind of detectors were tested. Detectors using different absorbers (see §4.3.1), but also detectors using different sensors.

It is interesting to mention here the results obtained with a $AgReO_4$ crystals coupled to NTD sensors. The sensors, the so called NTD Germaniun flat-packs manufactured by J. W. Beeman at the Lawrence Berkeley Laboratory, had linear dimensions of $300\times100\times20\,\mu m^3$, with two boron ion implanted contacts covered by Au pads ($100\times50\,\mu m^2$) deposited on both ends of the same $300\times100\,\mu m^2$ side of the thermistor. The sensors belonged to the series # 27 with a Ge doping giving a T_0 of about 11 K. Very interesting results were obtained with one detector where two 17 μm diameter pure aluminum wires were ultrasonically bonded to the gold pads and a 430 μg $AgReO_4$ crystal was glued to the opposite side of the sensor. The glue was a tiny drop of the ST2850FT epoxy resin.

The set-up used to test this detector was similar to the one described in §4.3.4 but still not optimized to minimize the parasitic electrical capacity. Figure 4.25 show the data collected at the best working point at a temperature of about 63 mK where the resistance was about 52 MΩ. The baseline width was about 25 eV FWHM and the energy resolution was about 29 eV FWHM around 3 keV where the fluorescent L lines of tin were observed. The risetime was about 500 μs.

Chapter 5

MARE-1

5.1 The goal of MARE-1

The results obtained by the MANU and MIBETA experiments and presented in the previous chapter prove the potential of the thermal detection technique applied to the direct search for the neutrino mass. Although their achieved sensitivity is about one order of magnitude worse than the present limit set with the electrostatic spectrometers, there is a large margin for improvements.

As described in §1.3 we are committed to realize a new calorimetric neutrino mass experiment with a statistical sensitivity of 0.2 eV and with a time-line almost overlapping the KATRIN schedule. The first phase of this project aims at an intermediate neutrino mass sensitivity of few electronvolts. The scientific motivations for this phase are:

- to scrutinize the Mainz/Troitzk results with a completely independent approach; this result can be achieved *before* KATRIN full data taking;
- to improve our understanding about the possible systematic uncertainties peculiar of the calorimetric approach; (see §5.1.2)
- to gather further experience on the rhenium-based thermal detectors and on the running of a large array experiment.

At the end of MARE-1 the collaboration must be able to decide whether to proceed with the effort of MARE-2. To this purpose it is crucial also to sustain a parallel R&D activity for MARE-2 detectors (see §6).

As anticipated in §1.3 and extensively discussed in the following sections, the experience of the Genova and Milano groups together with the techniques developed by the groups involved in the present proposal allow to successfully reach the MARE-1 goals. To obtain a 10 fold improvement on the sensitivity with respects to the present MANU and MIBETA results, the main technical issue is to increase the total statistics by 4 orders of magnitude, i.e. from about 10^6 to about 10^{10} β decays. Only moderate improvements are required for what concerns the performance of the detectors.

5.1.1 Monte Carlo approach to the statistical sensitivity

We have developed a Montecarlo code to estimate the statistical sensitivity of a neutrino mass experiment performed with thermal calorimeters. The approach is to simulate the β spectra

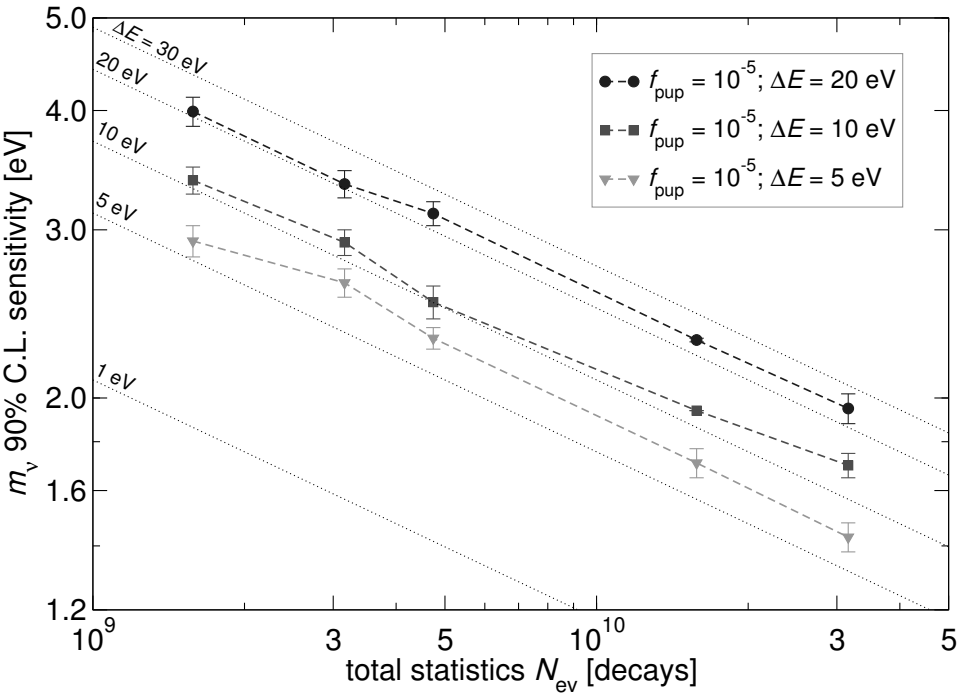

Figure 5.1 - Results of the Montecarlo simulations for different experimental configurations as a function of the accumulated statistics N_{ev} (see text) in absence of background. The dotted lines are the predictions of the formula given in the text.

that would be measured by a large number of experiments carried out in a given configuration: the spectra are then fit as the real ones [29] and the statistical sensitivity is deduced from the distribution of the obtained m_ν^2 parameters. The Montecarlo parameters describing the experimental configuration are the total statistics N_{ev}, the FWHM of the gaussian energy resolution ΔE, the fraction of unresolved pile-up events f_{pup} and the constant background level b. These input parameters can be derived from the ones actually characterizing a real experiment: $N_{ev} = N_{det} \times A_\beta \times t_M$ and $f_{pup} \approx A_\beta \times \tau_R$, where N_{det} is the number of detectors, A_β is the β decay activity of a single detector, t_M is the measuring time and τ_R is the pulse-pair resolving time – of the order of the detector rise time.

As a first step the function $S(E)$ describing the expected experiment outcome is numerically evaluated: $S(E) = (N_{ev}(N_\beta(E) + f_{pup} N_\beta(E) \otimes N_\beta(E)) + b) \otimes g(E)$, where $N_\beta(E)$ is the ^{187}Re β spectrum normalized to unity (usually for $m_\nu = 0$) and $g(E)$ is the gaussian detector energy response function.

The large number of simulated spectra (usually 1000) are then generated by introducing Poisson distributed statistical fluctuations in the spectrum bins according to their content. The 90% C.L. m_ν statistical sensitivity $\Sigma_{90}(m_\nu)$ of the simulated experimental configuration is given by $\Sigma_{90}(m_\nu) = (1.64\sigma)^{1/2}$, where σ is the standard deviation of the distribution of the m_ν^2 found by fitting the spectra.

Fig. 5.1 and Fig. 5.2 show the results obtained for experiments with sensitivities around 3 eV in absence of background. The simulation results are compared with the prediction (dotted lines) of the formula $\Sigma_{90}(m_\nu) \approx (E_0^3 \Delta E / N_{ev})^{1/4}$ which can be obtained from statistical considerations for the ^{187}Re β spectrum – with end-point E_0 – neglecting the effect of pile-up and

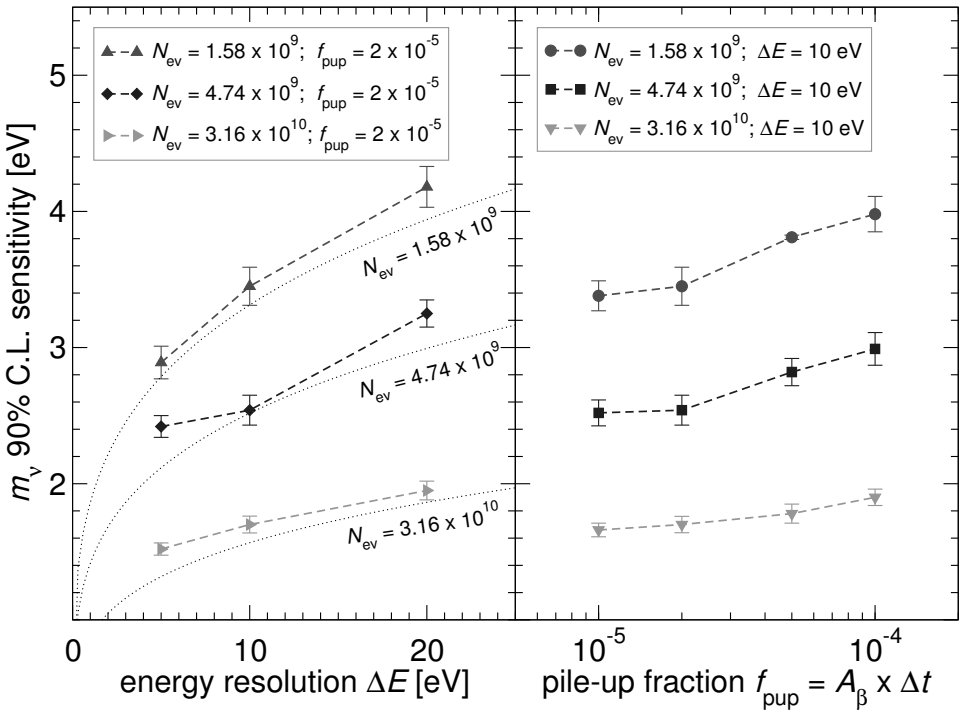

Figure 5.2 - Results of the Montecarlo simulations for different experimental configurations as a function of the detector energy resolution ΔE and of the pile-up unresolved fraction of events f_{pup} (see text) in absence of background. The dotted lines in the left panel are the predictions of the formula given in the text.

background. It is evident how the Montecarlo results can be usefully scaled with the help of this formula to give further interesting predictions.

The effect of background is shown in figure 5.3 as a function of the signal-to-background ratio integrated in the beta decay energy range.

We have also run a simulation of the present experimental situation of the Milano neutrino mass search (see §4.3.9) obtaining $\Sigma_{90}(m_\nu) = 16 \pm 1$ eV: the good agreement with the result quoted in §4.3.9 show the reliability of the approach.

Finally we have used this approach to estimate also the effect of the various sources of systematic uncertainties. Some results are reported in the following section where the systematic uncertainties are discussed.

5.1.2 Discussion of the systematic uncertainties

One of the purposes of MARE-1 is to verify the effect of the known systematic uncertainties and to check for the presence of unknown ones, with a substantially higher statistics. The main sources of systematic uncertainties identified in the past MANU and MIBETA experiments are those related to

- the theoretical spectral shape of the first forbidden ^{187}Re β decay;
- solid state effects, in particular BEFS;
- the detector response function;

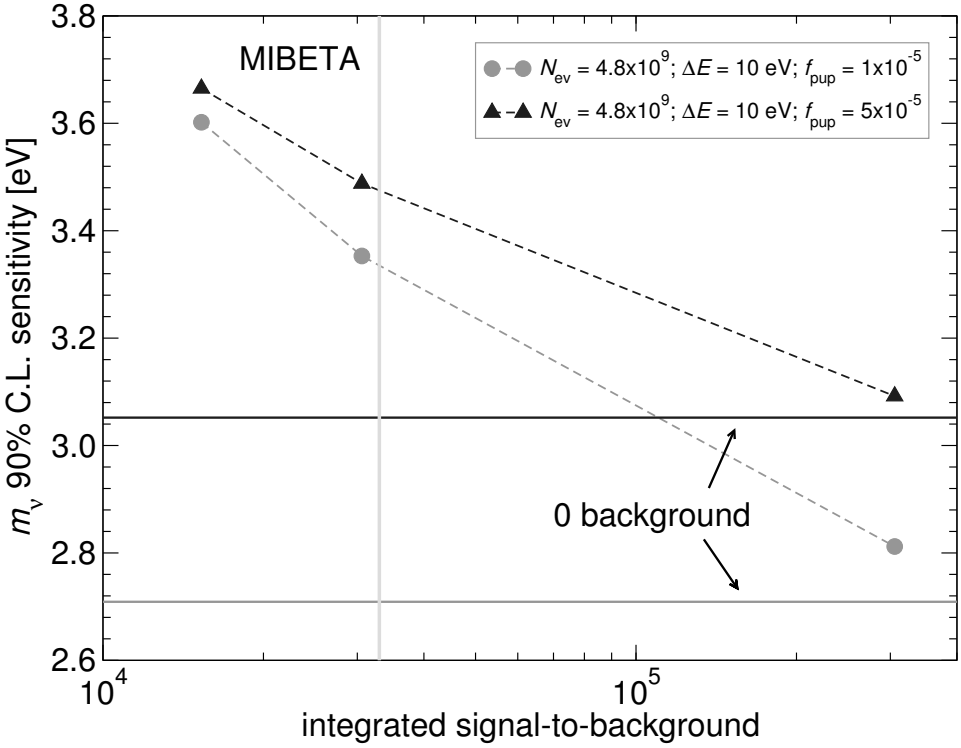

Figure 5.3 - Effect of the background on the evaluation of m_ν^2.

- the unidentified pile-up spectrum;
- the external radioactive background;
- the energy scale;
- the surface β electron escape;
- the data reduction.

In the following we discuss our present knowledge and understanding of some of these sources together to some ideas about how to minimize the uncertainties. For what concerns the last one it is strongly dependent on the data reduction procedure itself and it can be discussed only when the procedure is settled at the end of the data taking. One other source of systematics may be the summing of many independent spectra.

The ^{187}Re beta decay: nuclear physics

Of paramount importance in the extraction of the anti-neutrino mass from the β-spectrum is a complete understanding of the basic spectral shape and the higher order corrections. The β-decay of ^{187}Re is first-order unique forbidden and its theoretical form is represented by

$$\frac{dN}{dW} \propto F(Z,W)S(W)p_eW(W_0 - W)^2 \tag{5.1}$$

with

$$W = \frac{E_{Kin} + M_e c^2}{M_e c^2} \tag{5.2}$$

where E_{Kin}, M and p are the kinetic energy, the rest mass and the momentum of the beta electron respectively, and W_0 is the maximum energy of the electron emitted during beta-decay. The primary correction factors to the beta spectrum include F(Z,W), the Fermi function and S(W), the Shape factor. The Fermi function, accounts for the Coulomb influence to the outgoing beta-electron of the charge Z of the nucleus. The Fermi function has been calculated explicitly by Bühring using the Tables of Behrens and Jahnecke. In this analysis the charge screening effect of the atomic electrons surrounding the nucleus is also included by considering a screened Coulomb atomic potential of the Hulthen type. The Shape factor S(W) associated with the first unique forbidden character of the ^{187}Re beta-transition, to first approximation, is of the form

$$S(W) = p_\nu^2 + \lambda p_e^2 \tag{5.3}$$

,

where p_ν is the momentum of the anti-neutrino and λ is a Coulomb amplitude. This amplitude, inclusive of screening effects, has also been evaluated specifically for the isotope ^{187}Re by Bühring.

Solid state effects: general discussion

When the $^{187}Re^{75}$ undergoes the β-decay, the final state is the ground level of $^{187}Os^{76}$ atom in the rhenium crystal. Therefore, the end-point energy of the $^{187}Re^{75}$ in the crystal is decreased with respect to the one of the decay of the isolated isotope. It can be written that

$$E_{endpoint} = (Q - m_e c^2)(e\phi - E_{Fermi}) - \Delta B_{lattice} \tag{5.4}$$

where Q is the energy disposable to the nuclear decay, $m_e c^2$ is the energy for creating the electron mass, ($e\phi$ - E_{Fermi}) is the electron binding energy in the crystal as sum of the electronic work function (5.1 eV) and of the Fermi energy (11.2 eV), Δ $B_{lattice}$ is the change in the potential energy of the isotope in the crystal due to the change of one unit of the nuclear charge. The last contribution is negligible in this case: it corresponds to about 2.6% of the total binding energy of rhenium atoms in the crystal, which have been evaluated to be 16.9 eV/atom. Then, the major contribution to the change of the end-point energy, when the decay occurs in the crystal, results in the final state of the electron, which binding energy is 16.3 eV. Regarding the problem of the final excited states, it is necessary that the microcalorimetric detector is able to measure them if their relaxation time is shorter than the heat pulse formation time, which is generated by the nuclear decay. The decay can leave the daughter isotope in an excited level with half-life much longer then the thermal pulse formation time. Then the relaxation energy is lost, because is not summed to the heat pulse produced by the decay. Despite the probability of half-life longer than few hundred of microseconds being small, the probability of final excited states is also negligible. Indeed, because of a very similar atomic wave-functions and levels of Re^{75} and Os^{76}, the probability of a transitions toward un excited level is very small, being the Os excited eigenstate orthogonal to the Re ground state. An evaluation of this probability provides values lower than 7^{-5}.

The possibility of a loss of energy in a dislocation of the daughter isotope during the recoil can be excluded. The energy of the recoil is lower than 8 meV and therefore not sufficient to

give rise to this process, but only to generate phonons belonging to the elastic branches, which contributes to the heat formation. Another process, that in principle could smear the position of the end-point, is the recoil-free beta decay. This effect has been not observed until now, but it can be foreseen on the basis of the extension of the theory of the well-known Mössbauer effect to the beta decay. In the case of recoil-free decay the neutrino-electron couple energy is increased by an amount equal to the nucleus recoil energy. Since this corresponds to a small amount of energy, the effect on the shape of the end-point region is negligible. Collective excitations in the crystal can also contribute to the generation of long life metastable states, which can trap a variable amount of energy for a long time. Since the rhenium crystal is superconducting at temperature below 1.69 K, long living quasiparticle states are predicted from the model that extent the BCS theory to superconducting systems out of the thermal equilibrium. In our rhenium crystal, which operate at 1/20 1/15 of the critical transition temperature, the quasiparticles created in narrow volume around the decaying nucleus, live for about 10^{-8} s, if we apply the hot spot model, in which the temperature rise locally about T_c. Otherwise, for an average temperature of $1/15T_c$, the lifetime of the quasi-particle can be as high as 10^6 s. This means that part of the decay energy should be trapped and, therefore, not disposable for the heat pulse formation. An experimental study of the thermalization efficiency, as described before, showed that it is about 100% for the rhenium down to temperature of about 90 mK.

Solid state effects: BEFS and its role in neutrino mass evaluation

As discussed in § 2.4.3, the BEFS might be a source of systematic uncertainties peculiar to rhenium based thermal detectors. In fact, Koonin [61] in 1991 suggested that a β spectrum could be deformed by an effect called BEFS, motivated by the controversial reports by Simpson [62] and Sur et al. [63] on the observation of a kink below the end-point of ^{3}H spectrum (which at that time was interpreted as an indication of the existence of a neutrino with a mass of 17 keV). Koonin had theoretically evaluated the oscillatory patterns expected for implanted ^{3}H and ^{14}C, as well as for molecular tritium. BEFS has not been searched for in these nuclei, but the effect has been detected in metallic rhenium [64] in the β decay of ^{187}Re, which has the lowest known transition energy (~ 2.5 keV) [65].

While the decays of ^{3}H and ^{14}C are allowed, that of ^{187}Re to ^{187}Os is a $5/2^+ \rightarrow 1/2^-$ first forbidden unique transition. The Koonin theory was therefore extended to correctly consider the electron final states for forbidden β-decays [70]. The nuclear angular momentum change, $\Delta I = -2$, implies a Gamow-Teller process. Consistently with the selection rules, the (vector) sum of electron and antineutrino orbital angular momenta ($l_e + l_{\overline{\nu}}$) must be as low as possible in order not to centrifugally suppress the overall transition rate. This implies two possible final states, according to whether the residual angular momentum is carried away by the antineutrino (s-wave electron emission, $\{e(s_{1/2}), \overline{\nu}(p_{3/2})\}$) or by the electron (p-wave electron emission, $\{e(p_{3/2}), \overline{\nu}(s_{1/2})\}$) [67]. The BEFS correction ΔP to the probability P that an electron with a wave number k (or, equivalently, an energy E) is emitted in the decay process, can be derived in complete analogy with the EXAFS description [71]. Anyway, in BEFS the β-decay electron is emitted with no preferred directions, so in our formula the EXFAS geometrical factor is averaged to 1. The resulting fractional BEFS modulation χ can be expressed as:

$$\chi(k, N, F_p) = \frac{\Delta P}{P} =$$

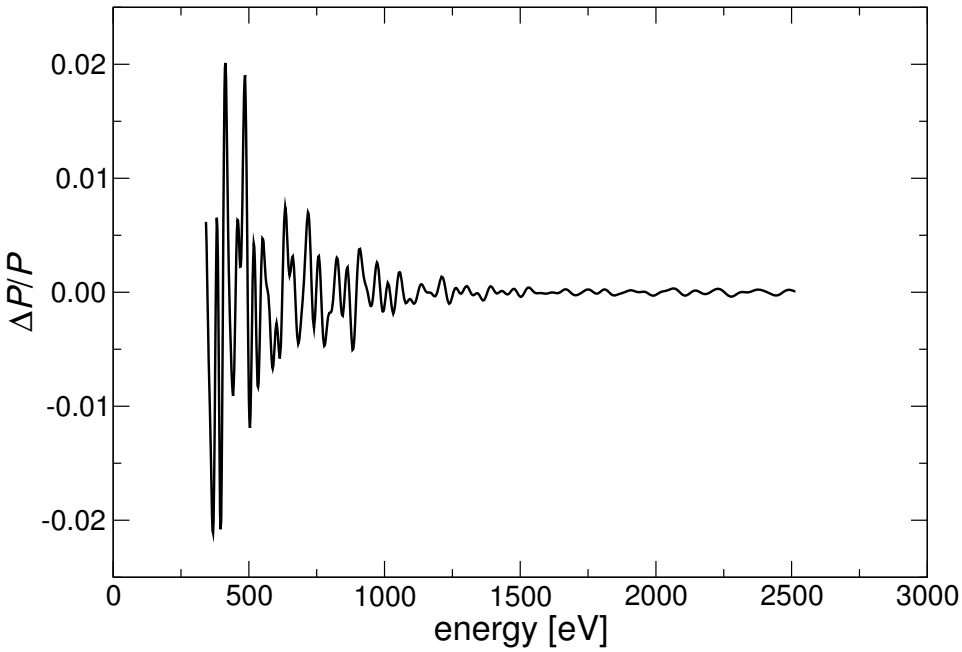

Figure 5.4 - BEFS effect on the beta spectrum.

$$= \sum_{j=1}^{N} \frac{B_j(k)N_j}{kR_j^2} e^{-2k^2\sigma_j^2} \{(1-F_p)\sin[2kR_j + \phi_c^{l=0}(k) + \\ +\phi_j^{l=0}(k)] - F_p \sin[2kR_j + \phi_c^{l=1}(k) + \phi_j^{l=1}(k)]\} \quad (5.5)$$

The sum is extended to all the neighbouring shells of atoms (labeled by j) up to the Nth one, each shell having N_j atoms at a distance R_j from the emitting nucleus. The truncation at the Nth atomic shell is justified by the finite mean free path of the electron for elastic scattering. k is the emitted electron wave-number (expressed in Å^{-1}), and R_j directly determines the oscillation frequency generated by the jth shell in k-space. $B_j(k)$ is the backscattering amplitude as a function of wave-number. ϕ_c^l and ϕ_j^l are the phase shifts due to the central atom and to the j-shell surrounding atoms, respectively. The exponential factor gives the Debye-Waller attenuation due to the thermal mean square displacement $\sigma_j^2(T)$ of the j-th neighbour atom with respect to the central atom. In the case of our detectors, which work at temperatures below 1 K, the only contribution to the Debye-Waller term arises from the zero-point energy. The nature of the decay final states is included in the parameters F_p and $F_s = 1 - F_p$, which indicate the fractions of p-wave ($l = 1$) electrons and s-wave ($l = 0$) electrons, respectively. In fig. 5.4 one can appreciate $\Delta P/P$ as a function of the electron energy.

We have first estimated the amplitude of BEFS in a metallic rhenium single crystal at a temperature of 100 mK. Rhenium forms a hexagonally close packed (h.c.p.) crystal; at room temperature, its lattice parameters are a =2.7609 Å and c=4.4576 Å, whose ratio c/a = 1.614 is close to the ideal ratio for h.c.p. crystals, that is, c/a = 1.6333. There is a weak temperature dependence of the lattice parameters which extrapolates linearly to temperature T = 0.01 K to give a = 2.7578 Å, c = 4.4514 Å. We note in figure 5.4 that the period of the oscillations ranges from 100 eV to 150 eV; a detector with good energy resolution is required to resolve the structure of the individual oscillations. This effect has not been observed experimentally in

any existing β-decay spectral study, up to now, owing to the limitations of traditional radiation detectors. But cryogenic particle detectors bypass these limitations and are the best candidates for BEFS detection. The low operating temperature results in negligible thermal motion of the lattice which would otherwise reduce the coherence. The BEFS effect should dominate in the energy range less than 2 keV, because at high energies and correspondingly shorter wavelengths the effects of zero-point and thermal motion (the Debye-Waller effect) become more critical in the reduction of overall coherence. The measured spectrum shown in Figure 5.5 has been fitted by the theoretical spectral shape without BEFS; the difference between the real data and the fit in the range 450 ± 1650 eV, is shown in Figure 5.6, which also shows the BEFS theoretical calculation, convoluted with the detector response (continuous line).

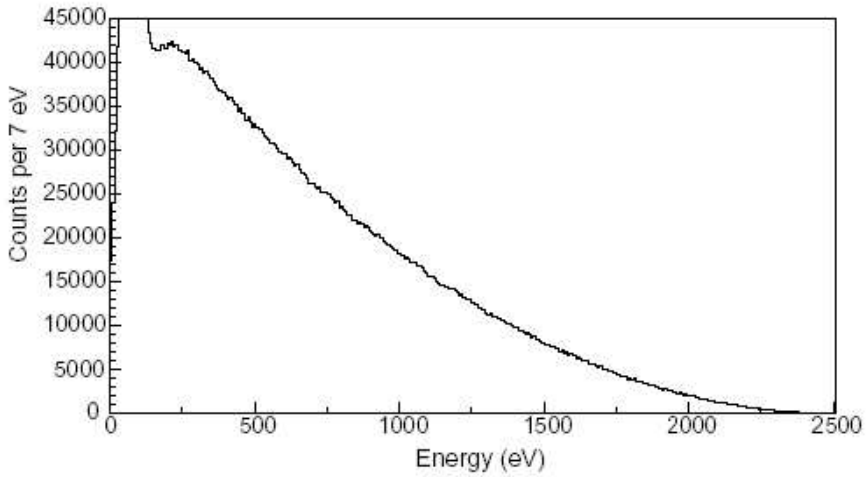

Figure 5.5 - First high statistics calorimetric spectrum of ^{187}Re

An oscillatory modulation may be seen in the data collected with the metallic Re calorimeter described in § 4.2; a χ^2 statistical analysis indicates that the data are in disagreement with a straight line (no BEFS) with a 5σ confidence limit (χ^2=128.8 with n=59 degrees of freedom). When the BEFS is introduced, the experimental data are in agreement with the theoretical prediction within a 1σ confidence limit (χ^2=66, n=59). The MANU experiment has confirmed the hypothesis of Koonin regarding the existence of BEFS, which should therefore be taken into account when analysing low-energy neutrino experiments with solid targets. The results with cryogenic microcalorimeters should allow the use of BEFS as a kind of internal EXAFS for structural studies; the relatively small size of the experimental setup, the possibility of studying different absorber materials (crystals or molecules), the circumvention of the need for a large synchrotron light source and the present sophistication of EXAFS will probably encourage such studies.

$AgReO_4$ crystallizes in the scheelite-type tetragonal structure ($a = b \neq c$) with space group $I4_1/a$. Oxygen atom positions are the only degree of freedom within the unit cell, since the positions of Ag and Re are fixed. Chemically they surround the Re atoms with almost tetrahedral symmetry. The length of such bindings at room temperature is about 1.7 Å. The cell values have been recently evaluated by X-ray photoelectron spectroscopy at two different temperatures [74]: at T=298 K $a = b = 5.3742$ Å and $c = 11.792$ Å, while at T=95 K

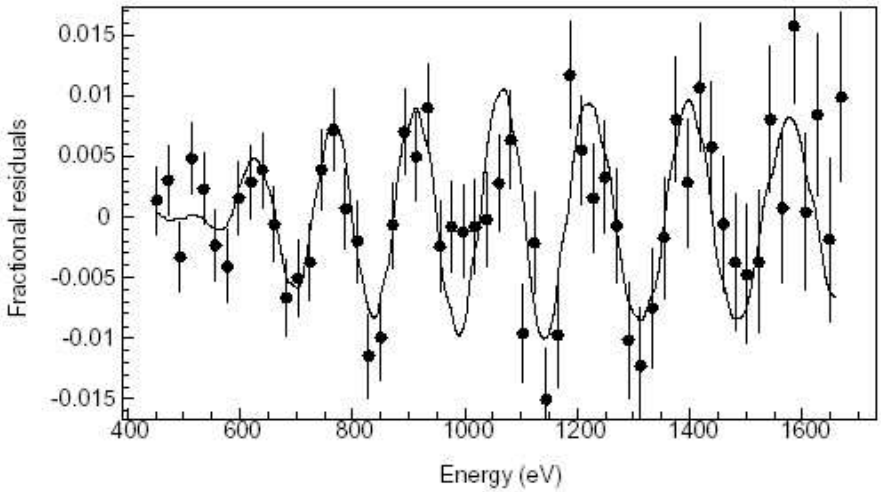

Figure 5.6 - Measured BEFS signal from the beta spectrum of ^{187}Re in single hcp crystal and data fit of the expected signal(line) ,convoluted with the spectral response function of the detector.

$a = b = 5.3585$ Å and $c = 11.722$ Å. No other experimental values below room temperature exist in the literature. We have therefore linearly extrapolated both a and c at the detector operating temperature of 100 mK: the result is $a = b = 5.3512$ Å and $c = 11.689$ Å. It is so implicitly assumed that no phase transformation occurs below 95 K; the oxygen fractional positions within the cell are fixed at the values determined at 298 K. In other words, we consider a simple cell contraction with no distortion or phase transformations.

To check the effect of BEFS on an experiment searching for the electron neutrino mass we have used the Montecarlo code described in § 5.1.1. The code was extended to include the BEFS effect in the experimental β spectra generated. When fitting the experimental spectra no BEFS was then considered. The results of this simulation is shown in figure 5.7. Here the BEFS for $AgReO_4$ is included and it is evaluated with the parameters reported in [75]. In all simulations the total statistics is 10^{10} events, the energy resolution ΔE is 20 eV and the fraction of unresolved pile-up events f_{pup} is 10^{-4}. The simulations differ for the low energy end of the interval used for fitting the experimental spectra. The squares and the circles are respectively the simulation where the BEFS is or is not included. In figure 5.7 the average square neutrino mass is plotted. The error bars represent the $1\,\sigma$ width of the square neutrino mass distribution which was used in § 5.1.1 to estimate the experimental sensitivity. A large negative average square neutrino mass is clearly a symptom of systematic uncertainty. From these simulations it appears that including the BEFS in the analysis of the data maybe necessary only when fitting from less than about 1 keV. This means that only the low energy large oscillations of BEFS can influence the analysis of the data and therefore the determination of the neutrino mass. The small amplitude oscillations extending up the β end-point can be neglected.

The detector response function

We have used the Montecarlo code also to estimate the effect of the precision with which the response function is known. For the moment only gaussian symmetric response functions are considered. To see the effect of a precision $\sigma(\Delta E)/\Delta E$ the simulated experiments have a

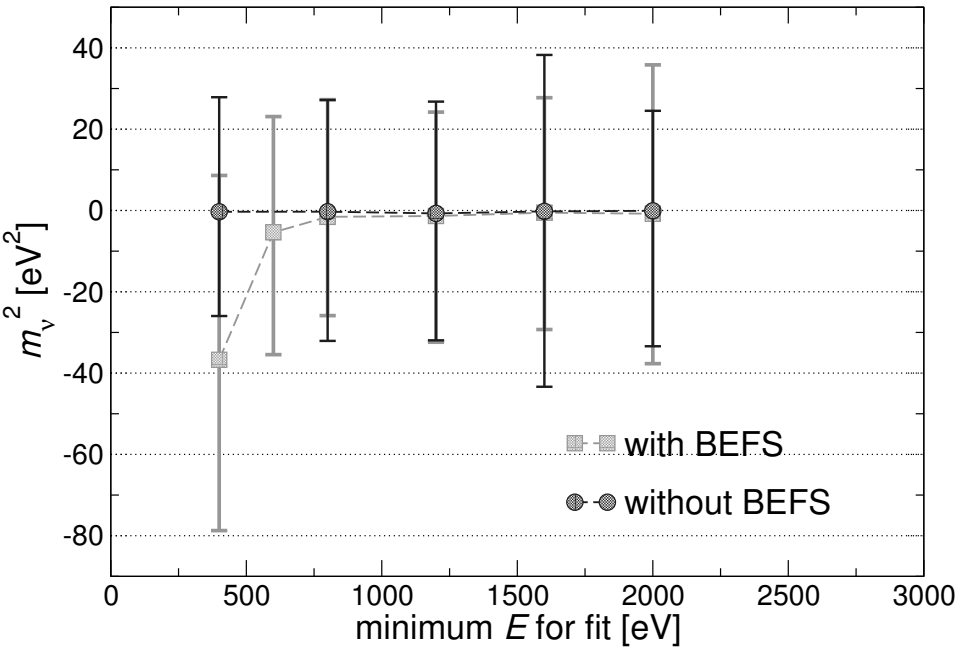

Figure 5.7 - Effects of BEFS on the determination of m_ν^2

response functions whose FWHM is normally distributed around a value ΔE with a variance $\sigma(\Delta E)$. The experimental spectra are then all fitted assuming always a response function with FWHM ΔE. Figure 5.8 shows the results of the simulation for experiments with 10^{10} events, with a fraction of unresolved pile-up events f_{pup} of about 10^{-4}, and with 10 eV and 20 eV for the central values of ΔE. The $1\,\sigma$ width of the square neutrino mass distribution is plotted as a function of $\sigma(\Delta E/)\Delta E$. A poor knowledge of the response function can introduce large systematic uncertainties if $\sigma(\Delta E/)\Delta E$ is larger than 0.01. The average square neutrino mass is systematically shifted towards positive or negative values when the response function width is over- or under-estimated respectively. The effect importance decreases with improving energy resolution.

A more delicate point concerns how well the response function is described by a simple symmetric gaussian distribution. Ideally one would expect a perfectly guassian response function for thermal detectors, but mechanisms could be thought of which could introduce tails in the response function. This is the case for $AgReO_4$ as discussed in §4.3.9, while the MANU Rhenium detectors have a clean guassian response. The response function is usually measured irradiating the absorber with mono-energetic X-rays. Their absorption produces photo-electrons which behaves exactly as the electrons emitted in the ^{187}Re decay. The only difference is the position in the absorber where they deposit their energy. X rays near 2.5 keV will be absorbed near the surface of a $AgReO_4$ or Re crystal, so there could be concern about the conditions there being systematically different than further into the bulk.

This unresolved ambiguity introduces a systematic uncertainty on m_ν^2 which in the case of the MIBETA experiment is a shift of m_ν^2 of from -112 eV^2 to about -53 eV^2 when changing from a pure gaussian to a tailed response function.

A possible tool to establish the true detector response to electrons from ^{187}Re β decay consists in the use of the X-ray escape process [28]. In such a process, a photon with energy

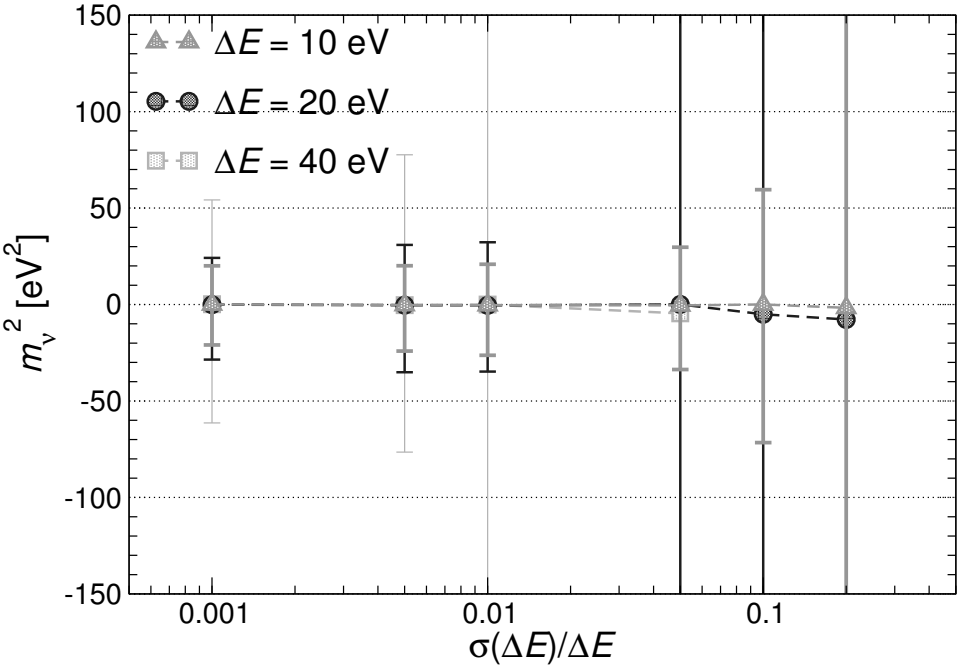

Figure 5.8 - Effects of the response function uncertainties on the determination of m_ν^2.

above the Re K-edge at 71.7 keV undergo a photoelectric interaction on a K Re electron: for an energy of about 70 keV the attenuation length in $AgReO_4$ is about 400 μm and the interactions are therefore uniformly distributed in the absorber. If the Re K X-ray emitted while filling the vacancy left over by the photoelectric effect exits the absorber, one observes a so called escape peak at an energy equal to the difference between the energy of the incident photon and the energy of the escaping X-ray. Properly choosing the energy of the incident photon, the escape peak can be in the region of interest.

A preliminary experiment was done with the MIBETA detectors using a ^{44}Ti ($\tau \approx 60$ year) source which emits γ rays with an energy of 78 keV. The main difficulty consists in the deconvolution of the intrinsic Lorentzian broadening of the Re X-ray line of about 42 eV to extract the detector response.

5.2 Approach to MARE-1: temporal profile and branch points

MARE-1 aims at putting at work the established expertise of the Genova and Milano groups to reach by 2010 a neutrino mass sensitivity of few electronvolts. Therefore this result will be achieved *before* KATRIN full data taking. Both groups have presently the know-how to set-up an experiment with this sensitivity. The Genova group has developed microcalorimeters with TES sensors coupled to metallic rhenium absorbers for the MANU2 experiment. The Milano group together with the NASA/GSFC and Wisconsin groups has developed array of silicon implanted thermistors coupled to $AgReO_4$ absorbers.

In the beginning of MARE-1 we plan to start two experiments located in Genova and Milano and based on the technologies developed by the two groups. In case the two experiments are both successfully run until their expected sensitivity one would

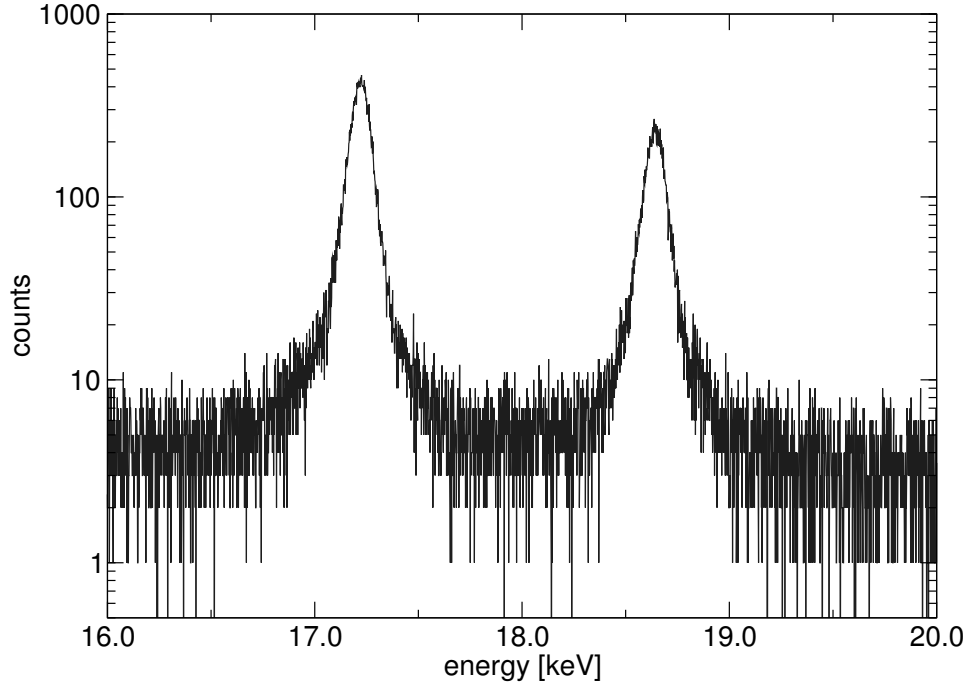

Figure 5.9 - Line-shapes of escape peaks, corresponding to events uniformly distributed in the absorber volume.

- obtain a further increase in the sensitivity by analysing the data from both experiments simultaneously

- gather more informations on the intrinsic sources of systematic uncertainties for the two absorber materials; in particular for what concerns the BEFS and the response function; these informations are fundamental for the definition of MARE-2;

- cross-check the results and be less exposed to the risk of finding a unexpected systematics weakening the sensitivity;

- robustly scrutinize the Mainz/Troitzk results with a completely independent approach.

The situation would be similar to that of the electrostatic spectrometer experiments, where the presence of two different experiments with similar sensitivity helped validating their neutrino mass limits.

Nevertheless we feel we must fix a deadline beyond which any of the two experiments would be abandoned in case of overwhelming technical difficulties. This deadline can be safely fixed at end 2007: in order to go on each experiment has to be running with at least 50 channels and 6 months of live time and the projected sensitivity at the end of 2010 must be lower than 5 eV at 90% C.L..

In the following sections we give the details about the design and the time schedule for both the experiments.

5.3 The TES-based section of MARE-1 experiment: MANU2

MANU2 is a second generation microcalorimetric experiment on the β-decay of ^{187}Re for direct measure of the neutrino mass, making use of the full absorption method, in which all the energy released on the $^{187}Re^{75}$ β-decay is detected. The temperature rises induced by the beta decays will be measured with specially designed TES. The experiment will be executed with about 300 detection channels, with a total rhenium mass of 250 mg with an expected count-rate of about 10^{10} for one year of live time measurement, providing a best estimation neutrino mass sensitivity of 1.5 eV/c^2 (90% C.L.). Each channel is composed of a Re single crystal absorber, an IrAu TES and a non-conventional voltage amplifier readout using a low temperature transformer. MANU2 has completed the first phase of R&D, in which we have developed from scratch the TES sensors and the readout-electronics. Meanwhile, we have built all the facilities for sensor production and tooling: pulsed laser deposition system, electron gun evaporator, DC magnetron sputtering system, reactive ion and oxygen plasma etching and microlitography tools. The second phase of MANU2 is starting. The assembling and commissioning are gradually being performed, adding each time an element containing eighteen detectors. Each element consists of a disk-shaped holder made of OFHC on to which the detectors, wiring and low temperature transformers are mounted. The first element is attached to the dilution refrigerator mixing chamber, and the subsequents attached to the last one, assuming a final cylindrical structure. Two dilution refrigerators (Oxford TLE200 and Oxford Kelvinox100) will be needed in order to operate simultaneously all the 300 detectors. A schematic view of the detector setup is shown in Figure 5.10. In the following we will present the results of the first phase. Further detail on the overall experiment will published as an addendum to this proposal.

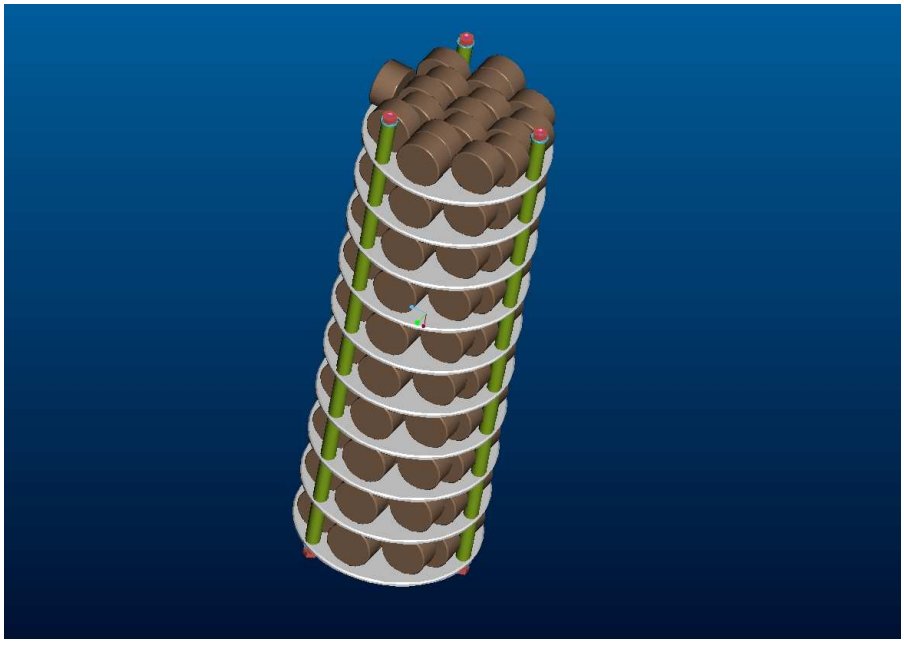

Figure 5.10 - A schematic view of the MANU2 detector setup. Each of the ten disks, contains 18 detectors and 18 transformers (cylinder)

5.3.1 Al-Ag TES

This work has been motivated by positive results obtained with Al-Ag TES which showed in several cases a very long term stability and remarkable performance. In the first phase of the MANU-2 the resolution of 13 eV FWHM at 5.9 keV was achieved on samples that have shown undetectable changes of transition temperature and transition width up to nine months. Moreover the same detector was used over a long period, suffering several thermal cycles, in an experiment at European Synchrotron Radiation Facility in Grenoble for an x-ray material analysis. Despite this, the reliability demonstration of Ag-Al TES has not been fully achieved due to unexplained poor performance of a few TES produced in the same conditions. Other group also reported similar problems. These problems were attributed to chemical instability by inter-diffusion and chemical activity. We have extensively studied Ag-Al pursuing the aim to solve these problems. The reasons causing the worsening of the malfunctioning sensors were investigated, in particular we have analyzed the damages produced by the fabrication processes such as litography for patterning evaporated films, the conservation of these samples after preparation and the chemical diffusion process at the interface of the two layers.

5.3.2 T_c of Al-Ag TES

The superconductive transition temperature of Ag-Al in the proximity regime can be predicted by several models , that are dependent on the films parameters. In order to apply one of these models, it is important to know the values of the Debye temperature Θ_D and the coherence length ξ for Al and Ag. The TESs produced in the laboratories of Genoa consist of four layers forming the sequence Ag-Al-Ag-Al: the first two are thicker, then determining the transition temperature, while the last two act as protective layers. The first protective layer, made of silver serves as protection of the main aluminum film against fast and deep oxidation, which are activated by the wet PMMA stripping processes. The second protective layer is a sacrificial aluminum film, which acts as barrier between the PMMA and the silver layer. The proximity regime was obtained by fixing the thickness of the Ag film in the main bilayer (ex. 80 nm), and varying the thickness of Al film (ex.: from 30 to 40 nm), causing the critical temperature of the TES to vary from 55 to 250 mK.

The film thicknesses allows us to use the Cooper limit to estimate the law governing the transition temperature by changing the ratio between the normal d_N and the superconducting d_S layer thicknesses. The Cooper limit considers the order parameter Δ constant in the whole thickness, therefore the spatial pair interaction is defined as:

$$[N(0)V]_{eff} = \frac{d_S[N(0)V]_S}{d_S + d_N} \tag{5.6}$$

This potential replaces the BCS potential in the relation to have the transition temperature:

$$T_c = 1.14\Theta_D e^{-\frac{1}{[N(0)V]_{eff}}} \tag{5.7}$$

By fitting the data of the transition temperature vs the thickness of aluminum in the Cooper limit, we were able to calculate with good accuracy the relative film thickness for a wanted transition temperature of the sensor.

5.3.3 Physical and chemical investigation of TES's

In order to understand and improve the performances of our Al-Ag sensors, several tests were carried out to investigate the causes of chemical degradation. Using X-ray Photoemission Spectroscopy on TES, it is possible to analyze the chemical composition and the presence of bonding states due to compounds formation on the surface. Two types of damages have been found and attributed to preparation procedure and damages due to casting. In Figure 5.11one of these measurements is presented, in each box the relative abundance of one element on the TES surface is shown.

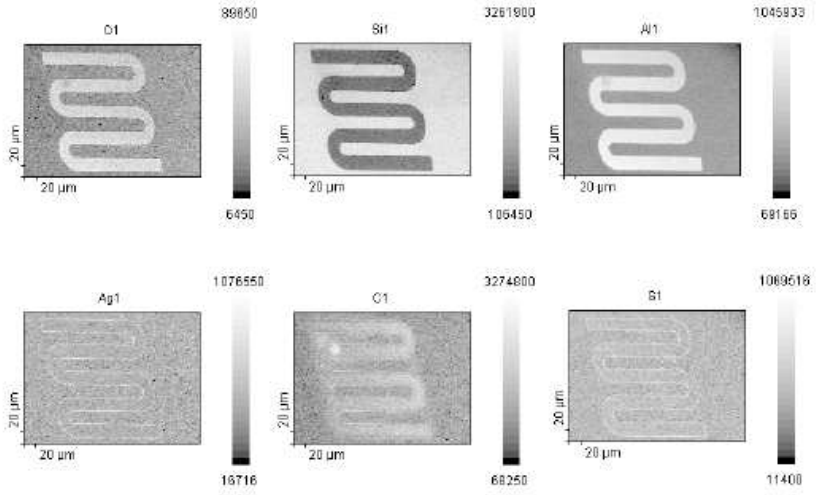

Figure 5.11 - XPS surface chemical analysis. Each picture shows the presence of one element; the carbon and oxygen come from atmosphere contamination, the sulfur in the same zones where silver is present comes from the photoresist.

In this group, two elements appear as impurity on the film: sulphur and boron. The first comes from the pholitographic process, since it is present in the triphenylsulfonium hexaflouroantimonate onium salt, one of main component of photoresist, while the second comes from the evaporation since the silver is evaporated from BN liner. Both elements are bound to silver, but while sulphur is more superficial, boron is present over the whole layer. This means that if the damage by the presence of S may just change the relation between thicknesses and transition temperature, boron may lead the film to be not superconducting depending on its concentration. For the casting contamination, the aluminum passivation is the more relevant effect; this is a superficial effect not involving the internal part, it behaves as a protection layer just decreasing the effective superconducting thickness. Other smaller effects are the carbon contamination and slight acid etching. After these measurements it was possible to improve the fabrication of TES sensors especially for the evaporation of silver. The diffusion process between aluminum and silver layers has also been studied. The analysis was done with sputtering cycles over the sensor surface followed by XPS acquisition, taking into account the fact that for high precision measurements the results obtained may be influenced by the sputtering, which enhances the diffusion, and due to the Ar ions different scattering with Ag and Al. The diffusion being a natural process, unavoidable, causes a time instability on transition tempera-

ture, leading several research groups to abandon Ag-Al system. However, our studies indicated that the different behaviors of various Ag-Al TES, is due to the amount of aluminum and silver used and to their ratio. A model explaining how to produce stable Al-Ag systems is based directly on the Al and Ag properties.

5.3.4 Al-Ag superconducting hcp δ-phase

Both materials show a fcc crystallographic structure, with lattice parameters 2.889 A and 2.863 A for Al and Ag, respectively, and the lattice mismatch is about 0.9%. The segregation properties of the two metals depend on the surface free energy of each material, which is smaller in Al (1.16 J/m^2) than in Ag (1.25 J/m^2), implying that Al tends to segregate at the surface of Al/Ag alloy (3% of Ag). On the other hand, since the mixing heat between the two metals is negative (-0.61 eV), Al and Ag can easily form alloys in the bulk phase with different proportions. The Ag/Al phase diagram indicates that the solubility of Al in Ag is high even at room temperature, while for same temperature the solubility of Ag in Al is negligible. The Ag-Al equilibrium ground states are therefore: fcc-based Ag, complex cubic β-Mn-based Ag_3Al, hcp Ag_2Al and fcc-based Al. The Al-rich alloy segregates into the fcc Al-rich terminal solid solution and the hcp intermediate δ-phase. When the relative amount of Al in the alloy is between 33-40%, the formation of a very stable and superconducting hcp-phase occurs. This superconducting -phase is the very promising for our applications, since besides showing superconducting properties, the alloy T_c depends on the Al concentration, being a free parameter for best fit as a microcalorimeter.

Ag-Al superconducting hcp δ-phase: bulk sample. A first bulk sample of Ag35%Al was prepared using a tantalum crucible filled with 2.814 g of Ag and 0.379 g of Al, closed by arc welding under the flow of pure argon. Initially it was heated up to 1200 C in an induction furnace, then moved into a resistance furnace where it was kept at 620 C for three days. Subsequently, the sample was gradually cooled down to room temperature. The bulk metal was characterized using X-ray diffraction technique, as shown in Figure 5.12.

The lattice parameters obtained from this measurements were a=2.876 A and c=4.608 A, in agreement with the expected values. The superconducting-to-normal phase transition was found at a T_c of about 115 mK, in good agreement with previously reported measurements.

Ag-Al superconducting hcp δ-phase: thin film.

Different film evaporation techniques were tested in order to obtain δ-phase growth directly onto the substrate of Si(110). The first test was the evaporation of the Ag35%Al bulk alloy, with pulsed-laser deposition (PLD), maintaining the same stoichiometry of the bulk. We used both unheated and 500 C heated substrates. An increase of the δ-phase formation with temperature was observed. Analysis of the X-ray diffraction pattern, showed a strong line at 38.1 degrees attributed to an excess of pure Ag metal. The lines with smaller intensity observed at 35.9, 39.0 and 40.5 degrees, respectively, are attributed to the δ-Ag/Al phase. These results may be interpreted as a direct consequence of the PLD technique. In fact, the Al and Ag ion plasmas produced by the laser pulse, tend to be depleted of Al due to its higher diffusivity, consequently, an excess of Ag is found on the substrate. A different technique, using e-beam evaporation of Al and Ag separately, was tested to improve the purity of the δ-phase. This technique provides the possibility to form the δ-phase in situ, making use of the natural diffusion between the two metals. A sequence of very thin and alternated layers of Al and Ag was grown onto

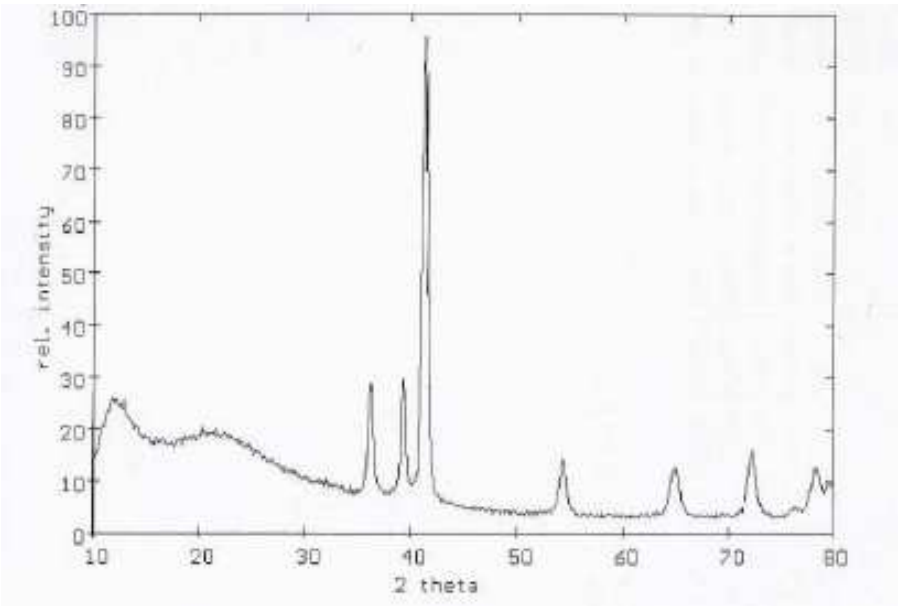

Figure 5.12 - X-ray diffraction pattern of δ-Al/Ag bulk (620 C), with hcp lattice.

a heated (300 C) substrate, enhancing the internal diffusion. The Al-Ag evaporation atomic ratio was kept equal to 1:2. The substrates used were Si(110) and Si(111). The interpretation of X-ray diffraction results, indicates the success in producing films that contain the δ-phase, using a simple and first tested technique of in situ alloy growth. Despite the fact that both hexagonal and non-superconducting β-cubic phases are still present in film; a clear decrease of the contribution of this last one was achieved with this technique. This is, however, an unexpected result according to common wisdoms, since no cubic phase should be formed for operating temperatures below 600 C, well above the experimental film growth temperature. On the other hand, the presence of Al or Ag pure metals was fully eliminated.

In conclusion, we have demonstrated a successful production of superconducting δ-phase with Al and Ag metals in thin films using two different techniques: the PLD where an excess of pure metals was observed and justified in terms of the plasma kinematics and e-beam deposition, demonstrated promising feasibility for in situ film fabrication. We consider these δ-phase a promissing solution for MARE. Therefore, we plan to continue the investigation of this single phase film, in particular, with a co-deposition technique using two Knudsen cells providing simultaneous metal evaporation.

5.3.5 Iridium and iridium-gold TES

Iridium is a very interesting superconducting material for high-resolution spectroscopy applications, due to its excellent chemical and physical stability, and low transition temperature (112 mK). In iridium thin films, the transition temperature is a property of the material and does not depend on relative thickness between layers or on the quality of an interface layer. For this reason, when compared to bilayer TES devices, the proposed relatively simple, single layer devices have the potential to drastically improve both the reproducibility of the transition temperature between fabrication runs and the uniformity of the detectors when building

arrays. There is some evidence that iridium films may have poorer thermal conductivity than bilayers. However, the fabrication process requires a particular attention since a few ppm of ferromagnetics impurities produce a considerable shift down of the superconductive transition. Moreover, its melting point (2719 K)and the very low contamination limits make difficult the use of conventional deposition techniques. For this the reason we have chosen the PLD technique, using an infrared Nd:YAG laser with a wavelength of 1064 nm, normal-incidence reflection for Ir being about 0.45 in the IR region compared to 0.8 in the UV.

The use of PLD for depositing more complex substances, such as high T_c superconductors, has grown significantly in the last decades, while more conventional sputtering/evaporation techniques are now often used to deposit high quality metal films - with a few exceptions, such as iridium. A variety of techniques including PLD, radio-frequency (RF) magnetron sputtering, and electron-beam evaporation have recently been used to deposit thin films of iridium. However, it was demonstrated that the PLD process produces higher quality films than the RF sputtering process, and that the PLD process leads to higher purity films with enhanced adhesion. Each of these qualities is of paramount importance for TES applications: the detrimental effects of ferromagnetic impurities were apparent in who used e-beam evaporation, while who used RF sputtering had to increase the substrate to a fairly high temperature of 900 K in order to increase the adhesion between the substrate and the Ir film. We found that PLD yields good adhesion at lower temperature, and zero-stress levels in Ir films deposited at room temperature on Si(100)and Si(111) substrates. The high quality of PLD films is believed to result from the energetic ablated species together with the supersaturated vapor flux. One of the problems often associated with PLD is the emission of particles from the target with a few microns in diameter. In our system we empirically observed that most large particles are emitted at large angles, outside the substrate area. The effect of particulates on the film transition temperature is still not clear, however, it is known that few particles per mm^2 does not affect the TES performance. On the hand, with the proper choice of the deposition parameters, such as spot size and energy, we were able to reduce the particulate formation to a negligible level.

Our PLD facility consists in a vacuum chamber capable of reaching the pressure range of 10^{-11} mbar, a target carrousel that can accommodate four 1" diameter targets. Through a load chamber it is possible to change the substrate without breaking the vacuum. The laser is focused outside the chamber and enters through a anti-reflection coated glass window. The typical deposition conditions are: starting pressure: 10^{-9} mbar, plasma pressure: 10^{-7} mbar, substrate temperature: room temperature,laser repetition rate: 10 Hz and pulse-laser energy: 500 mJ.

The deposition substrate being a Si single crystal enables the formation of iridium silicates (Ir_x $Si_1 - x$). It is clear that iridium silicate formation is strongly enhanced at high temperatures. In our case, working at room temperature, the iridium silicates thickness does not exceeds a few tens of angstrom. It is still not understood how its presence affects the transition temperature. Contradictory results are found in the literature. We take the advantage of the thin Ir layer deposited on the substrate to act not only as a sticking but also as matching layer to the superconducting film. In order top avoid contamination from the substract to the film, a thin Au layer is grown before the main film. The main Ir films are ablated at room temperature. We studied different ratios between Au and Ir, in order to take the advantage of the proximity effect explained before.In this way, we can tune the transition temperature from 50 to 112 mK. We found that the proximization of the Ir provides more reliable results then with Al. The calibration of the ablation rate was performed with an X-ray diffractometer measuring the thickness of the Ir and Au films after the ablation. Typical deposition rates are around

10_{-2} nm/shot for both Au and Ir. We tested two different patterning methods: the lift-off and sputter etching. The lift-off was initially executed with PMMA, but with poor results. Consequently, we substituted it with a sacrificial 1 micron thick Ag or Al layer evaporated by electron beam on a Si substrate where the TES area was previously protected by a 6 mm thick positive photoresist. The Ag or Al mask was than stripped away by wet etching with HNO3 or NaOH, respectively. The metallic lift-off mask allows the deposition of the first Ir sticking layer and the Au buffer layer with the Si substrate. The patterning of the film before the deposition permits to avoid the use of very aggressive wet etchant solutions necessary to etch Ir (hydrochloric acid plus nitric acid plus hydrofluoric acid). A cleaner method has been used subsequently with a negative mask after the film production. The photoresist mask acts as a shield to the sputter etching process with Ar.

A typical Ir-Au TES transition curve is shown in Figure 5.13.

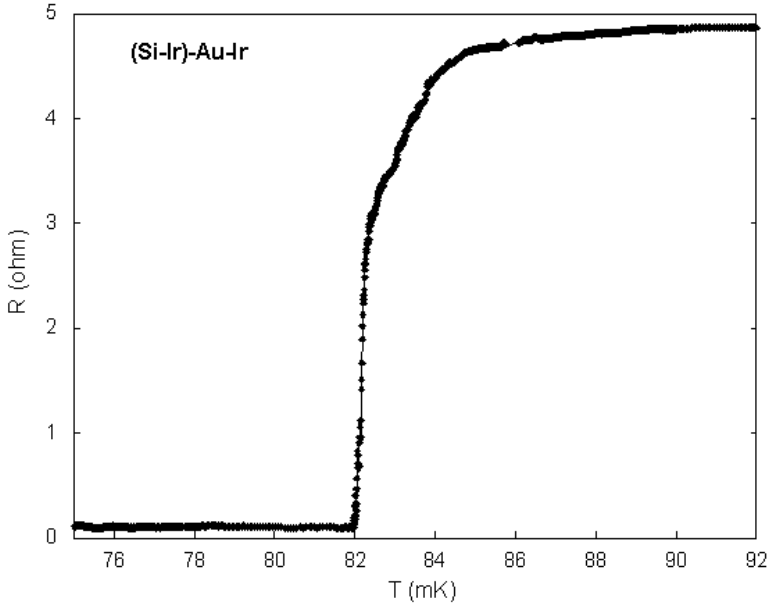

Figure 5.13 - Typical transition curve of an Ir-Au TES fabricated with PLD.

5.3.6 Rhenium TES detectors and expected sensitivity of MANU2

The MANU-2 experiment will be executed with rhenium microcalorimeters with IrAu TES mounted in front-back geometry: on to a front side of a high purity silicon thin substrate is deposited the IrAu film and wiring, while on the back side the Rhenium single crystal is mounted.

TES provides higher performance detectors respect the Ge-NTD based microcalorimeters of the previous experiment MANU, as it can be seen in table 5.14, in which the last column refers to a present TES detector.

The expected energy resolution is about 6 times better than a similar Ge-NTD based microcalorimeter. The measured energy resolution is 3 times better and it can be further

Calorimeter	μc #18	μc #35	μc #55
Sensor	Ge-NTD	Ge-NTD	Ir/AuTES
Re (μg)	60	210	215
C_{Re} (pJ/K)	0.11	0.5	0.5
C_{sensor} (pJ/K)	3.6	1.8	0.02
Calculated ΔE(eV) FWHM@5.9keV	28.2	33	5.8
Measured ΔE(eV) FWHM@5.9keV	30.6	37.6	11

Figure 5.14 - Table 1.

improved, being two times higher than the intrinsic resolution. The corresponding energy spectrum of Mn K_α doublet is shown in Figure 5.15

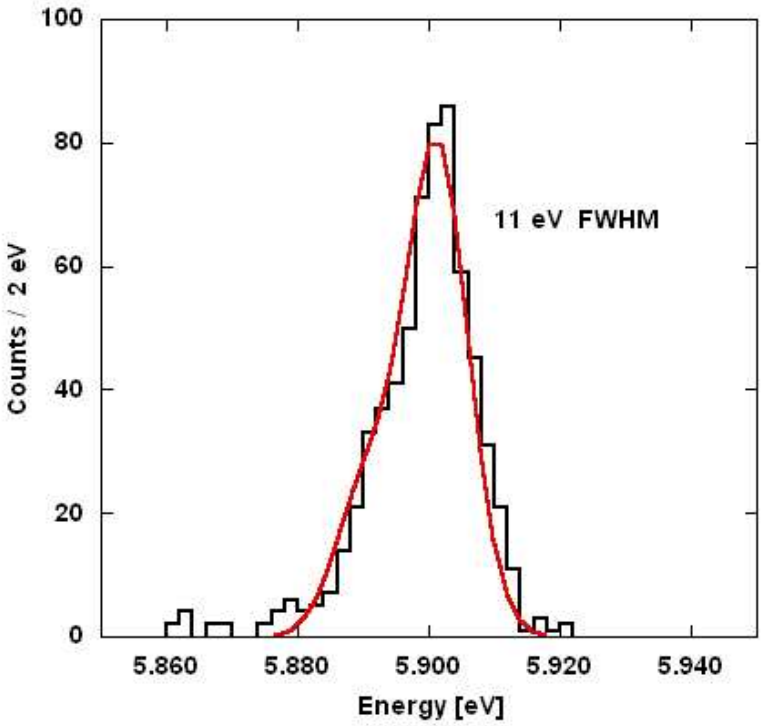

Figure 5.15 - Energy spectrum of Mn K_α doublet seen by the microcalorimeter #55 of table.1. The energy resolution is 11 eV FWHM.

In Figure 5.16 is shown the sensitivity to the neutrino mass limit that has been calculated for 5 and 10 eV FWHM of energy resolution, which covers the expected final experimental value.

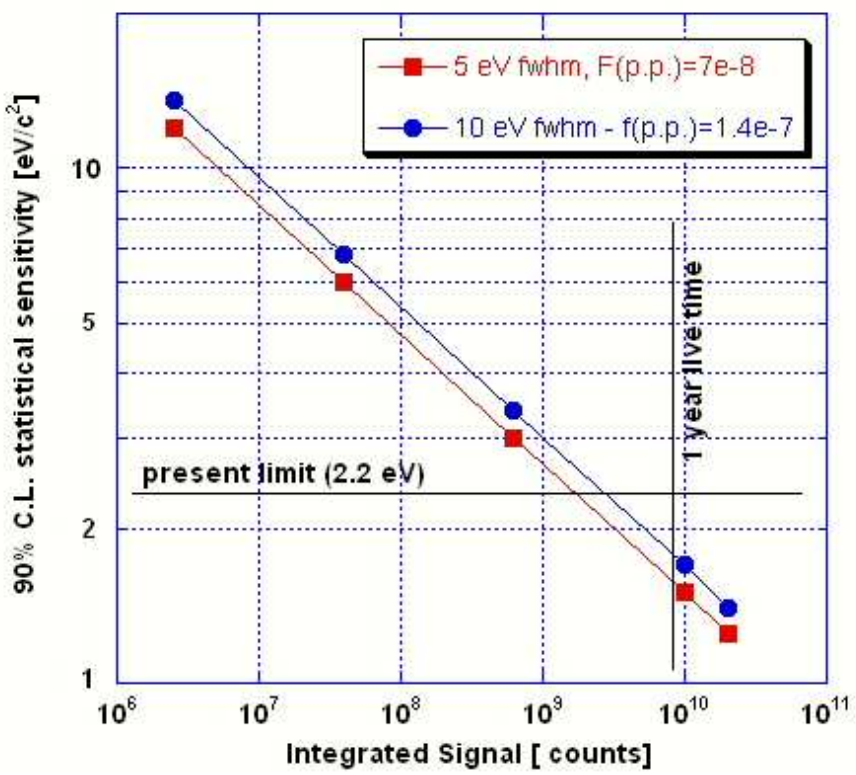

Figure 5.16 - Neutrino mass sensitivity vs. acquired counts for MANU2 experiment. The 1 year data taking reference line is shown.

5.4 The semiconductor-based section of MARE-1 experiment: MIBETA2

5.4.1 Detectors with thermistor phonon sensors

In order to achieve a sensitivity of few electronvolts a total statistics of about 10^{10} events is necessary. For what concerns the detector energy resolution and the fraction of unidentified pile-up events the requirements are not too stringent to be unreachable using the technology developed for the MIBETA experiment. It is then more a question of using the brute force by simply increasing the number of detectors and their size. A statistics of 10^{10} events can be collected in about 4 years running of a 300 detector array, with each detector having an activity of about 0.3 decays/s. Montecarlo simulations simulations show that such a statistics together with an energy resolution ΔE and a fraction of unidentified pile-up events f_{pup} similar to those of the MIBETA experiment can result in a statistical sensitivity of few electronvolts. Of course maintaining the same ΔE and f_{pup} while doubling the mass of the $AgReO_4$ absorbers requires some improvements. More challenging may be to achieve these performance uniformly over a 300 detector array. The following deals with these aspects of the MIBETA2 experiment.

The MIBETA experiment detectors were the results of a only partial optimization. A further thermistor and detector design optimization can give the required performance. The thermometers were too small and too thin for best results. Moreover it has been found that

the $1/f$ noise observed in these detectors is a 2-d effect, and can be eliminated by making the doped region thicker. The total thermometer volume also must be optimized to trade off between electron-phonon decoupling and thermometer heat capacity. A new design could have a thicker implant, and a volume optimized for the thermal conductivity of the link to the heat sink. Making reasonable guesses at the heat capacity, we could expect about 5 (10) eV FWHM resolution at 50 (100) mK using optimized detectors. Another consideration is the pulse-pair

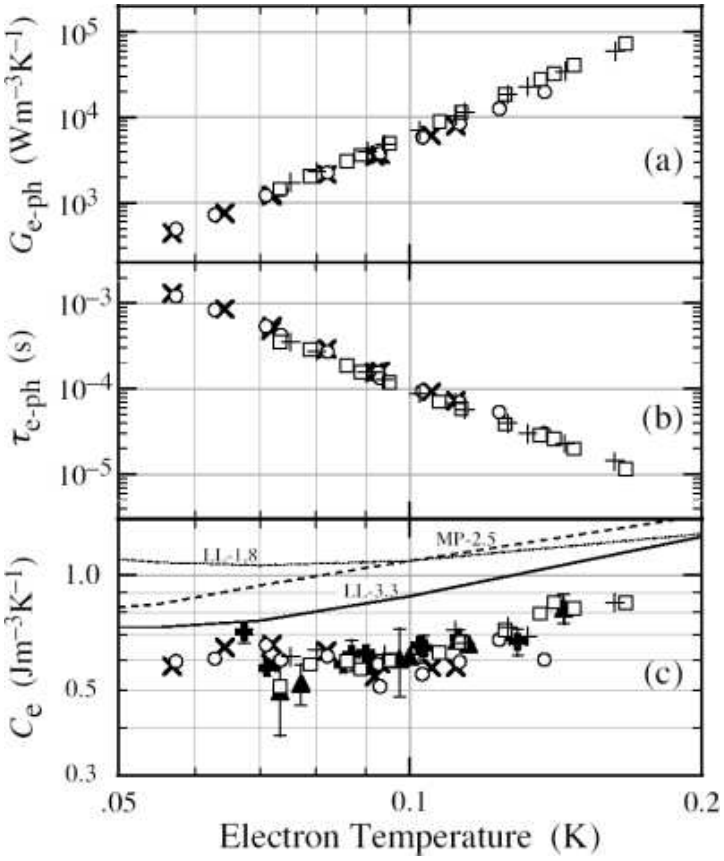

Figure 5.17 - Risetime as given by $\tau_{e-ph} = C_e/G_{e-ph}$ in Si thermistors as a function of the electron temperature.

resolving time, τ_R. This depends on many details, but ideally scales as the detector risetime divided by the square root of the high frequency signal to noise ratio. The most fundamental limitation on the risetime is the electron-phonon coupling time in the thermometer ($\tau_{e-ph} = C_e/G_{e-ph}$), which for silicon doped in the optimum range goes from 100 μs at 100 mK to 2 ms at 50 mK (see figure 5.17). The detector rise time reduces to the electron-phonon coupling time when the absorber has the largest heat capacity in the detector. This makes reaching an effective τ_R of 50 μs appear straightforward, since the signal to noise ratio is very high over most of the beta spectrum. But it also shows that optimization of operating temperature, where improved resolution at lower temperatures must be balanced against much slower risetimes, could be an important consideration. Picking the operating temperature is part of the detector design, since the doping level must then be chosen to give a reasonable detector resistance.

The best trade off operating temperature is around 100 mK, and the target resistance for this operating temperature is about 1 MΩ in order not to spoil the detector rise time by RC

integration over the parasitic input capacitance of the preamplifier. The tests reported in the following paragraphs are made using the same electronics used for the MIBETA experiment which is not optimized for such a low resistance.

The scale-up problem: micromachined arrays

The technique used for the MIBETA experiment is not suitable to build a 300 detector array. The use of micromachining techniques is mandatory. Depending on the kind of sensor there are few approaches possible.

For silicon implanted thermistors the Micro Electro Mechanical Systems (MEMS) semiconductor techniques offer two possibilities. One exploits the anisotropic silicon etching with chemicals like TMAH or KOH. The other makes use of the Deep Reactive Ion Etching (DRIE) technique. The first has been used in the past by the NASA/GSFC and Wisconsin groups for the sounding rockets arrays and for the first XRS instrument installed on the ASTRO-E satellite. Also the MEMS group at ITC-irst has made silicon implanted thermistor arrays with this technique. The latter is now applied by the NASA/GSFC and Wisconsin groups for the new arrays.

For germanium NTD thermometers the most suitable technique makes use of SiN membranes on micromachined (wet or dry) holes in silicon wafers.

All these techniques are adopted and planned for many far infrared (sub-millimiter) imaging instruments for astrophysics research.

Detector assembly with new $AgReO_4$ crystals

New AgReO4 crystals are being developed by Mateck GmbH (Germany). The aims of this R&D are:

- grow better quality crystals by producing a higher purity starting raw material;
- grow larger crystal in order to be able to shape them;
- prepare regularly shaped crystals to allow their handling with a micropositioner and to achieve an higher detector reproducibility.

After growing large single crystals, slices as thin as few hundred microns and with two flat parallel faces are obtained by lapping. This slices have masses of few milligrams, so more cutting is required to obtain the target mass for the experiment of about 450 μg. We are currently making the final cutting ourselves using a razor-blade, but Mateck is setting up the whole procedure to produce the parallelepiped shaped 450 μg crystals.

The assembly of the crystals on thermistors is made using a specially designed micropositioner (figure 5.18).

The micropositioner is composed by a series of translation and rotation stages which permit the perfect positioning of the crystals on the sensor so that crystal faces are parallel with thermistor surface. In particular it is composed by:

- A syringe needle to vacuum pick-up the crystals.
- XYZ micrometer-driven translation stages with travel ranges of 18 mm. The carriage is spring preloaded against the micrometer tip for excellent repeatability and elimination of backlash. Precision crossed roller bearings guarantee straightness of travel of better

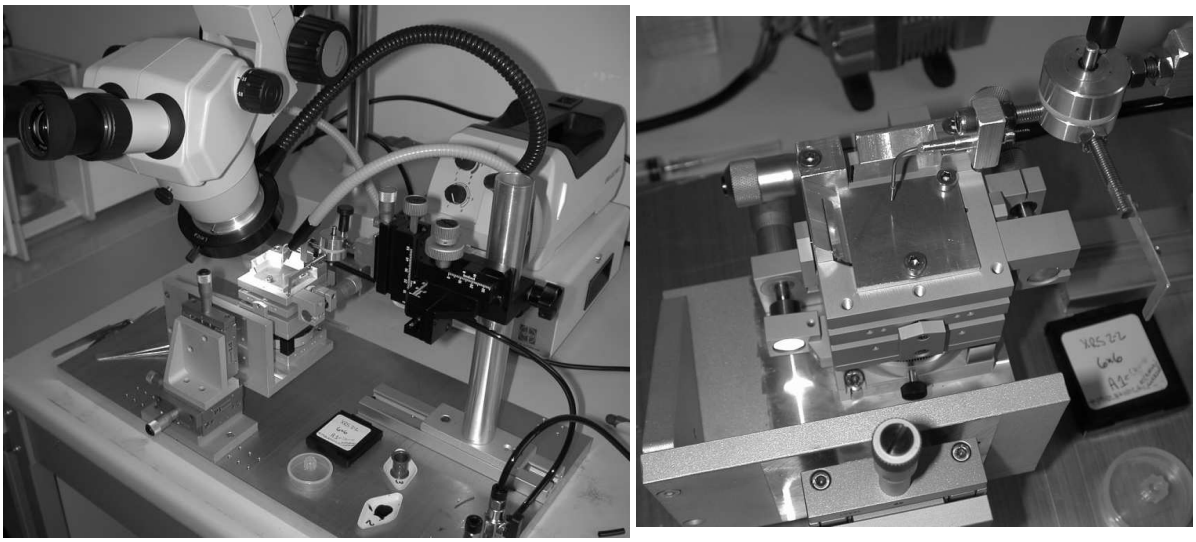

Figure 5.18 - Views of the micropositioner developed in Milano for $AgReO_4$ crystal manipulation.

Figure 5.19 - View of the ISO 6 work area in Milano for $AgReO_4$ crystal detectors preparation with wire-bonder, precision balance, micropositioner and dry box.

than 2 microns. The vertical stage in the XYZ assembly supports the load through the micrometer spindle (not the preload springs) providing excellent stability.

- Two axis tilt stages for small loads (θ_x, θ_y). They are spring preloaded for elimination of backlash and feature resolution and repeatability superior to that of goniometric cradles. It is equipped with manual micrometer drives providing 80 microrad minimum incremental motion.

- Tangent arm rotation stages: it feature high resolution, excellent repeatability and minimum wobble. The stages are equipped with double-row ball bearings for minimum backlash and high load capacity. Both the rotation platform and the scale ring (graduated in 2-degree increments) can be independently coarse positioned over 360 degrees and then locked with screws. It is equipped with a micrometer drive and a zero-backlash magnetic coupling. The micrometer provides a positioning range of ± 9.5 degrees.

The all system can be upgraded for computer controlling the movements.

A laminar airflow over the work area, where the micropositioner and other instruments needed for detector preparation are placed, provides at least a ISO 6 (class 1000) condition to minimize the dust contamination of the detectors (figure 5.19).

Detectors with new silicon implanted phonon sensors

A silicon implanted thermistor array produced at NASA/GSFC has been tested. The array was originally developed for the XRS2 (X-Ray Spectrometer) instrument to be flown on Astro-E2 in 2005. XRS2 is an improvement of the XRS instrument launched on the Astro-E in 2002. Unfortunately Astro-E failed after launch in 2002, but the time before the new mission has been used for developing the new improved XRS2 instrument.

The XRS2 arrays make use of three innovative technologies applied for the first time to silicon implanted microcalorimeters:

- deep reactive-ion etching (DRIE) together with the use of silicon-on-isolator (SOI) wafers to produce 1.5 μm thick free standing pixels with complex shapes without mechanical stress;
- uniform sensor doping throughout the pixel 1.5 μm thickness;
- SU8 structural polymer photolithographically shaped for the absorber mounting points.

The combination of these technologies allow a substantial increase of the electron-phonon coupling, the elimination of any low frequency excess noise, and a greater reproducibility of the assembled microcalorimeters. All these improvements resulted in the remarkable performance of the XRS2 instrument as shown in figure 5.20.

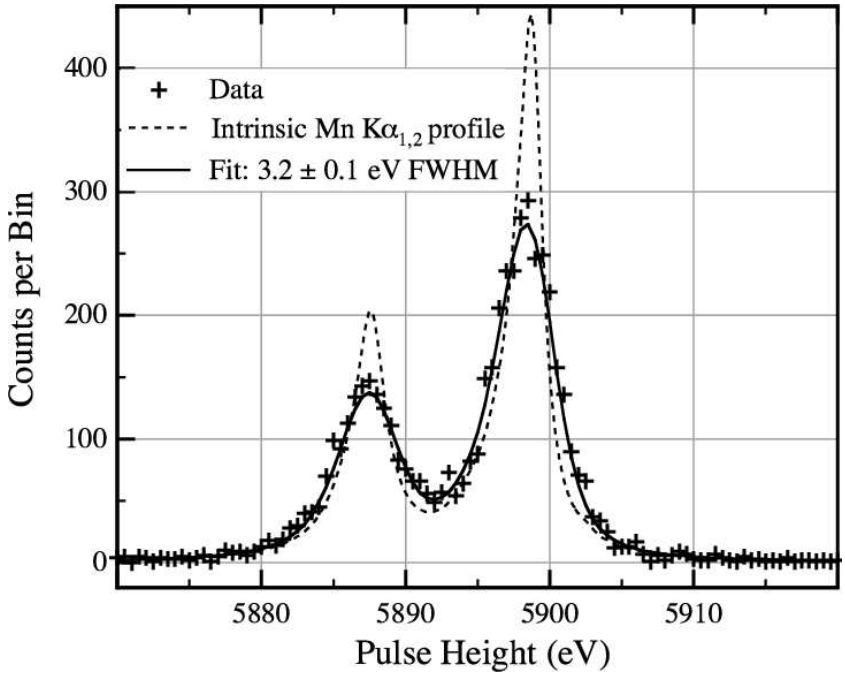

Figure 5.20 - Separation of the MnK_α line in its two components in a spectrum collected with a XRS2 array element.

The XRS2 6×6 silicon array consists of a grid of 36 suspended pixel (see figure 5.21). Each 1.5 μm thick pixel (see figure 5.22) has an ion-implanted 300×300 μm^2 thermistor, four thin silicon beams to form thermal links to the heat-sink, ion-implanted traces, four absorber

support tabs and four SU8 patternable polymer absorber spacers on the four tabs. The XRS2 design is very strong and compliant in the axial direction. The thermal links give a thermal conductance to the heatsink of about 7×10^{-11} W/K at 100 mK.

The array we have tested is taken from wafer C3. The $R(T)$ of these devices can be modeled using the modified VRH formula $R(T) = R_0 \exp(\sqrt{T_\circ/T_e}) + R'_0 \exp(\sqrt{T'_0/T_e})$, where $R_0 = 270\,\Omega$, $T_\circ = 7.2\,\mathrm{K}$, $R'_0 = R_0 \exp(2.522 T_\circ^{-0.25} - 8.733)$ and $T'_0 = 2.715 T_\circ + 1.233\,\mathrm{K}$. A satisfactory description of the $R(T)$ curve can be obtained also using the Mott formula (3.2) with $R_0 = 2737.12\,\Omega$, $T_0 = 1.03461\,\mathrm{K}$, $p = 0.7954$.

Some preliminary crystal attaching test showed that the crystals cannot be fit either on all four SU8 supports simultaneusly or in the space between them, because they have too irregular shapes. To avoid these problems thin silicon chips must be used to support the crystals. Two approaches were tested. The first approach consisted in gluing $0.5\times0.5\,\mathrm{mm}^2$ wide and $18\,\mu$m thick silicon chips on all four SU8 supports using epoxy resin ST1266. The $AgReO_4$ crystals were then glued to these *platforms* with different kind of epoxy resins. The second approach consisted in gluing $0.3\times0.3\,\mathrm{mm}^2$ wide and $10\,\mu$m thick silicon chips directly to the thermistor to act as a *spacer* fitted between the four SU8 supports. In this case different epoxy resins were used.

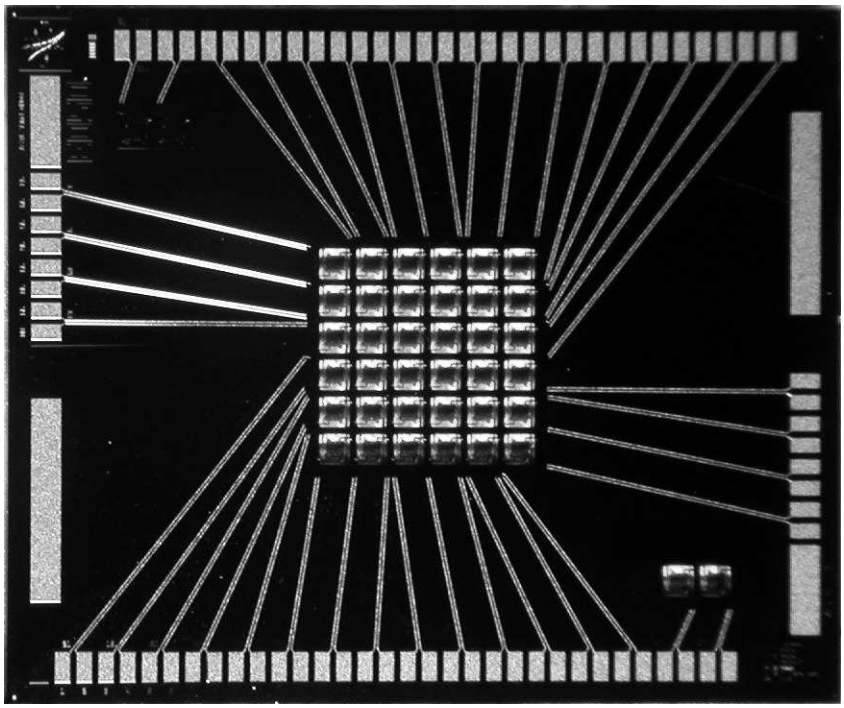

Figure 5.21 - 6 × 6 XRS2 array.

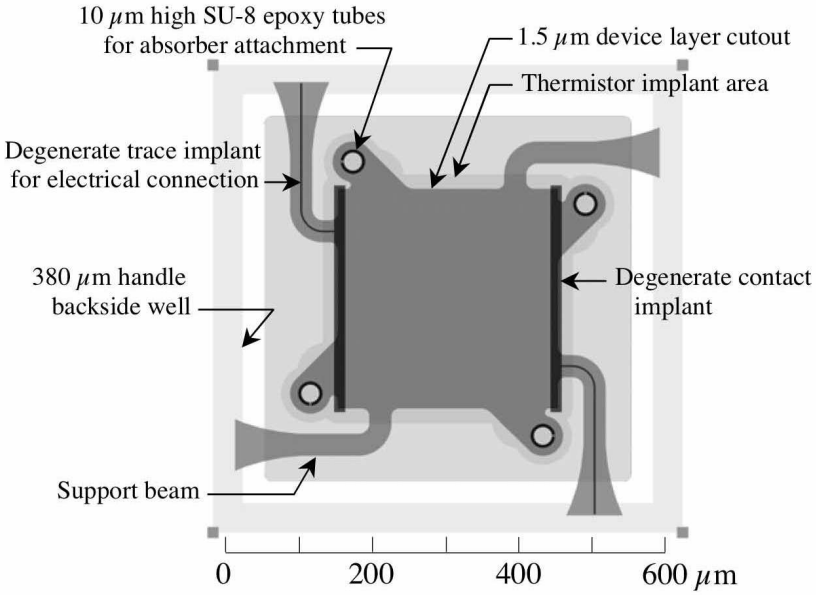

Figure 5.22 - Detail of the single element of the XRS2 array.

Two cooldowns were devoted to establish the best approach for mounting the $AgReO_4$ crystals on the XRS2 array.

For the first cooldown the detectors were prepared at GSFC and sent over to Milano. Eight $AgReO_4$ crystals with masses around 450 μg were attached on eight pixels of the array (see figure 5.23). Seven crystals were glued with epoxy resin ST1266 to seven *platforms* and one was glued with epoxy resin ST1266 to a *spacer*.

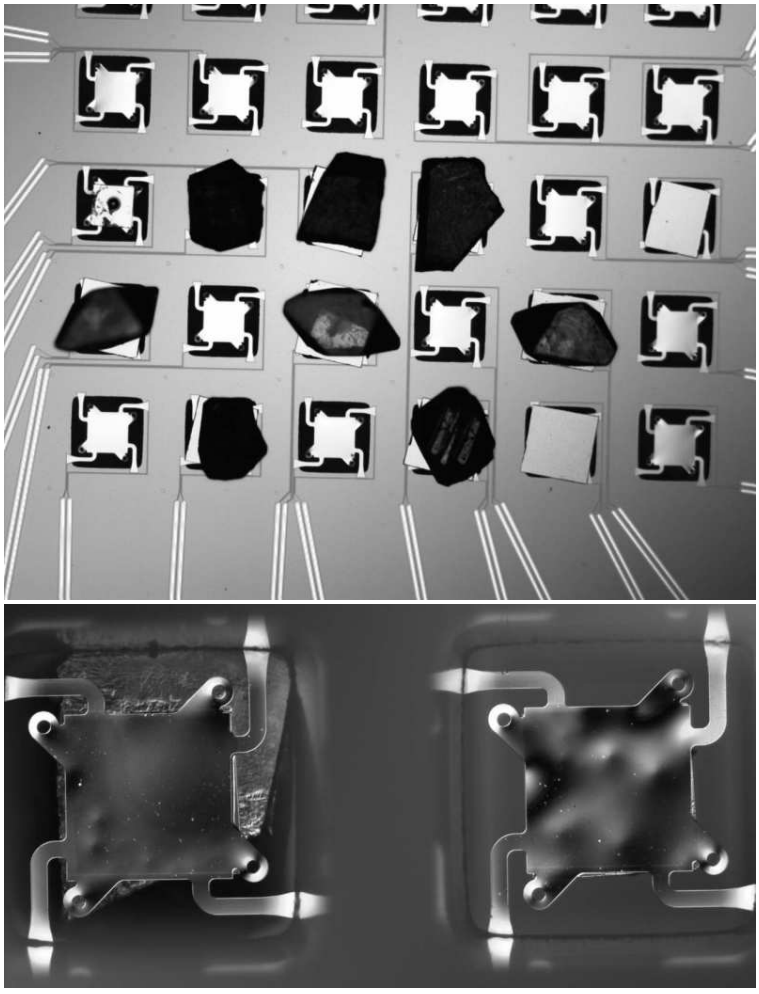

Figure 5.23 - XRS2 array: view of several pixels with $AgReO_4$ absorbers (top); single element close bottom view (bottom).

The array was tested at several working temperatures between 60 and 110 mK. The detectors made with the *platforms* glued on the four SU8 supports show very slow and small pulses due to the weak thermal link introduced by the SU8 between the crystals and the sensors.

Much better results are obtained with the detector with the smaller *spacer* glued directly to the thermistor. The best performance are shown by this detector at about 100 mK: figure 5.24 shows the data collected at this working point where the resistance is about 2.4 MΩ and the temperature is about 94 mK. The energy resolution is about 35 and 43 eV FWHM at 1.5 and 2.6 keV respectively. The baseline width is about 25 eV. As already mentioned this data

Table 5.1 - Detector characteristics and performance.

T_{op}	R_{op}	ΔE_{FWHM} baseline	ΔE_{FWHM} @ 1.5 keV	ΔE_{FWHM} @ 2.6 keV	τ_{rise}	τ_{decay}
[mK]	[MΩ]	[eV]	[eV]	[eV]	[μs]	[ms]
78	6.8	14.3	28±1	38±2	400	2.2
94	2.4	25.4	35±1	43±1	220	2.4
109	1.1	41.0	52±2	51±2	150	2.7

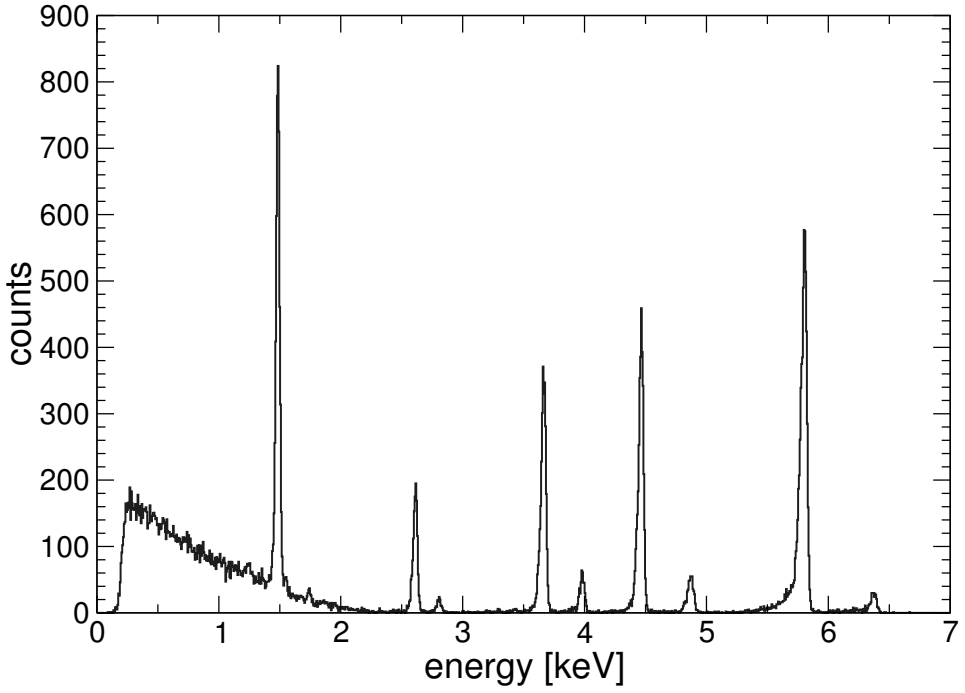

Figure 5.24 - Energy spectrum obtained with the best pixel of the XRS2 array during the first cooldown.

has been acquire with the MIBETA electronics which is not matched to a resistance of few megaohms. With the new MIBETA2 electronics discussed below the baseline width would improve to about 15 eV. As a consequence the FWHM at 1.5 and 2.6 keV would also improve to about 29 and 38 eV respectively. The rise time for this detector at this temperature is about 220 μs. The new electronics is likely to allow some improvement on the rise time as well.

A striking and somehow disappointing feature of this detector is the excess peak broadening which rapidly increase with the energy. A deeper investigation of this issue is needed: it is known that excess peak broadening may be due to high energy phonon transmission in the thermometer and this transmission may be controlled by means of the thermistor-crystal coupling (i.e. the glue).

The second cooldown was devoted to study different gluing methods using the *spacer* approach. The aim was to improve the detector performance, to check the crystal attaching reproducibility and to reduce the energy dependent excess peak broadening. For this new run

ten $AgReO_4$ crystals were attached to ten pixel in Milano (see figure 5.25) using the set-up described in §5.4.1. Eight of the crystals were mounted on a 10 μm thick silicon *spacer* as described above. Different combinations of glues were used for the couplings crystal-spacer and spacer-termistor (see table 5.2). The remaining two were again mounted on a *platform* (see last two entries in table 5.2).

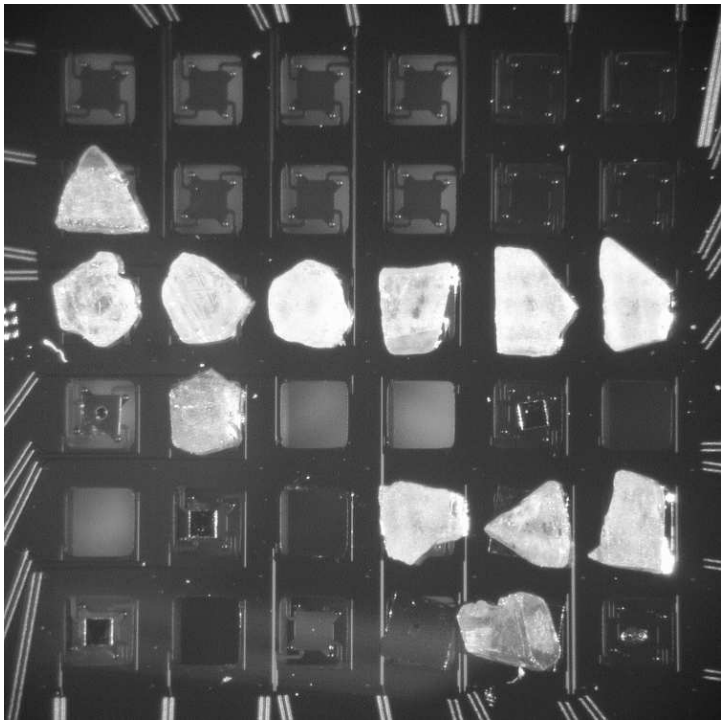

Figure 5.25 - XRS2 array: view of several pixels with $AgReO_4$ absorbers for the second cooldown.

A summary of the most interesting results is presented in table 5.2. These data confirm that the *platform* approach gives slow detectors with small pulses (detectors 7 and 8). Similar results are obtained in the *spacer* approach when epoxy resin ST2850FT is used for both couplings (detectors 6 and 9). The other combinations of epoxy resins used in the *spacer* approach give better and homogeneous results. Only detector 1 shows a clearly superior performance (figure 5.26), even though yet unexplained. Another striking feature can be appreciated with help of figure 5.27: the energy dependence of the excess peak broadening in not influenced by the epoxy resin used for the crystal mounting. Therefore it looks like it is a peculiarity of the crystals themselves. In figure 5.27 also the data from the MIBETA array are reported (see also figure 4.22): the slope of these data is clearly less steep. Whether this difference is due to the crystal size or the crystal quality is still under investigation.

Table 5.2 - Detector characteristics and performance.

det	$AgReO_4$ mass	sensor spacer	spacer $AgReO_4$	T_{op}	R_{op}	τ_{rise}		ΔE_{FWHM}	
							baseline	@ 1.5 keV	@ 2.6 keV
#	[μg]	glue	glue	[mK]	[MΩ]	[μs]	[eV]	[eV]	
1	402	Araldit	Araldit						
				79	6.5	410	11	19	24
				85	4.2	310	14	21	28
				90	2.9	260	16	23	28
				94	2.3	230	21	28	31
2	388	Araldit	Araldit						
				81	5.4	400	22	29	36
				87	3.5	300	28	34	36
				93	2.5	240	31	37	45
				97	2.0	210	42	49	52
3	456	Araldit	ST2850						
				77	7.2	450	17	27	35
				84	4.4	350	21	30	37
				88	3.2	300	23	31	37
				93	2.5	260	30	37	44
10	470	Araldit	ST2850						
				81	5.5	470	24	29	34
				88	3.4	350	33	33	38
				93	2.4	300	38	41	42
				97	1.9	270	49	53	55
4	406	ST1266	ST2850						
				79	6.5	410	16	28	37
				85	4.0	320	22	33	38
				90	2.9	260	24	34	41
				94	2.3	240	31	41	48
5	442	ST1266	ST2850						
				81	5.3	500	23	30	39
				88	3.3	390	30	35	41
				93	2.5	320	33	38	42
				97	1.9	300	43	47	52
6	506	ST2850	ST2850						
				82	4.9	600	113	30	39
				89	3.2	500	113	35	41
9	430	ST2850	ST2850						
				80	5.8	700	132	30	39
				86	3.7	600	132	35	41
7	390	SU8	ST1266						
				84	4.2	750	113	30	39
				91	2.7	650	113	35	41
8	386	SU8	ST1266						
				80	5.8	700	132	30	39
				86	3.7	600	132	35	41

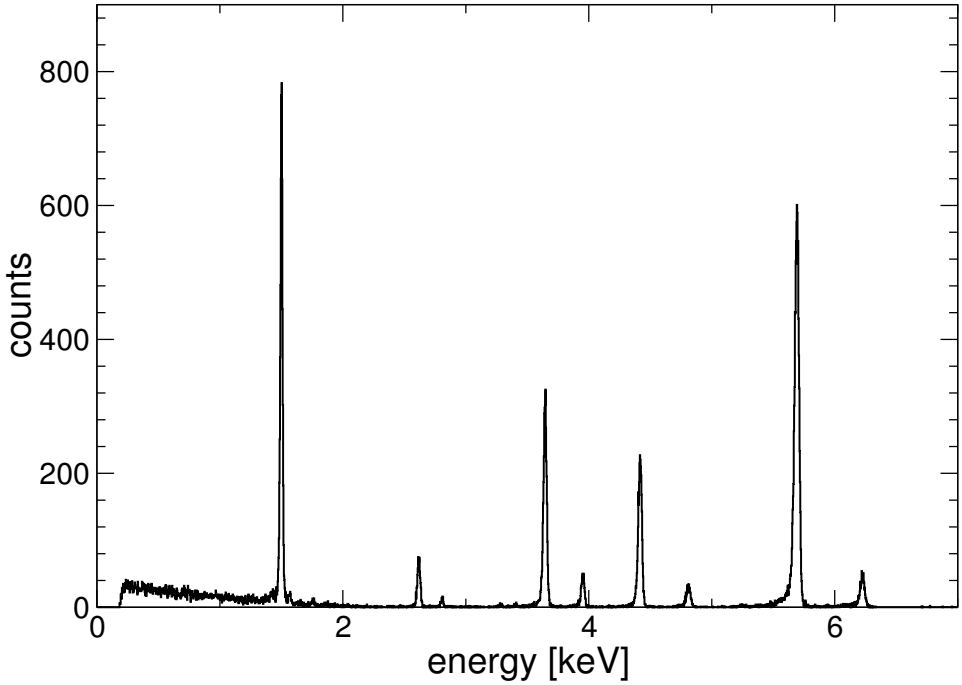

Figure 5.26 - Energy spectrum obtained with detector 1 of table 5.2 at 85 mK.

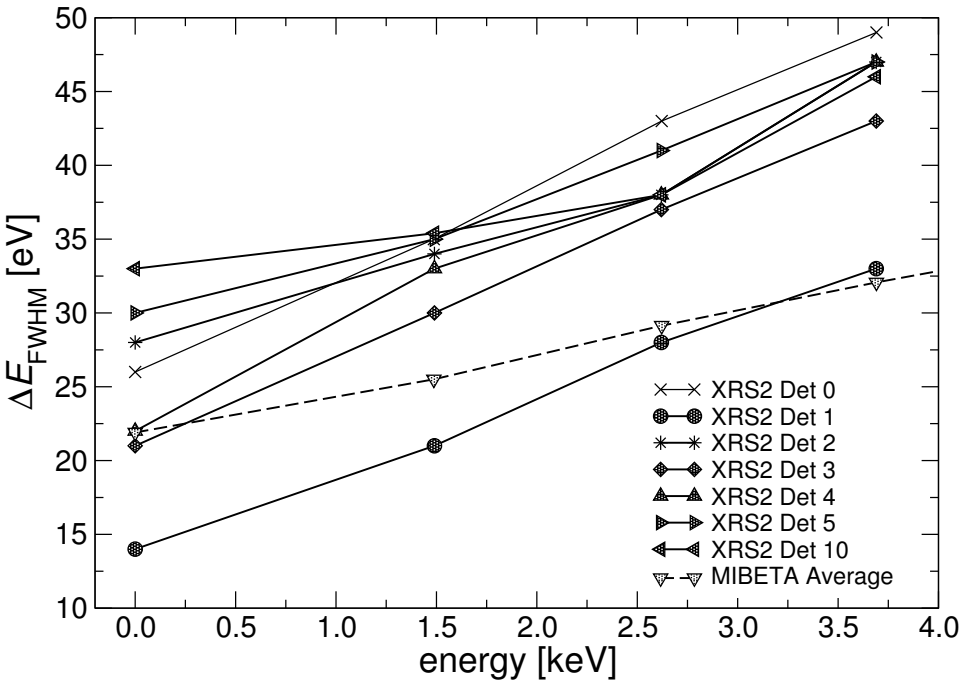

Figure 5.27 - Energy dependence of energy resolution for detectors of table 5.2 (detectors 1, 2, 3, 4, 5 and 10 at about 85 mK), for the best detector measured during the first cooldown at about 94 mK (Det 0) and the sum of all detectors in the MIBETA array (see also figure 4.22).

Figure 5.28 may help to estimate the neutrino mass statistical sensitivity achievable with the detectors presented above. The grey scale 2D plot gives the sensitivity expected for a total statistics of about 6×10^9 events and an activity of the single detector of about 0.24 decay/s as a function of the detector time and energy resolutions. This statistics is the one expected at the end of the forth measuring year with a detector deployment scheme as described in §5.4.9 (see table 5.4.9 and figure 5.40). The superimposed curves are the actual time and energy resolutions of the detectors 1, 2, 3, 4, 5 and 10 of table 5.2 at different operating temperatures.

From this plot it is clear that, in spite of their not optimal performance, these detectors are an acceptable baseline design for the MIBETA2 experiment. In particular the optimal operating point may be around 90 mK.

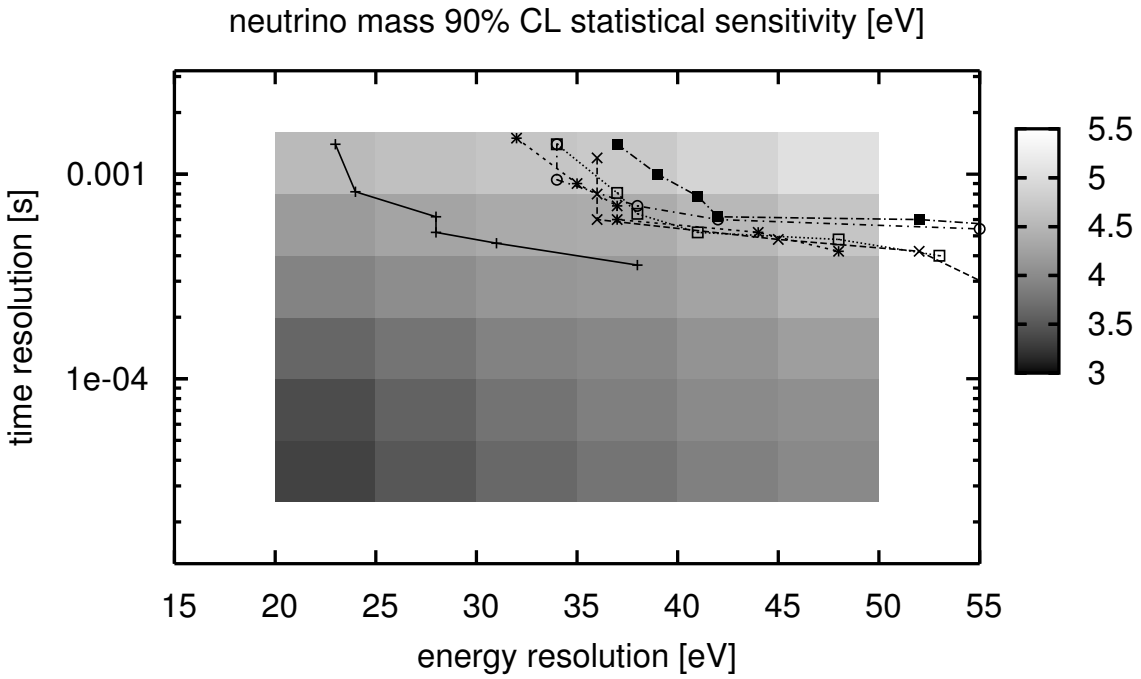

Figure 5.28 - Neutrino mass statistical sensitivity expected for the tested detectors at different operating point.

New silicon implanted thermistor arrays are also being prepared by the MEMS group at ITC-irst. The single element structure is depicted in fig. 5.29. Although they are made with the somewhat older technique of multiple implanted thermistor and TMAH anisotropic wet etching, these arrays are optimized for the MIBETA2 experiment. The sensors are larger ($800\times800\,\mu\mathrm{m}^2$ area) than the ones used for the MIBETA experiment and have a length-to-width ratio of 4. The heat sink coupling G_{fb} is provided by three silicon legs. For a better control over the absorber gluing there are SU8 supports on a silicon structure with limited coupling (G_{af}) to the thermistor. The heat sink and thermistor coupling are optimized for the new larger $AgReO_4$ crystals and for the larger thermistors. The detectors have also a high doping implant on the crystal support to be used has heating resistor for continuous monitoring of the detector stability.

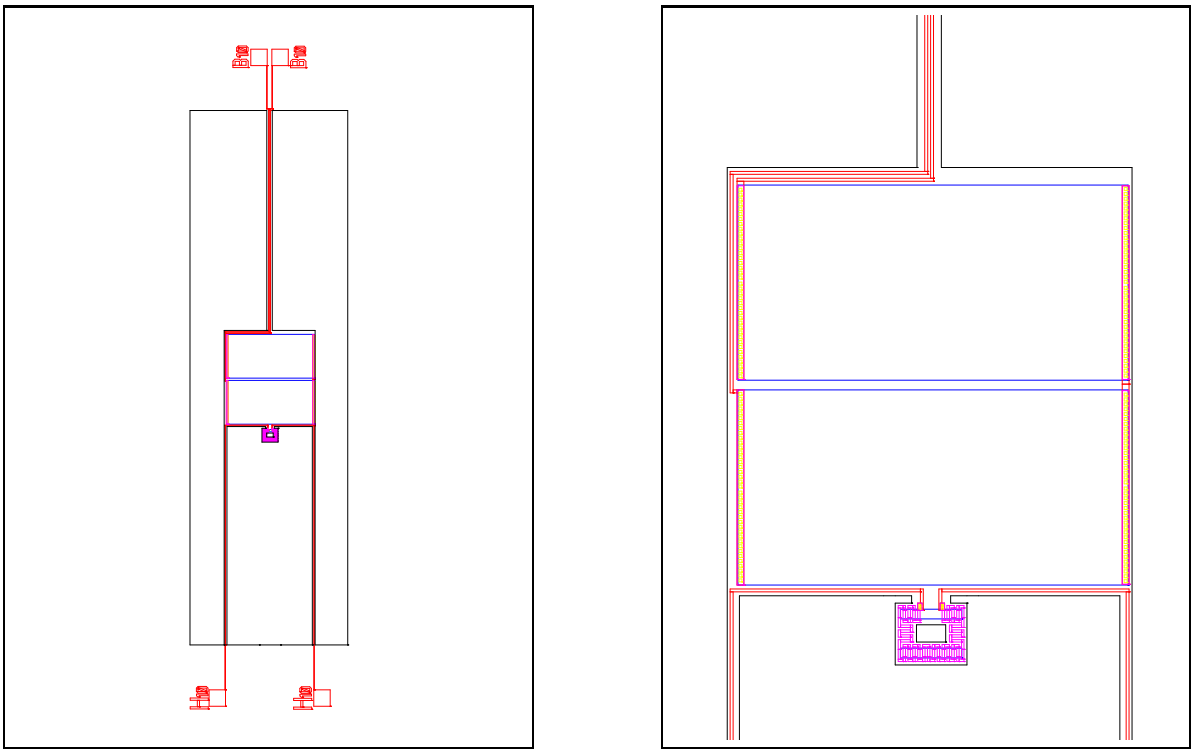

Figure 5.29 - Single element of the silicon array developed by ITC-irst.

Detectors with Neutron Transmutation Doped Ge sensors

As an alternative to the silicon implanted thermistors we are also studying the feasibility of an array with NTD germanium thermistors. The main reason for this attempt are the encouraging results discussed in §4.3.10. Moreover it has been observed that [35] for germanium thermistors τ_{e-ph} (figure 5.17) is about a factor 6 smaller than for silicon thermistors at the same temperature.

The array we have tested was made by E. Kreysa at Max-Planck-Institut für Radioastronomie in Bonn (Germany) using NTD flat-packs similar to the one described in §4.3.10 supplied by J. Beeman at Lawrence Berkeley Laboratory in Berkeley (USA). These arrays have been developed by E. Kreysa for millimeter and submillimiter detectors operated at about 300 mK. Some views of the array and of the single elements are shown in fig. 5.30.

The array is based on a $23\times25\,\mathrm{mm}^2$ silicon chip with 37 low stress SiN membranes. Each membrane is about $2.2\times2.2\,\mathrm{mm}^2$ wide and $0.8\,\mu$m thick. This size should give a thermal coupling G to the heatsink of about $4\times10^{-10}\,\mathrm{W/K}$ at 100 mK.

A Nb wiring has been evaporated on top of the SiN layer for contacting the NTD sensors. Each Nb wire is 80 nm thick and $100\,\mu$m wide. Each membrane has two Nb wires ending in its middle with two gold plated pads. The NTD flat-packs are bump bonded on these gold pads by means of two indium sphere with $25\,\mu$m diameter. For the first test only 10 NTD were attached. The NTD dimensions are $300\times100\times25\ \mu\mathrm{m}^3$ (see §4.3.10). Of the 10 NTDs, 3 come from series # 27 ($R_0 = 69\ \Omega$, $T_0 = 11.092$ K) and 7 come from series # 26 ($R_0 = 74.22\ \Omega$, $T_0 = 13.302$ K).

Along the 25 mm sides there are two long gold pads for thermal contact. The array is mechanically and thermally coupled to the heatsink by means of several $50\,\mu$m gold wires ultrasonically bonded to these pads. This avoid the mechanical stress due to the different coefficients of thermal expansion of copper and silicon. Along each of the 23 mm sides there are 19 gold pads for the electrical connection to the sensors.

Ten $AgReO_4$ crystals with sizes around $450\,\mu$g were manually attached to the ten NTDs using small drops of epoxy resin. Half of them were attached using resin ST2850FT with Catalyst 9, while for the other half the ST21266 resin was used. Thanks to the wider spacing of the sensors the preparation of this array was relatively easier than for the XRS2 array.

It is worth to mention that this is the first array of low temperature microcalorimeters ever made with this technique. The array was characterized collecting data at various working temperatures between 70 and 100 mK. We observed some spread in the detector performance and also the pulse amplitude were smaller than expected from our previous tests with $AgReO_4$ crystals coupled to NTD. First of all there is a large difference in the response which depends on the resin used for attaching the crystal: crystals glued with ST1266 resin exhibit too fast and small pulses. A more regular response was shown by the other detectors. A deeper investigation reveals that the sensor are mechanically stressed and their resistivity is increased. This is a very well known phenomenon for NTD sensors. The actual $T_\circ$ of series # 26 NTDs appears to have become about 18 K. The consequent underestimation of the working temperature explains the smallness of the observed signal because: data were actually collected between 100 and 130 mK. The stress can also alter other functional parameters of the sensors like the electron-phonon coupling, causing a further deterioration of the performance. The sensors appear to be rather uniformly stressed across the array, but still the spread in the performance could be due to slightly different stressing conditions. The origin is yet unknown and needs more investigations. Most probably it is due to the different thermal contractions of the NTD and

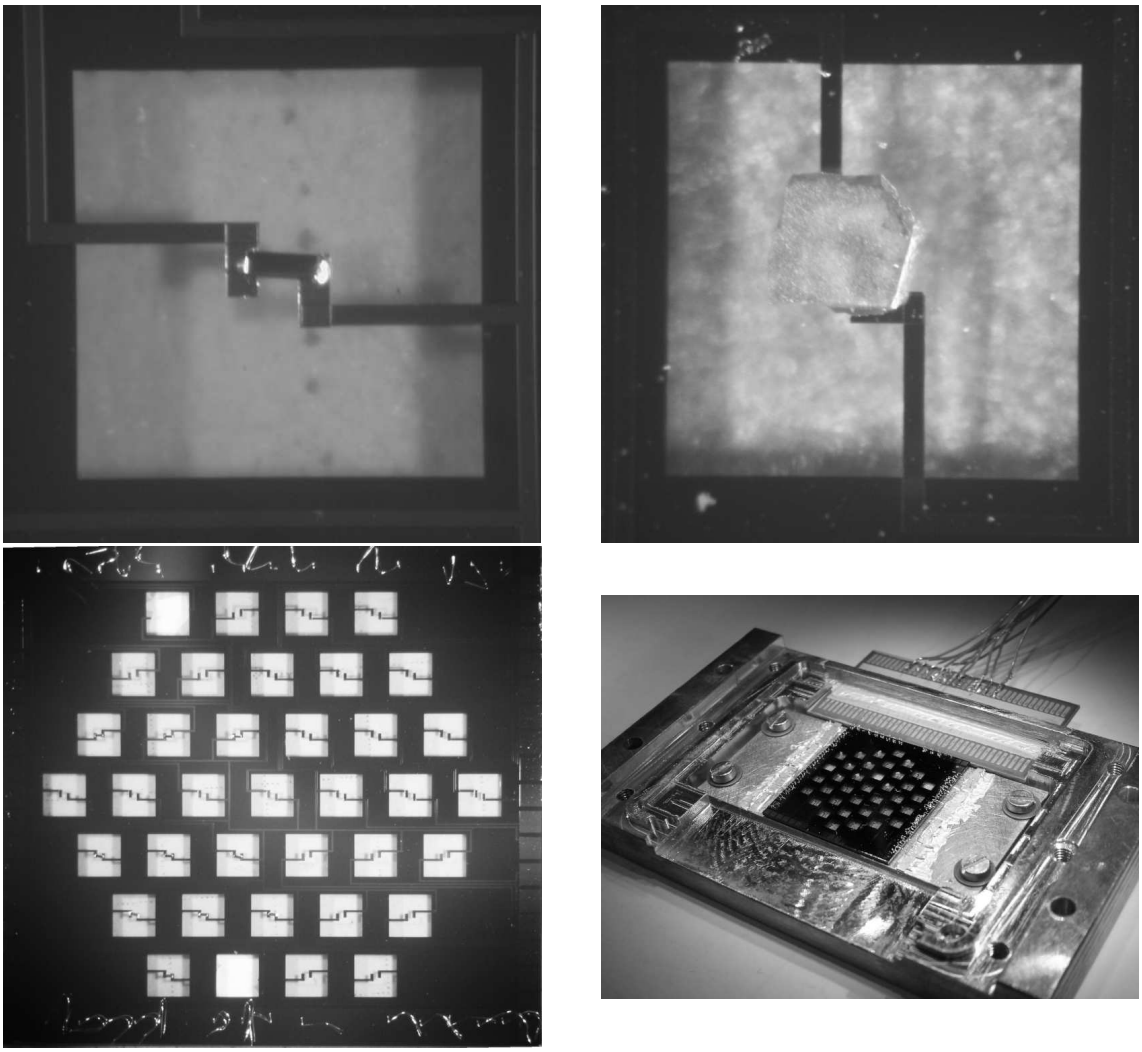

Figure 5.30 - Array and single elements of NTD sensors.

of the SiN membrane or of the indium bonding.

The best result obtained with this array is shown in figure 5.31. This detector has a 446 μg $AgReO_4$ crystal glued with resin ST2850FT, the data shown are taken at a temperature of about 100 mK with a resistance of about 60 MΩ. The energy resolution is about 50 eV FWHM at 1.5 keV and the baseline width is about 49 eV FWHM. In spite of the large static resistance, thanks to the very small dynamic impedance, this detector appeared to be quite fast showing a rise time of about 270 μs.

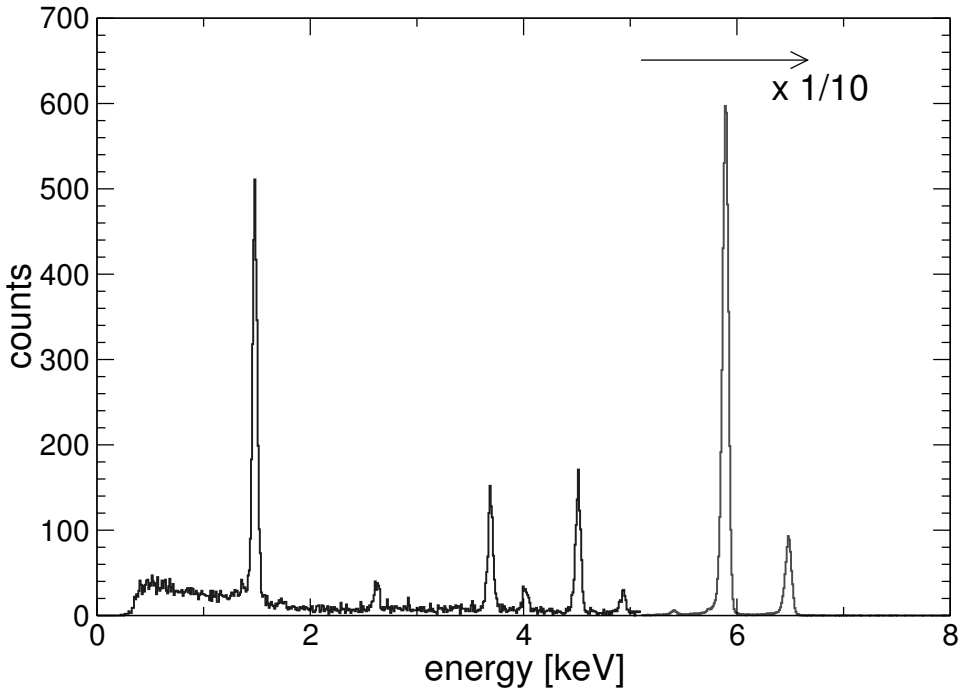

Figure 5.31 - Energy spectrum obtained with a silver perrhenate absorber and an NTD sensor.

5.4.2 Detector holders and front-end electronics

As for MIBETA the front-end will have JFETs cooled at about 120 K and placed very near the detectors. The close coupling of the detector and amplifier requires careful thermal design. The main issues here are:

- protect the detectors from the thermal radiation of the JFET operated around 100 K;
- thermally isolate the JFETs so they achieve their operating temperature only from the power dissipation of the drain current;
- provide low thermal conduction electrical connections between the JFET gates and the detectors;

There is already a large experience in setting up cold readouts for hundreds of channels in refrigerators. The MIBETA2 experiment design makes use of the experience of SHARC-II and HAWC infrared cameras together with the experience accumulated with MIBETA and with the XRS and sounding rocket instruments of the NASA/GSFC and Wisconsin groups.

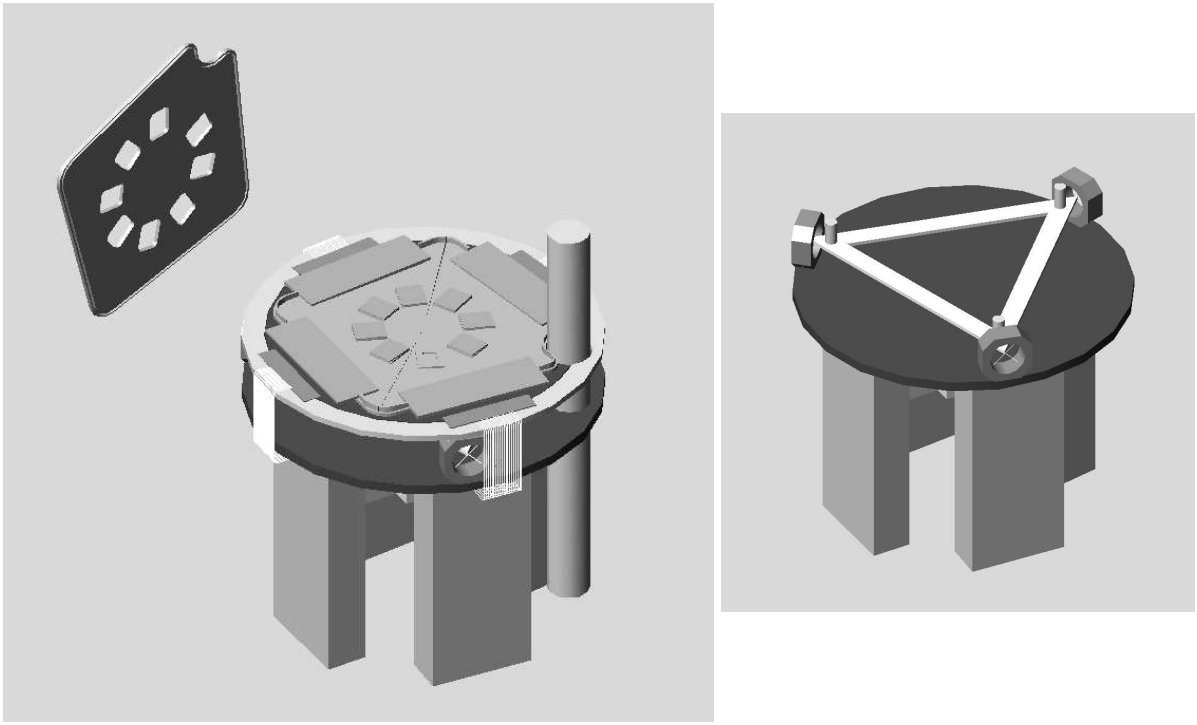

Figure 5.32 - Experimental set-up inside the refrigerator for MARE-1 (MIBETA) detectors.

Figure 5.32 shows a preliminary design of the experimental set-up which will placed below the refrigerator mixing chamber. The whole structure is rigidly mounted on the refrigerator 4 K thermal anchorage extending in the experimental space below the mixing chamber and described in the next paragraph. On top of the set-up there are 4 independent detector boxes. The detector boxes are mounted on a copper plate thermally connected to the mixing chamber by means of flexible copper strips. A Kevlar kinematic suspension system mechanically connects the cold plate to the main 4 K structure. The suspension system consists of 3 Kevlar assemblies

at 120 degrees in horizontal plane. Each assembly has two Kevlar spring-loaded fibers at 90 degrees in the vertical plane. The cold plate is glued to the three Kevlar crossing points. Kevlar is chosen because it has among the highest ratio of strength and stiffness to thermal conductivity at low temperature. The total power flowing from 4 K to the cold plate and therefore to the mixing chamber is about 3 μW. The lower part of the main 4 K structure hosts the JFET boxes.

The detector boxes contains two arrays for a total of 72 pixels each. The arrays are epoxied on alumina ceramic boards which have a coefficient of thermal expansion well matched to that of silicon. The ceramic circuit boards fan out the electrical connections from the arrays to the box edges. The electrical connections are brought out of the boxes by means of feedthroughs which must be opaque to 120 K radiation to prevent the warming of the detectors. Such feedthroughs are made by alumina ceramic sandwiches. Below the detector boxes there are the bias networks with load resistors epoxied on a printed circuit board. Each load resistor is made by the series of two $1 \times 1\,\mathrm{mm}^2$ silicon chips with 25 MΩ NiCr resistive film.

The about 288 JFETs will be enclosed in four independent light tight boxes. The boxes will be mounted on the structure mechanically and thermally connected to the 4 K thermal anchorage. Inside each box about 72 JFETs will be mounted on a multi-layered G10 printed board. The JFET board must be heated to about 120 K with less than about 25 mW (about 350 μW per JFET). The about 150 electrical connections (72 gates, 72 sources, 1 common drain, 1 ground, and some extra leads for diagnostics and redundancy) and structural support linking the board at 120 K and the box at 4 K must guarantee the adequate level of thermal isolation. The board will be supported by a pair of 10 mm long, 6.3 mm diameter Vespel SP1 tubes with a 0.1 mm thick wall. About 10 mW will flow through these standoffs. The electrical connection are provided by litographed cryogenic flat cables (cryo-flats) like the ones developed at NASA/GSFC for SHARC-II and HAWC. The cryo-flats made by the MEMS group at ITC-irst consist of silicon chips with metal traces evaporated on freestanding, serpentine polymide (see fig. 5.33). The serpentine is 20 μm wide and about 5 mm long. The metal layer is aluminum. The total power that flows through the 150 electrical connections should be less than 0.5 mW. The 120 K radiation blocking will be achieved by means of a labyrinth seal between the cover and the bottom of the boxes. The leads will go through feedthrough made by ceramic sandwiches opaque to 120 K radiation.

The electrical interconnection between the detectors boxes (at less than 50 mK) and the JFET boxes (at about 5 K) must provide a strong thermal decoupling as well. There are two viable options for this: cryo-flats with a titanium metal layer or NbTi on Kapton ribbon cables. The first gives a power flow of less than 5 μW, while the latter, though simpler, would give a power flow of about 20 μW.

Just below the detector boxes there is space for a large area PIN diode to be used as veto for cosmic ray showers.

5.4.3 Energy calibration and stability monitor

To maximize the duty cycle of the measurement we will separate the energy calibration and the gain stability monitor tasks. The energy calibration will be provided by a fluorescence source which will be activated only at the beginning and at the end of a acquisition stint. During the measurement the gain stability will be monitored by means of joule heating pulses. One acquisition stint will extend for about 3 days between two liquid helium refillings. Assuming 3 hours per refilling and 3 hours per calibration period, the duty cycle should be about 88%.

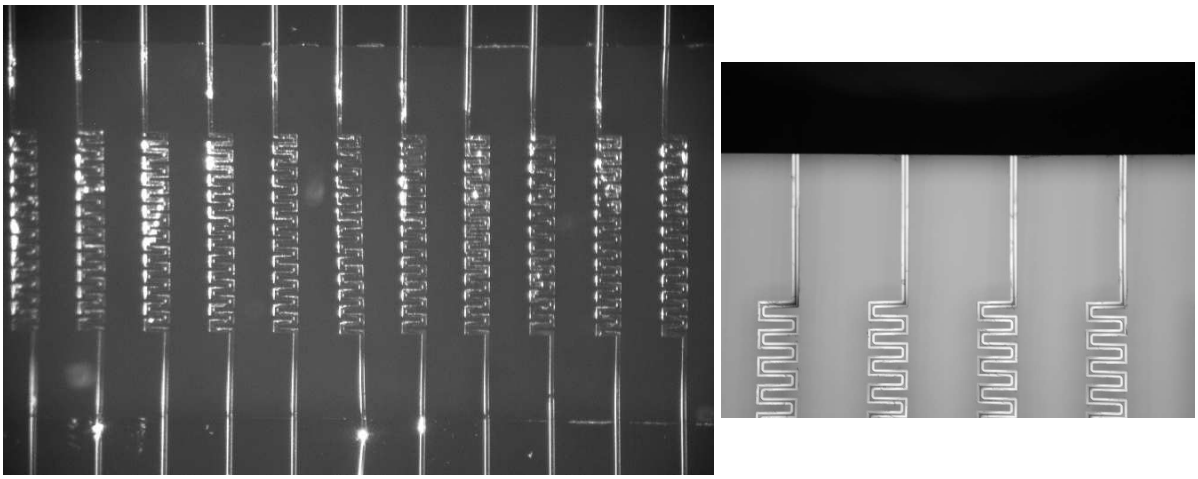

Figure 5.33 - Cryoflats realized by ITC-irst for electrical connections to preamps.

The energy calibration system is fitted between the detector boxes and the mixing chamber, thermally and mechanically connected to the cold plate above the mixing chamber. It consists of 4 fluorescence sources with 10 mCi ^{55}Fe as primary sources. The ^{55}Fe sources are movable from outside the refrigerator in order to shield them with about 2 cm of lead and avoid the background caused by the ^{55}Fe Internal Bremsstrahlung photons. The fluorescent targets will be made of Al, Si, S, Cl and Ca to allow a precise energy calibration around the end-point of ^{187}Re with the Kα X-rays at about 1.49, 1.74, 2.31, 2.62 and 3.69 keV. As shown in §5.1.2 the lineshape must be precisely determined. Assuming for the Al Kα line an activity of about 0.02 counts/s (similar to the MIBETA experiment), at the end one year the statistics for the single detector should be more 50000 counts in the peak. With an energy resolution of about 40 eV FWHM, considering also the presence of the β background, this should be enough to obtain a precision of the order of 1% for the FWHM of the peak. An activity of about 0.05 counts/s would give a precision about 0.1%. Similar or higher statistics should be collected for the other peaks closer to the end-point.

To monitor the stability heat pulses will be used. Only the new designed ITC-irst thermistor have a separate heater to deliver controlled amounts of energy by simply using a short precise voltage pulse. For the other arrays the reference pulse can be obtained only warming the thermistor itself with a voltage pulses added to the bias voltage. To minimize EMI disturbances the pulses are coupled to the bias network with a transformer. The reference pulses obtained with this method differ in shape from the particle pulses, nevertheless they can be used to track the gain of the detector as shown in figure 5.34 and to eventually remove periods characterized by gain drifts.

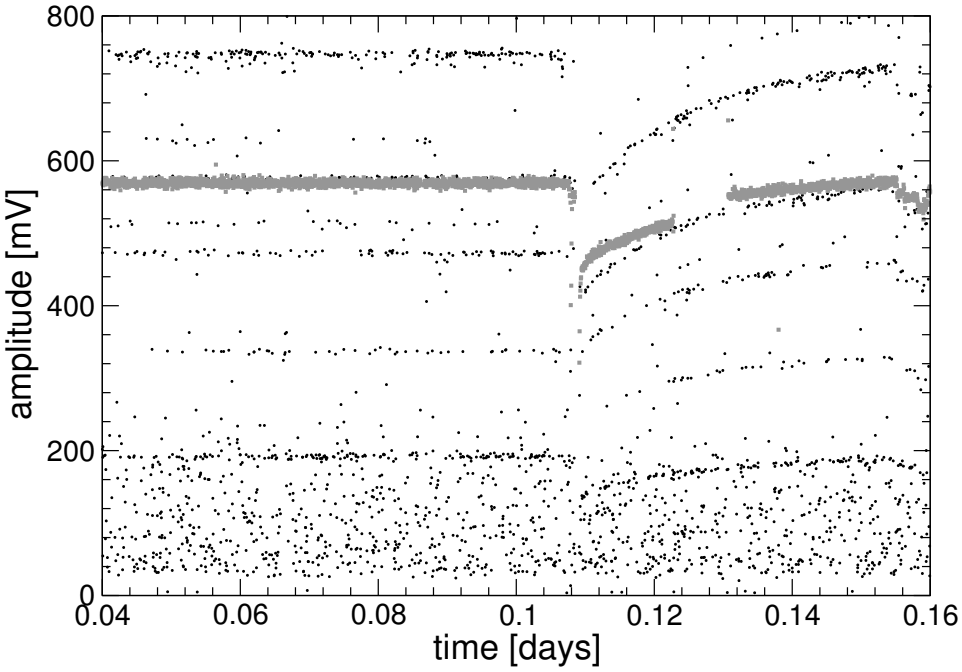

Figure 5.34 - Detector gain as a function of time monitored with heater pulses.

5.4.4 Background reduction

The effect of background is shown in figure 5.35 as a function of the signal-to-background ratio integrated in the beta decay energy range. The Montecarlo simulations shown in figure 5.35 are made for a total statistics of 10^{10} β decays. The signal-to-background ratio of the MIBETA experiment is shown for reference.

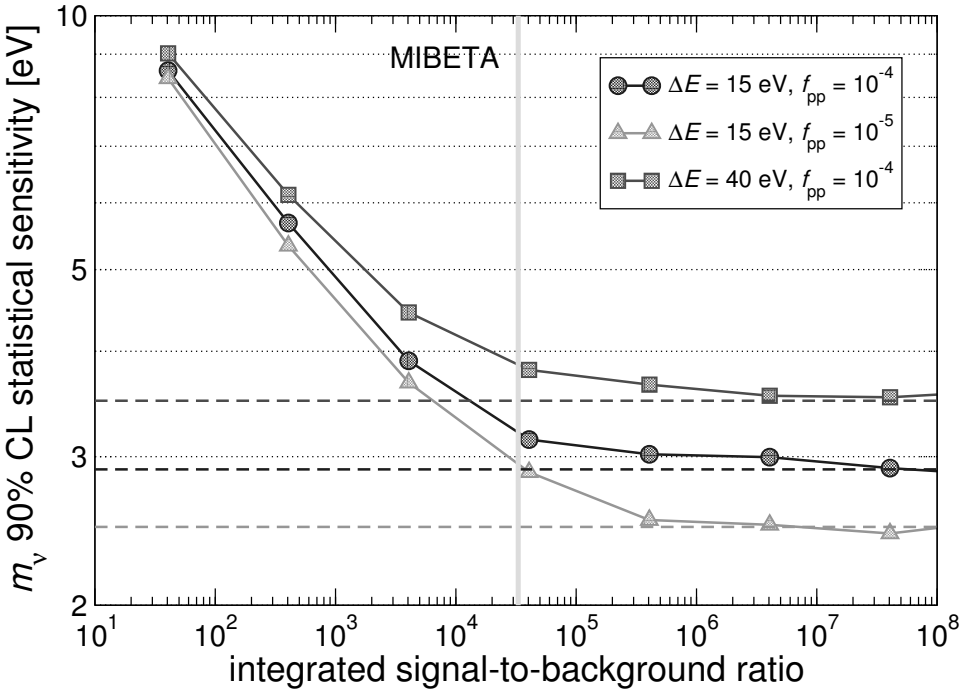

Figure 5.35 - Sensitivity as a function of background in MARE-1 (MIBETA).

To avoid spoiling the experimental sensitivity with a too high background it is therefore crucial a correct analysis of possible background contributions. Specific studies on cosmic rays and environmental background were done for the cryogenic laboratory where the experiment is going to be carried out. The laboratory is located in the basement of the Physics Department of the Milano-Bicocca University, about 12 m below the street level. The basic idea was the identification of the best shielding approach to minimize radioactive background contribution in the energy region of the rhenium beta spectrum.

The muon flux in the cryogenic laboratory was measured with a muon telescope realized with two scintillators placed at the two extremes of a movable bar [48]. In this way we were able to reconstruct the three dimensional distribution of the muon flux. The comparison between the data obtained in the laboratory respect to ground measurements indicates a reduction of a factor 3 in the flux of muon for vertical direction. Obviously the presence of building structures produce different results for different direction of propagation of muon and we were able to individuate different fluxes for different zenith angles related to the morphological configuration above the laboratory [48]. We can estimate that the cryogenic laboratory shows a coverage of 18.8 m.w.e. In practice the muon contribution to background will be reduced thanks to the underground location of the experiment. The building coverage is also sufficient to obtain a little reduction for electromagnetic showers: around a factor 2. This value is

strongly related with amount and type of the shielding materials used around detectors.

We had also tried to evaluate the possible cosmic ray background contribution near the end point spectra of a rhenium beta decay. To do this we collected energy spectra produced by cosmic rays interaction in NaI scintillator detectors of various size. These spectra give us a complete analysis of the muon interaction in the energy range between 10 and 100 MeV. Considering that large part of the interacting particle were muons at minimum ionizing energy we can scale the measured spectrum using a simple geometrical approach. Using spectra acquired with a 5"×5" NaI scintillator we can scale the possible spectrum for a 500 μg $AgReO_4$ cylindrical crystal, we consider the same diameter-height ratio as the NaI scintillator. Simulating the possible differences due to detector types and materials we are able to extract an indicative evaluation on the cosmic rays contribution in the energy range close to the experimental one: between 9 and 10 keV we evaluate a background contribution of $(3.4\pm1.2)\times10^{-3}$ counts/keV/h. Measurements obtained in previous MIBETA experiment indicate, in the same energy region, a value of $(3.32 \pm 0.03) \times 10^{-3}$ counts/keV/h with crystals of comparable masses but with very different shapes.

Obviously extrapolated data are not conclusive respect to the possible contribution of cosmic rays background in a rhenium experiment. In any case these indication must be taken into account for final design if a background reduction will be needed. To minimize this contribution a very simple solution can be realized placing a silicon ionization detector directly above the cryogenic one. They must be as close as possible in order to reduce at minimum level the dead time introduced by anticoincidence operation. We can demonstrate that, thank to the sufficiently good coverage at large zenith angles a silicon detector of relatively small surface will be sufficient to eliminate cosmic rays background contribution.

We had also studied the optimization of the radioactive passive shield to reduce contributions that come from environmental radioactivity [49]. For the energy range below 100 keV the approach will be the selection of materials able to minimize the environmental effect but with also a very low radioactive contents in order to avoid possible background produced by the shield. An analysis of shields made of lead and copper was carried out. Lead is very useful to reduce high energy gamma rays that come from the environment, copper is a very pure material that, thank to very good cryogenic properties, can be placed at low temperature in a very simple way.

Using two germanium detector, a coaxial one for the energy range above 10 keV and a planar one for energy range below 10 keV, we had studied three different shield configurations: a shield with only lead, another with only copper and finally a mixed one, copper plus lead.

The measurements performed in the various configurations give us some interesting information:

- a very big shield is not useful because the presence of shielding materials increase shower contributions, especially if we use high Z materials;
- the environmental background contribution measured with 5 cm of lead or 5 cm of copper is practically of the same order in the energy range below 10 keV;
- copper shows lower intrinsic background in low energy range thanks to the high purity that normally characterize this material, on the contrary the presence of lead very close the detector produce a very strong contribution due to its normal contamination in ^{210}Pb.

Starting from the general considerations reported above the best solution for background reduction will be the realization of a copper shield inside the cryostat and very close to the

detector plus a lead shield placed outside to reduce the environmental γ rays flux at higher energy that can produce some degraded photons in the energy range of interest. Considering the data on background reduction, at the fist stage, will be probably convenient to install only a copper shield inside the cryostat, the lead shield can be realized in a second stage.

In order to measure the background in the β spectrum energy region few microcalorimeters of the array will have the XRS2 HgTe absorbers. This will allow to estimate the background rate and shape for the $AgReO_4$ microcalorimeters and to identify possible low intensity background X-ray peaks. The XRS2 array has 2 extra pixels on the silicon chip which could serve for this purpose, but at least other 4 will be used from the 6×6 array.

5.4.5 The laboratory and the cryogenic set-up

For the MIBETA2 experiment the best suited dilution refrigerator is the Kelvinox KX400 installed in the Cryogenic laboratory in the Physics Department of Milano-Bicocca University. The refrigerator has a cooling power of about 400(32) μW at 100(50) mK and a base temperature of about 6 mK. The available experimental space has a diameter of about 17 cm and a height of about 30 cm and is enough to host the detectors and the JFET boxes described in the previous sections. A 4 K thermal anchorage is available below the mixing chamber. The thermal anchorage can stand a power dissipation of about 100 mW with a temperature increase of only 1 K and it is therefore perfectly suited for the heat sinking of the JFET boxes. Two ports with line-of-sight access down to the mixing chamber can be used for the source and bias wires. One other port is provided with a leak tight moving mechanism which can be used for the calibration source operation. The refrigerator has a vapor shielded dewar with a liquid helium holding time of about 4 days for minimizing the servicing times.

The refrigerator mounting has been designed for minimum vibration sensitivity. The refrigerator is affixed to a 1.5 tons $1.9 \times 1.9\text{m}^2$ square plate made by a stainless steel - wood - stainless steel sandwich. The plate is mounted on 4 stabilizer pneumatic isolators which filter horizontal and vertical vibrations above 1 Hz. The all structure rests on 4 concrete posts which are isolated from the laboratory floor. The laboratory is located at lowest level in the building.

All pumping lines are run through a sand box to reduce the vibration transmission and further mechanical isolation is provided by soft edge-welded bellows. In particular the 50 mm large ^{3}He pumping line is mechanically decoupled by means of a double-gimble assembly (figure 5.36).

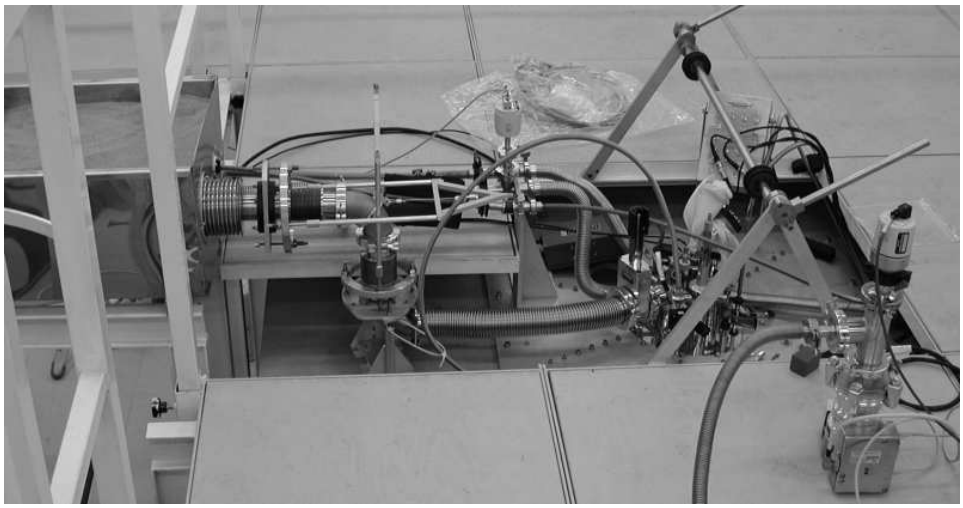

Figure 5.36 - Mechanical assembly for vibration isolation (double gimble).

In order to guarantee the correct electrical grounding of the instrument all pumping lines are also electrically decoupled.

5.4.6 Cold and room temperature electronics

The very front-end set-up One of the most important requirement for MIBETA2 are fast response detectors. The important parameters that allow achieving this goal are a large

value of both the electron-phonon thermal coupling G_{e-ph} and the thermal conductance between the detector and the heat sink, and a small value of the thermistor resistance. These features together tend to reduce the energy conversion gain of the detectors. The trade-off between response speed and signal amplitude depends on the technology adopted for thermistor implantation and on the assembling material used. In our application this is found at an operating temperature of about 90 mK with a thermistor static impedance of about 1 MΩ. The dynamic impedance of the detector around such an operating point is about 5 times smaller than the static one. Since at large excitation frequencies the heat capacity behaves as a thermal short to the heat sink, we expect that the dynamic impedance approaches the static impedance for fast excitations. As a result the thermistor has an inductive component superimposed to the real component.

The small value of the static impedance asks for a small noise of the front-end. In the case of MIBETA the front-end noise affected the energy resolution by a factor close to $\sqrt{2}$ (§4.3.5). For MIBETA2 we must push down the front-end electronic noise. The MIBETA2 front-end has again a cold buffer stage followed by a room temperature operated amplifying stage. We worked for the optimization of the performances of both stages. The first step has been the study of a new cold buffer stage matched to the target detector impedance. The optimization concerned the noise as well as the power dissipation, in view of the large number of channels. Our investigation led to select the SNJ450L109 Si JFETs from INTERFET. In figure 5.37 the

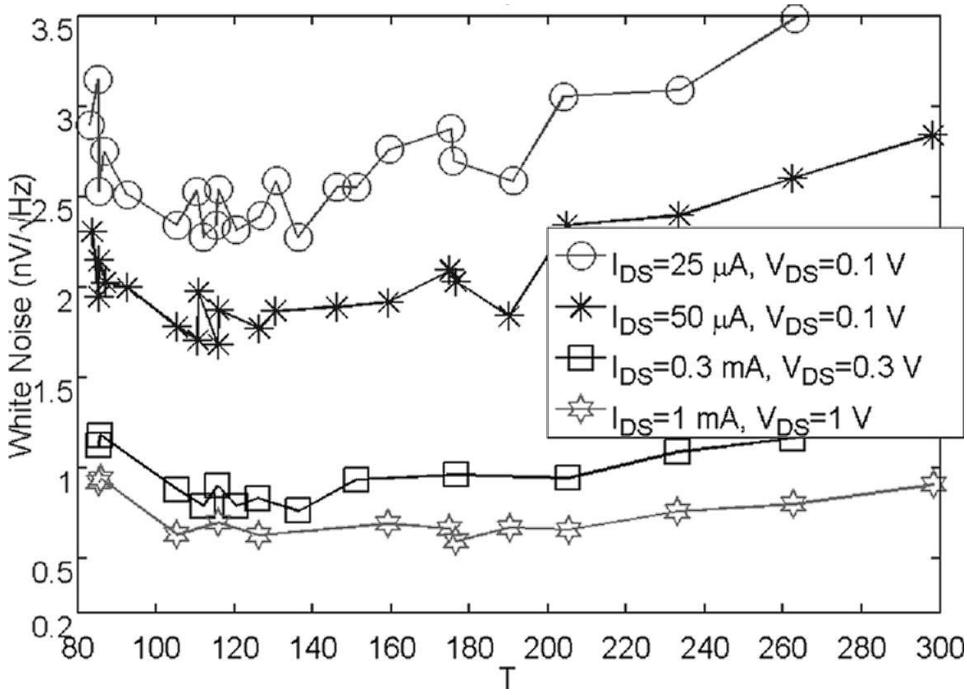

Figure 5.37 - White noise at different Drain current levels vs temperature for the Si JFET SNJ450L109 from INTERFET.

white noise as a function of temperature and at different biasing points are shown for the worst condition found so far in the measured samples. As it can be seen the noise can be optimized vs. power dissipation. At the optimum temperature of operation that in Si JFETs is around 120K, the noise ranges from about 0.8 nV/Hz$^{1/2}$ to 0.6 nV/Hz$^{1/2}$ when power dissipation is between

0.1 mW and 1 mW. A very good figure of merit has been obtained with the SNJ450L109 also for what concerns the $1/f$ noise. At 1 Hz, as a reference frequency, it is about $2\,\mathrm{nV/Hz^{1/2}}$ (figure 5.38). More details concerning the study on the cold JFETs can be found in [37].

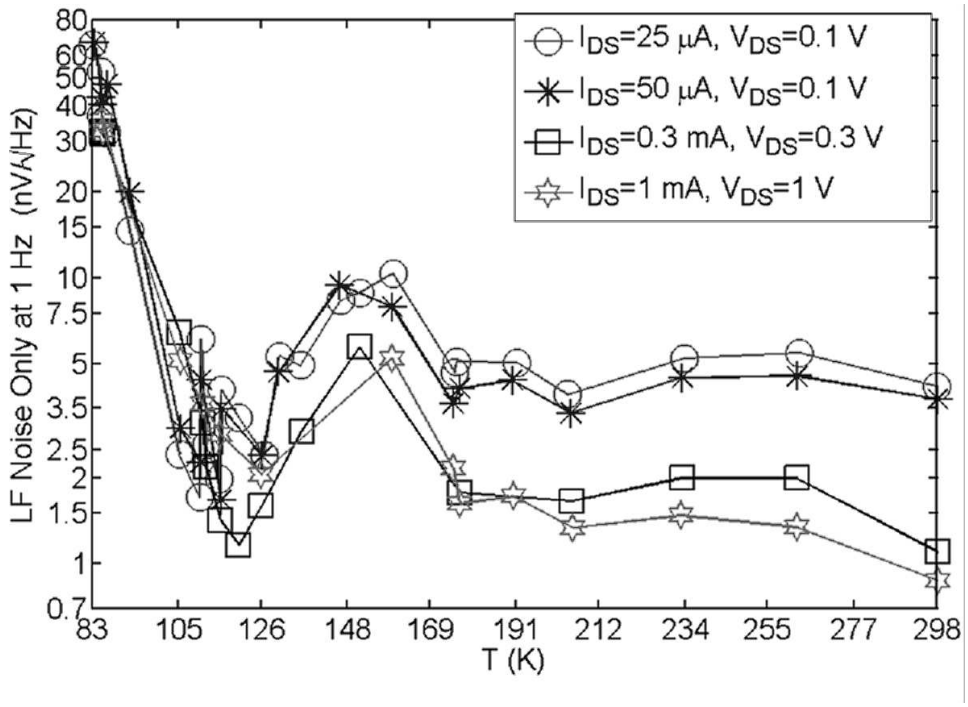

Figure 5.38 - Noise measured at 1Hz for the SNJ450L109 at different temperatures and biasing conditions. These measurements give an indication of the low frequency noise of these device.

The very small level of noise of the cold stage requires that the second amplifying stage has a very small noise as well, since it is reflected at the input without attenuation. For this reason the amplifier we have used in MIBETA [38] has been substantially revised to face the new stringent requirements. As can be inspected from figure 4.16 the front-end read-out for a bolometer consists of a cold unity gain buffer stage, followed by a room temperature operated amplifying stage. Since the noise must be small and the buffer input impedance very large, the standard way to read-out the detector is by single sided input [38]. The cold stage is places as close as possible to the detector. To suppress EMI both the output of the cold stage and the ground reference voltage, taken close to the detector itself, are read out. The difference between the two signals allows the suppression of common mode disturbances coming from ground loops. One of the essential features of the new second stage amplifier is that it is able to make the difference between the signal present at the cold buffer output and its ground using just one transistor at its input, and not a differential pair. In this way a factor 2 is spared on its noise. This result can be obtained if the ground signal has a very small impedance. The equivalent schematic diagram of the front-end is shown in figure 5.39. To obtain a small series noise a large gate area JFET has been used at the second stage input, and the feedback resistor R_S has been chosen of very small value, $10\,\Omega$. To AC couple at a frequency smaller than 1 Hz the cold buffer stage with the second stage a *super-capacitance* of 0.5 F has been used for C_A. The design of the amplifier has been made considering that the combination of

the output impedance of the cold buffer stage together with the gate capacitance of the JFET at the input of the second stage, gives the dominant pole of the amplifier. The part at cold

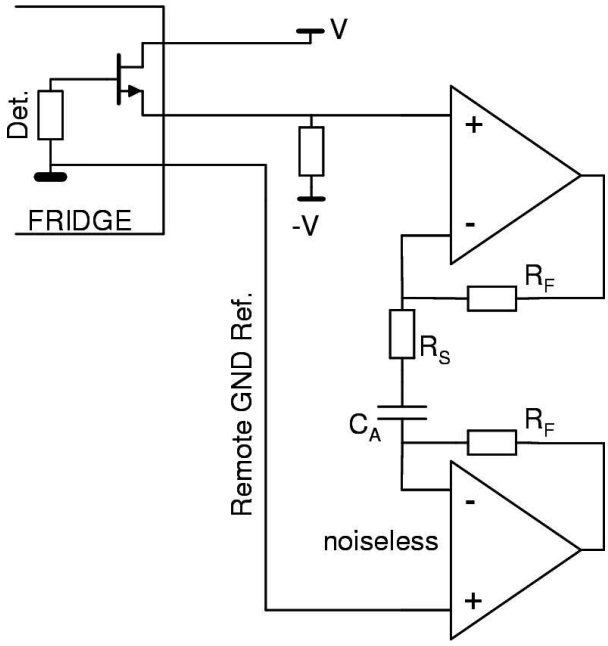

Figure 5.39 - Equivalent schematic of the very front-end set-up.

of the *Remote GND ref.* link of figure 5.39 has not a low impedance since it must be of small thermal conductance. To exploit the circuit solution described above a buffer of this signal with a unity gain amplifier is used having at its input a JFET larger than that of the second stage amplifier described above. For the array read-out, only one of theses units is needed to drive many channels.

The figure of the merit of the new set-up will be at worst $0.95\,\mathrm{nV/Hz^{1/2}}$, with a low frequency component less than $2.5\,\mathrm{nV/Hz^{1/2}}$ at 1 Hz. The input capacitance of the cold JFET for noise calculation is 40 pF, while the dynamic input impedance is a few pF. To perform a comparison, the quoted noise of the new set-up is equivalent to that of a resistor of 18 This resistor value is about 5.5 time smaller than that we expect for our thermistors. It has to be remarked that we improve the equivalent resistor noise by a factor of 20 with respect to the MIBETA set-up.

Antialiasing and Trigger The signal at the output of the second stage will be filtered with an active Bessel low pass antialiasing filter having 120 dB of roll-off. The location of the filter will be close to the acquisition system. A linear optical buffer amplifier [39] will provide for its galvanic isolation. Although we will study the possibility to perform a software trigger, for the moment we plan to use our present solution which has been designed to avoid re-triggering [40] in case signals present undershoots.

Front-end bias supply For a very long measurement time the stability of any part of the system is extremely important. For this reason the power for every channel is given by a set of power supplies especially designed to show a very low thermal drift, less than $5\,\mathrm{ppm/^\circ C}$, and noise, $< 50\,\mathrm{nV/Hz^{1/2}}$ on average. More technical details can be found in [41].

Front-end layout Three small Faraday cages will be put on the top of the cryostat. All the room temperature operated second stage amplifiers and the detector biasing will be allocated inside them. Another, larger, Faraday cage will be close to the acquisition system to contain the antialising filters and the trigger circuits. All the cages are standard crates that fit the "19 Inc. racks". The same "19 Inc. racks" standard will be adopted for the printed circuit boards sizes and connectors. Our cage will have the inner walls covered by SKUDOTECH [42], a special alloy with very high magnetic permittivity.

Remote programmability Since bolometers could show some spread in their characteristics all the necessary parameters that manage the whole front-end, starting from the detector biasing up to the antialising bandwidth, will be remote programmable [43] and monitored from the acquisition system and/or the operator. This way it will be possible to have a constant knowledge of any parameter that can affect the data taking.

5.4.7 Data acquisition system

From the data acquisition point of view, the MIBETA2 phase consists of 300 readout channels that will be grouped in blocks of 30 channels each. The 30 analog_out lines corresponding to the 30 detectors signals will be connected to a FTB (Frontend and Trigger Board, a VME mixed analog and digital board), which processes the signals and controls the ADC operation. Each FTB will amplify and discriminate the 30 signals. The discriminated signals will be processed by a ToT (Time over Threshold) unit allowing a clever management of the triggers. During the processing phase, all the 30 detector signals are sampled and stored in the ICS145 [46] ADC circular buffers. If a "good" event is detected in one or more channels, the FTB will generate a VME interrupt signal thus allowing the storage of the data of up to a maximum of 10 channels per FTB onto the PC disk. The digitized channels correspond to the hit ones and the surrounding detectors up to a maximum of 9. Each event will thus consist (at maximum) of 10 channels $\times$ 2048 samples/channel. Giving that the ICS145 is capable of transferring up to 500k samples/sec in normal mode and 2M samples/sec in block transfer mode, with a 50% time occupancy this corresponds to a trigger rate ranging from 12 Hz to around 50 Hz. If a higher rate is acquired, the number of neighbouring channels will be reduced. If only the hit channel is saved, a maximum rate of 500 Hz can be reached.

The DAQ will be written in C and will run on a dedicated PC with Linux operating system. The graphics interface will be developed in Tcl/Tk. The readout boards are VME boards and the interface with the VME system will be the SbS Bit3. The FTB boards will be designed by the Insubria University group thanks to the experience developed in the AGILE and ASACUSA experiments.

5.4.8 Off-line data analysis

The MIBETA analysis package described in §4.3.8 can still be used for the first MIBETA2 runs as long as the number of channels is less then 100. The same package with only few minor differences is presently being used for the analysis of the Cuoricino experiment which has 62 channels [44].

With an increasing number of channels some kind of automation must be developed and introduced. A new object oriented package is under development for the CUORE experiment

which will have 788 channels and which is due to start data taking in 2010 [45]. It will be straightforward to adapt this package to the MIBETA2 experiment.

A crucial analsysis issue for MIBETA2 is the time resolution, therefore new pile-up identification algorithms are being studied and tested using data sets simulated starting from real $AgReO_4$ detector data.

5.4.9 Time schedule and sensitivity for MIBETA2

The MIBETA2 array will consist of 288 elements, based on semiconductor thermistors, with typically 0.25 decays/s/element. Assuming an energy resolution of 15 eV FWHM and a time resolution of about 50 μs for each element (a reasonably safe extrapolation of the MIBETA present experimental parameters), the statistic gathered in three years would allow to set a limit of better than 2.9 eV on neutrino mass at 90 % of confidence level. The actual deployment of the whole 288 element array will be achieved through a gradual approach. The intermediate steps will allow the fine tuning of the final array.

The baseline design uses the XRS2 array realized by the NASA/GSFC group for the Astro-E2 satellite mission and described in §5.4.1. As an alternative the array could be made using the Neutron Transmutation Doped Ge thermistors on SiN membranes discussed in §5.4.1. The time schedule for the baseline MIBETA2 experiment is given in table 5.3. Figure 5.40 gives the time evolution of the statistical sensitivity for two experiment designs. The triangles in figure 5.40 are for the baseline design which is characterized by an energy resolution at the β end-point of $\Delta E = 40\,\mathrm{eV}$, a time resolution of about $400\,\mu$s, and a source activity of $0.3\,\mathrm{decays/s/det}$; the detector deployment schedule is detailed in table 5.3.

As discussed in the previous sections there are still some reasons to expect that the actual array will have better performance. The diamonds in figure 5.40 are for an energy resolution at the end-point of about $\Delta E = 15\,\mathrm{eV}$ and a time resolution of about $50\,\mu$s.

Table 5.3 - Milestones for the MIBETA2 experiment.

mid 2006	final optimization of baseline design array prototype cubic $AgReO_4$ crystals final design of cold electronics front end final design of cryogenic setup first test with 72 channel DAQ
end 2006	first 72 channel array installed wiring for 72 channels installed first 72 channel electronics and DAQ installed cryogenic set-up for 288 channels installed start data taking with 72 channel array
end 2007	second 72 channel array installed wiring for 288 channels completed first results from first 72 channel array
end 2008	third and forth 72 channel arrays installed
end 2009	data taking ends

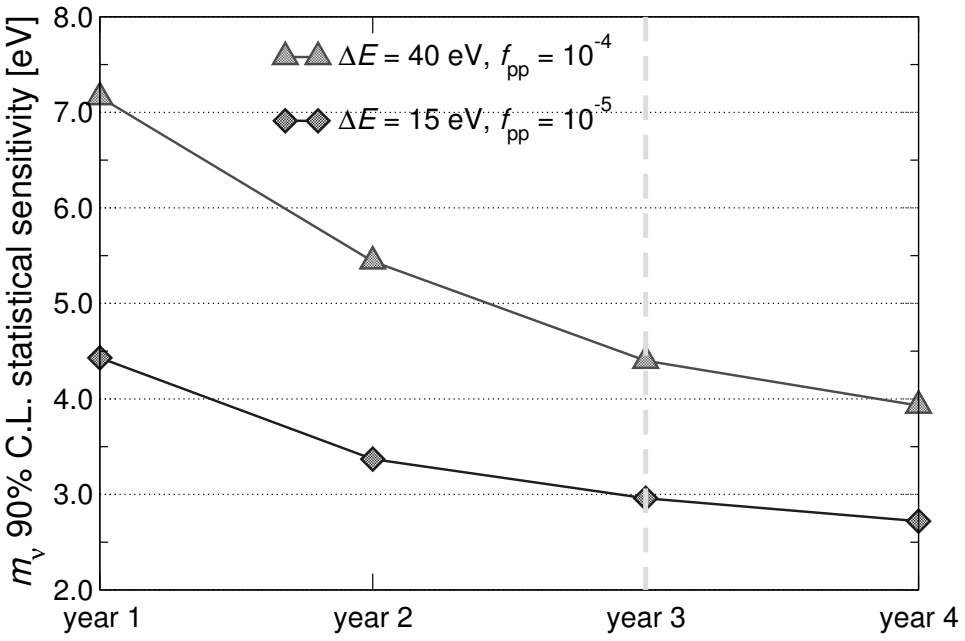

Figure 5.40 - Progress of sensitivity with time in MARE-1, for conservative and improved experimental configurations

Chapter 6

Towards MARE-2

6.1 The goal of MARE-2

The final aim of the MARE project is the search for the neutrino mass with a statistical sensitivity of about 0.2 eV. As it will be shown in the following, today it appears that with a feasable technical development this sensitivity is approachable with a plausibly smaller effort than KATRIN, and it would have the benefit of systematics which are entirely independent. Of course, as a boundary condition, the MARE-1 project must confirm

- all the known sources of systematic uncertainties can be sufficiently reduced and no new source comes up to impair the sensitivity;
- the ^{187}Re β decay spectrum can be understood with the required precision level;
- the estimated sensitivity can be maintained though the experiment is segmented in a large number of channels.

In case all the conditions will be successfully met the MARE project will give a fundamental contribution to the neutrino physics.

The MARE-2 target needs substantial improvements over MARE-1. Simulations shown figure 6.1 and figure 6.2 demonstrate how the total statistics of the experiment must reach about 10^{14} β decays, and both the energy and time resolution must be pushed to the limits of the thermal detector technique. Given that it is difficult to imagine a time resolution better than about 1 μs, a fraction of unidentified pile-up events of about 10^{-5} translates in an activity of 10 decay/s for each channel of the experiment. The target statistical sensitivity requires therefore about 3×10^5 detectors$\times$years. This may look like a daunting challenge: however new microdetector technologies are being developed right now that may allow to set up a several 10000s channel experiment in the near future.

Considering for example the TES calorimeters discussed in the following, there are many international efforts devoted to the development of large arrays. The SCUBA-2 submillimiter camera for the James Clerk Maxwell Telescope in Hawaii is a very promising indicator of the scalability of the TES technology: it is made of a 10000 pixel TES array scheduled to be installed in 2006.

Arrays of the required pixel count are therefore already being constructed. The use of low impedance TES devices has also many advantages. They have minimum sensitivity to microphonic noise, they can be instrumented with SQUIDs which dissipate much less power

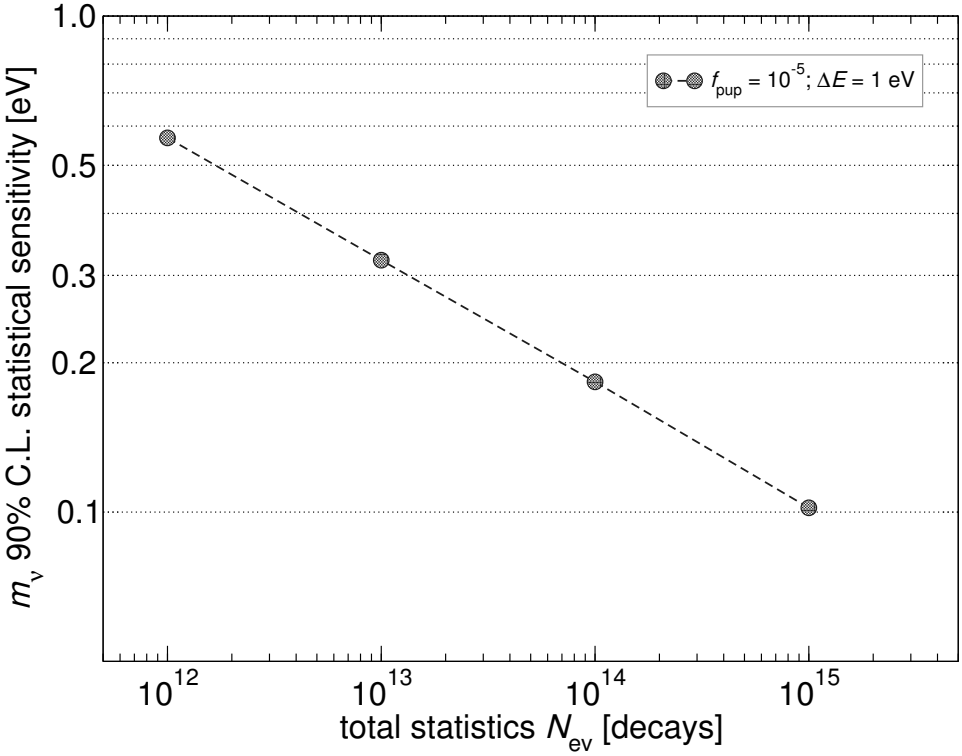

Figure 6.1 - Dependence of the sensitivity on the collected number of events

than JFETs and can operate at the same temperature as the detectors. Most importantly the existence of cryogenic multiplexing schemes makes possible to instrument the arrays with a practical number of wires.

Assuming that each pixel takes a space of about $1 \times 1\,\mathrm{mm}^2$, a 10000 pixel array would easily fit in a standard dilution refrigerator like the ones that are going to be used for the project MARE-1. Furthermore a new technology has being developed for SCUBA-2 which allows to have the multiplexer chip right under the array chip.

Considerations similar to the above ones are in principle valid for the Magnetic Micro-Calorimeters (MMCs) as well. In case of Kinetic Inductance Detector (KIDs) option, the possibility to multiplex looks even more straight forward.

The main technical challenge for the MARE project is then the realization of a single rhenium microcalorimeter based on the TES (baseline option), MMC or KID technique. The R&D for this purpose must start as soon as possible and will involve all the groups taking part to the MARE project, even if a specific working group will be in charge for each development. Efforts in this direction will profit also of the results of the MANU2 experiment. The Heidelberg group is already working on the development of large mass, high energy resolution and high speed MMCs with exciting results. The Wisconsin and NASA/GSFC groups are already involved in the realization of 1000 pixel TES arrays for the Constellation-X mission. They are also studying the feasibility of MMC arrays and the realization of SQUID multiplexers in collaboration with the NIST (Boulder, USA). The Rome, Cardiff and ITC-irst group is active on the development of KIDs for the study of the cosmic microwave background and will open a parallel research line to couple KIDs to metallic Rhenium absorbers.

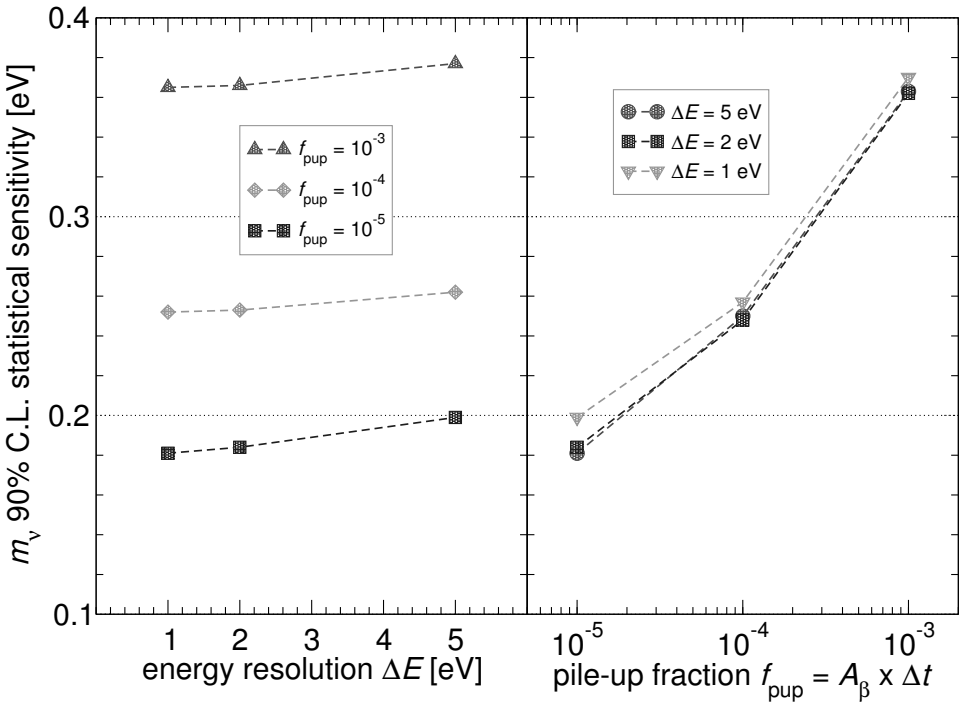

Figure 6.2 - Dependence of the sensitivity on the energy resolution and the pile-up fraction

6.2 The temporal profile of MARE-2

The scientific competitiveness of the MARE project requires that the target 0.2 eV neutrino mass limit is approached around year 2015. This means that data taking should start not later than 2011, which leaves about 5 years for the R&D. A shift of one or two years would probably not be dramatic.

Given the small size of a 10000 pixel array, the limited number of wires and the moderate refrigerator cooling power required it is conceivable that many such arrays can be disseminated in few dilution refrigerators. The approach could be that of designing a kind of modular 10000 pixel array *kit* which can be relatively easily installed in any available refrigerator. Figure 6.3 show the temporal evolution of the statistical sensitivity for one possible array deployment scheme: one 10000 array is deployed every year up to 5 arrays. The different curves are for 4 plausible detector characteristics. Of course the more groups participate installing one or more array *kits* the faster will be the approaching to the target limit.

6.3 TES for ^{187}Re calorimeters

A Transition Edge Sensor (TES), consisting of a metal, usually in the form of film, undergoes a sharp temperature phase transition from the superconducting to the normal state. Currently, it is the most sensitive thermistor widely used in advanced applications for Energy Dispersive X-ray Spectroscopy (EDXS) in the 0.1-10 keV band, single photon detection down to the Infrared light, atomic and molecular beam energy and mass spectroscopy, and cosmic microwave background sensitive measurements. TES behave as thermistors of composite microcalorimeters or

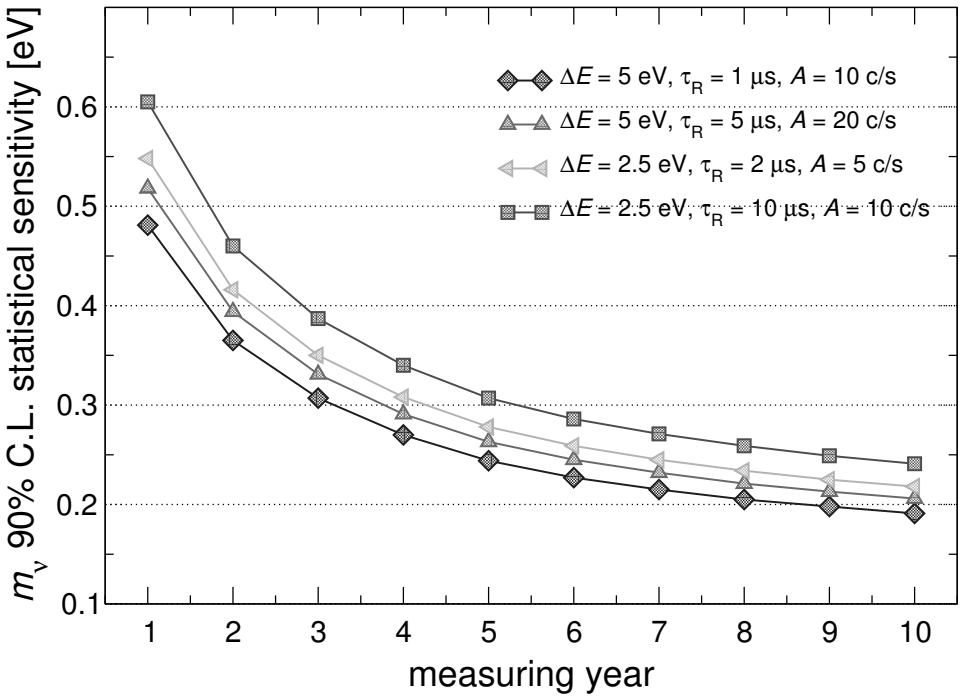

Figure 6.3 - Temporal evolution of the sensitivity to neutrino mass in MARE-2 experiment. Four different experimental configurations are considered.

bolometers. When the radiation energy is deposited in the detector, a prompt temperature rise occurs in the superconducting film, giving rise to a large change in film resistance which, usually, is sensed by a SQUID amplifier inductively coupled to the bias circuit. The superconducting film is usually represented by a simple variable resistor characterized by the dimensionless temperature coefficient, fully equivalent to the parameter A (logarithmic sensitivity) defined in § 4.3.2:

$$\alpha = \frac{dlogR}{dlogT} = \frac{TdR}{RdT} \tag{6.1}$$

α is an important merit parameter that influences the speed and the resolution of the calorimeter. If C is the detector heat capacity and G the thermal conductance to the heat sink:

the detector time constant τ=C/G, is decreased by a factor $(1+\ \alpha/\mathrm{n})^{-1}$, where n $(3\div5)$ is the logarithmic derivative of the bias power with respect to temperature T;

the intrinsic energy resolution $\Delta\mathrm{E}=2.36(\mathrm{kT^2C})^{1/2}$ improves by a factor of $1/\sqrt{(}\alpha)$.

Since practical values of α exceed easily 10^2, optimized TES detectors, working at temperatures around 100 mK, have attracted considerable attention for the extremely good energy resolutions. Values of $\Delta\mathrm{E}_{FWHM}$ of (2.37± 0.11) eV at 5.89 keV and (2.0± 0.1) eV at 1.49 keV have been reported with TES microcalorimeter.

The theory predicts resolution performances in the sub-eV range. In the last 20 years, a big effort is being made to achieve this goal. Presently, the major limitation to a further resolution improvement is the so called problem of the excess noise of the TES. Experiments have shown that the noise power spectrum of practical TESs, based on proximity bilayers, such as Ti/Au

and Mo/Au, is not completely described by the expected sum of Johnson noise, SQUID noise and phonon noise in the thermal link to the heat bath. It has been proposed that the thermal fluctuation noise (TFN) is responsible for the observed excesses.

Several attempts to model the TES behavior are on the way, for example using the two fluid model of superconductivity or adopting a modified Fermi function. However, the model outputs are not readily comparable to experimental transition data, due to the complexity of the system. Even in a perfectly uniform, impurity-free film, and neglecting edge effects, the TES performance must be expected to be a function of bias current, self-magnetic field, critical current, thermal diffusivity of the film, electrical and thermal coupling between film and substrate, film and absorber, as well as the intrinsic superconducting properties of thin films.

Considering the good results obtained by several groups that developed TES technology, and the promising resolution achieved in the first phase of MANU2, it is clear that one of the main streams of the the MARE experiment is the further TES investigation to improve their performance to the level required by the project.

As previously stated, the present an future challenge is the understanding of complex phenomenology of the phase transition of the TESs. This requires simultaneous experimental and theoretical investigations.

In what concerns the theoretical modelling, it is important to understand how parameters such as transition width R(T) and α(T) depend on the film properties and topology. As for example, create a model which provides the upper limit of the α parameter (current models provide a 10^5 limit, which has not been experimentally observed at all!). Vortex dynamics and normal region nucleation, for high biased current, that are considered by several groups one of the noise sources, is another key issue.

The optimization of the TES detector performance, must be directed in order to assure a high quality film, at the level predicted by realistic models. As MANU2 has demonstrated, the PLD provides an excellent tool that can be further improved, as for example, applying a new technique of fast pulsed laser (pulse duration of ten picoseconds, instead of the current ten nanoseconds). The application of this laser should solve the problem of particulate formation, since the target is no longer melt but sublimated on the spot. Further improvements of the film surface homogeneity can be achieved by implementing a rotative subtract holder. Finally, developing a method that starting for a rhenium single crystal, combines several techniques, such as micro-etching, micro-lithography and multilayers depositions, will allow the fabrication of several identical detectors in an integrated array.

The completion of the MANU2 project (the TES based section in MARE-1), extensively described in § 5.3 will provide a solid starting point for a breakthrough in the TES technology for the MARE-2 experiment.

6.4 Magnetic Micro-Calorimeters for ^{187}Re β spectroscopy

Particularly attractive possibilities are opened up by the development of novel calorimetric low-temperature detectors, based on magnetic calorimetry [148, 149]. In the following we will describe the principle of operation of such a device and we will discuss the targeted setup for a beta endpoint experiment. Furthermore we will outline the research that we indent to carry out to obtain necessary information for detailed planning, optimizing and designing a large scale beta end point experiment based on magnetic micro-calorimeters.

6.4.1 Principle of operation

A magnetic micro-calorimeter (MMC) consists of an absorber, suitable for the particles to detect, and a paramagnetic sensor exposed to a small magnetic field. The absorber and the sensor are in good thermal contact, and together they are weakly coupled to a thermal bath. If a particle is stopped in the absorber, its temperature rises. This leads to a change in magnetization of the sensor, which can be measured with very high sensitivity using a SQUID magnetometer. The change of magnetization δM depends on the total heat capacity C_{tot} of the calorimeter and is given by the relation

$$\delta M = \frac{\partial M}{\partial T}\delta T = \frac{\partial M}{\partial T}\frac{\delta E}{C_{\mathrm{tot}}} \tag{6.2}$$

Here δE denotes the energy deposited in the absorber. The detection scheme is shown in Figure 6.4.

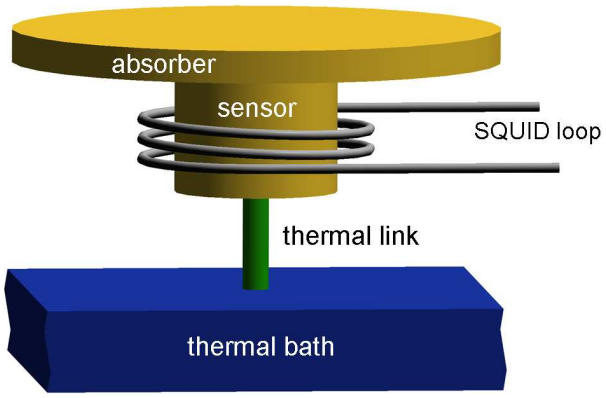

Figure 6.4 - Schematic of a magnetic micro-calorimeter.

State-of-the-art MMCs use localized paramagnetic ions in a metallic host as sensor material. A metallic host is important to obtain fast internal relaxation times. At the typical operational temperature of 50 mK the spin-electron relaxation times in materials suitable for MMC detectors are below 0.1 μs. Recently, MMCs optimized for x-ray detection have reached an energy resolution of 3.4 eV at 6 keV [150]. As an example we show in figure 6.5 the K_α-line of ^{55}Mn measured with an MMC detector.

An important advantage of MMC detectors is the fact that the paramagnetic sensor is a thermodynamic system whose response to a change in energy can be calculated provided the properties of the individual spins and the interactions among them are known. A thorough theoretical understanding of MMCs based on paramagnetic Au:Er alloys exists and they can be optimized for specific applications. The concept is sufficiently flexible to allow optimization of detectors for a wide range of energies with both small and large area absorbers. For measuring the beta endpoint spectrum of ^{187}Re we plan to develop a new type of MMC detector optimized for a superconducting absorber. To operate a large number of MMC detectors suitable multiplexing schemes will be developed.

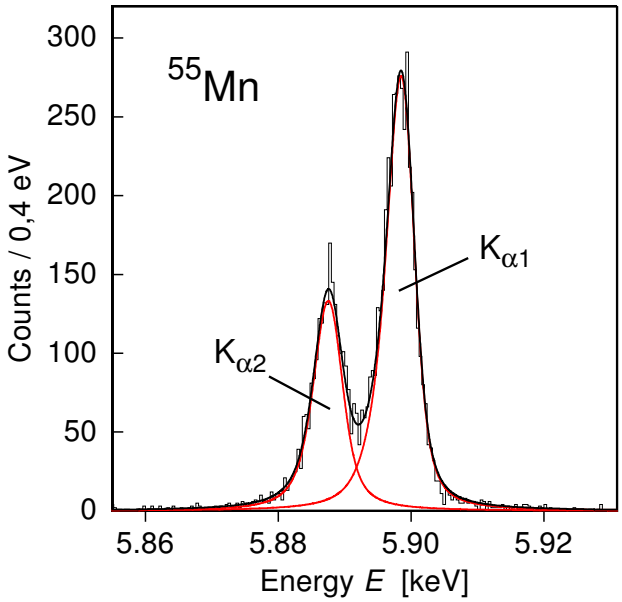

Figure 6.5 - K_α-line of ^{55}Mn as measured with a MMC detector. The solid line represents a fit of the data taking into account the natural linewidth as determined with a crystal spectrometer [151].

6.4.2 Detector physics

In order to carry out the beta endpoint experiment described above a new generation of detectors needs to be developed. Until recently, the typical MMC detectors consisted of small cylindrical sensors which were placed inside a superconducting loop and were operated in a small external magnetic field. Three different coupling schemes for such cylindrical sensors are shown in figure 6.6(a-c). These detectors were optimized for x-ray and gamma-ray detection.

For the proposed experiments we will develop MMC detectors with meander-shaped pick-up coil. One principle difference between meander coupling schemes shown in figure 6.6(d-f) and the schemes for disc like sensors shown in figure 6.6(a-c) is the fact that the meanders are not operated in a homogeneous external magnetic field. Instead, a persistent current I_0 is injected into the superconducting circuit of the flux transformer, e.g., by using a superconducting persistent current switch. The current I_0 produces a strongly inhomogeneous field around the meandering wire of the pickup loop within the volume of the sensor (see figure 6.7). Upon the deposition of energy δE in the sensor, its magnetic susceptibility decreases by $\delta\chi$, resulting in a change of inductance $\delta L \propto \delta\chi$ of the pickup coil and a change of flux $\delta\phi_s \propto \delta L \propto \delta E$ in the SQUID.

This setup is optimally suited for superconducting absorbers since the magnetic field associated with the current running in the meander-shaped coil vanishes exponentially in the direction perpendicular to the surface of the sensor. This means that the field at the position of the superconducting absorber can be kept rather small. In addition, as the bias field for the sensor is produced by the pickup coil itself, even sensor material outside the area enclosed by the pickup loop can contribute constructively to the flux signal in the coil. In this way the

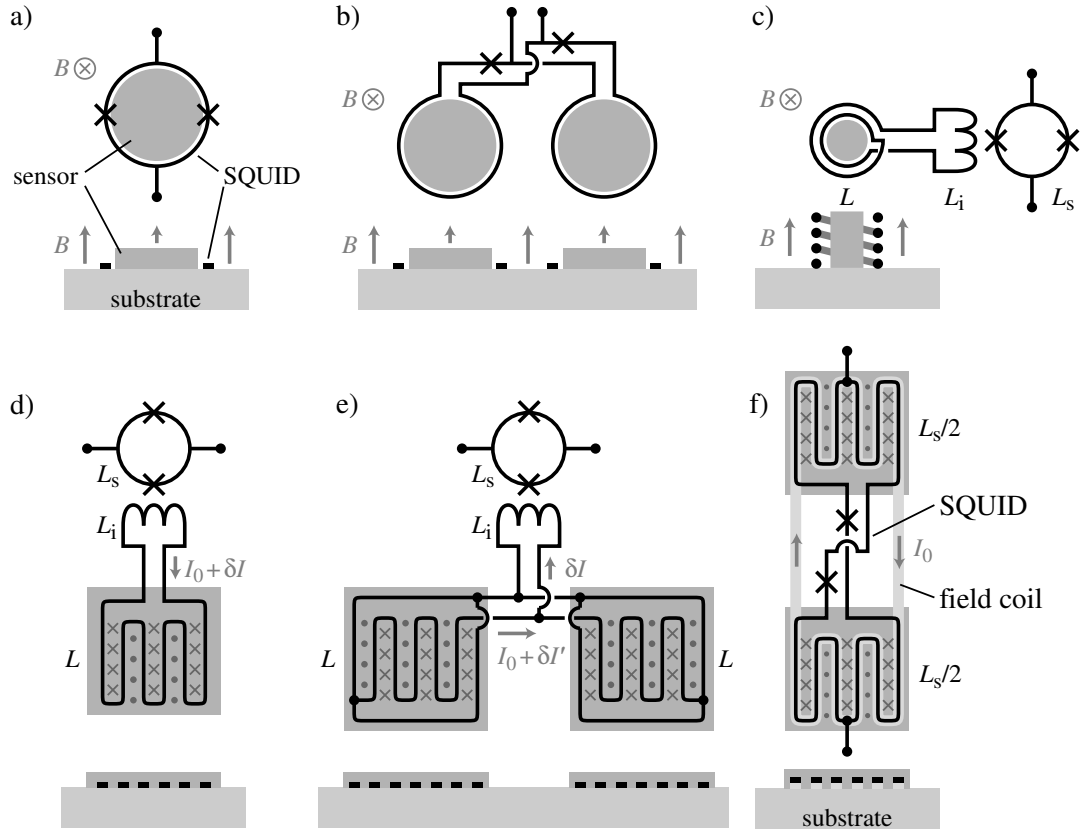

Figure 6.6 - Possible coupling schemes to measure the magnetization of paramagnetic sensors with a dc-SQUID. (a-c) assume a homogeneous external magnetic field B. In d) and e) a persistent current I_0 in the meandering superconducting wire of the pickup loop produces an inhomogeneous field in the volume of the sensor. In f) a persistent current I_0 flowing in a closed superconducting loop (light grey) underneath the SQUID loop generates an inhomogeneous magnetic field in the volume of the sensor.

sensor/coil configuration has a large filling factor.

This new type of MMC detector with meander-shaped pickup coil will be developed within the proposed project and will be optimized specifically for the detection of β-particles. The development of such detectors requires the study of fundamental aspects of potential sensor materials and to solve many challenging technical questions. Most importantly, we have to investigate the thermal and magnetic properties of thin paramagnetic films deposited by sputtering. A detailed understanding of these properties will be of crucial importance for the detector optimization. In addition, we have to study the noise spectrum produced by such thin film paramagnets. In bulk sensors we have observed a temperature independent $1/f$ noise component of unknown origin [150]. It will be very interesting to see whether such a noise component is also present in thin films. If this was the case we need to investigated this phenomenon carefully in order to minimize its impact on the detector performance by choosing a suitable detector design.

The main parameters characterizing a meander structure are: the width of the stripe w, the pitch p (center-to-center distance of two neighbor conductors), the area A covered by the meander the sensor and thickness h (see Fig. 6.7). It is useful to introduce the quantity $\xi = h/p$

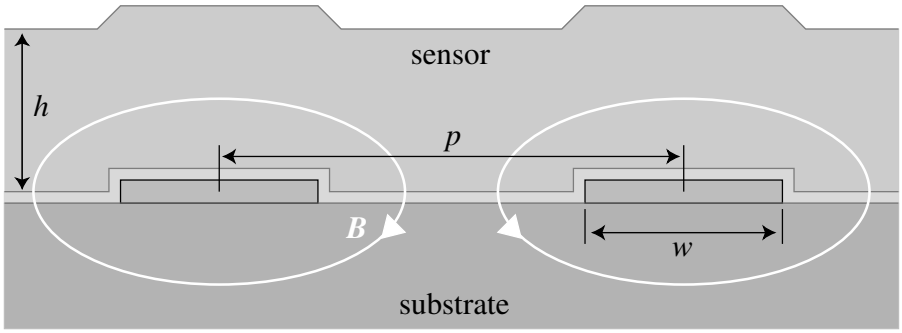

Figure 6.7 - Schematic of the cross section of the sensor and meander coil perpendicular to the current flow. The pitch p, the width of the stripes w and the height of the sensor h are indicated.

and w/p. In order to find the best parameters for the detector, the signal to SQUID noise ratio

$$\mathcal{S} = \frac{(\delta\Phi/\delta E)}{\sqrt{S_\Phi}} = \frac{\mu_0 A}{p}\sqrt{\frac{1}{L}}\frac{h}{C_\mathrm{a} + A\,h\,\langle c\rangle}\left\langle G\,\frac{\partial M}{\partial T}\right\rangle \ . \tag{6.3}$$

is the quantity to be optimized. Where L is the inductance of the meander, C_a the heat capacity of the absorber and c the specific heat of the sensor. The quantity G is a local coupling factor and is a function of the position inside the sensor. In general S depends on nine parameters:

$$\mathcal{S} = \mathcal{S}(C_\mathrm{a}, g, \alpha, T, x, \overline{B}, A, \xi, w/p) \ . \tag{6.4}$$

the first four parameters, the heat capacity of the absorber, the g-factor of the paramagnetic ions, the strength of the RKKY interaction α and the working temperature are fixed by the experimental conditions and by the choice of materials. The others, the concentration of ions x, the mean magnetic field and the geometrical parameter of the meander have to be chosen in order to maximize $\mathcal{S}$. The result of this optimization gives that the heat capacity of the sensor has to be the same as the heat capacity of the absorber, $\xi = 0.36$ and $w/p = 0.425$. The other quantities may be calculated by the knowledge of these [149].

Also very important is the realization of suitable flux transformers. The bias current necessary to operate the detectors in high resolution mode will be rather large and it is not trivial to produce superconducting coils that can carry this current and to inject it. First niobium thin film devices have been produced and tested, but we will have to study some more technical and fundamental questions in connection with this issue to achieve the large current densities for optimal detector performance.

In addition, the thermalization processes within the absorber have to be studied in order to design a large scale experiment. We will discuss this crucial point in a subsequent section. One other technical challenge is the realization of a readout for several hundred channels.

This can be done only by multiplexing large number of channels. Possible ways to do this without degradation of the signal are also discussed in a subsequent section. For this we need to develop suitable ways for a multiplexed readout, that does not degrade the detector performance. The search for such a readout scheme has to be based on the theoretical and experimental results obtained during the development and optimization of a single pixel detector.

6.4.3 Detector development

As discussed above we need to develop a new type of MMC detector for the experiments proposed here. The development will take place in several steps. In the first part of the project we need to study several fundamental questions regarding the solid state and detector physics. The best known candidate as sensor material is Au containing a few hundred ppm of Er. Therefore we will start our investigation by producing sputtered films of Au:Er and by investigating their properties in the relevant temperature range. Parallel to this we will work on fast superconducting persistent current switches which are needed for injecting a bias current into the flux transformers and superconducting thin film structures with high current density. In a second part we will investigate different meander coupling schemes and will produce the first round of micro-fabricated detectors. These detector will be produced and tested at the Kirchhoff-Institute of Physics (KIP).

What we will learn in the first phase studying single detectors will in part determine the development of multi channel detectors. We will start with a small number of detectors that principally can be read out directly. We will use these detectors to develop means of a multiplexed readout. The starting point here is to adopt concepts that already exist for micro-calorimeter arrays which are under development for x-ray astronomy.

6.4.4 Kirchhoff-Institute of Physics

The clean room facilities of the KIP include direct writing laser micro-lithography tools, wet and dry etching, thin film deposition techniques, like UHV sputtering and e-beam evaporation. State-of-the-art low-temperature laboratories are available for testing cryogenic detector devices. These laboratories are equipped with several dilution refrigerators (reaching temperatures below 10 mK), ADR cryostats (reaching temperatures below 25 mK) and a high precision SQUID magnetometer.

6.5 Multiplexed Kinetic Inductance Detectors (MKIDs) for ^{187}Re β spectroscopy

As demonstrated with extensive Montecarlo simulations (e.g. see § 6.1), the most challenging issue to be solved during the MARE-2 R&D is the realization of such a large number of channels ($> 10^4$). Moreover, the need for fast ($\sim \mu s$ scale) detectors gives an indication that the study should proceed in parallel between PMDs (e.g. TES, MMC) and pair-breaking detectors. While the final goals seem achievable pushing the "classical" multiplexing schemes to the limit, it is worth to start from the beginning a study and R&D in parallel to explore intrinsically multiplexable pair-breaking detectors like MKIDs [152]. In this case, starting from a promising read-out scheme, we will then optimise the single pixel design to achieve the required energy-time resolution performance. In principle, it is possible to multiplex up to $10^3 - 10^4$ channels on a single coaxial cable and with a single cold stage amplifier. A number of other imaging-like applications would be then be driven.

6.5.1 Principle of operation of MKIDs

The AC impedance of a superconductor strip kept well below T_c is largely dominated by an inductive term associated to the reaction of the superconductor itself to magnetic flux

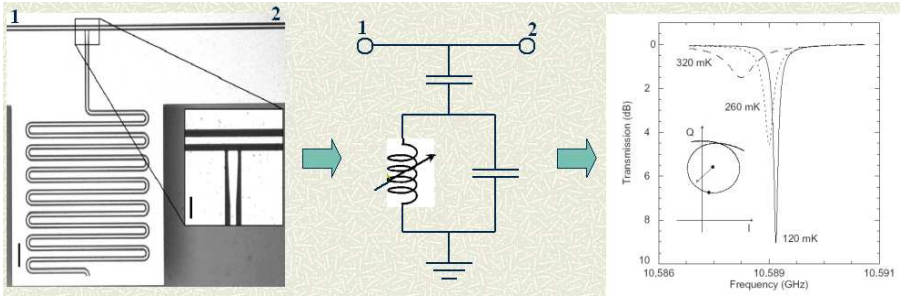

Figure 6.8 - Aluminium quarter-wave resonator physical layout, equivalent circuit and resonance shape (—S12— transmission coefficient) as a function of temperature. Credit: J. Zmuidzinas.

penetration. The penetration depth is only of the order of 50 nm, and the complex impedance is thus called "surface impedance":

$$Z_{sc} = R_{sc} + i\omega L_{sc} \tag{6.5}$$

where $R_{sc} \ll L_{sc}$ in case $T \ll T_c$. The energy of the external EM field is also stored in Cooper pairs that are accelerated in an effectively non-dissipative medium. By properly feeding power to the superconducting strip, both R_{sc} and L_{sc} are slightly changed in a way proportional to the number of quasi-particles produced (broken Cooper pairs). How to measure these small perturbations? An elegant approach has been proposed [153] and consists of making the superconductor strip part of a resonator circuit (e.g. quarter-wave LC resonator) and to let incident power change the resonator frequency. The quasi-particles then recombine with a characteristic, temperature-dependent, lifetime (τ_{qp}). The resonator frequency is inversely proportional to the length of the resonator strip, through a constant determined by the dielectric properties of the substrate. Instead of the actual resonator frequency, too difficult to measure, what is actually related to the incident power is a"phase pulse" at a given frequency coincident with the unperturbed resonance. In other words, the incident (or self-generated in case of a beta decay) power by temporary changing the number of quasi-particles, mimics a transitory temperature change. The quality factor Q of the resonator determines the ultimate sensitivity of the detector. Since the total phase change across the resonance is fixed, a higher Q implies also a higher sensitivity. The most fundamental noise is that associated with quasi-particle generation-recombination. The larger the quasi-particle lifetime is, the better is the energy resolution that can in principle be achieved:

$$NEP \propto \sqrt{\frac{N_{qp}}{\tau_{qp}}} \tag{6.6}$$

An excess phase noise, related to Two Levels Systems (TLS) at the substrate/metal interface is observed with a peculiar $f^{0.5}$ behaviour [155]. A stand-alone resonator is merely a "position-dependent" (fake) detector, and additional work is required to feed power in the proper way and to eliminate the position uncertainty. For example, it is possible to demonstrate that in the case of a quarter-wave resonator (see figure 6.8) the maximum sensitivity is achieved if power is dissipated at the grounded end of the strip [154]. Basically two different approaches have been proposed: quasi-optical absorbers and coupling with antennas. In the quasi-optical

absorbers case, the only interesting for the application we are studying in this proposal, quasi-particles are generated in another superconductor and directly transferred to the resonator through a metal-to-metal junction. The multiplexing, as shown in figure 6.9, is easily achieved by capacitively coupling a number of slightly different resonators to the same main line carrying enough power to excite them.

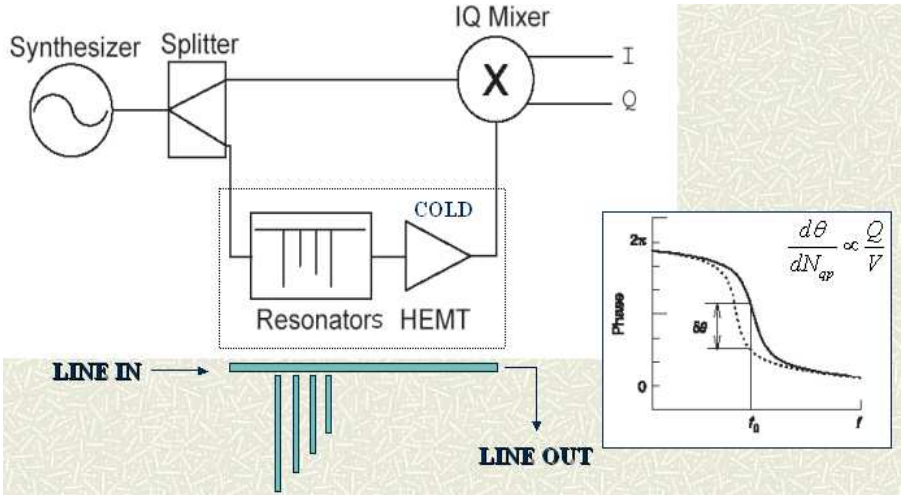

Figure 6.9 - Multiplexing scheme, read-out and phase change across the resonance. Different length resonators are coupled to the same line. A single cold HEMT (High Electron Mobility Transistor) is needed to read-out a large number of channels.

It is worth stressing again that the energy is basically not dissipated at all in the signal line or in the resonators (apart from the transient Ohmic resistance associated to the increasing in quasi-particles density). The output signal is largely determined by an inductance change causing a de-phasing.

6.5.2 MKIDs for a Rhenium experiment

The detector we intend to develop is made possible by the superconducting properties of metallic Rhenium. Following the scheme illustrated in the previous section, we plan to fabricate classical Aluminium (T_c=1.2 K) quarter-wave resonators and couple them with bulk Rhenium (T_c=1.7K) absorbers/emitters. The transition temperatures and hence the superconductors energy gaps are in the correct order, in the sense that Rhenium quasi-particles (originating from a contained beta decay) can be effectively transferred to Al resonators with negligible chance of feedback ($\Delta_{Re} > \Delta_{Al}$). The quasi-particle direction is thus correct: from the absorber to the resonator. As illustrated in figure 6.10, once a phonon is emitted in the resonator the quasi-particle does not have enough energy to return back to Rhenium. In case the gap difference is large enough (e.g. Ta absorber coupled to Al resonators) the emitted phonon can then generate further quasi-particles by breaking another Cooper pair directly in the resonator. This is not the case for a Re-Al device, resulting in a slightly decreased sensitivity. There are several other ways to increase the sensitivity if required (e.g. optimising the coupling design, minimizing the resonators film thickness), and this issue is not critical.

The study to design an optimally coupled Re-Al MKID will be the main subject of this R&D foreseen for MARE-2. Low noise Al and Nb resonators have already been fabricated

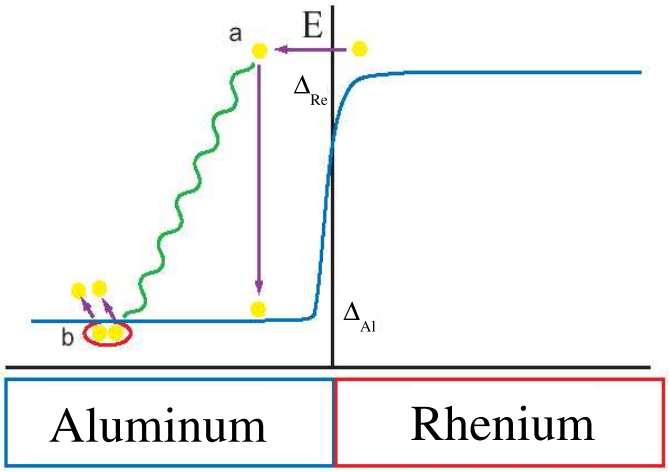

Figure 6.10 - A quasi-particles is generated in superconducting Rhenium as a result of a β decay. It diffuses into the Rhenium absorber to be then transferred into the Al resonator where a phonon is quickly emitted.

and tested by Caltech/JPL and SRON (Holland) mainly on Shappire substrates. The coupling of a bulk absorber (Rhenium) with a thin film (Aluminium resonator) will probably be the biggest problem as far as the detector itself is concerned. To enhance the metal-to-metal contact, a thin rhenium film could be first sputtered to ensure a high-quality Al-Re interface. The metallurgy details are still to be fixed and will result from the preliminary study. The quasi-particle lifetime in Rhenium is, as already discussed in this proposal, large enough to ensure a small generation/recombination noise. We will explore the possibility to preliminarily fabricate Rhenium resonators in order to study in detail the superconducting properties like the quasiparticles lifetime [153].

6.5.3 Detector development and technology at ITC-irst

The development of MKIDs detectors for radio-frequency photons detection is ongoing at ITC-irst in collaboration with INFN Roma-Perugia and AIG Cardiff. The final goal for that application is to couple Al resonators to Niobium planar antennas. In this sense, the resonators R&D would be common, and adapting the design to the Rhenium experiment would only require a detailed study of the absorbers/resonator coupling. The first prototype resonators, including trenches to minimize TLS-induced noise, have been fabricated in 2006 and is shown in figure 6.11. The process started from a 2 masks layout. We are designing now the multi-mask layout including the Niobium antenna.

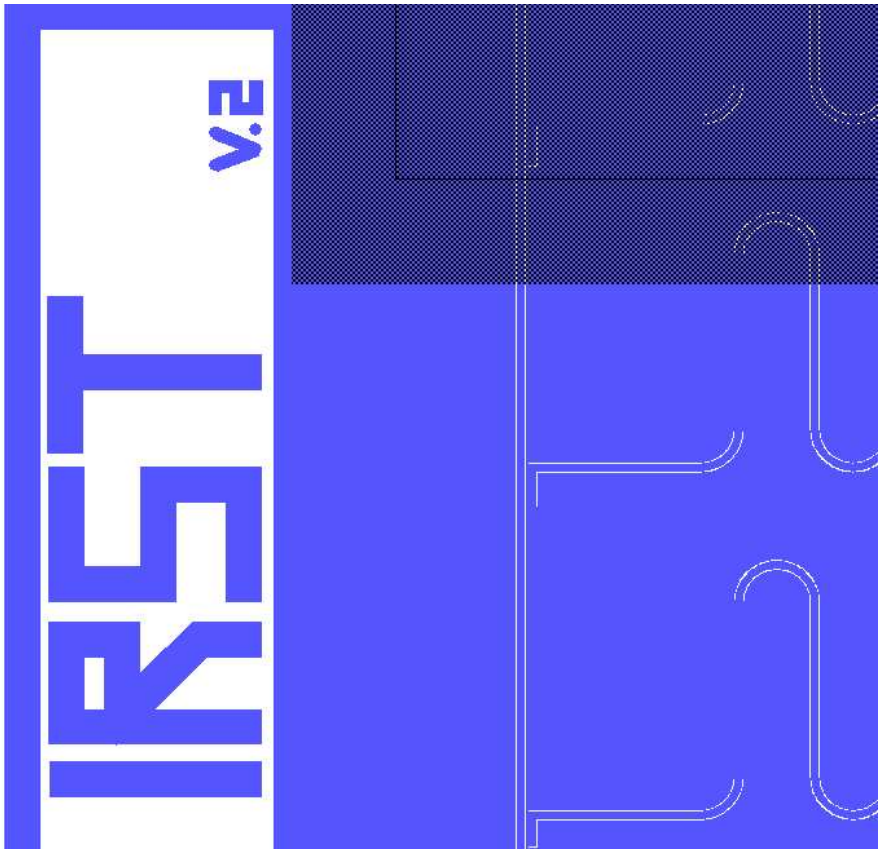

Figure 6.11 - Prototype resonators design with elbow coupling to the signal line.

Chapter 7

Structure of the collaboration, schedule and costs

7.1 Collaboration

The MARE Project will be carried out by the MARE collaboration, consisting of university and national laboratory groups listed below with a general indication of the main corresponding tasks.

- *University of Cardiff, UK* Development and optimization of kinetic inductance sensors (MARE-2).
- *University of Genova and INFN-Genova, Italy* Development of TES-based arrays for MARE-1; transformer read-out for TES; Research and Development for TES (MARE-2); data analysis and simulation.
- *Goddard Space Flight Center, NASA, Maryland, USA* Research and Development for TES (MARE-2); SQUID-based readout and multiplexing for MARE-2.
- *University of Heidelberg - Kirchhoff Institute of Physics* Development of magnetic microcalorimeters (MARE-2); SQUID-based readout and multiplexing for MARE-2.
- *University of Insubria (Como) and INFN-Milano, Italy* Data acquisition; temperature sensor characterization and development of microcalorimeter prototypes; Research and Development on single pixel for MARE-2.
- *University of Milano-Bicocca and INFN-Milano, Italy* Development of semiconductor-thermistor-based arrays for MARE-1; conventional electronics; data analysis and simulation; Research and Development on single pixel for MARE-2.
- *University of Roma "La Sapienza" and INFN-ROMA1, Italy* Development and optimization of kinetic inductance sensors (MARE-2).
- *ITC-irst, Trento, Italy* Development of Si implanted sensors for MARE-1 and of kinetic inductance sensors for MARE-2; elements of conventional electronics.
- *University of Wisconsin, Madison, USA* Development of arrays of semiconductor thermistors (MARE-1); simulation and analysis of detector performance; Research and Development on single pixel for MARE-2.

7.2 Organization and management

The organization and management of MARE will present different features in the first phase of the experiment (MARE-1 and MARE-2 R&D) with respect to the second phase (implementation and running of MARE-2).

In the first phase, MARE will consist of eleven working groups, listed below with the corresponding tasks, with rather independent objectives and funding sources. The two main goals of the first phase are the performance of a preliminary neutrino mass experiment with 2 eV sensitivity (crucial for the study of the sistematics of the second phase) and the definition of the technology for the second phase.

The second phase will have a unitary goal consisting of the implementation and the running of a neutrino mass experiment with a sensitivity of the order of 0.2 eV. The organization and management will change consequently, since the primary tasks will be the construction, installation and running of the experiment according to the technology defined in the first phase.

The first-phase MARE organization chart is shown in figure 7.1. The *spokesperson* is

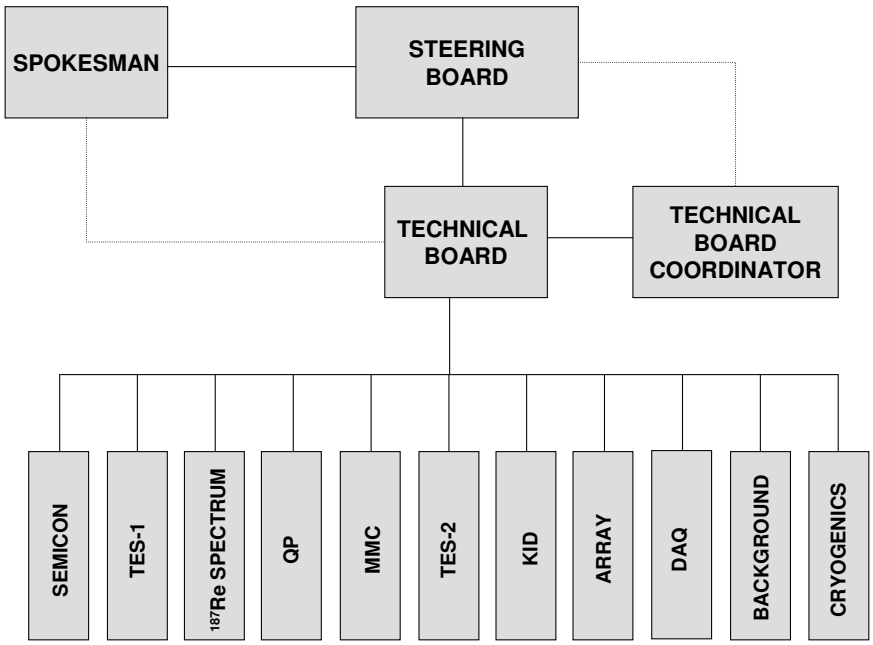

Figure 7.1 - Organization chart of MARE

responsible for the scientific success of the experiment and develops the scientific strategies and scope of the research.

The *technical board* will be coordinated by the *technical-board coordinator* and will include the leaders of all the working groups. The primary responsibility of the board will be to examine

the status of all working group activities and address issues which cross activity boundaries. Meetings will be called at the discretion of the coordinator and minutes will be made available to the steering board and to all the collaboration. In the second phase, the technical board will change its features, and will move from a sort of forum where the different technologies are critically compared to a committee responsible for the planning, construction and execution of the experiment. It will be chaired by a *project manager*.

The *steering board* includes the spokesperson, the technical-board coordinator (the project manager in the second phase) and representatives from the institutions collaborating to MARE. It monitors and reviews the activities of the MARE experiment and takes care of science, funding, proposal upgrade and image of MARE in the scientific community. It will be the "driving force" towards a second generation neutrino mass experiment, and will define the technology to be used for the second phase on the basis of the results achieved in the R&D activity and of the preliminary experiment on the neutrino mass.

The *project manager* will be responsible for the technical and operation aspects of the experiment and the management of the schedule and budget. As such, he or she must develop and maintain the project management plan, and manage all the construction, installation, and related operational activities. He or she develops and tracks the schedule for the project, ensuring that milestones are met, and the budget for the project, as outlined by the financial plan. Finally, it is also the responsibility of the project manager to provide reports summarizing the progress of the project to the spokesperson and the steering board.

All work required for the successful completion of MARE will be organized into a work breakdown structure, that will consist of eleven *working groups*:

- TES-1 WG: TES calorimeter medium size array (MARE-1). Development of a few hundred channel TES based array with a neutrino mass sensistivity around 2 eV.
- SEMICON WG: Semiconductor calorimeter medium size array (MARE-1). Development of a few hundred channel semiconductor based array with a neutrino mass sensistivity around 2 eV.
- ^{187}Re SPECTRUM WG: Experimental ^{187}Re beta decay spectrum analysis (MARE-1 and 2 R&D). Study of systematics, BEFS, detector response, theoretical spectral shape, other second order effects using MARE-1 results.
- QP WG: Physics of superconducting absorbers (MARE-2 R&D). Study of quasiparticles lifetimes in superconducting rhenium.
- MMC WG: MMC single element (MARE-2 R&D). Development of a MMC single element for MARE-2 with Re absorber.
- TES-2 WG: TES single element (MARE-2 R&D). Development of a TES single element for MARE-2 with Re absorber.
- KID WG: KID single element (MARE-2 R&D). Development of a KID single element for MARE-2 with Re absorber.
- ARRAY WG: MARE-2 arrayization (MARE-2 R&D). Large array development; SQUID based multiplexing schemes development.
- DAQ WG: DAQ (MARE-1 and 2 R&D). Large array data acquisition development.

- BACKGROUD WG: Background (MARE-1 and 2 R&D). Low energy background study in small detectors at sea level. Active and passive reduction techniques study.

- CRYOGENICS WG: Cryogenics for large arrays (MARE-2 R&D). Study of cryogenic systems suitable for large arrays.

The working group structure will be re-organized when moving from the R&D for the MARE-2 to construction and full operation in MARE-2.

7.3 Schedule

The schedule of MARE (fig. 7.2) consists of two overlapping plans, one for MARE-1 and another one for the R&D of MARE-2. In order to provide more details, a detail of the schedule of MARE-1 referring to the semiconductor thermistor section is provided in figure 7.3. An analogous schedules for the TES option is not necessary because full data taking is closer in this case. Data taking for MARE-1 is expected to start in 2006, while that for MARE-2 in 2011 after 4 full years of R&D activity and 1 year for the preparation of the first 10000 detector *kit*.

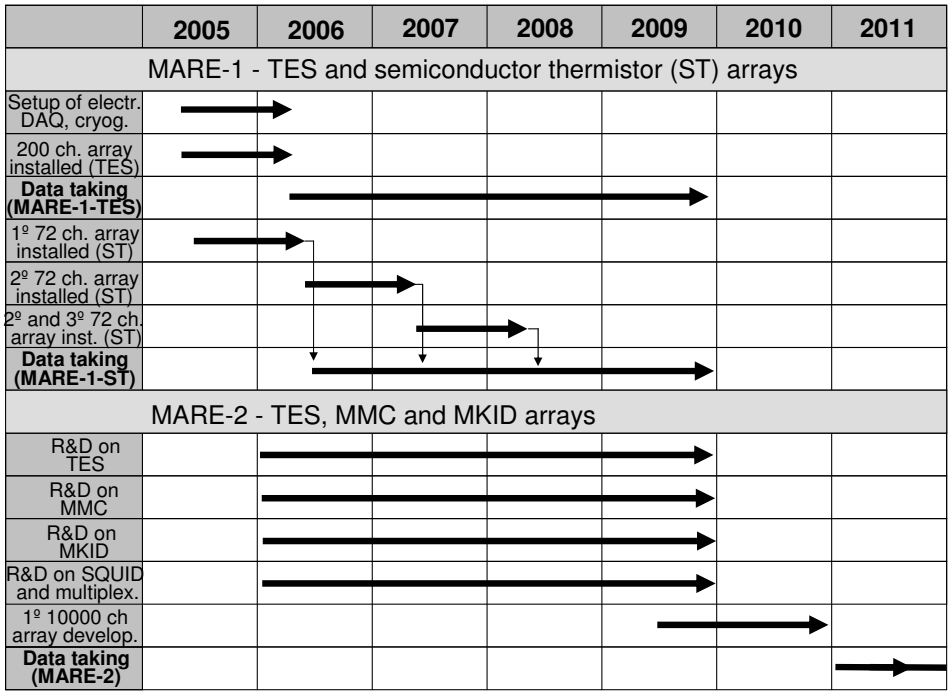

Figure 7.2 - General schedule of MARE

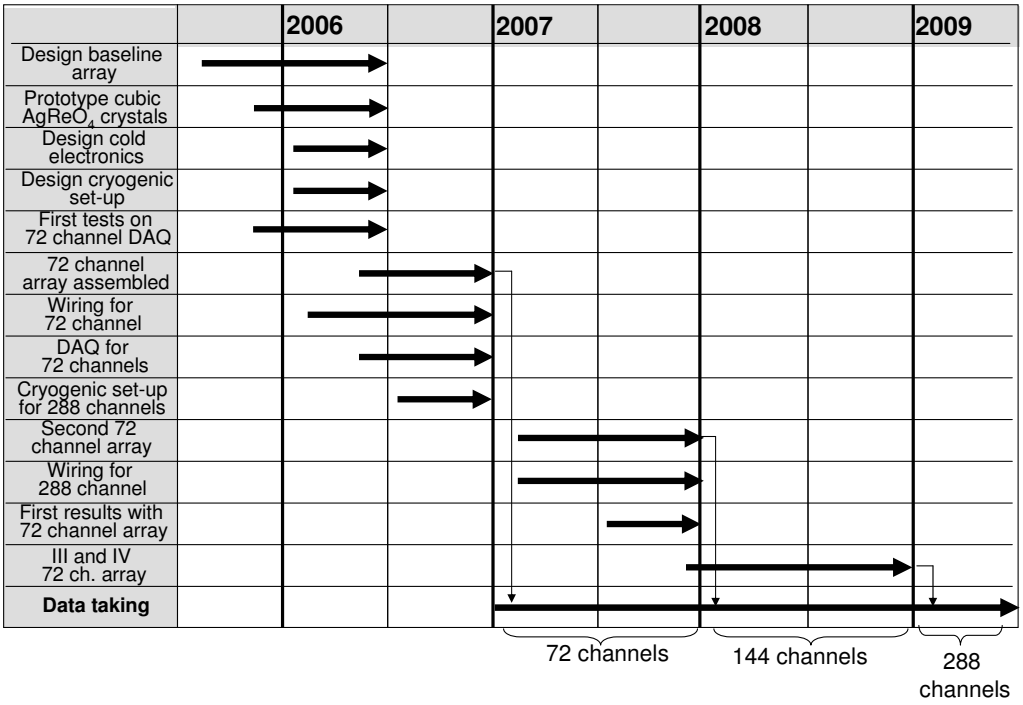

Figure 7.3 - Schedule of MARE-1 - Semiconductor thermistor arrays

7.4 Cost statement

A provisional plan of costs is reported in fig. 7.4. The costs for MARE-1 are reasonably well defined. On the other hand, the definition of the cost for the R&D of MARE-2, together with the total cost of the experiment, will be improved in the next versions of this document and will depend strongly on the sensor technology that will be selected after the R&D phase. The chosen technology affect relevantly also the cost of the read-out electronics. We can anticipate that, while MARE-1 will be mainly supported by INFN (with however not negligible contribution from the American, German and British institutions for the R&D parts), the success of MARE-2 presupposes an important financial involvement of all the parties.

	2006	2007	2008	2009	2010	TOTAL
MARE-1 - Arrays with transition edge sensors						
Liquid helium for running experiments	35000	40000	40000	40000	40000	
Data taking miscellaneuos	15000	15000	15000	15000	15000	
MARE-1 - Arrays with semiconductor thermistors						
Liquid helium for running experiment	20000	40000	40000	40000	40000	
AgReO4 crystals	25000					
Electronics	60000	75000	40000			
Data acquisition	40000	80000	80000			
Sub-total MARE-1	195000	250000	215000	95000	95000	850000
MARE-2 R&D						
Liquid helium for R&D	50000	50000	50000	50000		
Sensor production and electronics	20000	30000	30000	20000		
MARE-2 First arrays (10000 channels)						
Helium for running experiment					50000	
Re crystals				500000		
Sensors				200000		
Electronics and DAQ				250000	250000	
Sub-total MARE-2	70000	80000	80000	1020000	300000	1550000
Contingency (20%)	53000	66000	59000	223000	79000	480000
GRAND TOTAL	318000	396000	354000	1338000	474000	**2880000**

Figure 7.4 - Provisional financial plan of MARE (in EURO)

Bibliography

[1] V. A. Lubimov et al., *An estimate of the ν_e mass from the β-spectrum of tritium in the valine molucule*, Phys. Lett. **94B** (1980) 266.

[2] H. Kawakami et al., *New upper bound on the electron anti-neutrino mass*, Phys. Lett. **B256** (1991) 105.

[3] R. G. H. Robertson et al., *Limit on $\overline{\nu}_e$ mass from observation of β decay of molecular tritium*, Phys. Rev. Lett. **67** (1991) 957.

[4] E. Holzschuh, *Measurement of electron neutrino mass from tritium β-decay*, Phys. Lett. **B287** (1992) 381.

[5] W. Stoeffl et al., *Anomalous structure in the beta decay of gaseous molecular tritium*, Phys. Rev. Lett. **75** (1995) 3237.

[6] V. Lobashev, et al., *Nucl.Phys. B Proc. Suppl.*, **91** (2001) 280.

[7] J. Bonn, et al., *Nucl.Phys. B Proc. Suppl.*, **91** (2001) 273.

[8] S.B. Kaplan et al., Phys. Rev B **14**, 4854 (1976)

[9] A.G. Kozorezov et al., Phys. Rev. B **61** 11807 (2000)

[10] E. Cosulich et al., J. Low Temp. Phys. **93**, 263 (1993)

[11] first Dan's proposal for a LT calorimetric neutrino mass experiment

[12] S.Vitale et al., Proceedings of the International School of Physics of Exotic Atoms, Erice 1984, published in Fundamental Interaction in Low-Energy Systems, Edited by P.Delpiaz, G.Fiorentini, and G Torelli,(1985) p 429.

[13] S.Vitale et al., INFN Internal Report, INFN/BE-85/2, July 10, 1985.

[14] R.L. Brodzinski and D.C. Conway, Phys. Rev. 138, 6B (1965)

[15] E.Huster and H. Verbeek, Zeit. fur Phys. 203, 435 (1967)

[16] F.Gatti, PhD Thesys, University of Genoa, 1992.

[17] E.Cosulich, et al. Phys. Lett. B 295 (1992), 143.

[18] D. Twerenbold, *Rep. Prog. Phys.* **59** (1996) 349

[19] N. Booth, B. Cabrera and E. Fiorini, *Ann. Rev. Nucl. Sci.* **46** (1996) 471

[20] D. McCammon et al., *Nucl. Phys.* **A257** (1991) 821

[21] J. Zhang et al., *Phys. Rev.* **B57** (1998) 4472

[22] S.H. Moseley, J.C. Mather and D. McCammon, *J. Appl. Phys.* **56** (1984) 1257

[23] D. McCammon et al., proceedings of *Low Temperature Detectors for Neutrinos and Dark Matter III*, ed. L. Brogiato, D.V. Camin and E. Fiorini, Editions Frontières, Gif sur Yvette Cedex (France), 1990. Pag. 213

[24] A. Alessandrello, et al., *J. Phys. D: Appl. Phys.*, **32**, (1999) 3099.

[25] M. Sisti et al., *New limits from the Milano neutrino mass experiment with thermal microcalorimeters*, these proceedings.

[26] A. Alessandrello et al., Nucl. Instrum. and Meth. B 142 (1998) 163.

[27] J. Bonn, et al., *Nucl.Phys. B Proc. Suppl.*, **91** (2001) 273.
V. Lobashev, et al., *Nucl.Phys. B Proc. Suppl.*, **91** (2001) 280.

[28] M. Sisti et al., *Radioactive background reduction in the Milano neutrino mass experiment*, these proceedings.

[29] M. Sisti et al., *Data acquisition and analysis for the Milano neutrino mass experiment*, these proceedings.

[30] A. Nucciotti et al., *The cryogenic fluorescence source...*, these proceedings.

[31] A. Nucciotti et al., *How to improve...*, these proceedings.

[32] W. Bühring, Nucl. Phys. 61 (1965) 190; private communication by prof. Bühring (1999).

[33] S. Vitale, INFN Internal Report, INFN/BE-85/2, Genova 1985.

[34] G. Pessina et. al, these proceedings.

[35] Dan's paper in book on LT detectors

[36] D.V.Camin e G.Pessina DIFFERENTIAL OPTOCOUPLER AMPLIFIER WITH LOW NOISE, LOW POWER AND BALANCED OUTPUT IEEE Transaction in Nuclear Science, V.47, p.2039-2044, 2000.

[37] Claudio Arnaboldi, Giuliano Boella, Emanuele Panzeri, Gianluigi Pessina JFET TRANSISTORS FOR LOW NOISE APPLICATIONS AT LOW FREQUENCY IEEE Transaction on Nuclear Science, Vol. 51, pp. 2975-2982, 2004.

[38] A.Alessandrello, C.Brofferio, O.Cremonesi, A.Giuliani, A.Monfardini, A.Nucciotti, M.Pavan, G.Pessina, S.Pirro, E.Previtali. A FRONT-END FOR AN ARRAY OF MICROBOLOMETERS FOR THE STUDY OF THE NEUTRINO MASS IEEE Transaction in Nuclear Science, V.47, p.1851-1856, 2000.

[39] M.Malatesta, M.Perego e G.Pessina, A LINEAR OPTICAL COUPLER FRO CRYOGENIC DETECTORS Nuclear Instruments and Methods in Physics Research, Vol. 444A, p. 140-142, 2000.

[40] Claudio Arnaboldi and Gianluigi Pessina A VERY SIMPLE BASE LINE RESTORER FOR NUCLEAR APPLICATIONS Nuclear Instruments and Methods in Physics Researc A, vol. A512, p.129-135, 2003.

[41] G.Pessina, A LOW NOISE, LOW DRIFT, HIGH PRECISION LINEAR BIPOLAR (+/-10V) VOLTAGE SUPPLY REFERENCE FOR CRYOGENIC FRONT-END APPARATUS The Review of Scientific Instruments, Vol. 70, p.3473-3478, 1999.

[42] SKUDOTECH is a Registered trademark by SELITE, Milano, Italy.

[43] C.Arnaboldi, C.Bucci, S.Capelli, A.Fascilla, P.Gorla, A.Nucciotti, M.Pedretti, G.Pessina, S.Pirro, E.Previtali, M.Sisti THE FRONT-END READOUT FOR CUORICINO, AN ARRAY OF MACRO-BOLOMETERS AND MIBETA, AN ARRAY OF m-BOLOMETERS Nuclear Instruments and Methods in Physics Researc A, vol. A520, pp 578-580, 2004.

[44] C. Arnaboldi et al., Physical Review Letters 95, 142501 (2005)

[45] CUORE: A CRYOGENIC UNDERGROUND OBSERVATORY FOR RARE EVENTS: proposal available at crio.mib.infn.it/wig/Cuorepage/CUORE-proposal.pdf

[46] ICS-145 Analog to Digital Converter board, Interactive Circuits and Systems ltd.

[47] E. Gatti e P. F. Manfredi, *Processing the signals from solid-state detectors in elementary-particle physics*, Nuovo Cimento **9** (1986) 1.

[48] Egle Lisiero: "Misura del flusso di raggi cosmici all'interno del laboratorio di criogenia", graduate thesis of Milano-Bicocca University, 14 October 2004.

[49] Cecilia Maiano: "Schermature di rivelatori al germanio al livello del mare", graduate thesis of Milano-Bicocca University, 13 December 2004.

[50] The KATRIN collaboration, *KATRIN: A next generation tritium beta decay experiment with sub-eV sensitivity for the electron neutrino mass*, hep-ex/0109033.

[51] A. Nucciotti, et al., in *Proceedings of the 17th International Workshop on Weak Interactions and Neutrinos WIN99*, ed. C. A. Dominguez e R. D. Vollier (World Scientific, Singapore, 2000), p. 170.

[52] A. Nucciotti, et al., *Nucl. Instr. and Meth. A*, **444**, (2000) 77.

[53] A. Alessandrello, et al., *Nucl. Instr. and Meth. A*, **412**, (1998) 454.

[54] A. Alessandrello, et al., *Nucl. Instr. and Meth. B*, **142**, (1998) 163.

[55] A. Alessandrello, et al., *Phys. Lett. B*, **457**, (1999) 253.

[56] A. Nucciotti, et al., in *Proceedings of the Ninth International Workshop on Low Temperature Detectors LTD-9*, ed. F. Scott Porter, D. McCammon, M. Galeazzi, C. K. Stahle (AIP, New York, 2002), p. 453.

[57] Submitted to *Phys. Rev. Lett.*, hep-ex/0302006

[58] O. Alard, et al., *Earth and Planet. Sci. Lett.*, **203** (2002) 651, and references therein.

[59] See for instance S.N. Ahmed et al.*Phys. Rev. Lett.* **92** (2004) 181301 and references therein

[60] V.M. Lobashov,*Nucl. Phys.* A **719** (2003) 153 and references therein

[61] S.E. Koonin, *Nature* **354** (1991) 468.

[62] about 17 keV neutrino

[63] about 17 keV neutrino as well

[64] F. Gatti et al., *Nature* **397** (1999) 137.

[65] C. Arnaboldi et al., *Phys. Rev. Lett.* **91** (2003) 161802.

[66] For a recent review on cryogenic detectors see e.g. "Proceedings of the Tenth International Workshop on Low Temperature Detectors LTD–10", ed. F. Gatti, *Nucl. Instrum. Methods* A **520** (2004)

[67] R.D. Williams et al., *ApJ* **281** (1984) 363.

[68] M. Sisti et al., *Nucl. Instrum. Methods* A **520** (2004) 125.

[69] C. Arnaboldi et al., *Phys. Lett.* B (2004,to be submitted)

[70] G. Benedek et al., *Nucl. Instrum. Methods* A **426** (1999) 147.

[71] P.A. Lee et al., *Phys. Rev.* B **11** (1975) 2795.

[72] A.G. McKale et al., *J. Am. Chem. Soc.* **110** (1988) 3763.

[73] B.K. Teo and P.A. Lee, *J. Am. Chem. Soc.* **101** (1979) 2815.

[74] J. Spitaler et al., *Phys. Rev.* B **67** (2003) 115127.

[75] C. Arnaboldi et al. *Phys. Rev. Lett.* **96** (2006) 042503.

[76] A. Nucciotti et al., *Nucl. Instrum. Methods* A **520** (2004) 148.

[77] E. Holzschuh, *Neutrino mass from tritium β-decay*, Rep. Prog. Phys. **55** (1992) 1035-1091.

[78] G. Steigman, *Neutrinos, cosmology, and Dark Matters*, Nucl. Phys. (Proc. Suppl) **31** (1993) 343.

[79] C. S. Wu e S. A. Moszkowski, *Beta decay*, Wiley-Interscience, New York, 1966.

[80] R. G. H. Robertson e D. A. Knapp, *Direct measurements of neutrino mass*, Ann. Rev. Nucl. Part. Sci. **38** (1988) 185-215.

[81] E. W. Otten, *Direct neutrino mass measurements*, Nucl. Phys. **B38** (Proc. Suppl.) (1995) 26-35.

[82] H. Behrens e J. Jänecke, Numerical tables for beta-decay and electron capture, Landolt-Börnstein, Vol. 4, Springer-Verlag, Berlino (1969).

[83] R. L. Brodzinski e D. C. Conway, *Decay of Rhenium-187*, Phys. Rev. **138** (1965) 1368.

[84] K. Bergkvist, *A high-luminosity, high-resolution study of the end-point behaviour of the tritium β-spectrum* (I), Nucl. Phys. **B39** (1972) 317.

[85] K. Bergkvist, *A high-luminosity, high-resolution study of the end-point behaviour of the tritium β-spectrum* (II), Nucl. Phys. **B39** (1972) 371.

[86] K. Bergkvist, *On some atomic effects in the tritium β-spectrum*, Physica Scripta **4** (1971) 23.

[87] C. L. Bennett et al., *The X-ray spectrum following ^{163}Ho M electron capture*, Phys. Lett. **107B** (1981) 19.

[88] A. Rújula, *A new way to measure neutrino masses*, Nucl. Phys. **B188** (1981) 414-458.

[89] W. Bambynek et al., *Orbital electron capture by the nucleus*, Rev. Mod. Phys. **49** (1977) 77-221.

[90] A. De Rújula e M. Lusignoli, *Calorimetric measurements of ^{163}Holmium decay as tools to determine the electron neutrino mass*, Phys. Lett. **118B** (1982) 429.

[91] F. X. Hartmann e R. A. Naumann, *Observation of N and M orbital-electron capture in the decay of ^{163}Ho*, Phys. Rev. **C31** (1985) 1594.

[92] P. A. Baisden et al., *Measurement of the half-life of ^{163}Ho*, Phys. Rev. **28C** (1983) 337.

[93] K. Riisager et al., *The Internal Bremsstrahlung spectra from the EC beta decay of ^{193}Pt and ^{163}Ho*, Physica Scripta **31** (1985) 321.

[94] S. Yasumi et al., *The mass of the electron neutrino using electron capture in ^{163}Ho*, Phys. Lett. **B181** (1986) 169.

[95] P. T. Springer et al., *Measurement of the neutrino mass using the inner bremsstrahlung emitted in the elettron-capture decay of ^{163}Ho*, Phys. Rev. **A35** (1987) 679.

[96] F. Gatti, *Studio della m_ν attraverso tecniche bolometriche con il ^{187}Re*, Tesi di dottorato, Università di Genova, 1992.

[97] E. Cosulich et al., *Detection of ^{187}Re beta decay with a cryogenic microcalorimeter. Preliminary results*, Phys. Lett. **B295** (1992) 143.

[98] E. Cosulich et al., *The β-decay of ^{187}Re studied with a cryogenic μ-calorimeter*, Nucl. Phys. **A592** (1995) 59.

[99] J. J. Simpson, *Measurement of the β-energy spectrum of ^{3}H to determine the antineutrino mass*, Phys. Rev. **D23** (1981) 649.

[100] S. H. Moseley, J. C. Mather e D. McCammon, *Thermal detectors as x-ray spectrometers*, J. Appl. Phys. **56**(5) (1984) 1257.

[101] E. Fiorini e T. O. Niinikoski, *Low-temperature calorimetry for rare decays*, Nucl. Instr. and Meth. **224** (1984) 83.

[102] G. L. Knoll, *Radiation detection and measurement*, Wiley & Sons, New York (1989).

[103] Proceedings della conferenza "Fifth International Workshop on Low Temperature Detectors LTD-5", University of California at Berkley, 29 Luglio-3 Agosto 1993, pubblicati in J. Low. Temp. Phys. **93** (1993) 185-858.

[104] Proceedings della conferenza "Sixth International Workshop on Low Temperature Detectors LTD-6", Beatenberg/Interlaken, Svizzera, 28 Agosto-1 Settembre 1995, saranno pubblicati in Nucl. Instr. and Meth. **A**.

[105] A. Giuliani e S. Sanguinetti, *Phonon-mediated particle detectors: physics and materials*, Material Science and Engineering **R11** (1993) 1-52.

[106] N. F. Mott e J. H. Davies, *Metal-insulator transition in doped semiconductors*, Phil. Mag. **B42** (1980) 845.

[107] H. Fritzsche, *Effect of compensation on conduction near the metal non-metal transition*, Phil. Mag. **B42** (1980) 835.

[108] R. M. Hill, Phil. Mag. **24** (1971) 1307.

[109] N. Wang, F. C. Wellstood, B. Sadoulet, E. E. Haller e J. Beeman, *Electrical and thermal properties of neutron-transmutation-doped Ge at 20 mK*, Phys. Rev. **B41** (1990) 3761.

[110] M. Lakner e H. v. Löhneysen, *Localized versus intinerant electrons at the Metal-Insulator transition in Si:P*, Phys. Rev. Lett. **63** (1989) 648.

[111] B. I. Shklovskii e A. L. Efros, *Electronic properties of doped semiconductors*, Springer-Verlag, Berlino (1984).

[112] R. C. Jones, *The general theory of bolometer performance*, J. Opt. Soc. Am. **43** (1952) 1.

[113] J. C. Mather, *Bolometer noise: nonequilibrium theory*, Appl. Opt. **21**(6) (1982) 1125.

[114] J. C. Mather, *Bolometers: ultimate sensitivity, otpimization, and amplifier coupling*, Appl. Opt. **23**(4) (1984) 584.

[115] E. E. Haller, *Advanced far-infrared detectors*, Infrared Phys. Technol. **35**(2/3) (1994) 127-146.

[116] J. Zhang, *Hopping conduction in doped silicon and germanium: studies of their application as thermometers for x-ray calorimeters*, Tesi di Dottorato, University of Wisconsin-Madison, 1993.

[117] J. Zhang, W. Cui, M. Juda, D. McCammon, R. L. Kelley, H. Moseley, C. K. Stahle, e A. E. Szymkowiak, *Hopping conduction in partially compensated doped silicon*, Phys. Rev. **B48** (1993) 2312.

[118] J. Zhang, W. Cui, M. Juda, D. McCammon, R. L. Kelley, H. Moseley, C. K. Stahle, e A. E. Szymkowiak, *Non-ohmic effects in hopping conduction in doped silicon and germanium between 0.05 and 1 Kelvin*, bozza, Agosto 1995.

[119] P. E. Gregers et al., *Sign of the quadupole interaction in rhenium metal*, Phy. Rev. Lett. **27** (1971) 38.

[120] S. Tamura, *Spontaneous decay rates of LA phonons in quasi-isotropic solids*, Phys. Rev. **B31** (1985) 2574.

[121] Th. Peterrains, J. Jochum, F. Pröbst, F. v. Feilitzsch, H. Kraus e R. L. Mössbauer, *Nonequilibrium phonon detectors*, J. Appl. Phys. **69**(4) (1991) 1791.

[122] F. Pröbst, M. Frank, S. Cooper, P. Colling, D. Dummer, P. Ferger, A. Nucciotti, W. Seidel e L. Stodolsky, *Model for cryogenic particle detectors with superconducting phase transition thermometers*, J. Low Temp. Phys. **100** (1995) 69.

[123] A. Giuliani, *Studio e sviluppo di calorimetri a bassa temperatura per la ricerca di decadimenti rari e di particelle interagenti debolmente*, Tesi di Dottorato, Università di Milano (1989).

[124] S. B. Kaplan, *Quasiparticle and phonon lifetimes in superconductors*, Phys. Rev. **B14** (1976) 4854.

[125] L. D. Landau e E. M. Lifshitz, *Statistical Physics*, Pergamon, Londra (1980).

[126] S. Vitale, G. Gallinaro e F. Gatti, *Alpha- beta- and gamma-ray detection with microcalorimeters made with superconducting absorbers*, in "EUV, X-ray and γ-ray Instrumentation for Astronomy III", proceedings di SPIE **1743** (1992) 368.

[127] P. Colling, A. Nucciotti, C. Bucci, S. Cooper, P. Ferger, M. Frank, U. Nagel, F. Pröbst e W. Seidel, *Low-energy X-ray detection in cryogenic detectors with tungsten thermometers*, Nucl. Instr. and Meth. **A354** (1995) 408.

[128] K. D. Irwin et al., *A hot electron microcalorimeter for X-ray detection using a superconducting transition edge sensor with electrothermal feedback*, nei proceeding di LTD-6 [104].

[129] A. Alessandrello, D. V. Camin, E. Fiorini, A. Giuliani, M. I. Buraschi, G. U. Pignatel, *Study of new silicon bolometers for calorimetric particle detection*, nei proceedings del "Second european workshop on low temperature detectors: Low temperature detectors for neutrinos and dark matter II", LAPP, Annecy, Francia, 2-6 Maggio 1988, Editions Frontières.

[130] M. I. Buraschi, G. U. Pignatel e S. Sanguinetti, *Low-temperature conductivity behaviour of ion implanted silicon bolometers*, J. Phys.: Condens. Matter **2** (1990) 10011.

[131] S. M. Sze, *Semiconductor devices. Physics and technology*, Wiley & Sons, New York (1985).

[132] A. Maglione, *Progetto e realizzazione di bolometri integrati di silicio*, Tesi di Laurea, Università di Trento (1991).

[133] F. Pedrolli, *Studio e caratterizzazione a basse temperature di bolometri integrati in silicio*, Tesi di Laurea, Università di Trento (1992).

[134] A. Merlini, *Studio di bolometri al silicio per la misura della massa dell'antineutrino elettronico*, Tesi di Laurea, Università di Milano (1992).

[135] A. Alessandrello, C. Brofferio, D. V. Camin, C. Cattadori, O. Cremonesi, E. Fiorini, E. Garcia, A. Giuliani, M. Pavan, G. Pessina, E. Previtali e L. Zanotti, *Optimization of Si-implanted thermistors for high resolution calorimeters to be used in a neutrino mass experiment*, J. Low. Temp. Phys. **93** (1993) 185-858.

[136] M. Sisti, *Sviluppo di microcalorimetri a bassa temperatura per lo studio del decadimento beta*, Tesi di Laurea, Università di Milano (1994).

[137] R. L. Kelley, comunicazione privata.

[138] R. C. Richardson e E. N. Smith, *Experimental techniques in condensed matter physics at low temperatures*, Addison-Wesley, Reading (1988).

[139] S. G. O'Hara e A. C. Anderson, *Resonant scattering of thermal phonons by dislocations in superconducting aluminum*, Phys. Rev. **B9** (1974) 3730.

[140] R. M. Mueller et al., *Superconducting aluminum heat switch and plated press-contacts for use at ultralow temperatures*, Rev. Sci. Instrum. **49**(4) (1978) 515.

[141] A. Alessandrello, C. Brofferio, C. Bucci, D. V. Camin, O. Cremonesi, A. Giuliani, D. Geunzani, A. Nucciotti, M. Pavan, G. Pessina e E. Previtali, *Differential, voltage sensitive preamplifiers for bolometric detectors* presentato alla conferenza "Sixth International Workshop on Low Temperature Dtectors LTD-6", Beatenberg/Interlaken, Svizzera, 28 Agosto-1 Settembre 1995, i cui proceedins saranno pubblicati in Nucl. Instr. and Meth. **A**.

[142] Il disegno del preamplificatore criogenico è in gran parte ispirato all'analogo dispositivo sviluppato dai gruppi della collaborazione NASA/Wisconsin e descritto nei dettagli da R. L. Kelley e dai suoi collaboratori durante una visita ai laboratori NASA/GSFC nel Maryland.

[143] C. K. Stahle, *The development of high resolution calorimetric X-ray detectors for Compton scattering experiments*, Tesi di Dottorato, Standford University (1991).

[144] R. L. Kelley, comunicazione personale.

[145] M. Silva, *Realizzazione di microcalorimetri per la misura della massa del neutrino*, Tesi di Laurea, Università di Milano (1995).

[146] N. E. Phillips, *Heat capacity of aluminum between 0.1°K and 4.0°K*, Phys. Rev. **114** (1959) 676.

[147] R. L. Kelley, S. H.Moseley, C. K. Stahle, A. E. Szymkowiak, M. Juda, D. McCammon e J. Zhang, *Development of microcalorimeters for high resolution X-ray spectroscopy*, J. Low. Temp. Phys. **93** (1993) 225.

[148] C. Enss, A. Fleischmann, K. Horst, J. Schönefeld, J. Sollner, J.S. Adams, Y.H. Huang, Y.H. Kim, G.M. Seidel, J. Low Temp. Phys. **121**, 137 (2000)

[149] A. Fleischmann, C. Enss, G.M. Seidel, in *Cryogenic Particle Detection*, (ed. C. Enss), Topics Appl. Phys. **99**, 149 (Springer Berlin Heidelberg 2005)

[150] A. Fleischmann, T. Daniyarov, H. Rotzinger, C. Enss, G.M. Seidel, Physica B**329-33**, 1594 (2003).

[151] G. Hölzer, M. Fritsch, M. Deutsch, J. Hartwig, E. Förster, Phys. Rev. A **56**, 4554 (1997)

[152] P.K. Day, H.G. LeDuc, B. Mazin, A. Vayonakis, J. Zmuidzinas, Nature Vol. 425, Issue 6960, 817-821 (2003)

[153] B. Mazin, P.K. Day, J. Zmuidzinas, H.G. Leduc, LOW TEMPERATURE DETECTORS: Ninth International Workshop on Low Temperature Detectors. AIP Conference Proceedings, Volume 605, 309-312 (2002)

[154] B. Mazin, PhD Thesis, Caltech (2004). http://etd.caltech.edu/etd/available/etd-10042004-120707/

[155] K. Shwetank et al., American Physical Society, APS March Meeting, March 13-17, abstract B38.002 (2006)